A Theoretical Study of circadian clocks and circadian metabolism

MICHELE MONTI

This thesis was reviewed by:

Prof. dr. F. J. Bruggeman	Vrije Universiteit Amsterdam
Prof. dr. I. Axmann	Heinrich-Heine-Universität Düsseldorf, Germany
Prof. dr. J. Garcia-Ojalvo	Universitat Pompeu Fabra Barcelona, Spain
Dr. R. Hermsen	Universiteit van Utrecht
Dr. I. Van Stokkum	Vrije Universiteit Amsterdam

The research described in this thesis was performed at AMOLF, Science Park 104, 1098 XG Amsterdam, The Netherlands. This work is part of the research programme of the Foundation for fundamental Research on Matter (FOM), which is part of the Netherlands Organization for Scientific Research.

Cover Illustration: Hourglass towards synchronization.
Cover Design: Francesca Barchiesi, 2018
Printed by: Ipskamp, Amsterdam, The Netherlands

ISBN 978-94-92323-17-0
Titel: A Theoretical study of circadian clocks and circadian metabolism

A digital copy of this thesis is available online at `www.ub.vu.nl` and `www.amolf.nl`.
Printed copies can be obtained by request via `library@amolf.nl`.

VRIJE UNIVERSITEIT

A THEORETICAL STUDY OF CIRCADIAN CLOCKS AND CIRCADIAN METABOLISM

ACADEMISCH PROEFSCHRIFT

ter verkrijging van de graad Doctor of Philosophy
aan de Vrije Universiteit Amsterdam,
op gezag van de rector magnificus
prof.dr. V. Subramaniam,
in het openbaar te verdedigen
ten overstaan van de promotiecommissie
van de Faculteit der Bètawetenschappen
op donderdag 12 april 2018 om 11.45 uur
in de aula van de universiteit,
De Boelelaan 1105

door

Michele Monti

geboren te Rome, Italie

promotor:	prof.dr. P.R. ten Wolde prof.dr K.J. Hellingwerf
copromotor:	prof.dr. D.K. Lubensky

Il mare è appena increspato e piccole onde battono sulla riva sabbiosa. Il signor Palomar è in piedi sulla riva e guarda un'onda. Non che egli sia assorto nella contemplazione delle onde. Non è assorto, perchè sa bene quello che fa: vuole guardare un'onda e la guarda. Non sta contemplando, perchè per la contemplazione ci vuole un temperamento adatto, uno stato d'animo adatto e un concorso di circostanze esterne adatto: e per quanto il signor Palomar non abbia nulla contro la contemplazione in linea di principio, tuttavia nessuna di quelle tre condizioni si verifica per lui. Infine non sono "le onde" che lui intende guardare, ma un'onda singola e basta: volendo evitare le sensazioni vaghe, egli si prefigge per ogni suo atto un oggetto limitato e preciso.

[The sea is barely wrinkled, and little waves strike the sandy shore. Mr. Palomar is standing on the shore, looking at a wave. Not that he is lost in contemplation of the waves. He is not lost, because he is quite aware of what he is doing: he wants to look at a wave and he is looking at it. He is not contemplating, because for contemplation you need the right temperament, the right mood, and the right combination of exterior circumstances; and though Mr. Palomar has nothing against contemplation in principle, none of these three conditions applies to him. Finally, it is not "the waves" that he means to look at, but just one individual wave: in his desire to avoid vague sensations, he establishes for his every action a limited and precise object.]

— Italo Calvino *Palomar*

CONTENTS

1

INTRODUCTION

1.1. BIOLOGICAL QUESTIONS AND BACKGROUND

All organisms on our planet live in a rhythmic environment, arising from the light-dark cycle set by the sun. Evolution has driven many organisms to develop strategies to actively interact with this cycle. Indeed, many organisms, in essentially all kingdoms of life, have synchronized their cellular and behavioural activities with the day-night cycle. It is generally believed that this synchronization provides a fitness benefit, although this benefit has rarely been quantified experimentally.

In order to synchronize its activities with the day-night cycle, the organism needs to know the time of the day. To this end, many organisms, ranging from cyanobacteria to fungi, plants, insects and mammals, have developed a circadian clock. A circadian clock is a biochemical oscillator that can tick autonomously, i.e. in the absence of any driving, with an intrinsic clock period that is approximately 24 hours. The clock is formed by biomolecules, such as proteins and DNA, that chemically and physically interact with one another in what is called a biochemical network. These interactions generate oscillations in the concentrations or activities of the biomolecules, and it is these oscillations that encode the information on time. Because chemical reactions and physical interactions are fundamentally probabilistic in nature, clocks are inherently noisy. Moreover, the clocks are read out by biochemical networks downstream of the clock, which are also stochastic in nature. This raises one of the overarching questions of this thesis, which is how organisms can reliably estimate the time of the day.

Because clocks are inherently noisy, they tend to run out of phase with their environment, which would lead to the loss of information on time. To keep the clock in phase with the day-night cycle, clocks are coupled to daily cues from the environment, such as light, temperature, or even nutrients. This coupling "entrains" the clock, such that the oscillations of its components have a fixed phase relationship with the external day-night rhythm. Indeed, all circadian clocks exhibit this phenomenon of phase locking. This locking behaviour is characterized by a so-called phase-response curve, which describes how much the clock is pushed forward or pulled backwards by the input signal as

a function of the phase of the clock. While these phase-response curves can have complex shapes, they often share features such as a "dead zone": a phase window or interval, in which the coupling of the clock to the input signal is very weak. What determines the shape of the phase-response curve is a wide-open question, which is studied in detail in this thesis.

While it is generally believed that circadian behaviour provides a fitness benefit for organisms living in a circadian environment, this benefit has rarely been quantified. One interesting exception is provided by the prokaryotic cyanobacteria, which is the model organism of this thesis. Cyanobacteria perform photosynthesis during the day, and, indeed, many cyanobacteria possess a circadian clock to anticipate the changes between day and night. Johnson and co-workers competed wild-type cells against mutant cells with different clock periods and against arrhythmic strains that harbour an impaired clock [38, 39]. The wild-type cells rapidly out-competed the arrhythmic cells when the cells were exposed to cycles of 12 hours of light followed by 12 hours of darkness (so called LD 12:12 cycles). Yet, when they were grown in constant light conditions (LL), the arrhythmic strain grew slightly faster than the wild-type cells [39]. These observations indicate that the clock may confer a fitness benefit, but only if the organism lives in a circadian environment. In another set of experiments, mutants with different clock periods were competed with wild-type cells and with each other, in light-dark cycles of varying period lengths [38, 39]. The striking finding was that the strains that were in circadian resonance, having a clock period that matches the period of the light-dark cycle, won the competition. All cultures were subjected to equal average light intensity, which is important since light is the principal energy source of cyanobacteria; indeed, only the frequency of the cycles differed. These experiments thus vividly demonstrated that in rhythmic environments, the strain that grows in resonance with the environment, tends to have the highest growth rate.

While the experiments of Johnson and co-workers [38, 39] show that circadian behaviour can provide a fitness benefit to cells living in a circadian environment, the origin of the benefit remains poorly understood. Cyanobacteria perform photosynthesis during the day to fix the carbon atoms in CO_2. Yet, during the day not all the fixed carbon atoms are used for protein synthesis, energy generation and hence cellular growth: a fraction is stored in the form of a large polymer called glycogen, which then provides the principal source of carbon during the night. In fact, some types of cyanobacteria not only fix carbon, but also nitrogen, in the form of another polymer, cyanophycin. Moreover, because nitrogen fixation involves an enzyme which is intolerant to oxygen—a product of photosynthesis—nitrogen fixation happens during the night. These cells thus fix carbon during the day, yet nitrogen during the night. Clearly, these cells have to dramatically repartition their proteome every 12 hours. However, how the cyanobacteria should adjust their proteome, how much glycogen and cyanophycin they should store, and how this affects their growth rate, are questions that so far have not been answered.

In this thesis, I first use mathematical modelling and computer simulations to investigate the optimal design of circadian clocks to estimate the time of the day. I then address the question how the capacity to estimate the time provides a fitness benefit by studying circadian metabolism. In chapter 2, I consider the scenario where a clock drives a number of readout systems, and then ask the question how the capacity to infer the

time depends on the number of oscillatory readout signals. I show that the knowledge on time increases with the number of readout signals, and that there exists an optimal phase relation between the oscillatory readout signals that maximizes the precision on time.

In chapter 3, I investigate the optimal coupling of circadian clocks to entrainment signals such as light, in the presence of internal noise. Perhaps the most surprising result is that the precision of estimating the time does not increase monotonically with the coupling strength: there exists an optimal coupling strength that maximizes the precision. Yet, the optimal coupling strength does increase with the strength of the internal noise. I also find that the optimal intrinsic clock period can differ significantly from 24 hrs, depending on the coupling strength and the noise in the system. Also the optimal width of the dead zone of the phase-response curve depends on the noise in the system. I then show that all these results can be understood as a trade-off between linearity and stability. Finally, I show that the system can be described by three different theories, which each apply in a different parameter regime.

While many cyanobacterial cells possess a bonafide circadian clock that can run autonomously in the absence of any driving, some cyanobacterial species possess what is called an hour-glass, which relies on periodic driving by the entrainment signal to exhibit oscillations from which the time can be inferred. In chapter 4, I address why some species have evolved a bonafide clock while others have evolved an hour-glass clock. The hypothesis is that the answer depends on the noise in the input signal: clouds, for example, will lead to fluctuations in one of the most important entrainment cues, light. By performing extensive stochastic simulations of different mathematical models of cyanobacterial clocks, I show that when the input noise is weak, both a bonafide clock and an hour-glass clock perform equally well; yet, when the noise in the input signal is large, then the bonafide circadian clock is a much more accurate timekeeper. My results thus suggest that bonafide clocks have evolved, because they allow organisms to accurately estimate the time even in the presence of large fluctuations in the input signal. I end this chapter by analysing a generic model of a weakly non-linear oscillator. This analysis shows that my findings are universal, i.e. independent of the details of the clock design.

In chapter 5, I study circadian metabolism. To this end, I employ the framework that Hwa and co-workers have developed to describe the relation between growth and proteome composition in the bacterium *Escherichia coli* [40]. This framework provides a coarse-grained description of the proteome in terms of quantities that can be measured experimentally. In the past years, it has been successfully applied to a range of problems [40–43] and very recently it has been demonstrated that it can even capture the transient proteome dynamics in response to a nutrient shift [44, 45]. I here extend this framework to describe the circadian metabolism of cyanobacteria. The model includes the dynamics of the carbon and nitrogen reservoirs, as well as the relaxation of the proteome after the shift from day to night and vice versa. I first show that the bacterial growth laws [40], together with the need to build a carbon and/or nitrogen reservoir, tend to generate an extreme growth strategy, in which the cells predominantly grow during the day, as observed experimentally. However, cyanobacteria grow relatively slowly, with cell-division times that are on the order of 24 hours, which means that the relaxation of their pro-

teome after the change from day to night and vice versa will be slow. As my results show, this puts a severe constraint on implementing the optimal growth strategy. Interestingly, however, their circadian clock allows these cyanobacteria to anticipate the changes between day and night, and hence start adjusting the proteome before the end of the day and night. Indeed, my analysis reveals that anticipation not only enhances the average growth rate, but makes it in fact possible to effectively implement the optimal growth strategy.

In the following section, I first discuss the key concepts from information theory, which are used throughout my thesis. I then provide an overview of my thesis, with a more detailed discussion of the main results.

1.2. INFORMATION THEORY

One of the main goals of this thesis is to elucidate the design principles of circadian clocks. A central performance measure is a concept from information theory. It is widely recognized that organisms need to infer the time from the concentrations of the clock components. This inference will be imprecise, because of the noise in the clock. We will quantify the accuracy of information transmission via the mutual information, which is a measure for how many distinct time states can be resolved from the concentrations of the clock components. In this section, I will introduce the concept of mutual information and illustrate it with some simple examples.

1.2.1. INFORMATION IN BIOCHEMICAL NETWORKS

Life depends on how much information and energy flows through biochemical networks. Information theory is a general framework that can be applied to any stochastic system to quantify the amount of information that is transmitted through the system. It has been applied to a wide range of biological problems ranging from gene expression to neural networks [31, 32, 46–62]. In this thesis we have used this theory to quantify the amount of information that cells possess on time. Below, we introduce the key quantities of information theory often used in the following chapters.

In statistical mechanics, it is possible to define the uncertainty in the specification of a physical system through its entropy:

$$H[P(x)] = -\int dx P(x) \log P(x) \tag{1.1}$$

where $P(x)$ is the probability that the system is in state x.

It is possible to show that in a system with N different states, the uncertainty is maximal when $P(x)$ is uniform, $P(x) = 1/N$. We then have:

$$P(x) = 1/N \Longrightarrow H[P(x)] = \log N. \tag{1.2}$$

We can recognize the expression above as the entropy of a micro-canonical system. The entropies in other ensembles, including the canonical ensemble, are then obtained via a Legendre transform. Physically, these transformations correspond to different additive constraints on the system. For example, the canonical ensemble keeps the temperature constant while allowing fluctuations in the energy of the microstates. In this ensemble,

$P(x)$ is not uniform, but follows the Maxwell-Boltzmann distribution. Therefore, there are some states that appear more likely than others, as a result of which the uncertainty is reduced compared with the micro-canonical case. Indeed, it is clear that the canonical ensemble, compared to the micro-canonical one, contains the information about temperature, so the uncertainty on the determination of the current state of the system is lower.

Following this definition, in 1948 Shannon [63] has associated the uncertainty with the maximum amount of information that can be gained from a physical system. Shannon's uniqueness theorem leaves open a choice of units, for instance if we want to use the bits, the logarithm has to be in base two.

Going more in details, given two variables, e.g. to physical degrees of freedom s and x, it is possible to define the uncertainties for both of them, $H(s)$ and $H(x)$, respectively. Thus, if these physical degrees of freedom are connected and the variables thus correlated, there is a (unique) distribution of x given a fixed value of s. This probability is given by the conditional distribution $P(x|s)$. In turn it is possible to define the uncertainty for the output x given the input s:

$$H[P(x|s)] = -\int dx P(x|s) \log P(x|s). \tag{1.3}$$

The difference between the two entropies is how much our uncertainty about x has been reduced by knowing s. It can be interpreted as the information that we gain on the value of x by knowing the value s:

$$I(x;s) = H[P(x)] - H[P(x|s)] \tag{1.4}$$

The definition of mutual information between s and x is the average information that we get from the knowledge of s on x, so Eq. 1.4 has to be averaged over $P(x)$:

$$I(x;s) = \int dx P(x)(H[P(s)] - H[P(s|x)]). \tag{1.5}$$

Calling $P(s,x)$ the joint distribution between s and x, and using Bayes rule,

$$P(s,x) = P(x|s)P(s) = P(s|x)P(x), \tag{1.6}$$

it is possible to show that

$$I(s;x) = \int ds \int dx P(s,x) \log \frac{P(s,x)}{P(s)P(x)}. \tag{1.7}$$

Eq.1.7 allows us to make a few points that are worthy of note:

- $I(s;x)$ is symmetric in s and x: the information that flows from s to x is the same that flows from x to s:
$$I(s;x) = I(x;s)$$
- If s and x are independent variables, the joint distribution factorizes:
$$P(s,x) = P(s)P(x)$$
so the information that you can gain from the knowledge of one variable to the other is 0.

- $I(s,x)$ is maximized by $H[P(s)]$ and $H[P(x)]$:

$$I(s;x) \leq H(s), \tag{1.8}$$
$$I(s;x) \leq H(x) \tag{1.9}$$

  This means that it is not possible to reduce the uncertainty more than the intrinsic uncertainty of the variables involved.

- It can be defined for continuous or discrete quantities.

- It is re-parametrization invariant:

$$I(s;x) = I(h(s);f(x)) \tag{1.10}$$

  This feature of mutual information is important because other statistical measures, like correlation coefficients, depend on transformations of the data.

- It obeys data processing inequality. Assuming that there are three variables where x depends on s and k depends on x, $s \to x \to k$, the mutual information respects the following intuitive inequalities:

$$I(s;k) \leq I(x;k), \tag{1.11}$$
$$I(s;k) \leq I(s;x) \tag{1.12}$$

  Loosely speaking, in each step of a physical system's chain, information can only be lost.

- The mutual information between variables s and x is related to the correlation between them. Yet, the mutual information goes beyond the concept of correlation, as elucidated in Figure 1.1. Indeed, there are cases where the mutual information is different from 0 but the correlation is not.

1.2.2. INPUT-OUTPUT RELATION

Here I would like to present a simple application of information theory, regarding the information that flows between an input and an output signal. We consider a physical system with some input signal s, an output signal x and some functional relation between them, $x = f(s,\eta)$ where η represents the noise in the system that corrupts the mapping from s to x.

For simplicity, we consider the relation between s and x to be linear:

$$x = gs + \eta, \tag{1.13}$$

where g is the gain. We will consider the noise to be Gaussian such that

$$P(\eta) = P(x|s) = \frac{1}{\sqrt{2\pi\sigma^2}} e^{-\frac{(x-gs)^2}{2\sigma^2}} \tag{1.14}$$

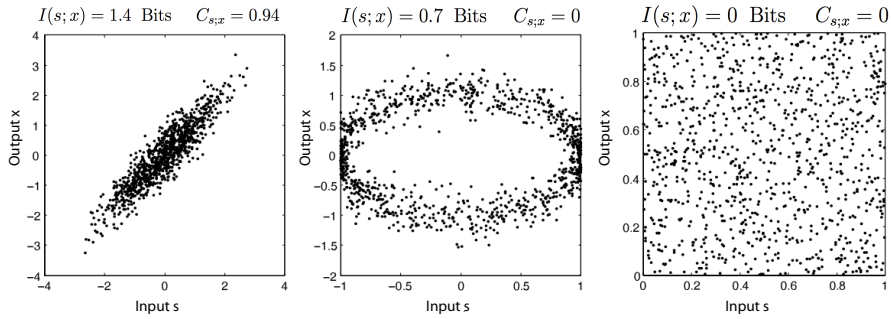

Figure 1.1: *Mutual information between two variables s and x for different systems. In the left panel it is seen that the two variables are linearly correlated and both the mutual information $I(s;x)$ and the correlation coefficient $C_{s,x}$ are different from 0. In the center panel we can appreciate a case where the mutual information is different from 0 even though the correlation between s and x is 0 (see [53]). The right panel shows a case where both the mutual information and the correlation coefficient are 0.*

The Gaussian approximation introduced above will often be used in this thesis. Moreover, let us assume that the input signal s is Gaussian with variance σ_{ss}^2. This means that the joint distribution $p(s,x) = p(x|s)p(s)$ has the canonical Gaussian form:

$$p(s,x) = \frac{1}{2\pi\sqrt{|\mathbf{Z}|}} \exp\left[-\frac{1}{2}(s \quad x)\,\mathbf{Z}^{-1}\begin{pmatrix} s \\ x \end{pmatrix}\right] \tag{1.15}$$

$$= \frac{1}{2\pi\sqrt{|\mathbf{Z}|}} e^{-\frac{1}{2|\mathbf{Z}|}(\sigma_{ss}^2 x^2 + \sigma_{xx}^2 s^2 - 2\sigma_{sx}^2 sx)}, \tag{1.16}$$

with $\mathbf{Z}$ the variance-covariance matrix

$$\mathbf{Z} = \begin{pmatrix} \sigma_{ss}^2 & \sigma_{sx}^2 \\ \sigma_{sx}^2 & \sigma_{xx}^2 \end{pmatrix}. \tag{1.17}$$

Here, the variance of the output x is $\sigma_{xx}^2 = \sigma^2 + g^2\sigma_{ss}^2$ while the covariance $\sigma_{sx}^2 = g\sigma_{ss}^2$. The determinant is given by $|\mathbf{Z}| = \sigma_{ss}^2\sigma_{xx}^2 - \sigma_{sx}^4 = \sigma_{ss}^2\sigma^2$.

For this model, the mutual information is then

$$I(s;x) = H(x) - H(x|s) \tag{1.18}$$

$$= \frac{1}{2}\log_2\left[1 + \frac{g^2\sigma_{ss}^2}{\sigma^2}\right]. \tag{1.19}$$

The quantity $g^2\sigma_{ss}^2/\sigma^2$ can be interpreted as a signal-to-noise ratio, illustrating that the mutual information can be related to that quantity. This simple example illustrates that the mutual information depends not only on the noise in the system, as quantified by σ^2, but also on the input-output relation, here assumed to be linear with slope (gain) g, and the input distribution, here assumed to be Gaussian with variance σ_{ss}^2. The mutual information decreases as the noise σ^2 increases, while it increases not only with the

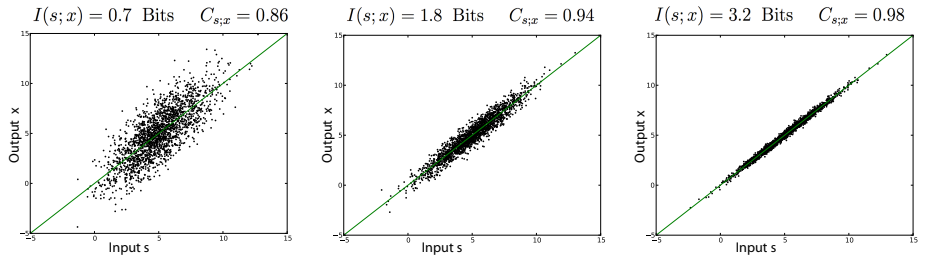

Figure 1.2: *Linear input-output relation between two variables s and x, with gain $g = 1$. Clearly, the lower the noise, the higher the mutual information.*

width of the input distribution σ_{ss}^2 but also with the gain g because that helps to raise the signal above the noise.

By noting that the correlation coefficient r_{sx} is defined as $r_{sx}^2 \equiv \sigma_{sx}^4/(\sigma_{ss}^2\sigma_{xx}^2)$, the above expression can be rewritten as

$$I(s;x) = -\frac{1}{2}\log(1 - r_{sx}^2). \tag{1.20}$$

Indeed, for a Gaussian model, the mutual information is also given by the correlation coefficient.

Figures 1.1 and 1.2 help to develop an intuitive understanding of the mutual information. When the input-output relation is very noisy, it is very difficult to infer from x what s is, and vice versa, and hence the mutual information will be low. Yet, when the noise decreases, the mapping between s and x becomes more unique and the mutual information increases.

1.3. OVERVIEW

In chapter 2, I address the question how accurately a cell can infer the time from an ensemble of protein oscillations, which are driven by a circadian clock. The instantaneous value of the oscillatory concentration of one protein does not make it possibly to uniquely infer the time, because one concentration level can correspond to at least two moments in time. However, this ambiguity can be resolved when the time is inferred from more than one protein concentration. Interestingly, it is known that in the cyanobacterium *S. elongatus*, the clock drives the expression of multiple genes, raising the question how the reliability of inferring time depends on the number of readout proteins. By combing mathematical modelling with information theory, I show that the accuracy increases with the number of protein oscillations and their amplitude relative to their noise. This analysis also reveals that there exists an optimal phase relation that minimizes the error in the estimate of time, which depends on the relative noise levels of the protein oscillations. I also show that cross-correlations in the noise of the protein oscillations can enhance the mutual information, which suggests that cross-regulatory interactions between the proteins that read out the clock can be beneficial for temporal information transmission.

In chapter 3, I study the optimal coupling of a noisy clock to an entrainment signal such as light or temperature. Due to internal noise, the clock will inevitably run out of phase with the environment if it is not coupled to the driving input signal. Yet, while it is clear that entrainment is essential, it is far less obvious how the clock should be coupled to the entrainment signal: What is the optimal shape of the coupling function, i.e. phase response curve, that maximizes the accuracy of telling time? More specifically, why do many phase-response curves feature a so-called dead zone (a phase interval in which the coupling strength is zero)? And how large should the coupling strength be? Because these are very generic questions that apply to all circadian clocks, here I address this question by studying the most generic model of a clock: a stochastic phase oscillator that is coupled to an input signal. In this model, the clock is described by a single phase variable that evolves as a result of 1) a fixed driving force, corresponding to the intrinsic frequency of the clock; 2) the coupling to the input signal as characterized by a phase-response curve; 3) a stochastic force that mimicks the internal noise arising from the stochastic nature of the chemical and physical interactions between the clock components. The first surprising result is that the accuracy of telling time does not monotonically increase with the coupling strength, as one might expect intuitively: there exists an optimal coupling strength that maximizes the fidelity. The optimal coupling strength does, however, increase with the noise in the system. The second result is that the optimal intrinsic period of the clock is, in general, not equal to 24 hour: depending on the noise in the clock, it can either be larger or smaller. The third result is that the optimal phase-response curve can, depending on the noise in the clock, exhibit a dead-zone; this suggests that the shape of the phase-response curve has evolved to maximize information transmission. In this chapter I also show that the optimal design of the phase response curve can be understood as arising from a trade-off between linearity and stability: when the clock is inherently stable, the coupling should be weak so that the phase evolves linearly with time (this maximizes the number of distinct time points that can be inferred), while if the clock is inherently noisy, it needs to be coupled more strongly. Finally I show that the clock can be described by different theories—phase averaging method, linear-response theory, linear-noise approximation—which each apply in a different parameter regime.

In chapter 4, I try to answer to a very fundamental question: why do some organisms have a circadian clock at all? Even when we accept the premise that it is beneficial for the organism to know the time, which is not entirely obvious as discussed below, then it is still not clear that a bonafide clock is necessary. The central idea here is that if the entrainment signal (e.g. light) would be very stable, there would be no need for a clock: the stable signal could simply drive a passive system, and the oscillatory nature of the stable signal would generate a stable oscillatory output signal of the response system, which could then act as a clock. Indeed, the hypothesis of this project is that bonafide clocks, which exhibit free-running rhythms, only evolve when the input signal is sufficiently noisy (clouds, for example, make the light signal stochastic). Inspired by the different types of clocks in cyanobacteria, I have tested this hypothesis by performing simulations of three types of systems: 1) a push pull network; 2) an ensemble of KaiC hexamers (the central components of the cyanobacterial clock) that are not coupled to each other and hence cannot generate free-running oscillations, but can yield stable oscillations when

coupled to light; 3) an ensemble of KaiC hexamers that are coupled to each other, such that they can generate stable, free running oscillations even when they are not coupled to light. The simulations reveal that when the input signal is stable, all three systems yield stable oscillations from which the time can be inferred accurately. Yet, when the input becomes very noisy, the first two systems fail to act as a reliable clock, and only the third system makes it possible to reliably infer the time of the day from the phase of the clock. While these results provide strong support for our hypothesis, I then developed an analytical framework in order to understand the physical principles of these results. I studied a Stuart-Landau model with noise in the input signal. Using the linear-noise approximation, I analytically derive the variance of the clock output, which makes it possible to compute the mutual information between the output of the system and time. This description provides a general analysis of why a limit cycle oscillator is intrinsically more robust to input noise than a damped oscillator.

In chapter 5, I describe the physical principles of circadian metabolism. The light-dark rhythm drives the metabolism of many, if not most, organisms. A striking example is provided by cyanobacteria, which exhibit photosynthesis during the day. Importantly, to fuel the metabolic activities during the night, they need to store glycogen during the day. Moreover, some cyanobacteria also need to store nitrogen during the night, in order to grow during the day. It is not obvious how much they should store in order to maximize the growth rate. Moreover, it is far from clear how fast they should grow during the day and the night so as to maximize the average growth rate over 24 hours. Inspired by the approach developed by Hwa and coworkers [40], I have developed a coarse-grained model of the proteome. While this model is highly coarse-grained, it does enable clear testable predictions, concerning for example how the ribosome fraction and the growth rate varies with the quality of the nutrient source. Moreover, while the model is applied to the problem of storing glycogen during the day and fixing nitrogen during the night, the results are much more generic. Indeed, this framework could, e.g., also be applied to the scenario where the organism only builds a store during the day to fuel processes during the night, but not the converse. The model reveals an interesting growth strategy, which at least some cyanobacteria seem to pursue: when, by storing more nitrogen during the night, the benefit of growing faster during the day outweighs the cost of growing slower during the night, then the optimal strategy is to hardly grow at all during the night: this enhances the growth rate during the day so that the average growth rate over 24 hours is maximized. The model also makes it possible to address another question: when is it advantageous to know the time? The hypothesis here is that it becomes vital to know the time only when the response of the system to a change in the environment (i.e. day- night) is slow: if it were fast, it could simply respond and adapt, but if it is slow the organism must anticipate the change and mount a response before the change occurs. To address this question, I first show that in the absence of active protein degradation, the time-scale for adjusting the proteome is set by the growth rate. The proteome relaxation time is thus given by the cell division time, which is often on the order of the clock period (24 hrs). This means that proteome relaxation is slow, which means that anticipation becomes important. I then show that the average growth rate is indeed strongly enhanced when the cells exploit their knowledge of time and mount a response before the change from day to night (and vice-versa) occurs. This is arguably the first modelling

result that shows that cells can grow faster by anticipating the daily changes in their environment.

2

THE ACCURACY OF TELLING TIME VIA OSCILLATORY SIGNALS

ABSTRACT

Circadian clocks are the central timekeepers of life, allowing cells to anticipate changes between day and night. Experiments in recent years have revealed that circadian clocks can be highly stable, raising the question how reliably they can be read out. Here, we combine mathematical modelling with information theory to address the question how accurately a cell can infer the time from an ensemble of protein oscillations, which are driven by a circadian clock. We show that the precision increases with the number of oscillations and their amplitude relative to their noise. Our analysis also reveals that their exists an optimal phase relation that minimizes the error in the estimate of time, which depends on the relative noise levels of the protein oscillations. Lastly, our work shows that cross-correlations in the noise of the protein oscillations can enhance the mutual information, which suggests that cross-regulatory interactions between the proteins that read out the clock can be beneficial for temporal information transmission.

INTRODUCTION

Among the most fascinating timing devices in biology are circadian clocks, which are found in organisms ranging from cyanobacteria and fungi, to plants, insects and animals. Circadian clocks are biochemical oscillators that allow organisms to coordinate their behaviour with the 24-hour cycle of day and night. Remarkably, these clocks can maintain stable rhythms for months or even years in the absence of any daily cue from the environment, such as light/dark or temperature cycles [64]. In multicellular organisms, the robustness can be explained by intercellular interactions [65, 66], but it is now known that even unicellular organisms can have very stable rhythms. An excellent example is provided by the clock of the bacterium *Synechococcus elongatus*, which is one of the most studied and best characterized model systems [64]. This clock has a corre-

lation time of several months [67], even though the clocks of the different cells in the population do not seem to interact with one another [67]. Clearly, the clock is designed in such a way that it has become resilient against the intrinsic stochasticity of the chemical reactions that constitute the clock [15, 28]. The observation that clocks can be very stable, suggests that they are also read out reliably. Yet, how cells could do so is a wide open question [68].

In this manuscript we combine information theory with mathematical modelling to study how accurately cells can infer time from cellular oscillators. While our analysis is general, it is inspired by the circadian clock of *S. elongatus*. The central clock component of *S. elongatus* is KaiC, which forms a hexamer [69]. KaiC has two phosphorylation sites per monomer, which are phosphorylated and dephosphorylated in a well-defined temporal order, yielding a protein-phosphorylation cycle (PPC) with a 24 hour period [12, 70]. This PPC is coupled to a transcription-translation cycle (TTC) of KaiC [71], which is a protein synthesis cycle with a 24 hr rhythm, via the response regulator RpaA. KaiC in the phosphorylation phase of the PPC activates the histidine kinase SasA, which in turn activates RpaA via phosphorylation [72–75]. In contrast, KaiC that is in the dephosphorylation phase of the PPC and bound to KaiB, activates the phosphatase CikA, which dephosphorylates and deactivates RpaA [74, 75]. Active, phosphorylated RpaA drives genome-wide transcriptional rhythms, which include the expression of the clock components [76].

Intriguingly, while time could be uniquely encoded in the modification state of the two phosphorylation sites of KaiC, cells do not seem to employ this mechanism [75, 76]. RpaA, the central node between the clock and the downstream genes, has only one phosphorylation site [75, 76]. This makes the question how accurately the cell can infer time a very pertinent one, because a single readout—the phoshorylation level of RpaA—leads to an inherent ambiguity in the mapping between time and clock output: a given level of active RpaA corresponds to two possible times (see Fig. 2.1). On the other hand, it is known that RpaA controls the expression of many downstream genes [76]. While their expression levels cannot contain more information about time than that which is available in the *time trace* of RpaA, it is possible that, collectively, their expression levels do contain more information about time than that present in the *instantaneous* level of RpaA.

In this manuscript, we study how the accuracy of telling time depends on the number of genes that read out a clock, their phase difference, the level of biochemical noise, and the cross-correlations between the gene expression levels. In the next section, we first describe the set up of our analysis, and then the measures that we employ to quantify information transmission. We then show that there exists an optimal phase difference that maximizes information transmission. Interestingly, the optimal phase difference depends on the amplitude of the noise in the expression of the readout genes, and on the cross-correlations between them, akin to what has been observed in neuronal coding [52] and in the gap-gene expression system of *Drosophila* [53, 56].

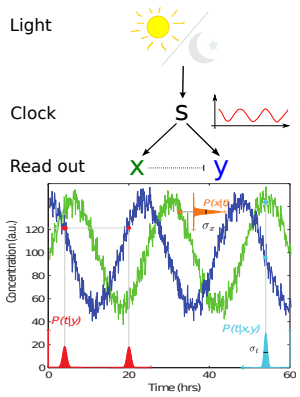

Figure 2.1: Cells can infer time from an ensemble of protein oscillations. The day-night rhythm entrains a circadian clock, a biochemical oscillator with a 24 hours period, which in turn drives the oscillatory expression of a number of readout genes. $P(x|t)$ (orange) is the conditional distribution of the protein concentration x given the time t, with σ_x its standard deviation. $P(t|y)$ (red) is the conditional distribution of the time t given the protein concentration y; importantly, this distribution is bi-modal, reflecting the idea that even for a perfect, deterministic, noise-free signal, a given concentration y maps onto 2 different time points, causing an inherent ambiguity in telling the time. This ambiguity can be lifted by using two proteins to tell time, as illustrated by $P(t|x,y)$, which is the conditional probability of t given the protein concentrations x and y, respectively. This distribution is uni-modal, meaning that the time, in the absence of noise, can be inferred uniquely. The standard deviation σ_t of this distribution is the error in the estimate of time, as indicated. The error depends on the amplitude of the oscillations, A_x and A_y, their variance σ_x^2, σ_y^2, their co-variance $\sigma_{x,y}^2$, and their phase shift $\Delta\phi = \phi_x - \phi_y$.

2.1. METHODS

2.1.1. MODEL

The analysis we present below applies to any readout system that obeys Gaussian statistics. Yet, to set the stage, and to introduce the key quantities that we will study, it is instructive to consider a concrete system. To this end, imagine an oscillatory clock protein, like RpaA, that drives the expression of a set of downstream genes. Assuming that the system can be linearized, the dynamics of the system is given by

$$\frac{d\mathbf{x}(t)}{dt} = \mathbf{f}s(t) + \mathbf{B}\mathbf{x}(t) + \xi(t). \tag{2.1}$$

Here $\mathbf{x}(t)$ is a vector with components $x_i(t)$, which denote the concentration x_i of protein X_i, $s(t)$ is the concentration of the clock protein, $\mathbf{f}$ is a vector with components f_i, which describe how the downstream protein X_i is driven by $s(t)$, $\mathbf{B}$ is the matrix that describes the regulatory interactions between the downstream proteins, and $\xi(t)$ is a vector with components $\xi_i(t)$ that describe the noise in the expression of X_i. In what follows, we imagine that the clock protein oscillates according to $s(t) = A_s \sin(\omega t) + r_s + \xi_s$, where A_s sets the amplitude of the oscillations, r_s its mean, and ξ_s describes the noise in the input signal.

This linear system can be solved analytically. For example, if the downstream genes do not interact with each other and protein X_i decays with rate μ_i, then each protein oscillates as

$$x_i(t) = A_i \sin(\omega t + \phi_i) + r_i + \eta_i(t), \tag{2.2}$$

where

$$\eta_i(t) = \int_{-\infty}^{t} dt' e^{-\mu_i(t-t')} \left[\xi_i(t') + f_i \xi_s(t')\right], \tag{2.3}$$

$$A_i = \frac{f_i A_s}{\sqrt{\mu_i^2 + \omega^2}}, \tag{2.4}$$

$$\phi_i = \arcsin\left(\frac{-\omega}{\sqrt{\mu_i^2 + \omega^2}}\right), \tag{2.5}$$

$$r_i = \frac{f_i r_s}{\mu_i}. \tag{2.6}$$

Importantly, even in this simple system, the difference in the phase ϕ between the expression of the downstream genes can be modulated, namely by changing the protein degradation rate μ_i. Also the amplitude A_i can be adjusted; it can be set independently from the phase via the synthesis rate f_i. Both quantities affect the precision by which the system can estimate the time.

Another key quantity is the noise in the expression of the downstream genes. Following the linear-noise approximation, we assume that the noise in the concentration x_i is Gaussian, such that

$$P(\eta_i) = P(x_i|t^*) = \frac{1}{\sqrt{2\pi\sigma_i^2}} e^{-\frac{(x_i - \bar{x}_i(t^*))^2}{2\sigma_i^2}} \tag{2.7}$$

where $\bar{x}_i(t^*)$ is the mean concentration of protein X_i at time t^*, $\sigma_i^2 = \sigma_i^2(t^*)$ is the variance of x_i around its mean $\bar{x}_i$, and t^* is the given time. The noise $\sigma_i^2(t)$ has an extrinsic contribution coming from the noise in the input signal, an intrinsic contribution from the noise in the expression of X_i, and a contribution from the regulatory interactions. Our analysis does not depend on the precise origins of these noise contributions: in the analysis below, we specify the variance $\sigma_i^2(t)$ and the co-variance of the fluctuations in x_i and x_j, and then study how this affects the precision of telling time. Yet, in general, we expect that $\sigma_i^2(t)$ depends on the mean $\bar{x}_i(t)$. If gene expression can be modelled as a Poissonian birth-death process, then $\sigma_i(t) = \sqrt{\bar{x}_i(t)}$; if, however, the noise in x_i is dominated by the noise in the input signal, the regulatory interactions, or by the noise in the promoter state, then $\sigma_i(t) \simeq \bar{x}_i(t)$ [77]. On the other hand, if the mean r_i of the protein oscillations is large compared to their amplitude A_i, then we may assume that $\sigma_i^2(t)$ is constant in time, $\sigma_i^2(t) = \sigma_i^2$. The value of σ_i^2 will depend on r_i, and hence $x_i(t)$. But how σ_i^2 depends on x_i is, in this scenario, relevant only to the extent that the precision of telling time depends on σ_i—the control variable is σ_i, not r_i itself. In the next section, we thus discuss three scenarios: 1) $\sigma_i(t) \simeq \sqrt{\bar{x}_i(t)}$; 2) $\sigma_i(t) \simeq \bar{x}_i(t)$; 3) $\sigma_i^2(t) = \sigma_i^2 =$ constant; for simplicity, we assume here that $\sigma_i = \sqrt{r_i}$, but different systems will give identical results as long as A_i and σ_i are the same.

As will become clear in the next section, the importance of noise depends on the amplitude of the oscillations: the key control parameter is the relative noise strength $\widetilde{\sigma}_i \equiv A_i/\sigma_i$. This ratio can be varied independently from gene to gene, $A_i/\sigma_i \neq A_j/\sigma_j$ in general, and below we will study how this affects the precision. If there is no noise in the input $s(t)$ and if the downstream proteins do not interact with each other (as in the example considered here), then the cross-correlation between the fluctuations of the concentrations of the downstream proteins is zero: $\langle \eta_i \eta_j \rangle = \langle \eta_i^2 \rangle \delta_{ij} = \sigma_i^2$, where δ_{ij} is the Kronecker delta. However, in general, the noise in the expression of the downstream genes will be correlated, which, as we will show, can either enhance or reduce the accuracy by which the downstream proteins can infer time.

Below, we will consider how the accuracy of telling time depends on the cross-correlations between the expression of the downstream genes, their phase difference, and on $\widetilde{\sigma}_i$, and how this varies from gene to gene.

2.1.2. RELIABILITY MEASURES

The central idea of our analysis is that the system infers the time from the collective expression of the N downstream proteins, $\{x_i\} \equiv \{x_1(t), x_2(t), \ldots, x_{N-1}(t), x_N(t)\}$. Following work on positional information in *Drosophila* [56], we use two approaches to quantify the accuracy on telling time. The first is based on the error in the estimate of a given time t, $\sigma_t(t)$; a related approach has been widely used to derive the fundamental limits on the accuracy of sensing [31, 78–92]. The second approach is based on the mutual information, which in recent years has been used extensively to quantify cellular information transmission [31, 32, 46–61].

THE ERROR IN ESTIMATING TIME

To determine the error in estimating the time, we start from the generalization of Eq. 2.7 to multiple downstream genes:

$$P(\{x_i\}|t) = \frac{1}{\sqrt{2\pi|\mathbf{C}|}} \exp\left[-\frac{1}{2}\sum_{i,j}^{N} \delta x_i C_{ij}^{-1} \delta x_j\right]. \tag{2.8}$$

Here $\delta x_i(t) = x_i(t) - \bar{x}_i(t)$, $\mathbf{C}$ is the covariance matrix with elements C_{ij}, $|\mathbf{C}|$ is its determinant and $\mathbf{C}^{-1}$ is its inverse.

The idea is now to invert the problem, and ask what is the distribution of possible times t, given that the expression levels are $\{x_i\}$. This can be obtained from Bayes' rule:

$$P(t|\{x_i\}) = P(t)\frac{P(\{x_i\}|t)}{P(\{x_i\})} \tag{2.9}$$

where $P(t) = \frac{1}{T}$ is the uniform prior probability of having a certain time and $P(\{x_i\})$ is the joint distribution of the expression levels of the downstream genes. If the noise η is small compared to the mean, then $P(t|\{x_i\})$ will be a Gaussian distribution that is peaked around $t^*(\{x_i\})$, which is the best estimate of the time given the expression levels [56, 93]:

$$P(t|\{x_i\}) \simeq \frac{1}{\sqrt{2\pi\sigma_t^2}} \exp\left[-\frac{(t - t^*(\{x_i\}))^2}{2\sigma_t^2}\right]. \tag{2.10}$$

Here $\sigma_t^2 = \sigma_t^2(t*)$ is the variance in the estimate of the time, and it is given by [56]

$$\sigma_t^{-2} \simeq \sum_{i,j}^{N} \left[\frac{d\bar{x}_i(t)}{dt} C_{ij}^{-1} \frac{d\bar{x}_j(t)}{dt} \right] \Bigg|_{t=t^*(\{x_k\})} \tag{2.11}$$

We first consider the scenario in which the noise in the expression of the downstream genes, η_i, is uncorrelated from one gene to the next. In this case **C** is a diagonal matrix where the diagonal elements are the variances of the respective protein concentrations: $C_{ii} = \sigma_i^2$. Substituting C_{ii} and Eq 2.2 in Eq 2.11 we find that

$$\sigma_t^{-2}(t) = \omega^2 \sum_{i=1}^{N} (A_i/\sigma_i)^2 \cos^2(\omega t + \phi_i). \tag{2.12}$$

Clearly, the accuracy of telling time depends on the relative noise strength, *i.e.* the standard deviation σ_i divided by the amplitude A_i, of the respective genes, the frequency ω of the oscillations, and the phase difference between the different oscillations. It also depends on time, which means that the precision with which the time can be determined, depends on the moment of the day. The average error in the estimate, $\sigma_t(t)$ averaged over the oscillation period T, is

$$\langle \sigma_t \rangle = \int_0^T P(t)\sigma_t(t)dt \tag{2.13}$$

$$= \frac{1}{T}\int dt \left(\sqrt{\omega^2 \sum_{i}^{N} (A_i/\sigma_i)^2 \cos^2(\omega t + \phi_i)} \right)^{-1} \tag{2.14}$$

It is not possible to solve this analytically, and below we have optimized $\langle \sigma_t \rangle$ numerically. It is also of interest to know how much the error is constant as a function of time. To this end, we compute

$$(\delta\sigma_t)^2 = \int_0^T P(t)(\sigma_t(t) - \langle \sigma_t \rangle)^2 dt \tag{2.15}$$

In the next section, we will systematically study the dependence of σ_t on $\sigma_i(t)$, A_i, and ϕ_i. We will not vary ω, which is fixed by the 24 hr rhythm of the circadian clock. We thus do not study the dependence on ω, except to note that, in general, the error in the estimate of time decreases as ω increases (see Eq. 2.12) because a higher frequency causes steeper oscillations, which means that an error in the estimate of x will propagate less strongly to the error in the estimate of time, σ_t.

With cross-correlations in the expressions of the downstream genes, the off-diagonal terms of **C** will be non zero, which leads to additional terms in the expression for σ_t^2. Rather than giving the generic expression, we show the more informative expression for $N = 2$, with $x_1(t) = x(t) = A_x \sin(\omega t)$ and $x_2(t) = y(t) = A_y \sin(\omega t + \phi)$. The covariance matrix, which is symmetric and semi-definite positive, is defined as

$$\mathbf{C} = \begin{pmatrix} \sigma_x^2 & \mathrm{cov}_{xy} \\ \mathrm{cov}_{xy} & \sigma_y^2 \end{pmatrix} \tag{2.16}$$

which yields for its inverse

$$\mathbf{C}^{-1} = \frac{1}{|\mathbf{C}|}\begin{pmatrix} \sigma_y^2 & -\mathrm{cov}_{xy} \\ -\mathrm{cov}_{xy} & \sigma_x^2 \end{pmatrix}, \tag{2.17}$$

where the determinant is $|\mathbf{C}| = (\sigma_x^2\sigma_y^2 - \mathrm{cov}_{xy}^2)$. Combining this with Eq. 2.11 yields:

$$\begin{aligned}\sigma_t^{-2}(t) = \frac{1}{|\mathbf{C}|}\Big[&\sigma_y^2 A_x^2\cos^2(\omega t) \\ &-2\mathrm{cov}_{xy}A_xA_y\cos(\omega t+\phi)\cos(\omega t) \\ &+\sigma_x^2 A_y^2\cos^2(\omega t+\phi)\Big].\end{aligned} \tag{2.18}$$

This expression reduces to that of Eq. 2.12 when the co-variance is zero. However, in general, the error on telling time depends on the co-variance of the fluctuations in the expression of gene x and gene y.

The quantity $\sigma_t(t)$ is a local quantity in that it provides the error in estimating the time as a function of the time of the day. This quantity can be useful when certain moments of the day have to be determined with higher precision than others. In the next section, we discuss another quantity, the mutual information, which makes it possible to determine how many distinct moments in time can be specified.

MUTUAL INFORMATION

The mutual information quantifies how many different input states can be propagated uniquely [63]. In this context, it is defined as

$$I(\{x_i\};t) = \int d\mathbf{x}\,dt\,P(\{x_i\},t)\log\frac{P(\{x_i\},t)}{P(\{x_i\})P(t)}. \tag{2.19}$$

The mutual information measures the reduction in uncertainty about t upon measuring $\{x_i\}$, or vice versa. The quantity is indeed symmetric in $\{x_i\}$ and t:

$$I(x,y;t) = H(x,y) - \langle H(x,y|t)\rangle_t \tag{2.20}$$

$$= H(t) - \langle H(t|x,y)\rangle_{x,y} \tag{2.21}$$

where $H(a) = -\int da P(a)\ln P(a)$, with $P(a)$ the probability distribution of a, is the entropy of variable a; $H(a,b|c) = -\int da\int db P(a,b|c)\ln P(a,b|c)$ is the information entropy of a,b given c, with $P(a,b|c)$ the conditional probability distribution of a and b given c, and $\langle f(c)\rangle_c$ denotes an average of $f(c)$ over the distribution $P(c)$. In our context, Eq. 2.21 is perhaps the most natural expression, since it quantifies how accurately the cell can infer the time of the day t from the expression of x and y.

The mutual information is a global quantity, which in contrast to $\sigma_t(t)$, does not make it possible to quantify how accurately a given moment in time can be specified. The latter could be useful when the system needs to change, e.g., its metabolic program at a well-defined moment in time. On the other hand, the mutual information does allow us to quantify how many different moments in time can be specified, and thus how many temporal decisions the organism could make. As Eq. 2.20 shows, the magnitude

of the mutual information depends on both $H(x,y)$ and $\langle H(x,y|t)\rangle_t$. As we will show below, cross correlations between the expression of the downstream genes x and y will modify $P(x,y)$, reducing its entropy; this tends to reduce information transmission. Yet, cross-correlations can also decrease $\langle H(x,y|t)\rangle_t$, meaning that, on average, the distribution of expression levels x and y for a given time t is more narrow—a given time t then maps more uniquely onto an expression pattern x,y; this tends to increase the mutual information. The balance between these two opposing factors determines the cross correlations that maximize information transmission.

2.2. RESULTS

2.2.1. NO CROSS-CORRELATIONS

In this section, we consider the scenario in which there are no cross correlations between the noise in the expression of the downstream genes. We first study the case in which the relative noise strength, $\widetilde{\sigma}_i \equiv \sigma_i / A_i = \widetilde{\sigma}_x$, is the same for all genes i; in this scenario, we use the subscript x to remind ourselves that we are considering the standard deviation in x and not in the estimate of time. We will also first assume that $\sigma_x(t) = \sigma_x$ is constant in time, depending only on the mean of x, i.e r_x, but not its mean instantaneous level $\bar{x}(t)$. The latter is reasonable when the amplitude of the oscillations is small compared to the mean.

To determine the optimal phase relation that minimizes the average error in telling time, given by Eq. 2.14, we solve

$$\frac{d\langle\sigma_t\rangle}{d\Delta\phi_i} = 0 \qquad i = 1...N, \tag{2.22}$$

where $\Delta\phi_i = \phi_i - \phi_1$. Setting the phase of the first oscillation to zero, i.e. $\phi_1 = 0$, we find that the optimal phase relation that minimizes the average error is given by

$$\Delta\phi_i = (i-1)\frac{\pi}{N} \qquad i = 1...N. \tag{2.23}$$

Clearly, in the optimal system the phases of the downstream oscillations are evenly spaced when $\widetilde{\sigma}_x$ is the same for all genes, and σ_x is constant in time.

The next question is what is the phase relation that minimizes the variance of $\sigma_t(t)$ over the oscillation period T, i.e. minimizes Eq. 2.15. In the appendix we show that the solution is also given by Eq. 2.23. Hence, the phase relation that minimizes the average error on telling time, $\langle\sigma_t\rangle$, is also the phase relation that minimizes the variance of $\sigma_t(t)$. Thus, in the optimal system, the phases are evenly spaced; this not only minimizes the average error in telling time, but it also yields the same accuracy for all times t. Moreover, for this optimal system, the average error, obtained from Eq. 2.12, is given by

$$\langle\sigma_t\rangle = \frac{\widetilde{\sigma}_x T}{2\pi}\sqrt{\frac{2}{N}} \tag{2.24}$$

This shows that the average error is proportional to the relative noise strength $\widetilde{\sigma}_x = \sigma_x / A$ and inversely proportional to the square root of the number of readout genes, N.

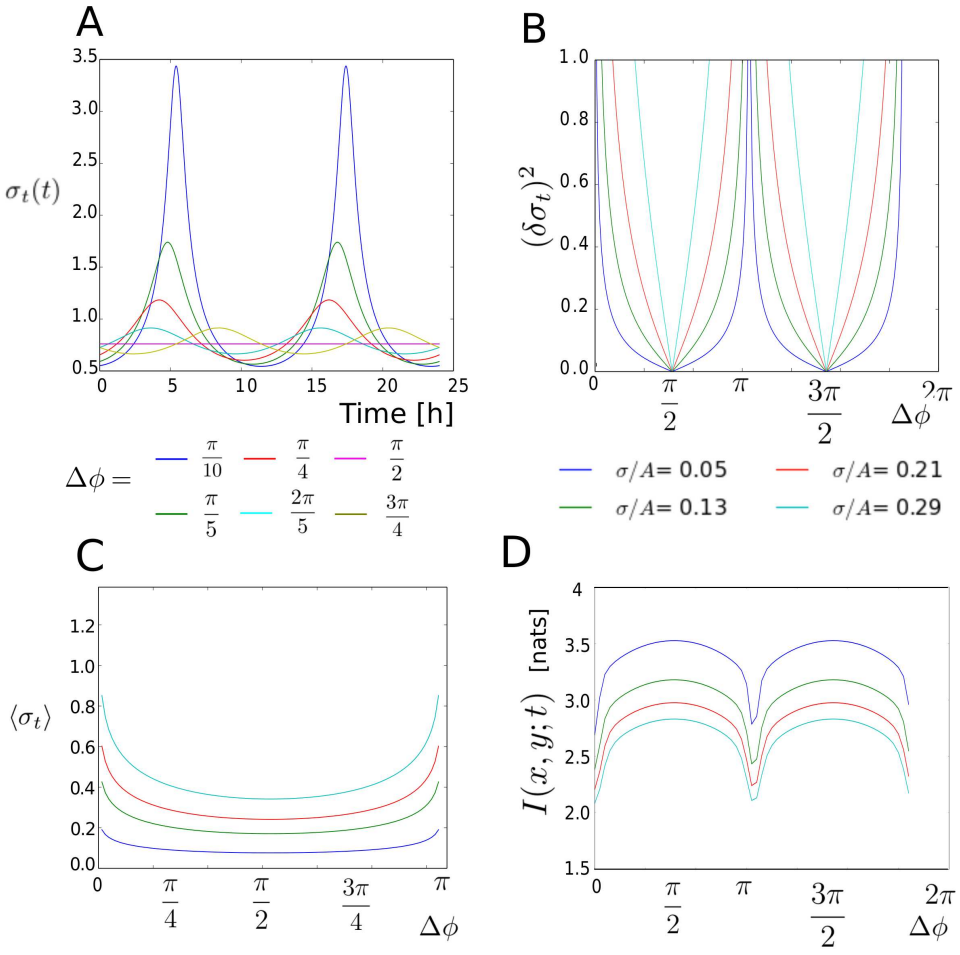

Figure 2.2: Estimating time via $N = 2$ readout-protein oscillations, which have the same relative noise strength $\tilde{\sigma}_x = \sigma_x / A$. Here A is the amplitude of the oscillations and σ_x is the noise in the oscillations, which is here assumed to be constant in time, and given by the mean of the oscillations, r, taken to be the same for both oscillations; there are also no cross correlations. (A) The error in the estimate of time $\sigma_t(t)$ as a function of time t, for different phase differences $\Delta\phi$ between the two oscillations. Note that for $\Delta\phi = \pi/2$, the error $\sigma_t(t)$ is constant in time. (B) The variance $(\delta\sigma_t)^2$ in the estimate of time as a function of $\Delta\phi$, for different relative noise strengths $\tilde{\sigma}_x$. As expected from panel A, $(\delta\sigma_t)^2 = 0$ for $\Delta\phi = \pi/2$. (C) The mean error $\langle\sigma_t\rangle$ as a function of $\Delta\phi$, for different relative noise strengths $\tilde{\sigma}_x$. The error is proportional to $\tilde{\sigma}_x$, in accordance with Eq. 2.24. Note also that the mean error is minimized at $\Delta\phi = \pi/2$, although the dependence on $\Delta\phi$ near the optimum is weak. (D) The mutual information $I(x, y; t)$ between the two protein oscillations $x(t), y(t)$ and time t, for different relative noise strengths $\tilde{\sigma}_x$. The mutual information increases with decreasing $\tilde{\sigma}_x$, and is optimized at $\Delta\phi = \pi/2$. Note also that the dependence of $I(x, y; t)$ on $\Delta\phi$ is stronger than that of $\langle\sigma_t\rangle$ (panel C).

These results are illustrated in Figs. 2.2A-C, for $N = 2$. Panel A shows $\sigma_t(t)$ as a function of t, for different phase relations $\Delta\phi \equiv \phi_2 - \phi_1$. It is seen that, in general, $\sigma_t(t)$, depends on t. However, when $\Delta\phi = \pi/2$, then $\sigma_t(t)$ is independent of t. Panel B shows that for this phase relation, the variance $(\delta\sigma_t)^2$ is indeed zero, while panel C shows that in this case also the average error is minimal, in accordance with the theoretical analysis.

Lastly, Fig. 2.2D shows the mutual information $I(x, y; t)$, obtained numerically, as a function of the phase shift, for different noise levels. As expected, the mutual information increases as the relative noise strength $\widetilde{\sigma}_x$ decreases. Moreover, the phase relation that minimizes the average error, $\langle\sigma_t\rangle$, is also the phase relation that maximizes the mutual information.

When the noise amplitude σ_x depends on the mean instantaneous copy number $\bar{x}(t)$ (rather than its mean averaged over the oscillation period), the noise in the output $\sigma_x(t)$ varies in time. We first assume that $\sigma_x(t) \simeq \sqrt{\bar{x}(t)}$, and consider as above the case that the amplitude and the mean of the oscillations are the same for all genes, respectively: $A_i = A_j = \cdots = A$ and $r_i = r_j = \cdots = r_x$. Our analysis described in the appendix reveals that the optimal phase relation that maximizes the mutual information and minimizes both the variance $(\delta\sigma_t)^2$ and the mean $\langle\sigma_t\rangle$ of the error, is again given by Eq. 2.23. However, the minimal variance, obtained for the optimal phase relation, only reduces to zero in the limit that $r \to \infty$; in this limit, the noise $\sigma_x(t)$ becomes constant in time and we recover the case discussed above. Interestingly, the average error $\langle\sigma_t\rangle$ is larger than that in the case of constant relative noise strength, even when the average relative noise strength is the same. We have also studied the case in which $\sigma_x(t) = x(t)$. In this scenario the average noise is higher, which decreases the precision and the mutual information. Yet, qualitatively the results do not change. Specifically, the same optimal phase relation is obtained.

When $N = 2$ yet the relative noise strength is not the same for both genes, $\widetilde{\sigma}_x \neq \widetilde{\sigma}_y$, the optimal phase shift that minimizes the error and maximizes the mutual information is again $\Delta\phi_{xy} = \pi/2$; indeed, this result, for $N = 2$, does not depend on whether $\widetilde{\sigma}$ is the same for both genes. Also the variance $(\delta\sigma_t)^2$ is zero for this optimal phase shift, as before.

These results change markedly when the relative noise strength is not the same for all genes and $N > 2$. Then the optimal phase shift depends in a non-trivial manner on $\{\widetilde{\sigma}_i\}$. The principle is that the oscillations that contain more information about time because they are less noisy, should be spaced further apart. More specifically, the spacing between them should be closer to that which maximizes the mutual information between them and time. This principle is illustrated in Fig. 2.3A-B for three genes, where $\widetilde{\sigma}_x = \widetilde{\sigma}_y \equiv \widetilde{\sigma}_{x,y} < \widetilde{\sigma}_z$. Clearly, the oscillations of proteins X and Y contain more information about time than the oscillation of protein Z. As a consequence, the phase difference between $x(t)$ and $y(t)$, $\Delta\phi_{xy} = \phi_y - \phi_x$, is more important in accurately telling time than that between the two other pairs of oscillations. The phase difference $\Delta\phi_{xy}$ is therefore closer to $\pi/2$, the phase difference that maximizes $I(x, y; t)$, than those of the other pairs of genes. Indeed, the extent to which $\Delta\phi_{xy}$ approaches $\pi/2$ depends on $\widetilde{\sigma}_{x,y}/\widetilde{\sigma}_z$, as Fig. 2.3B shows: when $\widetilde{\sigma}_{x,y} = \widetilde{\sigma}_z$, all oscillations are equally informative and hence the oscillations are evenly spaced, yielding $\Delta\phi_{xy} = \Delta\phi_{yz} = \Delta\phi_{zx} = \pi/3$. In contrast, when $\widetilde{\sigma}_{x,y}/\widetilde{\sigma}_z = 0$, $\Delta\phi_{xy} = \pi/2$, the same result that would have been obtained if these two

genes were the only ones present. In this limit, $\tilde{\sigma}_z$ is infinite, and z carries no information on time, making its phase irrelevant. Fig. 2.3C gives the mean error $\langle \sigma_t \rangle$ and Fig. 2.3D the mutual information $I(x, y, z; t)$ for the optimal phase relation shown in panel B, as a function of $\tilde{\sigma}_{xy}/\tilde{\sigma}_z$. Here, in varying $\tilde{\sigma}_{xy}/\tilde{\sigma}_z$, $\tilde{\sigma}_{xy}$ is kept constant while $\tilde{\sigma}_z$ is varied between $\tilde{\sigma}_{xy}$ and infinity. These panels thus show the gain in employing an additional readout protein in accurately telling time, as a function of its noise level. The results interpolate between those for $N = 2$ equally informative genes when $\tilde{\sigma}_{xy}/\tilde{\sigma}_z = 0$, and those for $N = 3$ equally informative genes when $\tilde{\sigma}_{xy}/\tilde{\sigma}_z = 1$.

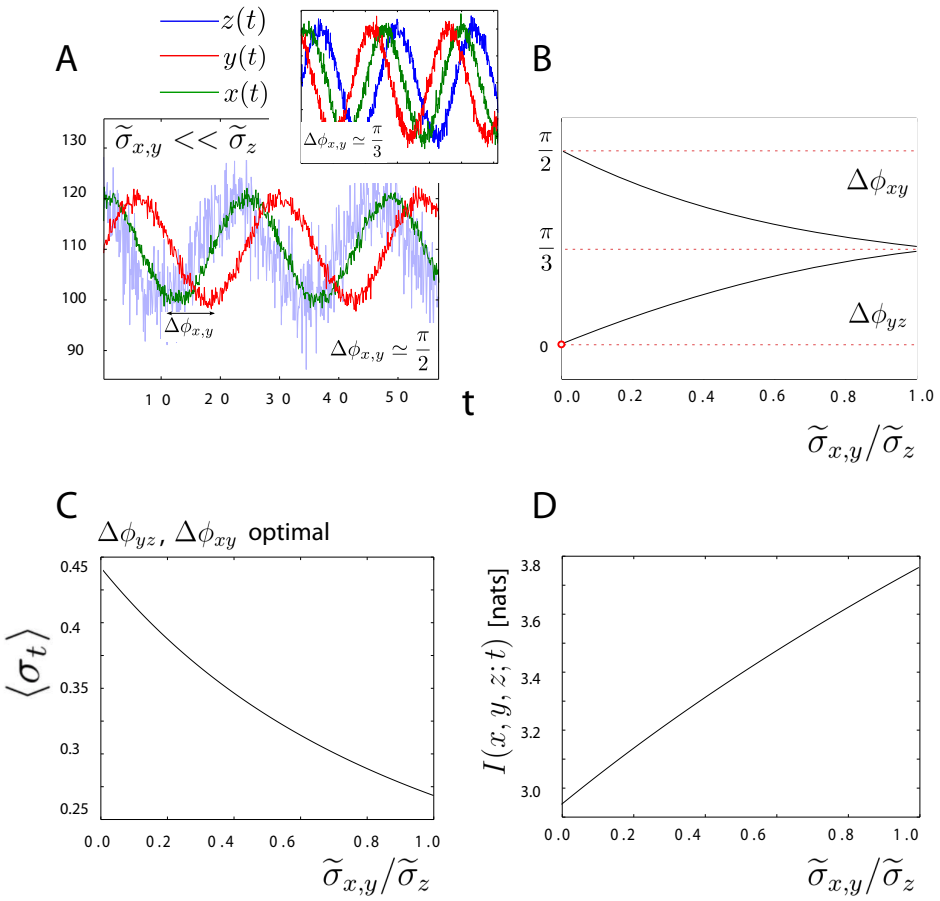

Figure 2.3: Estimating time via $N = 3$ readout-protein oscillations, where the relative noise strength $\widetilde{\sigma}_i \equiv \sigma_i / A_i$ of two oscillations is the same, $\widetilde{\sigma}_x = \widetilde{\sigma}_y \equiv \widetilde{\sigma}_{x,y} = 0.3$, and different from that of the third oscillation, $\widetilde{\sigma}_z$. The noise σ_i is assumed to be constant in time, and there are no cross correlations in the noise. (A) Sketch of the set up, with two reliable oscillations $x(t)$ and $y(t)$ and a third, more noisy oscillation $z(t)$. (B) The optimal phase relation that maximizes the mutual information $I(x, y, z; t)$ and minimizes the mean error $\langle\sigma_t\rangle$, as a function of $\widetilde{\sigma}_{x,y}/\widetilde{\sigma}_z$; here, and in panels C-D, $\widetilde{\sigma}_{x,y} = 0.3$ is kept constant while $\widetilde{\sigma}_z$ is varied. When $\widetilde{\sigma}_{x,y}/\widetilde{\sigma}_z = 0$, the third gene $z(t)$ carries no information, and the optimal phase difference $\Delta\phi_{xy} = \phi_y - \phi_x$ between the oscillations of x and y is $\Delta\phi_{xy} = \pi/2$, the result for $N = 2$ oscillations; in this limit, the phase of z is irrelevant and its optimal phase is thus undetermined, as indicated by the open circle. As $\widetilde{\sigma}_{x,y}/\widetilde{\sigma}_z$ increases, the third oscillation $z(t)$ becomes more important. The phase difference $\Delta\phi_{xy}$ between $x(t)$ and $y(t)$ decreases, while the phase difference $\Delta\phi_{yz}$ between $y(t)$ and $z(t)$ increases. When $\widetilde{\sigma}_{x,y}/\widetilde{\sigma}_z = 1$, all genes are equally informative and $\Delta\phi_{xy} = \Delta\phi_{yz} = \Delta\phi_{zx} = \pi/3$. (C) The mean error $\langle\sigma_t\rangle$ as a function $\widetilde{\sigma}_{x,y}/\widetilde{\sigma}_z$. It decreases as the third gene becomes more informative. (D) The mutual $I(x, y, z; t)$ increases with $\widetilde{\sigma}_{x,y}/\widetilde{\sigma}_z$.

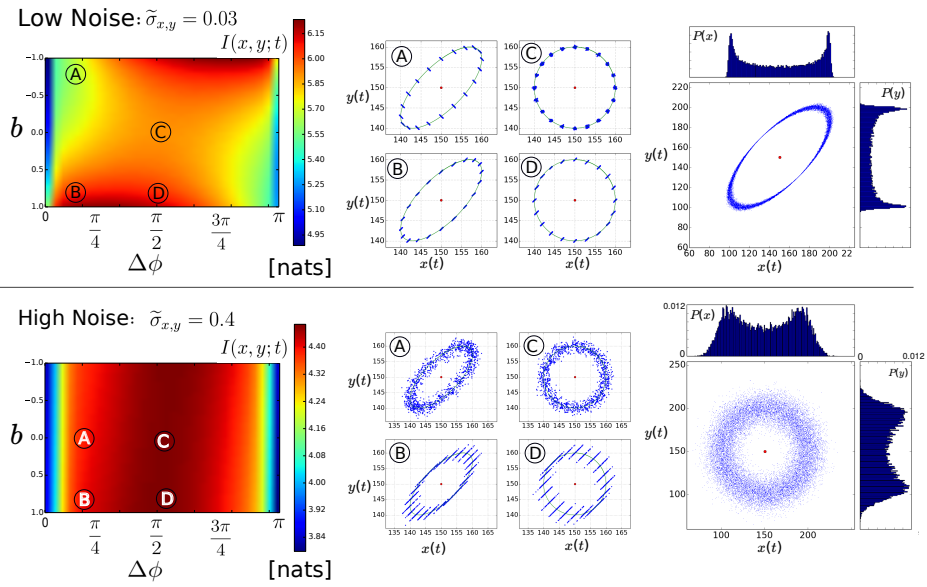

Figure 2.4: The importance of cross correlations between the fluctuations in the oscillations of the readout proteins, illustrated here for $N = 2$ readout proteins. The top row shows results for the scenario in which the relative noise strength $\tilde{\sigma}_i \equiv \sigma_i / A_i$ is low, while the bottom panel displays the results for when it is large. In all cases, the relative noise strength of the two oscillations is taken to be the same, $\tilde{\sigma}_x = \tilde{\sigma}_y = \tilde{\sigma}_{x,y} = 0.3$. The panels in the left column show a heat map of the mutual information $I(x,y;t)$ as a function of the phase difference $\Delta\phi = \phi_y - \phi_x$ between the two oscillations, and the correlation coefficient b. Due to the symmetry of the problem the mutual information is symmetric: $I(x,y;t)_{\Delta\phi,b} = I(x,y;t)_{\pi-\Delta\phi,-b}$. The top-left panel shows that when the relative noise strength is low, the mutual information is maximized for $|b| \to 1$ and $\Delta\phi \neq \pi/2$. Cross correlations thus change the optimal phase difference, and more, importantly, they can enhance the mutual information. However, when the relative noise is large, the cross correlations become less important and the optimal phase difference approaches $\Delta\phi = \pi/2$ (bottom left panel). The middle panels elucidate how cross correlations can affect the mutual information. Shown are, for different points in the heat map on the left, the average trajectory that $x(t)$ and $y(t)$ trace out during a 24 hr period (green solid line), with superimposed, for different times of the day, scatter points of $x(t)$ and $y(t)$, originating from gene expression noise. The main axis of the contour $\bar{x}(t), \bar{y}(t)$ is determined by the phase difference $\Delta\phi$, while the main axis of the noise (scatter points) is determined by the correlation coefficient b. There are moments of the day where cross correlations cause the distributions $P(x,y|t)$ of neighbouring times t to overlap less, thus increasing mutual information, but also moments where they increase the overlap, decreasing the mutual information. The net benefit depends on how these contributions are weighted. The system spends more time near the extrema of $\bar{x}(t), \bar{y}(t)$, as illustrated in the right panels. Consequently, when $\Delta\phi < \pi/2$, positive correlations $b > 0$ enhance the mutual information, especially when the relative noise strength $\tilde{\sigma}_x$ is low (point B top row). At higher noise (bottom row), cross correlations are less effective in reducing the overlap in $P(x,y|t)$ and the phase difference $\Delta\phi$ becomes the dominant control parameter.

2.2.2. THE IMPORTANCE OF CROSS-CORRELATIONS

So far we have assumed that the noise in the expression of the downstream genes is uncorrelated. However, in general, we expect their noise to be correlated. Direct or indirect regulatory interactions between the genes can lead to correlations or anti-correlations in the fluctuations of the protein concentrations [53]. And also noise in the input signal can lead to correlated gene expression. In fact, the extrinsic contribution to the noise in gene expression is often larger than the intrinsic one [94], which can induce pronounced correlations between the expression of the downstream genes. Intuitively, we may think that if we need to infer an input variable t from two output variables x and y, then cross-correlations between x and y reduce the accuracy of the estimate—asking two persons x and y a question about t seems to give more information when x and y give independent answers. However, this intuition is not always correct, as will become clear. Indeed, in this section we study how correlations between the expression of downstream genes affect the precision by which cells can tell time.

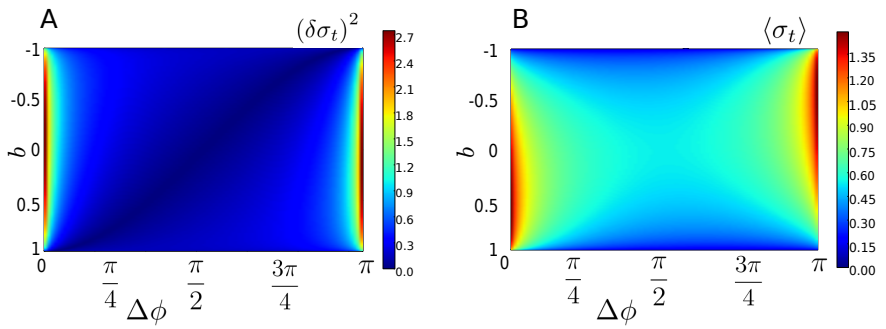

Figure 2.5: Importance of cross correlations in reducing the error in estimating the time, as estimated from $N = 2$ protein oscillations. Heat maps of the the variance in the error $(\delta\sigma_t)^2$ (A) and the mean error $\langle\sigma_t\rangle$ (B), as a function of the phase difference $\Delta\phi$ between the two oscillations and the correlation coefficient b of the fluctuations in the oscillations. The relative noise strength $\widetilde{\sigma}_x$ is the same for both oscillations, and equal to that of the low-noise scenario in Fig. 2.4, $\widetilde{\sigma}_x = 0.03$. It is seen that cross correlations can reduce the mean error. Comparing against the top-left panel of Fig. 2.4 shows, however, that the positions of the optima are different for the two quantities, the mean error $\langle\sigma_t\rangle$ and the mutual information $I(x,y;t)$, respectively. This is because the quantities $\sigma_t(t)$ (Eq. 2.14) and $H(t|x,y)$ (Eq. 2.26) are averaged over different distributions, the uniform distribution $P(t)$ and the non-uniform distribution $P(x,y)$, respectively.

In order to dissect the effect of cross-correlations, we study two downstream genes, $N = 2$, and take both the amplitudes of their oscillations and their expression noise to be equal: $A_x = A_y = A$, $\sigma_x = \sigma_y = \sigma_{x,y}$, respectively. Using the latter, we can renormalise the covariance matrix Eq. 2.16:

$$\mathbf{C} = \begin{pmatrix} \sigma_x & \mathrm{cov}_{xy} \\ \mathrm{cov}_{xy} & \sigma_y \end{pmatrix} = \sigma_{x,y} \begin{pmatrix} 1 & b \\ b & 1 \end{pmatrix}, \tag{2.25}$$

where b is the correlation coefficient, denoting the cross-correlation strength: $b = 1$ implies that the noise in the expression of X and Y is fully correlated, while $b = -1$ implies

full anti-correlation. We computed numerically how $I(x,y;t)$, $\langle \sigma_t \rangle_t$ and $(\delta t)^2$ depend on the phase shift $\Delta\phi = \phi_y - \phi_x$, the relative noise strength $\widetilde{\sigma}_{x,y} = \sigma_{x,y}/A$, and the correlation coefficient b.

Fig. 2.4 shows the mutual information $I(x,y;t)$ as a function of $\Delta\phi$ and b, both for low noise, with $\widetilde{\sigma}_{x,y} = 0.03$ (panels top row), and high noise, with $\widetilde{\sigma}_{x,y} = 0.4$ (panels bottom row). The following points are worthy of note. First, as expected, $I(x,y;t)$ is symmetric with respect to $\Delta\phi$ and b: $I(x,y;t)_{\Delta\phi,b} = I(x,y;t)_{2\pi-\Delta\phi,-b}$. Secondly, depending on the phase shift $\Delta\phi$, correlations ($b>0$) or anti-correlations ($b<0$) can enhance the mutual information, especially when the relative noise strength $\widetilde{\sigma}_{x,y}$ is low (top panel). Concomitantly, the optimal phase shift $\Delta\phi$ that maximizes the mutual information depends on the cross correlation b. At low noise, the mutual information is maximized either at $0 < \Delta\phi^* < \pi/2$ and $b \approx 1$ or at $\pi - \Delta\phi^*$ and $b \approx -1$. At high noise, cross correlations no longer help to improve the mutual information (bottom panel). Moreover, the optimal phase shift is at $\Delta\phi^* \approx \pi/2$. We now discuss the origin of these observations.

To elucidate these observations, we start from the definition of the mutual information (see Eq. 2.21):

$$I(x,y;t) = H(t) - \langle H(t|x,y) \rangle_{x,y} \tag{2.26}$$

Here, $H(t)$ is the entropy of the input signal, with $P(t) = 1/T$. It does not depend on the design of the downstream readout system. In contrast, the second term, $\langle H(t|x,y) \rangle_{x,y}$, does depend on it. We now describe how changing $\Delta\phi$ and b affects this term, using the scatter plots and distributions in the middle and right column of Fig. 2.4.

The middle panel shows for different combinations of b and $\Delta\phi$, corresponding to the points A,B,C,D in the heat map of $I(x,y;t)$ (left panel), scatter plots of $x(t)$ and $y(t)$. The overall shape of each scatter plot is determined by the phase difference $\Delta\phi$. When $\Delta\phi = \pi/2$ (points C and D), the average expression levels $\bar{x}(t)$ and $\bar{y}(t)$ trace out a circle in state space during a 24 hr period, while when $\Delta\phi = \pi/4$ (points A and B), they carve out an ellipsoidal path; these mean paths are indicated by thin solid green lines in the scatter plots. For each moment of the day, however, x and y will exhibit a distribution of expression levels, due to gene expression noise. This distribution $P(x,y|t)$ is shown as scatter points (x,y) for different yet evenly spaced times t in the respective sub-panels. When the main axis of $P(x,y|t)$ is perpendicular to the local tangent of the mean path of $\bar{x}(t), \bar{y}(t)$, then cross correlations reduce $H(t|x,y)$ for that period of the day: the cross correlations cause the distributions $P(x,y|t)$ for neighbouring times t to overlap less, meaning that a given point (x,y) maps more uniquely onto a given time t. This tends to increase the mutual information. However, as the middle panel illustrates, there are not only moments of the day when the main axis of the scatter points is perpendicular to the local tangent of the mean path, but also times when they are parallel, in which case cross correlations are detrimental. Whether the net result of cross correlations is beneficial, depends on how these different contributions are weighted: $H(t|x,y)$ has to be averaged over $P(x,y)$, see Eq. 2.26. When $\Delta\phi = \pi/2$, the mean path $\bar{x}(t), \bar{y}(t)$ is circular, yet the net effect of correlations on the mutual information is already positive (left panel), and independent of the sign of b. For $\Delta\phi \neq \pi/2$, the effect depends on the sign of b. Moreover, as the right panel illustrates, the effect is also stronger, since the system spends more time near the extrema of $\bar{x}(t), \bar{y}(t)$ (this is because oscillatory signals spend, in general, more time near their extrema).

When $\Delta\phi < \pi/2$, positive correlations in the expression of x and y ($b > 0$) cause the main axis of $P(x, y|t)$ to be perpendicular to the local tangent of $\bar{x}(t), \bar{y}(t)$ near the extrema (point B), thus increasing the mutual information, while anti-correlations ($b < 0$) cause $P(x, y|t)$ to be parallel to it (point A), decreasing the mutual information. For $\Delta\phi \to \Delta\phi - \pi/2$ precisely the opposite behaviour is observed, because the mean path of $\bar{x}(t), \bar{y}(t)$ (the ellipse) is flipped vertically. The principal observation is thus that cross-correlations can enhance the mutual information by allowing for a less overlapping tiling of state space, and hence a less redundant mapping between the input t and output (x, y).

For higher noise (panels in lower row of Fig. 2.4), each $P(x, y|t)$ becomes wider, which means that the benefit of introducing cross correlations in reducing the overlap between different $P(x, y|t)$ (corresponding to different times t), decreases. Indeed, at higher noise, the mutual information depends much more weakly on the magnitude of the cross correlations (left panel bottom row). The key control parameter is now the phase shift $\Delta\phi$. For $\Delta\phi = \pi/2$, the distributions $P(x, y|t)$ are most evenly spaced. This minimizes the overlap between them and maximizes the mutual information.

Fig. 2.5 shows the the variance in the error, $(\delta t)^2$, and the average error in telling time, $\langle\sigma_t\rangle$, as a function of $\Delta\phi$ and b, for $\tilde{\sigma} = 0.03$ (as in the top row of Fig. 2.4). It is seen that increasing correlations $|b|$ can reduce the average error. Surprisingly, however, for $|b| \approx 1$, the average error $\langle\sigma_t\rangle$ is minimized at a phase shift that does not maximize the mutual information, as a comparison with Fig. 2.4 shows. This is because of how the respective quantities are averaged. The quantity $\sigma_t(t)$ is averaged over $P(t)$, which is uniform in time, while $H(t|x, y)$ is averaged over $P(x, y)$, which gives more weight to those points (x, y) that are more probable.

To illustrate the importance of cross-correlations in enhancing information transmission, we have focussed here on the case $N = 2$. However, also for $N > 2$, cross-correlations can increase the precision of telling time, by minimizing the overlap in the conditional distributions $P(x, y|t)$.

2.3. DISCUSSION

Our results show that the precision of estimating the time and the mutual information depends on the relative noise of the oscillatory signals, their phase difference and their cross-correlations. The question that remains is how cells can optimize these.

CROSS-CORRELATIONS

Fluctuations in the input will lead to correlated fluctuations in the oscillations of the output components. Our analysis shows that these correlations can be beneficial. Moreover, they can be tailored via cross-regulatory interactions between the target genes downstream, as in the gap-gene system of *Drosophila* [49, 53, 56]. Here, it should be realized that in our analysis we assume that the noise is uncorrelated from the signal; indeed, the mean trajectory $(\bar{x}(t), \bar{y}(t))$ does not depend on the noise. Cross-regulatory interactions will, however, not only affect the noise and hence $P(x, y|t)$, but also the mean trajectory $(\bar{x}(t), \bar{y}(t))$. This will not change the principle that noise correlations can enhance the input-output mapping, but it will influence the magnitude of the effect. On the other

hand, extrinsic noise sources such as the availability of ribosomes, may lead to correlated fluctuations in the expression of $x(t)$ and $y(t)$, while leaving their mean unchanged, as assumed here. Experiments will have to tell whether cells use noise correlations to enhance the precision of telling time. The cyanobacterium *S. elongatus* is arguably the best model system to test these ideas. It will certainly be of interest to investigate whether *S. elongatus* exploits cross-regulatory interactions between the genes downstream from RpaA to enhance its information on time.

RELATIVE NOISE

The relative noise of the oscillations depends on the noise σ_i and the amplitude A_i of the oscillations. The contribution from the intrinsic noise is expected to scale with the copy number X as $\sigma_{\text{in},i} \sim \sqrt{X_i}$, which, if the amplitude is small compared to the mean r_i, means that $\sigma_{\text{in},i} \sim \sqrt{r_i}$. The relative intrinsic noise thus goes as $\widetilde{\sigma}_{\text{in},i} \sim \sqrt{r_i}/A_i$. For the model presented in section 2.1.1, it is given by

$$\widetilde{\sigma}_{\text{in},i} \simeq \sqrt{r_i}/A_i \tag{2.27}$$

$$= \sqrt{r_s/f_i}\sqrt{(\mu_i^2+\omega^2)/\mu_i}/A_s. \tag{2.28}$$

Clearly, the relative noise strength $\widetilde{\sigma}_{\text{in},i}$ decreases with A_s: the amplitude of the oscillations of the readout is proportional to that of the input. The relative noise strength decreases with the square root of f_i, because the gain f_i increases not only the amplitude of the output oscillations, $A_i \propto f_i$, but also their mean r_i and thereby the noise, $\sigma_{\text{in},i} \propto \sqrt{r_i} \propto \sqrt{f_i}$. It increases with the mean r_s of the input oscillations, because that increases the mean r_i of the output oscillations and thereby the noise $\sigma_{\text{in},i}$, but not their amplitude, thus decreasing the relative noise strength $\sigma_{\text{in},i}/A_i$. Finally, there exists an optimal protein decay rate $\mu_{\text{opt}} = \omega$ that minimizes the relative noise strength and hence maximizes information transmission. This optimum arises from a trade-off between the amplitude of the signal and the intrinsic noise: for $\mu \gg \omega$, increasing μ reduces the gain and hence the amplitude A_i as $A_i \propto 1/\mu$ (Eq. 2.4) while the noise decreases more slowly as $\sqrt{r_i} \propto 1/\sqrt{\mu}$, thus increasing the relative noise strength $\widetilde{\sigma}_{\text{in},i}$; in contrast, for $\mu \ll \omega$, the amplitude A_i becomes independent of μ_i (Eq. 2.4) while the noise continues to rise as μ_i decreases, thus again increasing the relative noise strength.

For the transmission of a fluctuating input signal, a similar trade-off between the gain and the intrinsic noise has been observed in [50] and a related trade-off between mechanistic error arising from the intrinsic noise and dynamical error due to the distortion of the input signal has been described in [57]. A seemingly similar but distinct trade-off, also leading to an optimal decay rate of the output component, has been reported in [61]: in that study the optimal decay rate arises from the trade-off between tracking the input signal and integrating out the noise in the input signal. Indeed, in our discussion here, we have so far ignored the extrinsic noise in the input signal, and only focused on the intrinsic noise. However, the decay rate μ_i does not only affect the output copy number and thereby the intrinsic noise, it also determines how effectively fluctuations in the

input signal can be integrated out. More specifically, if the noise in the input ξ_s (Eq. 2.3) is independent from the input signal, has amplitude σ_s and decays exponentially with correlation time λ, then we expect that the extrinsic contribution to the output noise is $\sigma^2_{\mathrm{ex},i} = g_i^2 \mu_i/(\mu_i+\lambda)\sigma_s^2$ [77, 95], where the gain is $g_i = f_i/\mu_i$. Hence, the relative extrinsic noise is

$$\sigma_{\mathrm{ex},i}/A_i = 1/\mu_i \sqrt{(\mu_i^2+\omega^2)\mu_i/(\mu_i+\lambda)}\sigma_s. \tag{2.29}$$

We first note that, in contrast to the relative contribution of the intrinsic noise, $\sigma_{\mathrm{in,i}}/A_i$, the relative extrinsic noise does not depend on f_i: increasing f_i raises not only the amplitude of the signal, but also that of the noise; increasing f_i is thus only useful in raising the signal above the *intrinsic* noise. Secondly, for $\mu_i \gg \omega, \lambda$, $\sigma_{\mathrm{ex},i}/A_i \simeq \sigma_s$, because the time integration factor $\mu_i/(\mu_i+\lambda)$ becomes constant (independent of μ_i), and both the amplitude of the signal, A_i, and the amplification of the input noise, g_i decrease as μ_i^{-1}. For $\mu_i \ll \omega, \lambda$, $\sigma_{\mathrm{ex},i}/A_i \simeq \omega\sigma_s/\sqrt{\mu_i\lambda}$, because the amplitude A_i becomes independent of μ_i, while the extrinsic contribution $\sigma_{\mathrm{ex},i}$ rises with decreasing μ_i as $1/\sqrt{\mu_i}$. In fact, the relative strength of the extrinsic noise $\sigma^2_{\mathrm{ex},}/A_i$ has a minimum at $\mu_{\mathrm{ex}}^{\mathrm{opt}} = (\omega^2/\lambda)(1+\sqrt{1+(\lambda/\omega)^2})$. We thus conclude that both the relative strength of the intrinsic and extrinsic noise exhibit a minimum as function of μ_i, meaning that there is an optimal protein lifetime that maximizes information transmission.

PHASE SHIFT

Lastly, how could cells optimize the phase relation between the oscillations of the readout proteins? In the simple model of 2.1.1 there is only one control variable, namely the protein degradation rate (Eq. 2.5). Clearly, it is not possible, in general, to simultaneously set the decay rate such that the relative noise strength is minimized, as described above, and the phase difference is optimized. However, the simple model of 2.1.1 ignores that gene expression is, in fact, a multi-step process leading to a delay, and it is possible that nature has tuned this delay so as to optimize the phase relation between the output oscillations. In addition, cells could use gene expression cascades to adjust the delay. Whether cells employ these mechanisms to optimize the phase relation is an interesting question for future work.

CONCLUSION

Cells can increase the transmission of temporal information by increasing the number of oscillatory signals N used to infer the time. In the analysis presented here, it is assumed that the system is linear and obeys Gaussian statistics. It is well known that protein distributions need not be Gaussian, and may exhibit, e.g., a gamma, negative binomial, or log-normal distribution [94]. In this case, one can construct a multivariate Gaussian model with the same second moments as the actual, non-Gaussian system. For this Gaussian model, $I(x,y;t) \geq I(x_G,y_G;t)$, because a Gaussian distribution has the largest entropy for a given variance [50, 96]; the results of the Gaussian model then present a lower bound on the mutual information. Moreover, especially at high noise, it might be beneficial to use non-linear input-output relations to enhance information transmission [59]. How much these effects can enhance information transmission is beyond the

scope of the current manuscript. Nonetheless, our linear model with Gaussian statistics already highlights that the problem of transmitting temporal information is very rich.

The precision of telling time depends on the relative noise $\widetilde{\sigma}_i = \sigma_i / A_i$ of the oscillatory signals, their phase shift, and the cross-correlations between them. When the relative noise $\widetilde{\sigma}_i$ is the same for all genes, the optimal phase relation that maximizes the mutual information and minimizes the error is one in which the phases are spaced evenly. Under this condition, the error in telling time is also uniform in time, provided that the noise $\sigma_i(t)$ is constant in time, which, to a good approximation, is the case when the amplitude of the oscillations is large compared to the mean. This is akin to what has been observed for the fruitfly *Drosophila*, where the expression pattern of the gap genes allows the nuclei to specify their position with nearly uniform precision along the anterior-posterior axis [56]. When the relative noise amplitudes $\widetilde{\sigma}_i$ are not the same for all signals, then the design principle for maximizing information transmission is that the oscillatory signals which are more reliable, should be spaced more evenly.

Lastly, we have addressed the role of cross correlations between the fluctuations in the oscillatory signals. When the relative noise is large, cross-correlations do not significantly affect information transmission. However, the situation changes markedly in the low-noise regime. In this regime, cross-correlations change the optimal phase shift that maximizes information transmission. More strikingly, they can increase the mutual information. At low noise, cross correlations can thus reduce the error in telling time and enhance the transmission of temporal information. This phenomenon is similar to what has been observed for neural networks [52] and spatial gene expression patterns during embryonic development, where cross-regulatory interactions between genes can enhance the precision by which cells or nuclei determine their spatial position within the developing embryo [49, 53, 56]. In all these cases the principle is that cross-correlations make it possible to tile the output space more efficiently, thus allowing for a less redundant input-output mapping. This is particularly important when the noise is low, and noise averaging is not important, but efficient tiling of state space is [49, 53].

APPENDIX:

2.4. THE OPTIMAL PHASE RELATION IN THE ABSENCE OF CROSS CORRELATIONS

We would like to compute the phase relation that minimizes the variance of the error, $(\delta\sigma_t)^2$, as given by Eq. 2.15, in the absence of cross correlations. However, the problem is that Eq. 2.11 is an expression for $\sigma_t^{-2}(t)$, not $\sigma_t(t)$. Hence, while it is fairly straightforward to derive the variance of σ_t^{-2}, i.e. $\langle(\sigma_t^{-2})^2\rangle - \langle\sigma_t^{-2}\rangle^2$, it is impossible, in general, to derive analytically the variance of the quantity we are interested in, $(\delta\sigma_t)^2 = \langle\sigma_t^2\rangle - \langle\sigma_t\rangle^2$. However, we know that if the variance of a function $g(t)$ is zero, $\sigma_g^2 = \int_0^T dt P(t)(g(t) - \langle g(t)\rangle)^2 = 0$, and $g(t)$ is thus a constant (independent of time), that then a) $\langle f(g(t))\rangle = f(\langle g(t)\rangle)$ and b) the variance of $f(t) = f(g(t))$ is zero, $\sigma_f^2 = \langle f^2\rangle - \langle f\rangle^2 = 0$. We now apply this logic with the identification $g(t) = \sigma_t(t)$ and $f(t) = g^{-2}(t)$. The trick that we thus employ is to establish that the variance which we can compute, $\sigma_f^2 = \langle(\sigma_t^{-2})^2\rangle - \langle\sigma_t^{-2}\rangle^2$,

is zero. If this is true, then we know that a) the variance of the quantity that we are interested in, $\sigma_g^2 = (\delta\sigma_t)^2$, must be zero as well. Moreover, we then also know that b) $\langle\sigma_t\rangle = \sigma_t = 1/\sqrt{\langle\sigma_t^{-2}(t)\rangle}$.

There are two points worthy of note. First, as mentioned, above, when $\sigma_f^2 = \langle(\sigma_t^{-2}(t))^2\rangle - \langle\sigma_t^{-2}(t)\rangle^2 = 0$, then $(\delta\sigma_t)^2 = 0$. In this case, the phase relation that minimizes σ_f^2 is the phase relation that minimises $\delta\sigma_t^2$ (making it zero indeed). However, when $\sigma_f^2 \neq 0$, then the phase relation that minimizes σ_f^2 is *not* necessarily the phase relation that minimises $\delta\sigma_t^2$. Secondly, the phase relation that minimizes $(\delta\sigma_t)^2$, is not necessarily the phase relation that minimizes σ_t, *even when* $(\delta\sigma_t)^2 = 0$. We need to check either numerically or, if possible, by analytically minimizing $\langle\sigma_t\rangle$ whether this is true or not. The same holds for the mutual information: the phase relation that minimizes $(\delta\sigma_t)^2$, is not necessarily the phase relation that maximizes the mutual information.

2.4.1. THE PHASE RELATION THAT MINIMIZES $(\delta\sigma_t)^2$ WHEN THE RELATIVE NOISE STRENGTHS ARE THE SAME

As explained above, to obtain the optimal phase relation that makes $(\delta\sigma_t)^2 = 0$, we aim to find the phase distribution for which:

$$\sigma_f^2 = \langle(\sigma_t^{-2}(t))^2\rangle - \langle\sigma_t^{-2}(t)\rangle^2 = 0. \tag{2.30}$$

When the cross correlations are zero, $\sigma_t^{-2}(t)$ is given by Eq. 2.12. The second term in the expression above, $\langle\sigma_t^{-2}(t)\rangle^2$, is then, for the case that the noise and the ampltidues are the same for all genes, given by

$$\langle\sigma_t^{-2}(t)\rangle = \left(\frac{2\pi A}{\sigma_x T}\right)^2 \frac{N}{2}. \tag{2.31}$$

The first term in Eq. 2.30 can be obtained recursively, and is given by

$$\langle(\sigma_t^{-2}(t))^2\rangle = K\left[\frac{N(2N+1)}{8} + \frac{1}{4}\sum_{i<j}^{N}\cos(2(\phi_i - \phi_j))\right] \tag{2.32}$$

where K is a constant, $K = \left(\frac{2\pi A}{\sigma_x T}\right)^4$. As expected this quantity depends on the phase relation.

Instead of finding the phase relation that makes the difference between the two terms of σ_f^2 in Eq. 2.30 zero, we now want to find the relation that makes the ratio of the two terms unity, which is equivalent, but mathematically more convenient. This yields

$$\frac{2}{N}\sum_{i\leq j}^{N}\cos(2(\phi_i - \phi_j)) = -1. \tag{2.33}$$

By solving this as a function of N, we can recognize a pattern, which reveals that the optimal phase relation that minimizes $(\delta\sigma_t)^2$ is given by

$$\phi_i - \phi_j = \frac{\pi}{N}(i-j). \tag{2.34}$$

This means that the i-th signal has a phase $\Delta\phi_i = (i-1)\frac{\pi}{N}$, as found for the phase relation that minimizes $\langle\sigma_t\rangle$, given by Eq 2.23. So in the case where the correlations are zero, the optimal phase shift minimizes both $\langle\sigma_t\rangle$ and its variance. Moreover, the mean error $\langle\sigma_t\rangle$ can then directly be obtained from Eq. 2.31.

2.4.2. THE PHASE RELATION THAT MINIMIZES $(\delta\sigma_t)^2$ WHEN THE NOISE σ_x IS NOT CONSTANT IN TIME

We now consider the case that $\sigma_i \simeq \sqrt{\bar{x}_i(t)}$, which means that $d\sigma_i/dt \neq 0$. In order to highlight the role of the time-varying noise, we keep $A_i = A_j = \cdots = A$, $r_i = r_j = \cdots = r$. The variance of $\sigma^{-2}(t)$ is given by:

$$\begin{aligned}\sigma_f^2 &= \langle(\sigma_t^{-2}(t))^2\rangle - \langle\sigma_t^{-2}(t)\rangle^2 \\ &= \left(\frac{A^3(2\pi)^2}{16T^2}\right)^2 \{N + 2N(N+1)r^2 + \\ &\quad \sum_{i\leq j}^{N}\left[\cos(\phi_i-\phi_j) + 4r^2\cos[2(\phi_i-\phi_j)\right] + \\ &\quad 4r^2\cos(\phi_i-\phi_j)]\} - \left(\frac{NA^3r(2\pi)^2}{2T^2}\right)^2 \end{aligned} \tag{2.35}$$

We note that this expression, in contrast to that for the case in which σ_i is constant in time, depends on the mean expression level of x, r. We find numerically that the phase relation that minimizes σ_f^2 is the same as that for the scenario in which σ_i is constant in time, Eq. 2.34. However, σ_f^2 and hence $(\delta\sigma_t)^2$ are only zero, when $r \to \infty$. We also find numerically that the phase relation that minimizes σ_f^2 equals the phase relation that minimizes the mean error $\langle\sigma_t\rangle$ and maximizes the mutual information.

2.4.3. THE PHASE RELATION THAT MINIMIZES $(\delta\sigma_t)^2$ WHEN THE RELATIVE NOISE STRENGTHS ARE ***not*** THE SAME

To assess the importance of differences in the relative noise strength, we will assume again that $\sigma_i(t) = \sigma_i$ is constant in time. Defining the relative noise *amplitude* $\widetilde{A}_i \equiv \widetilde{\sigma}_i^{-1} \equiv A_i/\sigma_i$, the variance of $\sigma^{-2}(t)$ is given by:

$$\begin{aligned}&\sigma_f^2 = \langle(\sigma_t^{-2}(t))^2\rangle - \langle\sigma_t^{-2}(t)\rangle^2 \\ &= \frac{1}{8}\left(\frac{2\pi}{T}\right)^4\left[\sum_{i=1}^{N} 3\widetilde{A}_i^2 + \sum_{i\leq j}^{N}\left(\left[4 + 2\cos[2(\phi_i-\phi_j)]\right]\widetilde{A}_i\widetilde{A}_j\right)\right] \\ &- \left(\frac{1}{2}\left(\frac{2\pi}{T}\right)^2\sum_{i=1}^{N}\widetilde{A}_i\right)^2 \end{aligned} \tag{2.36}$$

It can be verified that this reduces to Eq. 2.30 when σ_i/A_i is the same for all genes. Following the logic applied for that scenario, we find that the optimal phase relation that makes $\sigma_f^2 = 0$ is given by

$$\sum_{i\leq j}^{N} \cos\left[2(\phi_i-\phi_j)\widetilde{A}_i\widetilde{A}_j\right]\widetilde{A}_i^2\widetilde{A}_j = \sum_{i,j=1}^{N}\widetilde{A}_i\widetilde{A}_j - \frac{1}{2}\sum_{i=1}^{N}3\widetilde{A}_i^2 - 2\sum_{i\leq j}^{N}\widetilde{A}_i\widetilde{A}_j \tag{2.37}$$

This expression reduces to Eq. 2.33 when σ_i/A_i is the same for all genes. It can be verified numerically that the phase relation that makes σ_f^2 and hence $(\delta\sigma_t)^2$ zero, is also the phase relation that minimizes the mean error $\langle\sigma_t\rangle$ and maximizes the mutual information.

3

ENTRAINMENT OF CIRCADIAN CLOCKS IN THE PRESENCE OF NOISE

ABSTRACT

Circadian clocks are biochemical oscillators that allow organisms to estimate the time of the day. These oscillators are inherently noisy due to the discrete nature of the reactants and the stochastic character of their interactions. To keep these oscillators in sync with the daily day-night rhythm in the presence of noise, circadian clocks must be coupled to the dark-light cycle. In this manuscript, we study the entrainment of phase oscillators as a function of the intrinsic noise in the system. Using stochastic simulations, we compute the optimal coupling strength, intrinsic frequency and shape of the phase-response curve, that maximize the mutual information between the phase of the clock and time. We show that the optimal coupling strength and intrinsic frequency increase with the noise, but that the shape of the phase-response curve varies non-monotonically with the noise: in the low-noise regime, it features a deadzone that increases in width as the noise increases, while in the high-noise regime, the width decreases with the noise. These results arise from a trade-off between maximizing stability—noise suppression—and maximizing linearity of the input-output, *i.e.* time-phase, relation. We also show that three analytic approximations—the linear-noise approximation, the phase-averaging method, and linear-response theory—accurately describe different regimes of the coupling strength and the noise.

3.1. INTRODUCTION

Many organisms possess a circadian clock to anticipate the changes between day and night. Circadian clocks are biochemical oscillators that can tick without any external driving with an intrinsic, free-running period of about 24 hrs. In uni-cellular organisms these oscillations are formed by chemical reactions and physical interactions between molecules inside the cell, while in multi-cellular organisms these oscillations are typi-

cally shaped by a combination of intra- and inter-cellular interactions, which are, however, both mediated by molecular interactions. Due to the discreteness of molecules and the stochastic nature of chemical and physical interactions, circadian oscillations are inherently stochastic, which means that they have an intrinsic tendency to run out of phase with the day-night cycle. To keep the circadian oscillations in phase with the day-night rhythm, the oscillations must be coupled to daily cues from the environment, such as daily changes in light-intensity or temperature. This coupling makes it possible to lock the clock to, i.e. synchronize with, the daily rhythm. However, how the circadian clock should be coupled to entrainment cues is a question that is still wide open. It is neither clear what the natural performance measure for entrainment is, nor is it fully understood how this depends on the strength and form of the coupling, the characteristics of the entrainment signal, and the properties of the clock.

The function that is most commonly used to describe the coupling of the clock to the entrainment signal is called the phase-response curve [22]. It gives the shift of the phase of the clock as induced by a perturbation (a small change in, e.g., light intensity), as a function of the phase at which the perturbation was given. The phase-response curve has been measured for a wide variety of organisms, ranging from cyanobacteria, to fungi, plants, flies, and mammals [97]. Interestingly, these phase-response curves share a number of characteristic features: they typically consist of a positive and a negative lobe, and often possess a deadzone of no coupling during the subjective day (see Fig. 3.1). Yet, the width of the deadzone can vary significantly, and also the negative and positive lobe are not always equal in magnitude.

These observations naturally raise the question of what the best shape is for a phase-response curve. To answer this, a measure that quantifies the performance of the system is needed. Several measures have been put forward. A key characteristic of any locking scheme is the Arnold Tongue [22], which describes the range of system parameters over which the deterministic system is locked to the driving signal. In general, this range tends to increase with the strength of the driving signal, and one performance measure that has been presented is how the range – the width of the Arnold Tongue – increases with the magnitude of the driving; this derivative has been called the "entrainability" of the clock [98, 99]. Another hallmark of any stochastic system is its robustness against noise, and, in general, the stability of an entrained clock depends not only on its intrinsic noise, but also on the strength and shape of the coupling function; one way to quantify clock stability is the so-called "regularity", which is defined as the variance of the clock period [98, 99]. Another important property of any locked system, is its sensitivity to fluctuations in the driving signal. To quantify this, Pfeuty *et al.* have defined two sensitivity measures, one that describes the change in the phase difference between the signal and the clock due to a change in the input, and another that quantifies the change in the stability of the fixed point (the slope of the phase-response curve) in response to a change in the input signal [97].

These performance measures make it possible to make predictions on the optimal shape of the phase-response curve. Pfeuty *et al.* argued that the shape of the phase-responce curve is determined by the requirement that the clock should respond to changes in light intensity that are informative on the day-night rhythm, namely light-intensitiy changes during dawn and dusk, but should ignore uninformative fluctuations in light

intensity during the day, arising, e.g., from clouds [97]. This naturally gives rise to a deadzone in the phase-response curve, which allows the clock to ignore the input fluctuations during the day. Hasegawa and Arita argued that the shape of the phase-response curve is determined by a trade-off between regularity (stability) and entrainability [98, 99]. Entrainability requires not only changes in light intensity, but also that a change in the copy number n_i of a component i, as induced by the changing light signal, leads to a change in the phase ϕ of the clock: the gain $d\phi/dn_i$ should be large. However, a higher gain also means that the evolution of the phase becomes more susceptible to noise in n_i. Maximizing entrainibility for a given total noise strength integrated over 24 hrs then yields a phase-response curve with a deadzone: During the day, when informative variations in light intensity are low, a high gain will not significantly enhance entrainability but will increase the integrated noise, implying that the gain should be as low as possible during the middle of the day.

In this manuscript, we introduce another measure to quantify the performance of the system, the mutual information [63]. The mutual information quantifies the number of signals that can be transmitted uniquely through a communication channel. As such it is arguably the most powerful measure for quantifying information transmission, and in recent years the mutual information has indeed been used increasingly to quantify the quality of information transmission in cellular signalling systems [31, 32, 46–62]. In the context studied here, the central idea is that the cell needs to infer from a variable of the clock, e.g. its phase ϕ, the time of the day t. The mutual information then makes it possible to quantify the number of distinct time points that can be inferred uniquely from the phase of the clock. Importantly, how many time states can be inferred reliably, depends not only on the noise in the system, but also on the shape of the input-output curve, $\overline{\phi}(t)$, i.e. the average phase $\overline{\phi}(t)$ at time t.

We study how the mutual information between the clock phase and the time depends on the shape and magnitude of the phase response curve in the presence of intrinsic noise in the system; we thus do not consider fluctuations in the input signal. The clock is modelled as a phase oscillator and the phase-response curve is described via a piecewise linear function (see Fig. 3.1), which allows for optimization and analytical results. We find that for a given amount of noise in the system there exists an optimal coupling strength that maximizes the mutual information: Increasing the coupling strength too much will decrease the mutual information. However, as the noise in the system increases, the optimal coupling strength increases. Moreover, for a given shape of the phase-response curve featuring a deadzone, the optimal intrinsic (free running) period of the clock is non-monotonic: as the noise is increased, the optimal period first becomes larger than 24 hrs, but then decreases to become smaller than 24 hrs. Optimizing over not only the coupling strength and the intrinsic period, but also over the shape of the phase response curve, reveals that the optimal width of the deadzone is also non-monotonic. As the noise is increased, the width first increases, but then decreases. We show that all of these results can be understood as a trade-off between linearity and stability. At low noise, it is paramount to make the input-output relation $\overline{\phi}(t)$ as linear as possible, because this maximizes the mutual information; this is enhanced by a large deadzone and weak coupling. However, for large noise strengths, stability becomes key, which favours a small deadzone, a stronger coupling, and a smaller intrinsic period.

In the next section, we first briefly present the Chemical Langevin Description of a biochemical network, because this is important for understanding not only the phase-reduction method that reduces the system to a phase-oscillator model, but also for understanding some important characteristics of the mutual information. In the subsequent section, we then introduce the mutual information. We emphasize that the mutual information is insensitive to a coordinate transformation and that the mutual information between all degrees of freedom of the system (i.e. copy numbers of all components) and the input (i.e. time t) is always larger than that between one degree of freedom and the input. This means that the mutual information that we will compute between the phase of the clock and the time will provide a firm lower bound on the actual mutual information. We then briefly describe our phase-oscillator model and how we model the phase-response curve.

In the results section, we first present the results of stochastic simulations of our phase-oscillator model. By performing very extensive simulations we find the system parameters that maximize the mutual information, and by explicitly computing the linearity and stability as a function of parameters, we show that the optimal design as a function of the noise arises from the trade-off mentioned above between linearity and stability.

Finally, we present and apply three different analytic approximations (or "theories"), and show that each recapitulates the simulations in a different parameter regime. The linear-noise approximation accurately describes the regime of low noise and strong coupling. The phase-averaging method [22] captures the regime of low noise and weak coupling. Finally, the linear-response theory accurately describes the mutual information in the regime of high noise and weak coupling. Whereas the first two approximations are valid in the vicinity of the optimal coupling for an appropriate range of noise strengths, the third turns out to hold only far from optimality.

3.2. MODEL

3.2.1. CHEMICAL LANGEVIN DESCRIPTION

We consider a self-sustained oscillator of M components with copy numbers $n_1, n_2, \ldots, n_M$, denoted by the vector $\mathbf{n}$. Its dynamics is given by

$$\frac{d\mathbf{n}}{dt} = \mathbf{A}(\mathbf{n}), \tag{3.1}$$

where $\mathbf{A}(\mathbf{n})$ is determined by the propensity functions of the chemical reactions that constitute the network. The limit cycle of the free-running oscillator is the stable periodic solution of this equation, $\mathbf{n}(t) = \mathbf{n}(t+T_0)$, where T_0 is the intrinsic period of the oscillator.

Due to the stochasticity of the chemical reactions and the discreteness of the molecules, the evolution of the network is stochastic. When the copy numbers are sufficiently large such that there exists a macroscopic time interval dt during which the propensity functions remain constant and the Poissonian distribution of reaction events can be approximated as a Gaussian, then the dynamics is described by the chemical Langevin equation

[100],

$$\frac{d\mathbf{n}}{dt} = \mathbf{A}(\mathbf{n}) + \underline{\eta}(\mathbf{n}), \tag{3.2}$$

where the vector $\underline{\eta}(t)$ describes the Gaussian white noise, characterized by the noise matrix with elements $\langle \eta_i(\mathbf{n}(t))\eta_j(\mathbf{n}(t'))\rangle = D_{ij}(\mathbf{n})\delta(t-t')$.

A clock is only a useful timing device if it has a stable and precise phase relationship with the daily rhythm. Biochemical noise tends to disrupt this relationship. To keep the clock in sync with the day-night rhythm in the presence of noise, the clock must be coupled to the light signal:

$$\frac{d\mathbf{n}}{dt} = \mathbf{A}(\mathbf{n}) + \epsilon\mathbf{p}(\mathbf{n},t) + \underline{\eta}(\mathbf{n}). \tag{3.3}$$

Here $\mathbf{p}(\mathbf{n},t)$ describes the coupling to the light signal and ϵ the strength of the coupling. The coupling force $\mathbf{p}(\mathbf{n},t) = \mathbf{p}(\mathbf{n},t+T)$ has a period T and frequency $\omega = 2\pi/T$, which in general is different from the intrinsic period T_0 and intrinsic frequency $\omega_0 = 2\pi/T_0$, respectively, of the free-running oscillator. In this manuscript, we will assume that the light signal is deterministic. We thus only consider the biochemical noise in the clock.

3.2.2. MUTUAL INFORMATION

The organism needs to infer the time t from the concentrations of the clock components. This inference will be imprecise, because of the noise in the clock. We will quantify the accuracy of information transmission via the mutual information, which is a measure for how many distinct time states can be resolved from the concentrations of the clock components [63].

The mutual information $I(\mathbf{n};t) = I(\{n_1,\ldots,n_M\};t)$ between the copy numbers of all components and the time is given by

$$I(\mathbf{n};t) = \int d\mathbf{n} \int dt P(\mathbf{n};t) \log_2 \frac{P(\mathbf{n};t)}{P(\mathbf{n})P(t)}, \tag{3.4}$$

where $P(\mathbf{n};t)$ is the probability that copy numbers $\mathbf{n}$ are found at time t. $I(\mathbf{n};t)$ measures the reduction in uncertainty about t upon measuring $\{n_1,\ldots,n_M\}$, or vice versa. The quantity is indeed symmetric in $\mathbf{n}$ and t:

$$I\mathbf{n};t) = H(t) - \langle H(t|\mathbf{n})\rangle_{\mathbf{n}} \tag{3.5}$$

$$= H(\mathbf{n}) - \langle H(\mathbf{n}|t)\rangle_t, \tag{3.6}$$

where $H(\mathbf{a}) = -\int d\mathbf{a} P(\mathbf{a}) \log_2 P(\mathbf{a})$, with $P(\mathbf{a})$ the probability distribution of $\mathbf{a}$, is the entropy of $\mathbf{a}$; $H(\mathbf{a}|\mathbf{b}) = -\int d\mathbf{a} P(\mathbf{a}|\mathbf{b}) \log_2 P(\mathbf{a}|\mathbf{b})$ is the information entropy of $\mathbf{a}$ given $\mathbf{b}$, with $P(\mathbf{a}|\mathbf{b})$ the conditional probability distribution of $\mathbf{a}$ given $\mathbf{b}$; $\langle f(c)\rangle_c$ denotes an average of $f(c)$ over the distribution $P(c)$.

A key point worthy of note is that the mutual information is invariant under a coordinate transformation, which allows us to put a firm lower bound on the mutual information between time and the clock components. Specifically, we can first make a

non-linear transformation from $\mathbf{n}$ to some other set of variables $\mathbf{x}$, of which two components are the amplitude R of the clock and its phase ϕ. Because the mutual information is invariant under this transformation,

$$I(\mathbf{n}, t) = I(\mathbf{x}, t). \tag{3.7}$$

Secondly, if the time is inferred not from all the components of $\mathbf{x}$, but rather from R and ϕ, then, in general

$$I(R, \phi; t) \leq I(\mathbf{x}; t). \tag{3.8}$$

By combining this expression with Eq. 3.7, we find that

$$I(\mathbf{n}; t) \geq I(R, \phi; t) \tag{3.9}$$

Hence, once we have defined a mapping between $\mathbf{n}$ and $\mathbf{x}$ and hence (R, ϕ), the mutual information $I(R, \phi; t)$ between the combination of the amplitude and phase of the clock (R, ϕ) and time t, puts a lower bound on the mutual information $I(\mathbf{n}; t)$. A weaker lower bound is provided by the mutual information between the phase of the clock and time:

$$I(\mathbf{n}; t) \geq I(R, \phi; t) \geq I(\phi; t). \tag{3.10}$$

However, we expect this bound to be rather tight, since a reasonable, natural, mapping between $\mathbf{n}$ and (R, ϕ) should put the information on time in the phase of the clock.

3.2.3. PHASE OSCILLATOR

The bound of Eq. 3.10 makes it natural to develop a description of the clock in terms of the phase. Here, we review the derivation of such a description, largely following the standard arguments in [22], but paying special attention to the appropriate form of the effective noise on the phase variable. In the absence of any coupling and noise, the temporal evolution of the phase is given by

$$\frac{d\phi(\mathbf{n})}{dt} = \omega_0, \tag{3.11}$$

where $\omega_0 = 2\pi / T_0$ is the intrinsic frequency of the clock, with T_0 the intrinsic period. As the phase is a smooth function of $\mathbf{n}$, the evolution of ϕ is also given by

$$\frac{d\phi(\mathbf{n})}{dt} = \sum_i \frac{\partial \phi}{\partial n_i} \frac{dn_i}{dt}. \tag{3.12}$$

Combining the above two equations with Eq. 3.1 yields the following expression for the intrinsic frequency

$$\omega_0 = \sum_i \frac{\partial \phi}{\partial n_i} A_i(\mathbf{n}). \tag{3.13}$$

This equation *defines* a mapping $\phi(\mathbf{n})$. This mapping is defined such that for each point $\mathbf{n}$ in state space, the time derivative $d\phi(\mathbf{n})/dt = d\phi/dt$ of the phase is constant and

equal to ω_0. The surfaces of constant $\phi(\mathbf{n})$, defined according to this mapping, are called isochrones.

In the presence of noise, the phase dynamics is, combining Eqs. 3.2 and 3.12,

$$\frac{d\phi(\mathbf{n})}{dt} = \sum_i \frac{\partial \phi}{\partial n_i}\left[A_i(\mathbf{n}) + \eta_i(\mathbf{n})\right], \tag{3.14}$$

$$= \omega_0 + \xi(\mathbf{n}), \tag{3.15}$$

which yields for the noise on the phase variable

$$\xi(\mathbf{n}) = \sum_i \frac{\partial \phi}{\partial n_i}\eta_i(\mathbf{n}). \tag{3.16}$$

In general, the variance of ξ thus depends on all of the state variables $\mathbf{n}$, not just on the phase ϕ, and Eq. 3.15 does not give a closed description in terms only of ϕ. However, when the deviations from the limit cycle are small compared to the scale over which the noise strength changes as a function of distance from the limit cycle, we can estimate the noise by evaluating it at the limit cycle, $\mathbf{n}_0$:

$$\xi(\phi) = \sum_i \frac{\partial \phi(\mathbf{n}_0)}{\partial n_i}\eta_i(\mathbf{n}_0), \tag{3.17}$$

with Gaussian white noise statistics

$$\langle \xi(\phi(t))\xi(\phi(t'))\rangle = \sum_{i,j} \frac{\partial \phi}{\partial n_i}\frac{\partial \phi}{\partial n_j} D_{ij}(\mathbf{n}_0)\delta(t-t'), \tag{3.18}$$

$$\equiv 2D(\phi)\delta(t-t'). \tag{3.19}$$

When the system is coupled to light, the phase evolution becomes, from Eqs. 3.3 and 3.12,

$$\frac{d\phi(\mathbf{n})}{dt} = \sum_i \frac{\partial \phi}{\partial n_i}\left[A_i(\mathbf{n}) + \epsilon p_i(\mathbf{n},t) + \eta_i(\mathbf{n})\right]. \tag{3.20}$$

The force depends explicitly on time. This impedes a unique definition of the isochrones $\phi(\mathbf{n})$, because how the phase evolves at a particular point in phase space depends not only on $\mathbf{n}$ but also on t. Of course, one could still adopt the mapping of the free running system, in which case the evolution of the phase is given by

$$\frac{d\phi(\mathbf{n})}{dt} = \omega_0 + \epsilon \sum_i \frac{\partial \phi}{\partial n_i} p_i(\mathbf{n},t) + \xi(\phi). \tag{3.21}$$

The problem is that, because along the surface $\phi(\mathbf{n})$ the light-coupling term is not constant, $d\phi(\mathbf{n})/dt$ will depend on $\mathbf{n}$. One can then not reduce the dynamics to that of a single phase variable.

However, if ϵ is small and the force only leads to small deviations from the limit cycle of the free-running system, then one may approximate the effect of the forcing by evaluating the corresponding term at the limit cycle, $\mathbf{n}_0$. We then have

$$\frac{d\phi(\mathbf{n})}{dt} = \omega_0 + \epsilon \sum_i \frac{\partial \phi(\mathbf{n}_0)}{\partial n_i} p_i(\mathbf{n}_0,t) + \xi(\phi). \tag{3.22}$$

In this case the evolution of the phase no longer explicitly depends on **n**:

$$\frac{d\phi}{dt} = \omega_0 + Q(\phi, t) + \xi(\phi), \tag{3.23}$$

with

$$Q(\phi, t) = \epsilon \sum_i \frac{\partial \phi(\mathbf{n}_0(\phi))}{\partial n_i} p_i(\mathbf{n}_0(\phi), t). \tag{3.24}$$

How a circadian clock responds to a given light signal $L(t)$ depends on its phase ϕ; it does not explicitly depend on time. The coupling term can then be written as $Q(\phi, t) = Z(\phi)L(t)$, where $Z(\phi)$ is the instantaneous phase response curve, which describes how the clock responds to the light signal as a function of its phase ϕ. In addition, while in general the noise strength depends on the phase, we will, motivated by the experimental observations of Mihalecescu and Leibler on the *S. elongatus* clock[67], assume it is constant. We then finally arrive at the equation that describes the evolution of the phase in our model:

$$\frac{d\phi}{dt} = \omega_0 + Z(\phi)L(t) + \xi(t), \tag{3.25}$$

with $\langle \xi(t)\xi(t') \rangle = 2D\delta(t - t')$.

In what follows, we will study entrainment using the above equation not only when $Z(\phi)L(t)$ and D are much smaller than ω_0, so that the weak coupling assumptions necessary for the reduction to a phase oscillator clearly hold, but also when $Z(\phi)L(t)$ or D are of order ω_0 or larger. As we discuss in more detail in Section 3.5, however, this does not present any contradiction, because it is perfectly possible for the noise and the external driving to be small compared to restoring forces orthogonal to the limit cycle, so that the system always stays near the limit cycle and the phase is the only relevant variable, while simultaneously strongly perturbing motion along the limit cycle. We also note that ϵ can be varied independently of the noise strength. What is perhaps less obvious is whether $Z(\phi)$ and D can be varied independently. When the size of the system, e.g. the volume of the living cell, is changed, as was done for *Bacillus subtilus* [101], then the noise strength D will change, but the coupling strength $Z(\phi)$ will, to first order, not change because the concentrations remain constant. Moreover, typically the system is coupled to light only via a relatively small number of reactions, while the noise is determined by all reactions. Also in this case, it seems natural to assume that $Z(\phi)$ and D can be varied independently. We note that the arguments of Hasegawa and Arita do not contradict our arguments that $Z(\phi)$ and D can be varied independently: the fact that changing the gain $\partial\phi/\partial n_i$ affects both the coupling to light (entrainability) and the phase noise [98, 99], does not mean that the noise and the coupling cannot be varied independently if other parameters are changed (and vice versa). We thus imagine that $p_i(\mathbf{n})$ can be tuned (by evolution) independently of the $D_{ij}(\mathbf{n})$. We do not change the mapping $\phi(\mathbf{n})$, determined by the properties of the uncoupled system.

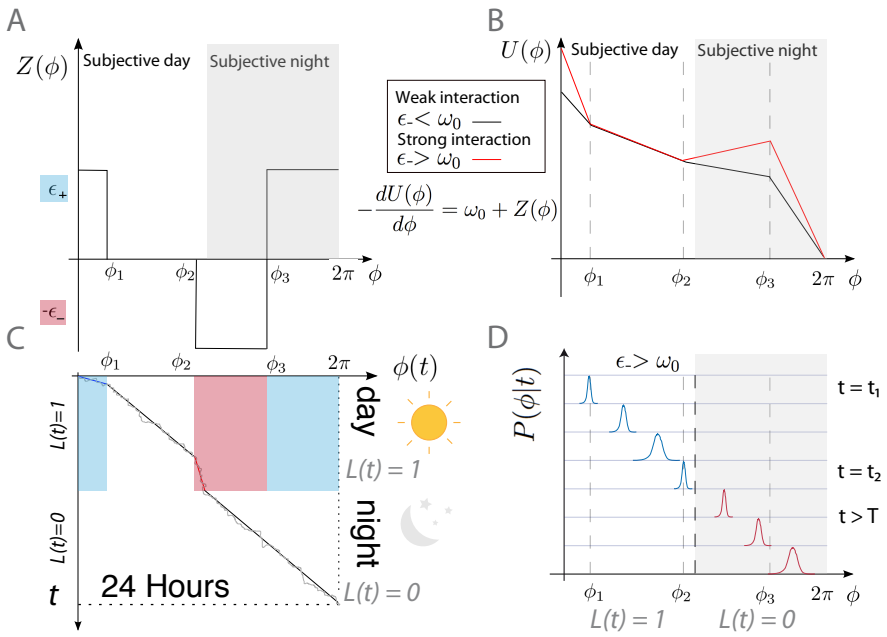

Figure 3.1: Cartoon of the system. (A) The instantaneous phase response curve $Z(\phi)$, characterized by the 5 parameters ϵ_+, ϵ_- and ϕ_1, ϕ_2, ϕ_3. The driving signal is given by $L(t) = 1$ during the day and $L(t) = 0$ during the night. (B) The phase evolution of the system, $d\phi/dt$, can be interpreted as that of a particle in a potential $U(\phi)$, with a force $-dU(\phi)/d\phi = \omega_0 + Z(\phi)L(t)$. Note that the particle only experiences a force during the day, when $L(t) = 1$, and not during the night, when $L(t) = 0$. (C) The phase evolution of the system, in the limit of small noise. During the night the deterministic system always evolves with its intrinsic frequency ω_0. During the day, it evolves with its intrinsic frequency ω_0 when the phase is between ϕ_1 and ϕ_2; between $\phi_3 - 2\pi$ and ϕ_1, the system is "pushed", moving with a frequency $\omega_0 + \epsilon_+$, while between ϕ_2 and ϕ_3 it is slowed down, moving at frequency $\omega_0 - \epsilon_-$. (D) Illustration of how $P(\phi)$ evolves in time, in the regime of strong coupling. At dawn, the system is pushed, narrowing the distribution; during the deadzone in which $Z(\phi) = 0$, the distribution tends to widen; near dusk, the system is slowed down, narrowing the distribution; during the night, the system evolves freely, widening the distribution again.

3.2.4. THE SYSTEM

We will approximate $Z(\phi)$ and $L(t)$ as step functions, shown in Fig. 3.1. This makes it possible to analytically obtain the Arnold tongue, i.e. the range of parameters for which the deterministic system locks to the day-night rhythm in the absence of noise. The light-dark function $L(t)$ is unity for $0 < t < T/2$ and zero for $T/2 < t < T$. The shape of the instantaneous phase response curve $Z(\phi)$ is inspired by experimentally characterized response curves, featuring a positive lobe, a dead-zone in which $Z(\phi)$ is essentially zero, a negative lobe, followed by a positve lobe again [97]. It is characterized by five variables,

the coupling strengths ϵ_+ and ϵ_-, and the phases ϕ_1, ϕ_2, ϕ_3:

$$Z(\phi) = \begin{cases} \epsilon_+ & 0 < \phi < \phi_1 \\ 0 & \phi_1 < \phi < \phi_2 \\ -\epsilon_- & \phi_2 < \phi < \phi_3 \\ \epsilon_+ & \phi_3 < \phi < 2\pi \end{cases} \tag{3.26}$$

where ϵ_+ and ϵ_- are greater than 0. With these 5 variables, a wide range of experimentally characterized phase response curves can be described.

3.3. RESULTS

3.3.1. ARNOLD TONGUE OF THE DETERMINISTIC SYSTEM

Motivated by the observation that circadian clocks typically lock 1:1 to the day-night rhythm, we will focus on this locking scenario, although we will also see that this system can exhibit higher order locking, especially when the intrinsic period of the clock deviates markedly from that of the day-night rhythm. To derive the Arnold tongue, we first note that when the clock is locked to the light-dark cycle, it will have a characteristic phase ϕ_s at the beginning of the light-dark cycle, $t_s = 0$. In the case of 1:1 locking, the phase of the clock will then cross phase ϕ_1 at time t_1, ϕ_2 at time t_2, and ϕ_3 at time t_3. To obtain the Arnold tongue, we have to recognize that there are in total 12 possible locking scenarios: 3 for ϕ_s and 4 for t_1, t_2, t_3. The scenarios for ϕ_s are: 1: $\phi_3 - 2\pi < \phi_s < \phi_1$; 2: $\phi_1 < \phi_s < \phi_2$; 3: $\phi_2 < \phi_s < \phi_3$. The 4 scenarios for t_1, t_2, t_3 are defined by where $T/2$ falls with respect to these times: 1: $T/2 < t_1 < t_2 < t_3$; 2: $t_1 < T/2 < t_2 < t_3$; 3: $t_1 < t_2 < T/2 < t_3$; 4: $t_1 < t_2 < t_3 < T/2$. For each of these 12 scenarios, we can analytically determine ϕ_s and t_1, t_2, t_3, which then uniquely specify $\phi(t)$. The 4 unknowns, ϕ_s, t_1, t_2, t_3, give each an inequality for T, and the range of T that satisfies all 4 inequalities determines the width of the Arnold tongue. For each of the 12 scenarios for the given ϵ_+, ϵ_-, we have an Arnold tongue, and those 12 tongues together give "the" Arnold tongue for those values of ϵ_+, ϵ_-. We now derive the tongue for scenario 1, which is also the most important one, as we will see: in this regime, the mutual information between time and the phase of the clock is the largest.

Scenario 1 is characterized by: $\phi_3 - 2\pi < \phi_s < \phi_1$; $0 < t_1 < t_2 < T/2 < t_3$. The solution depends on whether ϵ_- is larger or smaller than ω_0. If $\epsilon_- < \omega_0$, then the deterministic system locks 1:1 to the driving signal when

$$\begin{aligned} &\phi_s + (\epsilon_+ + \omega_0)\, t_1 + \omega_0 (t_2 - t_1) \\ &+ (-\epsilon_- + \omega_0)(T/2 - t_2) + \omega_0 T/2 = \phi_s + 2\pi. \end{aligned} \tag{3.27}$$

To solve this, we note that $\phi_1 = \phi_s + (\omega_0 + \epsilon_+)\, t_1$, $\Delta\phi_{12} \equiv \phi_2 - \phi_1 = \omega_0 (t_2 - t_1)$. The solution

is

$$t_1 = \frac{2\pi - T(\omega_0 - \epsilon_-/2) - \epsilon_- \Delta\phi_{12}/\omega_0}{\epsilon_+ + \epsilon_-} \geq 0, \tag{3.28}$$

$$t_2 = \frac{\Delta\phi_{12}}{\omega_0} + t_1 < T/2, \tag{3.29}$$

$$t_3 = \frac{\Delta\phi_{23}}{\omega_0 - \epsilon_-} + t_2 > T/2, \tag{3.30}$$

$$\phi_s = \phi_1 - (\omega_0 + \epsilon_+)\, t_1 > \phi_3 - 2\pi, \tag{3.31}$$

where $\Delta\phi_{23} \equiv \phi_3 - \phi_2$. The above inequalities lead to the following inequalities for the period T, respectively:

$$T \leq \frac{2\pi - \epsilon_- \Delta\phi_{12}/\omega_0}{\omega_0 - \epsilon_-/2}, \tag{3.32}$$

$$T > \frac{2\pi + \epsilon_+ \Delta\phi_{12}/\omega_0}{\epsilon_+/2 + \omega_0}, \tag{3.33}$$

$$T < \frac{2\pi + \epsilon_+ \Delta\phi_{12}/\omega_0 + \Delta\phi_{23}(\epsilon_+ + \epsilon_-)/(\omega_0 - \epsilon_-)}{\epsilon_+/2 + \omega_0}, \tag{3.34}$$

$$T > \frac{(\Delta\phi_{13} - 2\pi)(\epsilon_+ + \epsilon_-)/(\omega_0 + \epsilon_+) + 2\pi - \epsilon_- \Delta\phi_{12}/\omega_0}{\omega_0 - \epsilon_-/2}, \tag{3.35}$$

where $\Delta\phi_{13} \equiv \phi_3 - \phi_1 = \Delta\phi_{12} + \Delta\phi_{23}$. The width of the Arnold tongue is given by the range of T that satisfies all inequalities.

If $\epsilon_- > \omega_0$, then the equation to solve is:

$$\phi_s + (\epsilon_+ + \omega_0)\, t_1 + \omega_0 (t_2 - t_1) + \omega_0 T/2 = \phi_s + 2\pi. \tag{3.36}$$

The solution is

$$t_1 = \frac{2\pi - \omega_0 T/2 - \Delta\phi_{12}}{\epsilon_+ + \omega_0} \geq 0 \tag{3.37}$$

$$t_2 = \frac{\Delta\phi_{12}}{\omega_0} + t_1 < T/2 \tag{3.38}$$

$$t_3 = \infty > T/2 \tag{3.39}$$

$$\phi_s = \phi_1 - (\omega_0 + \epsilon_+)\, t_1 > \phi_3 - 2\pi \tag{3.40}$$

The third inequality, for t_3 does not contribute, if the other inequalities are satisfied. We thus have 3 inequalities:

$$T \leq \frac{2(2\pi - \Delta\phi_{12})}{\omega_0} \tag{3.41}$$

$$T > \frac{2\pi + \epsilon_+ \Delta\phi_{12}/\omega_0}{\epsilon_+/2 + \omega_0} \tag{3.42}$$

$$T > \frac{2\Delta\phi_{23}}{\omega_0} \tag{3.43}$$

It is seen that the locking region does not depend on the absolute values of ϕ_1, ϕ_2, ϕ_3, but only on the separation between them, leaving only two independent parameters that are related to the phase: $\Delta\phi_{12} = \phi_2 - \phi_1$ and $\Delta\phi_{23} = \phi_3 - \phi_2$; the remaining interval is given by $2\pi - \Delta\phi_{13} = 2\pi - (\Delta\phi_{12} + \Delta\phi_{23})$. Shifting the absolute values of ϕ_1, ϕ_2, ϕ_3 only changes the definition of the phase of the clock, not the moments of the day—t_1, t_2, t_3—at which $Z(\phi)$ changes. The system thus has 5 independent parameters, 4 related to $Z(\phi)$ — $\Delta\phi_{12}, \Delta\phi_{23}, \epsilon_P, \epsilon_M$—and one being the intrinsic frequency ω_0.

In the appendix, we derive the Arnold Tongues for the other scenarios. It turns out that only scenarios 1 - 4 yield stable solutions; the solutions of the other scenarios are unstable.

Fig. 3.2 shows the Arnold Tongues for the 4 scenarios. Since we imagine that the period of the light-day cycle is fixed while the clock can adjust its intrinsic frequency ω_0, we plot the range of $\epsilon = \epsilon_P = \epsilon_M$ over which the system exhibits a stable deterministic solution, as a function of ω_0/ω; $\Delta\phi_{12} = \Delta\phi_{23} = \pi/2$. The different colors correspond to the different scenarios. Clearly, the Arnold Tongues of the respective scenarios are adjoining. The region in the middle, around $\omega_0 = \omega$, bounded by the blue lines, corresponds to our natural scenario, i.e. scenario 1, discussed above. The green lines bound the Arnold Tongue of scenario 3. This is an unnatural scenario, because in this scenario the clock is driven backwards when the light comes up. Moreover, for $\omega_0/\omega > 2$, the system can also exhibit higher-order locking, which is biologically irrelevant. We will therefore focus on the regime $0.5 < \omega_0 < 2$.

Fig. 3.2 shows that for $\epsilon < 1$ the Arnold Tongue exhibits the characteristic increase in its width as the coupling strength is increased: coupling increases the range of frequencies over which the clock can be entrained. However, for $\epsilon > 1$, the width does not change significantly; in fact, it does not change at all when $\omega_0 > \omega$. This is because a) during the day, for $\epsilon_- = \epsilon = \epsilon_+ > 1$, the phase evolution comes to a halt at ϕ_3—the particle sits in the potential well of Fig. 3.1B and b) during the night the system evolves with a fixed speed ω_0, independent of ϵ.

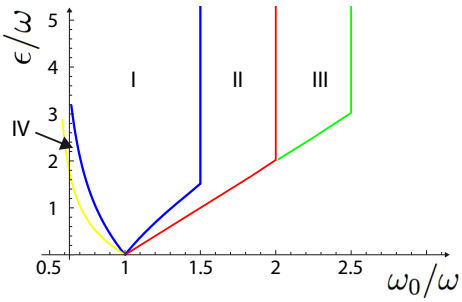

Figure 3.2: The Arnold Tongue for 1:1 locking in the deterministic model, with the coupling strength $\epsilon_+ = \epsilon_- = \epsilon$ in units of the (fixed) frequency of the day-night rhythm ω, plotted as a function of the intrinsic frequency of the clock, ω_0/ω. The different colors correspond to the different scenarios that yield a stable solution. The large region around $\omega_0/\omega = 1$, bounded by the blue lines, corresponds to the Arnold Tongue of scenario 1. The adjoining region to the right, with the red boundaries, corresponds to scenario 2. The green lines bound the Arnold Tongue of scenario 3, and the yellow lines on the far left yield the Arnold Tongue of scenario 4. The other key parameters of $Z(\phi)$ are kept constant: $\Delta\phi_{12} = \Delta\phi_{23} = \pi/2$.

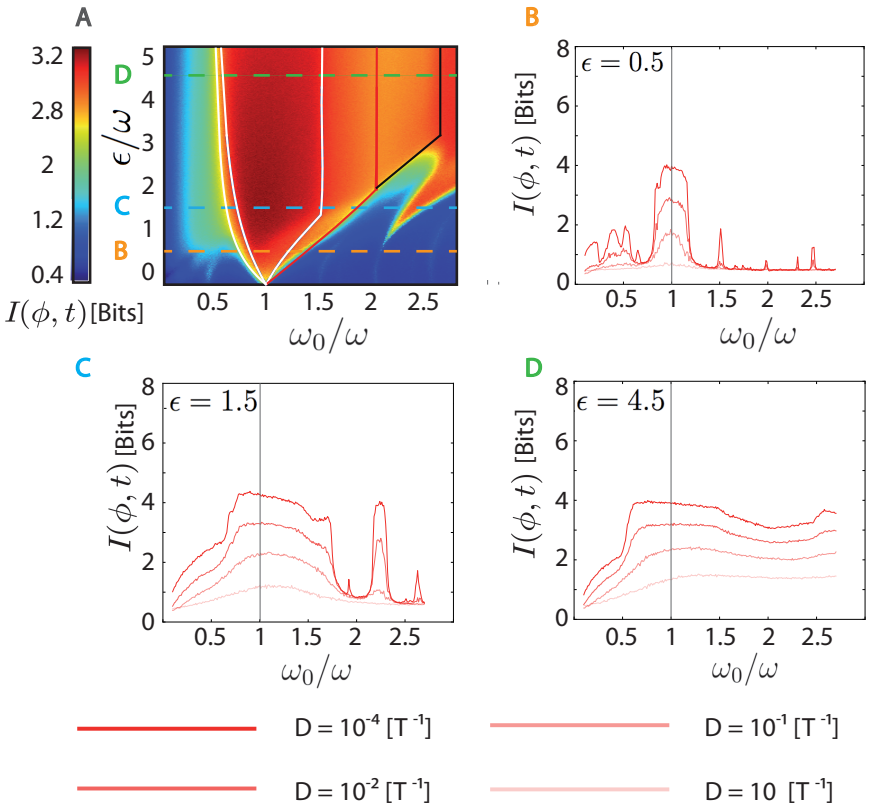

Figure 3.3: The mutual information as a function of ϵ, D, and ω_0, keeping $\Delta\phi_{12} = \Delta\phi_{23} = \pi/2$. (A) Heatmap of the mutual information as a function of ϵ/ω and ω_0/ω for $D = 0.1/T$, respectively. Superimposed are the Arnold Tongue for 1:1 locking in scenarios 1–4. It is seen that the mutual information is high inside the Arnold Tongues, with the region corresponding to scenario 1 being the most stable one. The mutual information can, however, also be high outside the 1:1 locking regions, because of higher-order locking, especially when $\omega_0/\omega > 2$. (B-D) The mutual information as a function of ω_0/ω for different values of the diffusion constant D, and for three values of the coupling strength ϵ/ω, as indicated by the dashed lines in panel A: $\epsilon/\omega = 0.5$ (B), $\epsilon/\omega = 1.5$ (C), and $\epsilon/\omega = 4.5$ (D). For all values of ϵ, the mutual information increases as D decreases. The peaks outside the main locking region around $\omega_0 \approx \omega$ correspond to higher order locking.

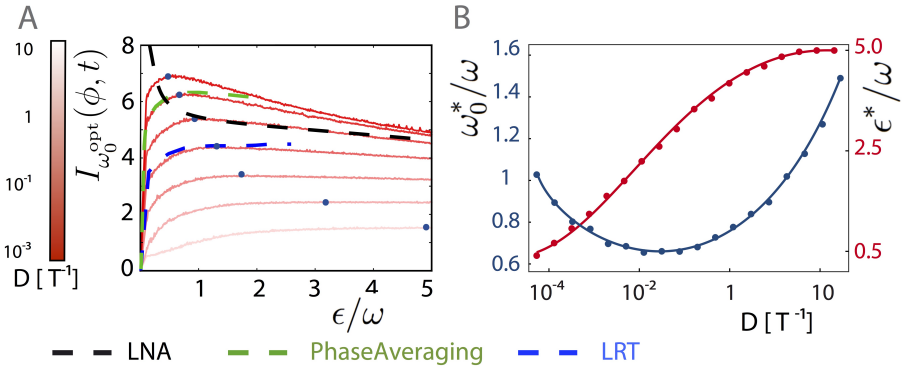

Figure 3.4: Optimal design of the clock: parameters $\epsilon = \epsilon_+ = \epsilon_-$ and ω_0 of the phase-response curve $Z(\phi)$ that maximize the mutual information $I(\phi, t)$ as a function of the intrinsic clock noise D, keeping the shape of $Z(\phi)$ constant (see Fig. 3.1A). (A) The mutual information $I_{\omega_0^{\mathrm{opt}}}(\phi;t)$ obtained by maximizing $I(\phi;t)$ over ω_0 as a function of ϵ, for different values of D. It is seen that there is an optimal coupling strength ϵ_{opt} that maximizes the mutual information, which depends on the magnitude of the diffusion constant D; the blue dot denotes the maximum for each value of D. The figure also shows the predictions of three theories, each for their own regime of validity: the linear-noise approximation (LNA), which captures the regime of strong coupling ϵ and low diffusion D (result shown for $D = 10^{-2}/T$); the phase-averaging method (PAM), which describes the regime of weak coupling and weak noise (result shown for $D = 10^{-3}/T$); and linear-response theory (LRT), which describes the regime of high diffusion and weak coupling (result shown for $D = 1/T$). For a more detailed comparision of the accuries of the respective theories, see Fig. 3.8. (B) The optimal coupling strength ϵ_{opt} (red dots) and the optimal intrinsic frequency ω_0^{opt} (blue dots), both obtained by maximizing $I(\phi;t)$ over *both* ϵ and ω_0, as a function of D. While ϵ_{opt} increases with D monotonically, ω_0^{opt} first decreases from $\omega_0 = \omega$, but then rises again to become larger than ω for higher D. The lines are a guide to the eye. Other parameters: $\Delta\phi_{12} = \Delta\phi_{23} = \pi/2$.

3.3.2. OPTIMAL COUPLING STRENGTH AND INTRINSIC FREQUENCY IN PRESENCE OF NOISE

While the Arnold Tongue shows the range of parameters over which the deterministic system can exhibit stable 1:1 locking, it does not tell us how reliably the time can be inferred from the phase in the presence of noise. To address this question, we have computed the mutual information $I(\phi;t)$ between the phase of the clock, $\phi(t)$, and the time t, by performing long stochastic simulations of the system, i.e. stochastically propagating Eq. 3.25.

Fig. 3.3A shows a heatmap of the mutual information as a function $\epsilon_+ = \epsilon_- = \epsilon$ and ω_0/ω, for $\Delta\phi_{12} = \Delta\phi_{23} = 0.5\pi$ and $D = 0.1/T$. Superimposed over the heatmap are the deterministic Arnold Tongues for scenarios 1–4, which are also shown in Fig. 3.2. It is seen that the mutual information is highest in the region bounded by the Arnold Tongue of 1:1 locking in scenario 1. Interestingly, however, the figure does also show that the mutual information can be large outside of the 1:1 locking regimes, especially when

$\omega_0/\omega > 2$. This is the result of higher order locking.

The results of Fig. 3.3A are further elucidated in panels B-D, which show the mutual information as a function of ω_0/ω for different values of the diffusion constant D, and for three different values of ϵ/ω, respectively; the results for $D = 0.1/T$ in the panels B-D correspond to three different cuts through the heatmap of panel A. The following points are worthy of note. First, it can be seen that for each value of ϵ/ω and ω_0/ω the mutual information always increases with decreasing D. Decreasing the noise makes the mapping from the time to the phase of the clock more deterministic, which means that the time can be more accurately inferred from the phase of the clock. Secondly, it is seen that the mutual information exhibits very characteristic peaks, which result from higher order locking. For example, the peak at $\omega_0/\omega \approx 2.3$ for $\epsilon = 1.5\omega$, corresponds to 2:1 locking.

Fig. 3.3 also shows that, for a given ω_0 and D, the mutual information initially increases with ϵ. This is not surprising, and is consistent with the observation that increasing the coupling strength ϵ tends to widen the Arnold Tongue; locking is enhanced by increasing the coupling strength. However, a closer examination of the different panels of Fig. 3.3 suggests that the mutual information not only saturates as ϵ is increased further, but even goes down. The second surprising observation is that the optimal intrinsic frequency ω_0 that maximizes the mutual information is not equal to ω. In fact, it seems to be smaller than ω when D is small, but then becomes larger than ω as D is increased (panel D).

To elucidate the optimal design of the clock that maximizes the mutual information further, we show in Fig. 3.4A the mutual information $I_{\omega_0^{\mathrm{opt}}}(\phi;t)$ that has been obtained by maximizing $I(\phi;t)$ over ω_0 as a function of ϵ, for different values of D. It is seen that for all values of D, $I_{\omega_0^{\mathrm{opt}}}(\phi;t)$ first rises with ϵ, as expected. However, $I_{\omega_0^{\mathrm{opt}}}(\phi;t)$ then reaches a maximum, after which it comes down: there exists an optimal coupling strength ϵ_{opt} that maximizes $I_{\omega_0^{\mathrm{opt}}}(\phi;t)$; increasing the coupling too much will actually *decrease* the mutual information. Fig. 3.4A also shows, however, that the optimal coupling ϵ_{opt} does increase with the diffusion constant. This is more clearly shown in panel B: ϵ_{opt} increases monotonically with D. This panel also shows the optimal intrinsic frequency ω_0^{opt} obtained by maximizing the mutual information over both ω_0 and ϵ, as a function of D. For $D \to 0$, ϵ_{opt} goes to zero, and ω_0 to ω—this is the free running clock. As D is increased, however, ω_0 first decreases, but then increases again to become larger than ω for higher diffusion constants. The optimal intrinsic period that maximizes the mutual information depends in a non-trivial, non-monotonic, manner on the noise in the clock.

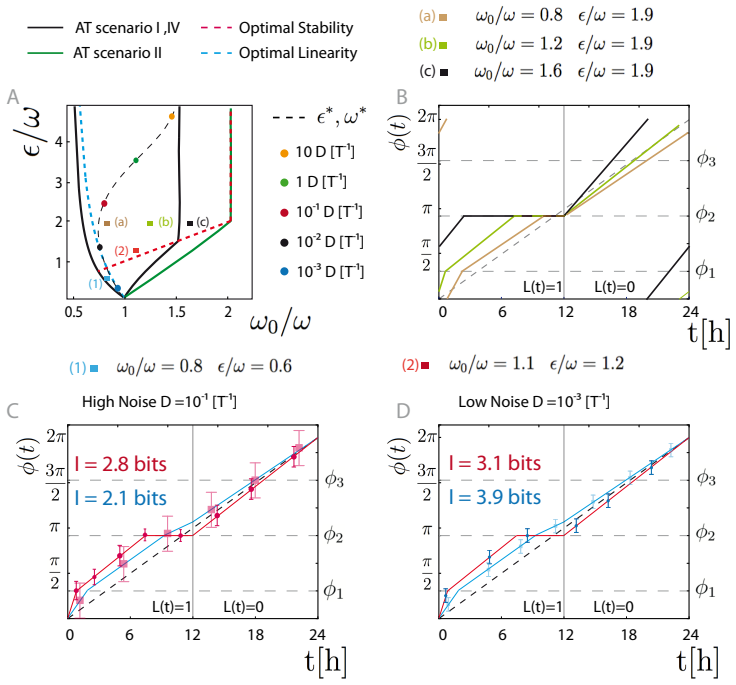

Figure 3.5: The optimal design arises from a trade-off between linearity and stability. (A) The black line shows the Arnold Tongue for scenario 1 and 4 while the green line shows the Arnold Tongue of scenario 2 (see also Fig. 3.2). The dashed blue line shows for each value of ϵ the value of ω_0 that makes the input-output curve, $\overline{\phi}(t)$, most linear, i.e. minimizes $\int_0^T dt(\overline{\phi}(t) - \omega t)^2$. The dashed red line shows for each value of ϵ the value of ω_0 that maximizes the stability. For $\epsilon/\omega < 2$, this line is $\omega_0 = \epsilon$, along which $F' = 0$; for $\epsilon = \epsilon_- > \omega_0$, $F' = 0$ for all values of ω_0 and ϵ; the line of maximal stability then corresponds to the line where the system spends most of its time in ϕ_2, which is the line $\omega_0 = \epsilon$ when $\epsilon < 2\omega$ and $\omega_0 = 2\omega$ when $\epsilon \geq \omega$; this is further illustrated in panel B. The dashed black line shows a parametric plot of the optimal system, i.e. the combination $(\epsilon_{\text{opt}}, \omega_0^{\text{opt}})$ that maximizes the mutual information as a function of D (values of D along this solid line are indicated by the coloured circles; see also Fig. 3.4B). It is seen that for low diffusion constant, the optimal system that maximizes the mutual information (black line) follows the dashed blue line where the input-output curve is most linear, while for high noise the optimal system moves towards the dashed red line, where the system is most stable. How this trade-off between linearity and stability maximizes information tranmission is further illustrated in panels (C) and (D). Panel (B) shows the average input-output curves for the three points labelled (a), (b), and (c) in panel A. It is seen that as the system moves towards the line of maximal stability, the time the system spends in ϕ_2 increases; for $\epsilon/\omega > 2$, at $\omega_0 = 2\omega$, the system starts the day at ϕ_2. Panel (C) shows the two average input-output curves corresponding to the two points (1) and (2) in panel (A), together with the output noise, for a high value of the diffusion constant, $D = 0.1/T$. Panel (D) shows the same, but then for a low value of the diffusion constant, $D = 10^{-3}/T$. It is seen that when the noise is small (panel D), the output noise of the more stable system (red line) is hardly smaller than that of the more linear system (blue line); consequently, the optimal input-output curve can be linear to maximize information transmission. In contrast, when the noise is large (panel C), the system with a more linear input-output curve (the blue line) has significantly more output noise than the more stable but more non-linear system (red line); in this regime, stability becomes important for taming the output noise, making the optimal system more non-linear (red line). Other parameters: $\Delta\phi_{12} = \Delta\phi_{23} = \pi/2$.

3.3.3. OPTIMAL DESIGN ARISES FROM TRADE-OFF BETWEEN LINEARITY AND STABILITY

To understand the optimal design of the clock, we have to recognize that, in general, the amount of information that is transmitted through a communication channel depends on the input distribution, the input-output relation, and on the noise that is propagated to the output. For a given amount of noise, the optimal shape of the input-output relation that maximizes the mutual information is determined by the shape of the input distribution. However, the shape that optimally matches the input-output curve to the input distribution, is not necessarily the design that minimizes the noise in the output. Our system provides a clear demonstration of this general principle, and, as we will see, the optimal design of the clock can be understood as arising from a trade-off between stability, i.e. noise minimization, and linearity, i.e. optimally matching the input-output curve to the statistics of the input.

When the noise is very weak, noise minimization is not important, and optimally matching the input-output curve to the input distribution is paramount. Since the input distribution $p(t)$ is flat, the optimal input-output curve is linear: the average phase $\overline{\phi}(t)$ should increase linearly with time t. This is indeed the solution of the free running clock, $\phi(t) = \omega_0 t$, and it explains why in the low-noise limit the optimal design is that of an essentially free running system that is only very weakly coupled to the input.

However, as the noise level is increased, the reliability by which each input signal is relayed, becomes increasingly important. Here, a trade-off could emerge: while increasing the coupling strength ϵ could reduce the noise at the output, which tends to enhance information transmission, it may also distort the input-output curve, pushing it away from its optimal linear-shape, decreasing information transmission. Can we capture this trade-off quantitatively?

To study the trade-off between linearity and stability, we have computed for each value of ϵ, the value of ω_0 that makes the average input-output relation $\overline{\phi}(t)$ most linear, i.e. minimizes $\int_0^T dt(\overline{\phi}(t) - \omega t)^2$. The result is the blue line in Fig. 3.5A, which lies in the Arnold tongue of scenario I. Along this line of maximal linearity, ω_0 decreases as ϵ increases, which can be understood intuitively by noting that increasing ϵ introduces a curvature in the input-output relation, leading to a deviation away from the straight line ωt: at the beginning of the day, till the time t_1 at which the system crosses ϕ_1, the phase evolves with a speed $\omega_0 + \epsilon$, whereas between the time t_2 at which the system crosses ϕ_2 and the end of the day at $T/2$, the phase evolves either follows ϕ_2 when $\epsilon = \epsilon_- > \omega_0$ or evolves with a speed $\omega_0 - \epsilon$ when $\epsilon = \epsilon_- < \omega_0$. While increasing ϵ tends to increase the curvature, this effect can be counteracted by decreasing ω_0.

To quantify the stability, we define the return map $F_t(\phi)$:

$$\phi(t+T) = F_t(\phi(t)) =, \tag{3.44}$$

where the subscript t for F indicates that the return map depends on time; this subscript will be suppressed in what follows below when there is no ambiguity, in order to simplify notation. The deterministic solution $\phi^*(t)$ is given by $\phi^*(t) = \phi^*(t+T) = F(\phi^*(t))$. We now expand $F(\phi)$ around $\phi^*(t)$:

$$F(\phi^* + \delta\phi) = F(\phi^*) + F'(\phi^*)\delta\phi, \tag{3.45}$$

where $\delta\phi = \phi - \phi^*$ and we have dropped the subscript t because $F'(\phi)$, which gives the rate of exponential relaxation back to the limit cycle over many cycles, must be independent of t. Indeed, by exploiting that $F(\phi^*(t)) = \phi^*(t+T)$, we find that

$$\delta\phi(t+T) = F'(\phi^*)\delta\phi(t). \tag{3.46}$$

The quantity $F'(\phi^*) \equiv \partial F(\phi)/\partial\phi|_{\phi^*} = \partial\phi(t+T)/\partial\phi(t)|_{\phi^*(t)}$ determines the linear stability of the system, with $F' < 1$ meaning that the system is stable. The quantity can be directly obtained from the deterministic solutions. We first note that, since $L(t) = 0$ during the dark, $F'(\phi^*(t=0)) = \partial\phi(T)/\partial\phi(0) = \partial\phi(T/2)/\partial\phi(0)$. For scenario 1, when $\epsilon_- < \omega_0$, $\phi(T/2) = \phi_2 + (\omega_0 - \epsilon_-)(T/2 - t_2)$. We then find that, exploiting Eqs. 3.38 and 3.40, $F'(\phi^*(t=0) = \partial\phi(T/2)/\partial\phi(0) = \partial\phi(T/2)/\partial\phi_s = (\partial\phi(T/2)/\partial t_2)(\partial t_2/\partial t_1)(\partial t_1/\partial\phi_s) = (\omega_0 - \epsilon_-)/(\omega_0 + \epsilon_+)$. Similarly, for scenario 2 we find that, for $\epsilon_- < \omega_0$, $F'(\phi^*(t=0) = (\omega_0 - \epsilon_-)/\omega_0$. Here, we consider the case that $\epsilon_- = \epsilon_+ = \epsilon$. Clearly, in both scenarios the stability is maximized when ϵ approaches ω_0 and $F'(\phi^*)$ becomes zero. This defines the line $\epsilon = \omega_0$, along which $F'(\phi^*) = 0$; it is the part of the red dashed line of maximal stability in Fig. 3.5A that corresponds to $\epsilon < 2\omega$.

For $\epsilon = \epsilon_- > \omega_0$, $F'(\phi^*) = 0$ for both scenarios I and II, because during the day the phase evolution of the system comes to a standstill at ϕ_2; any perturbation in ϕ will fully relax during one period. Can we nonetheless differentiate in the stability strength, even though the *linear* stability $F'(\phi^*) = 0$ for all points (ϵ, ω) above the line $\epsilon = \omega_0$? To answer this question, we turn to a global stability measure, which is defined by the amount of time the deterministic system spends at ϕ_2, which is the bottom of the potential well when $\epsilon = \epsilon_- \geq \omega_0$ (see Fig. 3.1). The value of ω_0 that maximizes the stability for a given ϵ according to this measure, is $\omega_0 = \epsilon$ when $\epsilon \leq 2\omega$ and $\omega_0 = 2\omega$ when $\epsilon \geq 2\omega$. This fully specifies the line of maximum stability shown in Fig. 3.5A. The reason why the stability is maximized along this line, is illustrated in Fig. 3.5B. During the night, the trajectories evolve freely, and because of noise they will arrive at the beginning of the day with a distribution of phases. Along the line of maximum stability, the stochastic trajectories are most likely to reach the bottom of the potential well at ϕ_2 during the day (see Fig. 3.1), where they will be confined, before they are released again during the night. Indeed, along this stability line the variance in the phase, $\langle\delta\phi^2\rangle$, will be lowest which tends to increase information transmission. However, the input-output relation $\overline{\phi}(t)$ is then highly non-linear. In fact, the globally most stable solution, for all possible values of ϵ and ω_0, is

$$\phi^{\text{stab}}(t) \equiv \phi_2\theta(T/2 - t) + \omega_0 t\theta(t - T/2), \text{ with } \omega_0 = 2\omega, \tag{3.47}$$

which is the most stable solution for any $\epsilon \geq 2\omega$. It is shown in Fig. 3.5B—it is the solution at the high-frequency boundary of the AT tongue of scenario 2. This solution maximizes the probability that trajectories that start of the limit cycle at the beginning of the day, will return to the limit cycle ϕ_2 before the end of the day. While this solution is maximally stable, no time points t can be inferred from $\phi(t)$ during the day, because $\overline{\phi}(t)$ is completely flat. This dramatically reduces information transmission.

The optimal values of ω_0 and ϵ that maximize the mutual information as a function of the noise in the system can now be understood as a trade-off between linearity and stability. This trade-off is illustrated in the bottom panels of Fig. 3.5, which show the

average input-output curves, together with their output noise, for the two points 1 and 2 in the map of panel A, both for a high diffusion constant (panel C) and a low diffusion constant (panel D). When the diffusion constant is low (panel D), the noise in the more stable but more non-linear system (red line, corresponding to point 2) is hardly lower than that in the more linear but less stable system (blue line, corresponding to point 1), which means that the benefit of linearity dominates and the mutual information is maximized in the more linear system. In contrast, when the noise is larger (panel C), the output noise in the more stable but more non-linear system (red line) is so much smaller than that in the less stable but more linear system (blue line) that it outweighs the cost of higher non-linearity, thus maximizing mutual information.

Finally, panel A also shows a parametric plot of the optimal (ϵ, ω_0) that maximizes the mutual information, with the noise D the parameter that is being varied (dashed black line; the colors of circles denote values of the diffusion constant). It is seen that for low D the optimal system traces the dashed blue line of maximal linearity, but then at a higher D makes a transition towards the dashed red line line of maximal stability.

3.3.4. THE OPTIMAL SHAPE OF THE PHASE RESPONSE CURVE

In the previous section, we showed how the optimal values of the coupling strength ϵ and the intrinsic frequency ω_0 depend on the noise D in the system, while keeping the shape of the coupling function $Z(\phi)$ constant. In this section, we will relax this restriction.

We first checked the effect of changing the magnitude of the positive and negative lobe of the coupling function $Z(\phi)$ as characterized by ϵ_+ and ϵ_-, respectively (see Fig. 3.1), keeping $\Delta\phi_{12} = \Delta\phi_{23} = \pi/2$ constant. We varied ϵ_+ and ϵ_- via a parameter α, defined as $\epsilon_+ = (1-\alpha)\epsilon$ and $\epsilon_- = \alpha\epsilon$; changing α thus keeps the total absolute coupling strength (the integrated modulus) constant. We found, however, that the results are not very sensitive to the precise values of ϵ_+ and ϵ_- (see Appendix 3.9).

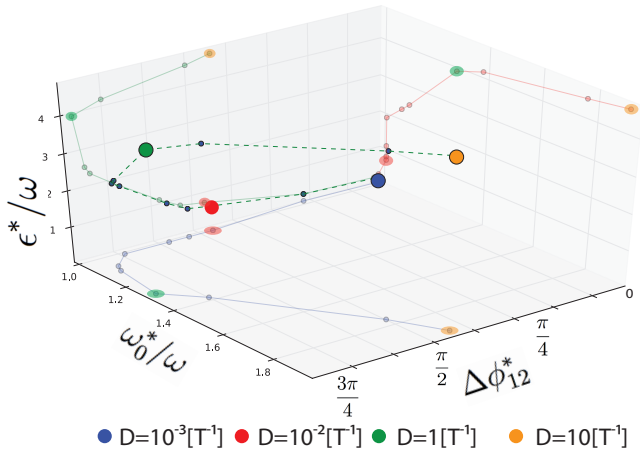

Figure 3.6: A paramteric plot of the optimal coupling strength $\epsilon^*(D)$, the optimal intrinsic frequency $\omega_0^*(D)$ and the optimal width of the deadzone $\Delta\phi_{12}^*(D)$ that maximize the mutual information, with the noise D being the parameter that is varied. The value of $\Delta\phi_{23} = \pi/2$ was kept constant. It is seen that ϵ^* rises with D, while ω_0^* remains initially close to ω, but then rises too. In contrast, $\Delta\phi_{12}^*$ first increases and then decreases. Coloured dots give the diffusion constants for which $(\epsilon^*, \omega_0^*, \Delta\phi_{12}^*)$ are optimal.

We then decided to compute the mutual information $I(\phi, t)$ as a function of $\Delta\phi_{12}$ and $\Delta\phi_{23}$ for different values of ϵ, ω_0, and D, keeping $\epsilon_+ = \epsilon_- = \epsilon$. We found that the mutual information is essentially independent of $\Delta\phi_{23}$. This can be understood as follows: The deterministic Arnold tongue and, to a good approximation, the dynamics of the stochastic system, does not depend on the absolute values of ϕ_1, ϕ_2, ϕ_3, but only on $\Delta\phi_{12}$ and $\Delta\phi_{23}$ (see section 3.3.1). Moreover, as long as ϕ_3 is crossed during the night (see Fig. 3.1), we can change ϕ_3 at will, because during the night, when $L(t) = 0$, the clock is not coupled to light (see Eq. 3.25), meaning that the clock runs with its intrinsic frequency ω_0. Changing $\Delta\phi_{23}$ by changing ϕ_3 will thus have no effect. Changing $\Delta\phi_{23}$ by changing ϕ_2 will also have no effect when ϕ_1 is simultaneously changed such that $\Delta\phi_{12}$ remains constant: while changing ϕ_2 and ϕ_1 keeping $\Delta\phi_{12}$ and ϕ_3 constant will alter $\Delta\phi_{23}$, we can always change ϕ_3 such that $\Delta\phi_{23}$ remains unchanged. In short, as long as ϕ_3 is crossed during the night (which it will for most values of ϕ_1 and ϕ_2), changing ϕ_1 and ϕ_2 keeping $\Delta\phi_{12}$ constant, does not change the dynamics; the times t_1 and t_2 at which ϕ_1 and ϕ_2 are crossed, respectively, do not change.

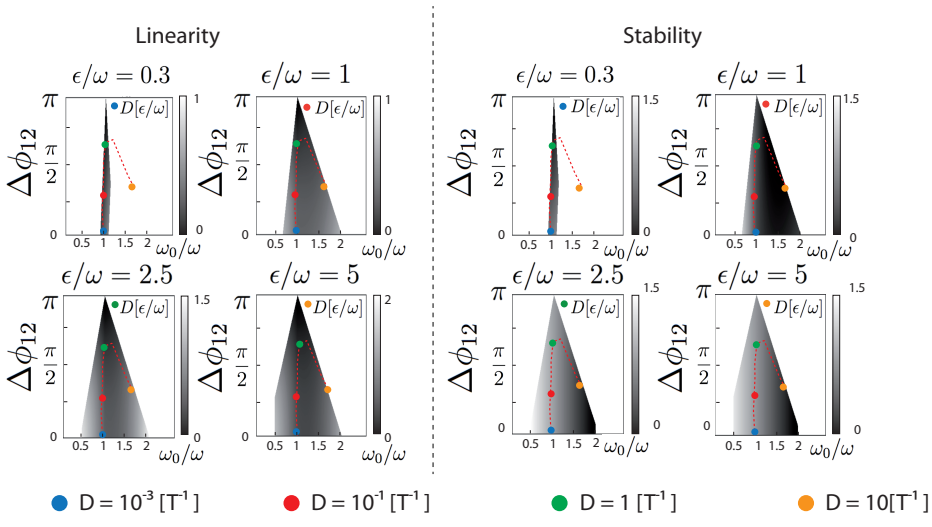

s

Figure 3.7: The optimal shape of the instantaneous phase response curve $Z(\phi)$ arises as a trade-off between linearity and stability. The linearity (A) is quantified via $\int_0^T dt(\overline{\phi}(t) - \phi^{\text{lin}}(t))^2$, which is the average deviation of the mean input-output relation $\overline{\phi}(t)$ away from the most linear solution $\phi^{\text{lin}}(t) = \omega t$. The stability (B) is quantified via $\int_0^T dt(\overline{\phi}(t) - \phi^{\text{stab}}(t))^2$, which is the average deviation of $\overline{\phi}(t)$ away from the most stable solution $\phi^{\text{stab}}(t)$, given by Eq. 3.47. These measures are computed as a function of the intrinsic frequency ω_0 and the width of the deadzone $\Delta\phi_{12}$, for different values of ϵ, inside the Arnold Tongue of scenario 1; note that smaller values correspond to higher linearity and stability, respectively. Superimposed is a parametric plot of the optimal intrinsic frequency $\omega_0^*(D)$ and optimal width of the dead-zone $\Delta\phi_{12}^*(D)$ that maximize the mutual information for a given D. The dots denote the values of D to which $\omega_0^*(D)$ and $\Delta\phi_{12}^*(D)$ correspond; the value of D for which the ϵ of a panel is the optimal coupling strength ϵ^* is given near the top of the Arnold tongue. It is seen that for small D, the optimal parameters $(\omega_0^*(D), \Delta\phi_{12}^*(D), \epsilon^*(D))$ that maximize the mutual information are those that make the input-output relation $\overline{\phi}(t)$ most linear (top left panel A), while for large D, the optimal parameters are those that make the system very stable (bottom right panel B). Other parameters: $\Delta\phi_{23} = \pi/2$.

Because ϕ_{23} is not critical, we kept $\Delta\phi_{23} = \pi/2$, and then performed very extensive simulations to determine the optimal coupling strength ϵ^*, speed ω_0^* and optimal deadzone $\Delta\phi_{12}^*$ that maximize the mutual information, as a function of D. Fig. 3.6 shows a parametric plot of $\epsilon^*(D), \omega_0^*(D)$ and $\Delta\phi_{12}^*(D)$, with D being the parameter that is varied. It is seen that for very low D, the optimal coupling strength ϵ^* is small, the optimal intrinsic frequency ω_0^* is close to ω, and the optimal value of $\Delta\phi_{12}^*$ is small. As the diffusion constant is increased, ϵ^* rises but ω_0^* initially remains close to ω and then increases too. The optimal value of $\Delta\phi_{12}$, however, first rises and then falls again.

The behaviour of $\Delta\phi_{12}^*$ can again be understood as a trade-off between linearity and stability. This is illustrated in Fig. 3.7. The figure shows for different values of ϵ the linearity and the stability of the input-output relation $\overline{\phi}(t)$ as a function of $\Delta\phi_{12}$ and ω_0, computed within the deterministic Arnold tongue of scenario 1 (where the mutual information is highest). The linearity of $\overline{\phi}(t)$ is quantified via $\int_0^T dt(\overline{\phi}(t) - \phi^{\text{lin}}(t))^2$, which is the

average deviation of $\overline{\phi}(t)$ away from the most linear input-output relation, $\phi^{\text{lin}}(t) = \omega t$. The stability of $\overline{\phi}(t)$ is quantified via $\int_0^T dt(\overline{\phi}(t) - \phi^{\text{stab}}(t))^2$, which is the average deviation of $\overline{\phi}(t)$ away from the most stable input-output relation $\phi^{\text{stab}}(t)$, given by Eq. 3.47.

The following observations can be made. First, the width of the Arnold tongue (the range of ω_0 that permits a deterministic solution) decreases as $\Delta\phi_{12}$ increases. Secondly, the linearity is maximal in the range $1 < \omega_0/\omega < 1.5$, and tends to increase with $\Delta\phi_{12}$: in the deadzone $\Delta\phi_{12}$ the system evolves freely with speed ω_0, which makes $\overline{\phi}(t)$ more linear, especially when $\omega_0 \sim \omega$. In contrast, the stability is highest when ω_0/ω is large and $\Delta\phi_{12}$ is small, particularly for higher values of ϵ. The large magnitudes of ω_0 and ϵ mean that at the beginning of the day the system is strongly driven, $\langle\dot{\phi}\rangle \approx \epsilon + \omega_0$, and the small deadzone $\Delta\phi_{12}$ means that after the system has crossed ϕ_1, it quickly reaches ϕ_2, where, with $\epsilon = \epsilon_- > \omega_0$, the system is then confined (see Fig. 3.1).

Fig. 3.7 also shows superimposed a parametric plot of the optimal $\Delta\phi_{12}^*(D)$ against the optimal $\omega_0^*(D)$. The colored dots denote the diffusion constants for which $(\omega_0^*, \Delta\phi_{12}^*)$ are optimal; the diffusion constant for which the ϵ of a panel is the optimal coupling strength ϵ^* is shown near the top of the Arnold tongue. It is seen that for very small D, the optimal system parameters $(\omega_0^*, \Delta\phi_{12}^*, \epsilon^*)$ put the system in the regime where $\phi(t)$ is linear (top left panel A); increasing $\Delta\phi_{12}^*$ would not make the system significantly more linear, since ϵ^* is still very small. Increasing D raises ϵ^*, while ω^* remains close to ω. The optimal width of the deadzone $\Delta\phi_{12}^*$ now increases, because for the higher value of ϵ^* the system becomes significantly more linear when $\Delta\phi_{12}^*$ is increased. Beyond $D = 1/T$, however, linearity is sacrificed for stability. The optimal coupling strength ϵ^* and intrinsic frequency ω^* increase, while the optimal size of the deadzone decreases, to maximize stability. Indeed, when the noise is even larger still, the width of the deadzone reduces to zero and the coupling strength and intrinsic frequency become even larger: during the day the system is rapidly driven to ϕ_2, where it then remains strongly confined till the beginning of the night (see Fig. 3.1 and also Fig. 3.5C). In this limit, the clock transmits one bit of information, and the system can only distinguish between day and night.

Fig. 3.6 thus generalises the finding of Fig. 3.5 that corresponds to a fixed deadzone and shows that the optimal shape of the instantaneous phase response curve can be understood as a trade-off between linearity and stability.

3.4. THEORY

The simulation results can be described quantitatively via three different theories, which each accurately describe a particular regime of parameters: The linear-noise approximation (LNA) describes the regime of strong coupling and low diffusion; the phase-averaging method (PAM) holds in the low diffusion, weak coupling regime; and the linear-response theory (LRT) applies in the regime of high noise and weak coupling. Here, we have borrowed the terminology LNA from the name of the theory to describe biochemical networks that is based on the same underlying principles: indeed, rather than linearising the Chemical Langevin Equation around the fixed point given by the mean-field chemical rate equations and taking the noise at that fixed point, we here linearise the return map $F(\phi)$ around its fixed point, and compute the noise at that fixed point. The

results of the respective theories in their regime of validity are shown in Fig. 3.4. A more detailed comparison between the simulation results and the theoretical predictions, discussed below, is shown in Fig. 3.8, where ϵ and D are varied for two different values of ω_0.

3.4.1. LINEAR-NOISE APPROXIMATION

The linear-noise approximation (LNA) is expected to be accurate when the driving is strong compared to the diffusion constant, so that the system closely follows the deterministic solution $\phi^*(t)$, which is given by the return map of Eq. 3.44: $\phi^*(t) = \phi^*(t+T) = F(\phi^*(t))$. Because in this regime the deviations from the deterministic solution are small, we can expand $F(\phi)$ up to linear order in $\delta\phi = \phi - \phi^*$ to obtain $F(\phi^* + \delta\phi)$, see Eq. 3.45. This makes it possible to derive how a deviation from the deterministic solution at time t will relax to the limit cycle at time $t+T$: $\delta\phi(t+T) = F'(\phi^*)\delta\phi(t)$ (see Eq. 3.46). The quantity $F'(\phi^*)$ thus determines the stability of the system near the deterministic fixed point. It can be readily obtained from the deterministic solutions.

Given a variance at time t, $\langle\delta\phi(t)^2\rangle$, the variance at time $t+T$, $\langle\delta\phi(t+T)^2\rangle$, is given by two contributions:

$$\langle\delta\phi(t+T)^2\rangle = F'^2(\phi^*)\langle\delta\phi(t)^2\rangle + V\left[\phi(t+T)|\phi^*(t))\right]. \tag{3.48}$$

The first contribution is a deterministic contribution, which is determined by how a deviation $\delta\phi(t) = \phi(t) - \phi^*(t)$ at time t regresses deterministically to the mean at time $t+T$: $\delta\phi(t+T) = F'(\phi^*)\delta\phi(t)$. The second contribution describes the variance of the distribution $P(\phi(t+T)|\phi^*(t))$ of $\phi(t+T)$ at time $t+T$, given that at time t the system was at the deterministic solution $\phi^*(t)$; in general, we should instead compute the variance at $t+T$ for an arbitrary initial $\phi(t) = \delta\phi(t) + \phi^*(t)$, but to leading order in small $\delta\phi$ it is sufficient to evaluate the noise at the deterministic solution ϕ^*. It is important to note that the variance $V\left[\phi(t+T)|\phi^*(t))\right]$ depends not only on the diffusion constant, but also on the deterministic force, as in a canonical LNA description: For example, in the simplest possible noisy dynamics, $\dot{\delta x} = -k\delta x(t) + \eta(t)$, with $\langle\eta(t)\eta(t')\rangle = 2D\delta(t-t')$, the deterministic contribution to the variance $\langle\delta x(t+T)^2\rangle$ at time $t+T$, given the variance $\langle\delta x(t)^2\rangle$ at time t, is $\langle\delta x(t)^2\rangle e^{-2kT}$, while the stochastic contribution to the variance at time $t+T$ is $V[\delta x(t+T)|x^*(t)] = (D/k)(1-e^{-2kT})$, which indeed depends on the force constant k. However, in the limit that the force is weak, the stochastic contribution is given by the variance of free diffusion: $V[\delta x(t+T)|x^*(t)] = 2DT$. We assume, and subsequently verify numerically, that a similar simplification applies for our phase oscillator model. Indeed, except at the boundaries ϕ_1, ϕ_2, and ϕ_3, our phase dynamics reduces to diffusion with a constant drift, for which it is rigorously true that $V\left[\phi(t+T)|\phi^*(t))\right] = 2DT$; our assumption hence amounts to neglecting any corrections to the integrated noise due to the brief "kicks" at these boundaries. Eq. 3.48 then reduces to

$$\langle\delta\phi(t+T)^2\rangle = F'^2(\phi^*)\langle\delta\phi(t)^2\rangle + 2DT. \tag{3.49}$$

This expression constitutes the fluctuation-dissipation relation for this system. In steady

state, $\langle \delta\phi(t+T)^2 \rangle = \langle \delta\phi(t)^2 \rangle$, from which it follows that

$$\langle \delta\phi(t)^2 \rangle = \frac{2DT}{1-F'^2(\phi^*)}. \tag{3.50}$$

Clearly, the variance depends not only on the diffusion constant, but also on the stability, which increases with the coupling strength; as derived below Eq. 3.46, for scenario 1, $F'(\phi^*) = (\omega_0 - \epsilon_-)/(\omega_0 + \epsilon_+)$ decreases (meaning the system becomes more stable) as ϵ_- and ϵ_+ increase.

In this linear-noise approximation, the distribution of the phase at time t is a simple Gaussian with a mean $\overline{\phi}(t)$ that is given by the deterministic solution, $\overline{\phi}(t) = \phi^*(t)$, and a variance that is given by Eq. 3.50:

$$P(\phi|t) = \frac{1}{\sqrt{2\pi\sigma_\phi}} \exp - \frac{(\phi - \overline{\phi}(t))^2}{2\sigma_\phi^2}, \tag{3.51}$$

where $\sigma_\phi \equiv \sqrt{\langle \delta\phi^2 \rangle}$. This variance is, in this approximation, independent of the phase.

To derive the mutual information, it is convenient to invert the problem and look for the distribution of possible times t, given ϕ. This can be obtained from Bayes' rule:

$$P(t|\phi) = P(t)\frac{P(\phi|t)}{P(\phi)} \tag{3.52}$$

where $P(t) = 1/T$ is the uniform prior probability of having a certain time and $P(\phi)$ is the steady state distribution of ϕ, which in the small noise limit can be computed via $P(t)dt = P(\phi)d\phi$. If the noise ξ is small compared to the mean, then $P(t|\phi)$ will be a Gaussian distribution that is peaked around $t^*(\phi)$, which is the best estimate of the time given the phase [56, 62, 93]:

$$P(t|\phi) \simeq \frac{1}{\sqrt{2\pi\sigma_t^2}} \exp\left[-\frac{(t - t^*(\phi))^2}{2\sigma_t^2} \right]. \tag{3.53}$$

Here $\sigma_t^2 = \sigma_t^2(t^*)$ is the variance in the estimate of the time, and it is given by [56]

$$\sigma_t^2 = \sigma_\phi^2 \left(\frac{dt}{d\overline{\phi}} \right)^2. \tag{3.54}$$

We note that σ_t^2 does depend on t because the slope $d\overline{\phi}/dt$ depends on t. Indeed, while the LNA assumes that σ_ϕ^2 is independent of ϕ, it does capture the fact that changing ϵ and ω_0 can affect the mutual information not only by changing the noise σ_ϕ^2 but also via the slope $d\overline{\phi}/dt$ of the input-output relation $\overline{\phi}(t)$.

The mutual information can now be obtained from:

$$I(\phi;t) = H(t) - \left\langle H(t|\phi)\right\rangle_{\phi} \tag{3.55}$$

$$= \log_2 T - \left\langle \frac{1}{2}\log_2\left(2\pi e\sigma_{\phi}^2\left(\frac{dt}{d\overline{\phi}}\right)^2\right)\right\rangle_{\phi} \tag{3.56}$$

$$= \log\left(\frac{T}{\sqrt{2\pi e\sigma_{\phi}^2}}\right) + \frac{1}{T}\int_0^T dt \log\frac{d\overline{\phi}}{dt}, \tag{3.57}$$

where $\langle\ldots\rangle_{\phi}$ denotes an average over $P(\phi)$, and we have exploited that in the LNA the variance σ_{ϕ}^2 is independent of ϕ. For the model presented here, $\overline{\phi}(t) = \phi^*(t)$ is piecewise linear, and the second integral can be obtained analytically, for each of the scenarios; for scenario 1, for example, the second term is $1/T\left(t_1\log(\omega_0+\epsilon_+) + (t_2-t_1)\log\omega_0 + (T/2-t_2)\log(\omega_0-\epsilon_-) + T/2\log\omega_0\right)$.

Fig. 3.4 shows that the LNA accurately predicts the mutual information $I_{\omega_0^{\rm opt}}(\phi;t)$ in the regime that the coupling strength ϵ is large and the diffusion constant D is small. A more detailed comparison is shown in Fig. 3.8, which shows the Kullback-Leibler divergence $D_{KL}(P_n||P_a)$ between the distribution $P_n = P_n(\phi|t)$ obtained in the simulations and $P_a = P_a(\phi|t)$ as predicted by LNA. Panels A and B show the result for $\omega_0/\omega = 1$, while panels C and D show the results for $\omega_0/\omega = 1.05$. Moreover, panels A and C show the results as a function of D for two values of ϵ, while panels B and D show the results as a function of ϵ for two values of D.

Panels A and C show that as D is decreased at fixed ϵ, the LNA becomes accurate for small D, as expected. Panels B and D show that for large D, the LNA never becomes accurate, even for large ϵ. However, for large values of ϵ, the assumption that the stochastic contribution to the variance is given by that of free diffusion, $V[\delta\phi(t+T)|\phi^*(t)] \simeq 2DT$, breaks down. This is also the reason why for the smaller value of D (crosses in panels B and D), the LNA works very well for low values of ϵ, but then becomes slightly less accurate for higher values of ϵ. Indeed, for $\epsilon = \epsilon_- > \omega_0$, $F' = 0$, and the key assumption of LNA—namely that the dynamics can be expanded to linear order around the deterministic fixed point—breaks down.

Comparing panel C against panel A and panel D against panel B shows that LNA is less accurate in the small D/ϵ regime when $\omega_0/\omega = 1.05$ (panels C/D) than when $\omega_0/\omega = 1.0$ (panels A/B). More specifically, while LNA is very accurate for $D < 10^{-2}/T$ for both values of ϵ when $\omega_0/\omega = 1.0$ (panel A), LNA becomes less accurate for $D < 10^{-2}/T$ when $\omega_0/\omega = 1.05$ and ϵ is small, *i.e.* $\epsilon/\omega = 0.1$ (panel C); only for $\epsilon/\omega = 0.9$ is LNA still accurate in this regime. Similarly, while LNA is very accurate for $\epsilon/\omega < 1$ when $D = 10^{-3}/T$ and $\omega_0/\omega = 1.0$ (panel B), LNA becomes less accurate for $\epsilon/\omega < 0.5$ when $D = 10^{-3}/T$ yet $\omega_0/\omega = 1.05$ (panel D). This observation can be understood by noting that when ω_0 is increased, the system moves to the boundary of the Arnold Tongue of scenario I, especially when ϵ is small (see Fig. 3.2). The system then switches under the influence of noise between the solution of scenario I and that of scenario II, meaning that the response becomes non-linear and LNA breaks down. Interestingly, however, another method, described in the next section, accurately describes this regime.

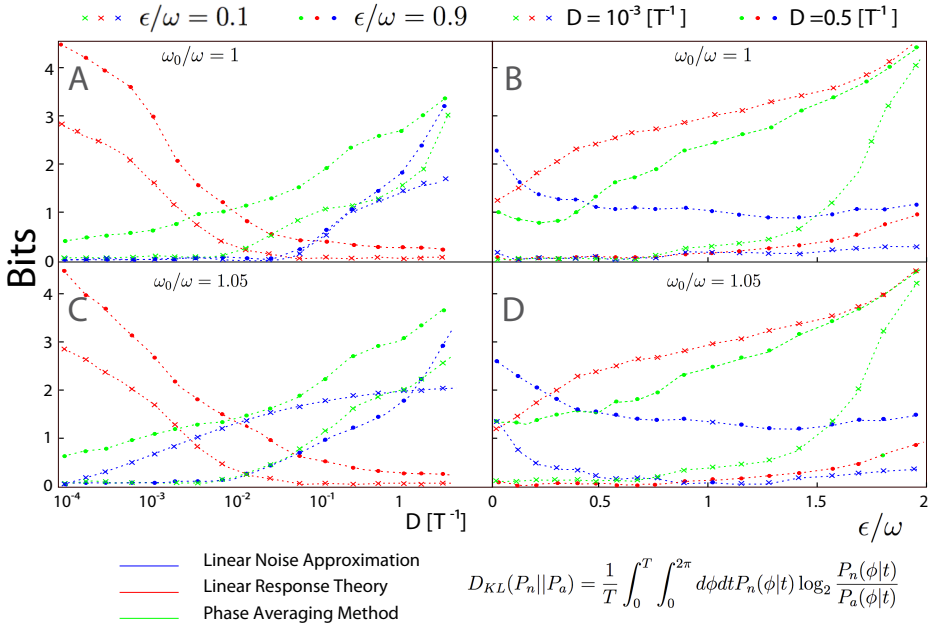

Figure 3.8: Comparison between simulation results and three different theories: linear-noise approximation (LNA), phase-average method (PAM), and linear-response theory (LRT). The comparison is performed by computing the Kullback-Leibler divergence $D_{KL}(P_n||P_a)$ between $P_n(\phi|t)$ as obtained in the simulations and $P_a(\phi|t)$ as predicted by the theory. For two values of ω_0, namely $\omega_0/\omega = 1$ (panels A,B) and $\omega_0/\omega = 1.05$ (panels C,D), we show $D_{KL}(P_n||P_a)$ as a function of D for two values of ϵ (panels A,C) and $D_{KL}(P_n||P_a)$ as a function of ϵ for two values of D (panels B,D). It is seen that the LNA accurately predicts the regime of strong coupling and low noise; PAM the regime of weak coupling and weak noise; and LRT the regime of high noise and weak coupling. Other parameters: $\Delta\phi_{12} = \Delta\phi_{23} = \pi/2$ for all data points.

3.4.2. PHASE-AVERAGING METHOD

In the limit that the coupling ϵ is weak, the diffusion constant D is small, and the intrinsic frequency ω_0 is close to the driving frequency ω, we expect that the evolution of ϕ is close to that of the free-running oscillator, $\phi_0(t) = \omega_0 t + \phi_0$. In this regime the phase will exhibit fluctuations that are slow, occurring on time scales much larger than the intrinsic period T_0. The detailed coupling within a clock cycle becomes irrelevant, and only the average coupling over a clock period matters. This leads to the notion of phase averaging, in which $P(\phi(t) - \omega t|t)$ no longer depends on t: $P(\phi(t) - \omega t|t) = P(\phi(t) - \omega t) \equiv P(\psi)$, with $\psi \equiv \phi(t) - \omega t$.

Following Pikovsky [22], we now make this intuitive notion concrete by rewriting the

coupling term as

$$Q(\phi, t) = Z(\phi)L(t) \tag{3.58}$$
$$= \sum_k \sum_l a_k b_l e^{i(k\phi + l\omega t)}. \tag{3.59}$$

If the coupling and the noise are weak, $\epsilon \to 0, D \to 0$, we may expect that $\phi \simeq \omega_0 t + \phi_0$ for all times t. If we substitute this into Eq. 3.59, we find

$$Q(\phi, t) = \sum_k \sum_l a_k b_l e^{ik\phi_0} e^{i(k\omega_0 + l\omega t)}. \tag{3.60}$$

When $\omega \approx \omega_0$, the terms $k = -l$ contribute most strongly to the integral. These terms correspond to variations in the force on long time scales. We thus expect that in the regime that $\epsilon, D \to 0$ and $\omega \approx \omega_0$, where the phase is expected to follow $\phi \approx \omega_0 t + \phi_0$, the terms $k = -l$ yield the strongest contributions to the force:

$$Q(\phi, t) = \sum_k a_k b_{-k} e^{ik(\phi - \omega t)} \tag{3.61}$$
$$= \int_0^T dt' Z(\psi + \omega t')L(t') \tag{3.62}$$
$$= Q(\psi). \tag{3.63}$$

where in Eq. Eq. 3.62 we have introduced the new phase variable $\psi \equiv \phi - \omega t$. The force $Q(\psi)$ is commonly referred to as the phase-response curve; it is thus a convolution of the instantaneous phase-response curve $Z(\phi)$ and the light-signal $L(t)$.

The temporal evolution of ψ, $\dot{\psi} = \dot{\phi} - \omega$, is, using Eq. 3.25:

$$\frac{d\psi}{dt} = \omega_0 - \omega + \epsilon Q(\psi) + \xi(t) \tag{3.64}$$
$$= -\nu + \epsilon Q(\psi) + \xi(t), \tag{3.65}$$

with $\nu = \omega - \omega_0$. The first two terms on the right-hand side are the deterministic force, which can be written as the derivative of a potential $V(\psi)$

$$-\nu + \epsilon Q(\psi) = -\frac{dV(\psi)}{d\psi}, \tag{3.66}$$

with the potential given by

$$V(\psi) = \nu\psi - \epsilon \int_{-\pi}^{\psi} Q(x)dx. \tag{3.67}$$

Indeed, the evolution of ψ can be described as that of a particle in a potential $V(\psi)$, which is a 2π-periodic potential with a slope given by $\nu = \omega - \omega_0$.

The evolution of the probability density $P(\psi, t)$ is given by the Fokker-Planck equation corresponding to Eq. 3.65:

$$\partial_t P(\psi, t) = -\partial_\psi \left[(-\nu + \epsilon Q(\psi))P(\psi, t)\right] + D\partial_\psi^2 P(\psi, t) \tag{3.68}$$
$$= -\frac{\partial J(\psi, t)}{\partial \psi}, \tag{3.69}$$

where we have defined the probability current

$$J(\psi,t) = -P(\psi,t)\frac{dV(\psi)}{dx} - D\frac{\partial P(\psi,t)}{\partial t}. \tag{3.70}$$

In steady state, $\partial P(\psi,t)/\partial t = 0$, which yields the following stationary solution that is 2π-periodic in ψ:

$$\overline{P}(\psi) = \frac{1}{C}\int_{\psi}^{\psi+2\pi} e^{\frac{V(\psi')-V(\psi)}{D}} d\psi'. \tag{3.71}$$

Here, C is the normalization constant.

Fig. 3.4 shows that the phase-averaging method (PAM) accurately predicts the mutual information $I(\phi;t)$ in the regime that both the coupling strength ϵ and the diffusion constant D are small. The more detailed comparison based on the Kullback-Leibler divergence $D_{KL}(P_n||P_a)$ between the distribution $P_n = P_n(\phi|t)$ obtained in the simulations and $P_a = P_a(\phi|t)$ as predicted by PAM confirms this interpretation: as shown in panel B of Fig. 3.8, when $\omega_0/\omega = 1.05$, PAM is accurate for $D < 10^{-2}/T$ when $\epsilon/\omega = 0.1$ (green crosses), while LNA breaks down in this regime (blue crosses). Similarly, as illustrated in panel D, when $\omega_0/\omega = 1.05$, PAM is accurate for $\epsilon/\omega < 0.7$ when $D = 10^{-3}/T$ (green crosses), whereas LNA again breaks down in this regime (blue crosses).

While the LNA breaks down when the distribution $P(\phi|t)$ becomes non-Gaussian as the coupling becomes too weak, the PAM accurately describes $P(\phi|t)$ in the low-coupling, low-noise regime, as it allows for non-Gaussian distributions. However, the PAM does assume that $\phi(t)$ follows ωt. As a result it breaks down when the coupling becomes large, causing the average input-output relation $\overline{\phi}(t)$ to deviate markedly from ωt, an effect that can be captured by the LNA. PAM also breaks down when ϵ is small and $\omega \approx \omega_0$, yet D is large: now the large diffusion constant causes the instantaneous $\phi(t)$ to deviate markedly from ωt. This regime can, however, be described by linear-response theory.

3.4.3. LINEAR RESPONSE THEORY

When the coupling strength is weak yet the diffusion constant is large, $\phi(t)$ at any moment in time will tend to deviate strongly from $\omega_0 t$, but the steady-state distribution will be close to that of a noisy, free running oscillator, $P_0(\phi) = 1/(2\pi)$. The full distribution can then be obtained as a perturbation to this distribution. This is the central idea of linear-response theory (LRT).

We start with the Fokker-Planck equation for the evolution of $P(\phi,t)$:

$$\partial_t P(\phi,t) = D\partial_\phi^2 P(\phi,t) + \omega_0\partial_\phi P(\phi,t) + L(t)\partial_\phi\left[Z(\phi)P(\phi,t)\right]. \tag{3.72}$$

We now consider the external signal $L(t)Z(\phi)$ to be a weak perturbation of the free-running system. To this end, we rewrite the above equation as:

$$\partial_t P(\phi,t) = \left[\mathscr{F}_0 + \epsilon\mathscr{F}_1(t)\right]P(\phi,t) \tag{3.73}$$

where $\mathscr{F}_0$ is the operator that defines the time evolution of the unperturbed system and $\mathscr{F}_1$ that due to the perturbation:

$$\mathscr{F}_0 = +D\partial_\phi^2 + \omega_0\partial_\phi \tag{3.74}$$

$$\mathscr{F}_1(t) = +L(t)\partial_\phi Z(\phi) + L(t)Z(\phi)\partial_\phi \tag{3.75}$$

Furthermore, we expand $P(\phi, t)$ as:

$$P(\phi, t) \simeq p_0(\phi, t) + \epsilon p_1(\phi, t) + \epsilon^2 p_2(\phi, t) + \mathscr{O}(\epsilon^3) \tag{3.76}$$

Substituting this expression into Eq. 3.73, and keeping only terms up to order ϵ, we find:

$$\mathscr{O}(0) \qquad \mathscr{F}_0 p_0(\phi, t) = \partial_t p_0(\phi, t) \tag{3.77}$$

$$\mathscr{O}(\epsilon) \qquad \partial_t p_1(\phi, t) - \mathscr{F}_0 p_1(\phi, t) = \mathscr{F}_1 p_0(\phi, t) \tag{3.78}$$

We are interested in the solutions that satisfy the periodic boundary conditions:

$$p_i(\phi, t) = p_i(\phi + 2\pi, t) \tag{3.79}$$

$$\partial_\phi p_i(\phi, t) = \partial_\phi p_i(\phi + 2\pi, t), \tag{3.80}$$

for both $i = 0, 1$. Moreover, in steady state, for $t \to \infty$, it must hold that

$$p_i(\phi, t) = p_i(\phi, t + T). \tag{3.81}$$

Eq. 3.77 describes the diffusion of a particle with drift. The steady-state solution, which obeys Eqs. 3.79-3.81, is

$$\lim_{t\to\infty} p_0(\phi, t) = \frac{1}{2\pi}. \tag{3.82}$$

Clearly, $p_0(\phi, t)$ in steady state is flat, which means that any deviation in the steady-state solution for $P(\phi, t)$ from the flat distribution must be contained in $p_1(\phi, t)$. Since $p_1(\phi, t)$ is, by construction, a small perturbation, this approach will be accurate only when the full distribution is sufficiently flat, which means that the diffusion constant cannot be too small.

To obtain $p_1(\phi, t)$, we proceed by substituting the solution for $p_0(\phi, t)$, Eq. 3.82, into Eq. 3.78, yielding

$$\partial_t p_1(\phi, t) - D\partial_\phi^2 p_1(\phi, t) - \omega_0\partial_\phi p_1(\phi, t) = L(t)p_0(\phi, t)\partial_\phi Z(\phi). \tag{3.83}$$

The solution to this non-homogeneous heat equation is given by

$$\begin{aligned} p_1(\phi, t) = &\int_0^{2\pi} d\xi G(\phi - \omega_0 t, \xi, t) f(\xi) \\ &+ \int_0^{2\pi}\int_0^t d\tau d\xi G(\phi - \omega_0 t, \xi, t - \tau) A(\xi, \tau), \end{aligned} \tag{3.84}$$

where $f(\phi)$ is the initial condition, $G(\phi - \omega_0 t, \phi_0, t, t_0)$ is the Green's function of the unperturbed diffusion operator with drift, and $A(\phi, t) \equiv L(t)p_0(\phi, t)\partial_\phi Z(\phi)$. This expression holds for any t, not only for the steady-state solution.

To obtain the steady-state solution, we aim to find the initial condition $P(\phi, t) = f(\phi)$ that folds back onto it self after a time T: $P(\phi, t+T) = P(\phi, t) = f(\phi)$. To this end, we evaluate Eq. 3.84 for $t = T$, to arrive at the Fredholm equation of the second kind:

$$f(\phi) = \int_0^{2\pi} d\xi f(\xi) G(\phi, \xi, t = T) + Q(\phi) \tag{3.85}$$

where $Q(\phi)$ is given by Eq. 3.183. The above equation can be solved analytically, see Appendix 3.8.

Fig. 3.8 and Fig. 3.4 show, respectively, that the LRT accurately describes $P(\phi, t)$ and hence the mutual information in the regime that the coupling is weak and the diffusion constant is large. In contrast to the phase-averaging method, the LRT breaks down for smaller diffusion constant. The reason is that then $P(\phi, t)$ deviates increasingly from the uniform distribution, $p_0(\phi, t) = 1/(2\pi)$, and the full solution $P(\phi, t)$ can no longer be treated as a weak perturbation to p_0.

3.5. DISCUSSION

The phase-response curves that have been measured experimentally often have a positive lobe and a negative one, separated by a deadzone where the coupling strength is zero [97]. However, the width of the deadzone varies considerably from organism to organism. Here, we asked how the optimal phase-response curve depends on the intrinsic noise in the system, using the mutual information as a performance measure.

Information theory predicts that the number of signals that can be transmitted reliably through a communication channel depends on the shape of the input distribution, the input-output relation, and the noise in the system. These arguments apply to any signalling system and the circadian clock is no exception.

When the input distribution is flat and the noise is low, then, in general, the optimal input-output relation is linear. The phase-oscillator model of the clock obeys this rule: the input distribution $p(t) = 1/T$ is flat, and the optimal input-output relation $\phi(t)$ is indeed linear in the low-noise regime (Fig. 3.5B,C). Such a linear input-output relation is obtained for an intrinsic period that is close to 24 hrs and for a deadzone that is relatively large (Figs. 3.6 and 3.7). Our analysis thus predicts that less-noisy circadian clocks exhibit a relatively large deadzone. Interestingly, the rule also explains why for a constant deadzone, in the low-noise limit, the optimal intrinsic frequency decreases as the coupling strength increases (see Fig. 3.5A).

In the large-noise regime, containment of noise becomes paramount. This inevitably requires a large coupling strength. While a strong coupling distorts the input-output relation, which tends to reduce information transmission, it also reduces the noise, enhancing information transmission (Fig. 3.5B,C). The stability is further enhanced by increasing the intrinsic frequency and reducing the width of the deadzone (Fig. 3.7). Indeed, our results predict that noisy circadian systems feature a smaller deadzone and a higher intrinsic frequency.

These results have been obtained by reducing the circadian clock to a phase-oscillator model. It is useful to briefly review the generality and limitations of this approach. The mutual information obeys $I(\mathbf{n}; t) \geq I(R, \phi; t) \geq I(\phi; t)$. Hence, any mapping of $\mathbf{n}$ to ϕ

makes it possible to put a lower bound on the mutual information. The bound will be tight when the phase, according to this mapping, contains most of the information on time.

Another question is whether the model that we use to describe the evolution of the phase is accurate. Phase-oscillator models have commonly been employed to describe oscillatory systems, yet they are typically described as being valid in the limits of weak driving and low noise: this ensures that the coupled system stays close to the limit cycle of the unperturbed, deterministic system, so that the coupling function and the diffusion constant can be approximated by their values on that limit cycle [22]. Here, having derived the phase oscillator description in the weak coupling limit, we then proceed to study it for arbitrary values of ϵ and D. This might at first glance seem self-contradictory. It should be realized, however, that biochemical noise and coupling can have two distinct effects: they can affect the dynamics *along* the limit cycle, i.e. of ϕ, and/or they can cause the system to move *away* from the limit cycle. Only perturbations in the latter direction, orthogonal to the limit cycle, need be small for the phase oscillator description to apply. Moreover, ϵ and D are dimensionful parameters that can only be meaningfully be said to be large or small in comparison to another parameter, and the appropriate parameter for comparison is different for perturbations along and orthogonal to the limit cycle. Thus, it is entirely possible for ϵ and D to be small compared to the rate of relaxation to the limit cycle, implying that neither the external driving nor the noise can force the system far from the limit cycle and that the phase oscillator model is a good approximation, but simultaneously for one or both of ϵ and D to be large compared to ω_0, so that perturbations to the phase dynamics are not weak. We imagine that just such a situation holds here: D and ϵ can become bigger than ω_0—meaning that the noise and the coupling can induce large changes in ϕ—but, even for large D/ω_0 and ϵ/ω_0, the system in our model does not significantly move off the limit cycle. It remains an open question how for a given, particular clock biochemical noise and strong coupling to an entrainment signal affect the dynamics: how far does the system move away from its limit cycle, and how much do the diffusion constant and the coupling function then change? The detailed and minimal biochemical network models that have been developed for the cyanobacterium *Synechococcus elongatus* would make it possible to investigate this question in detail [11, 12, 15, 17, 28, 102–104]

Our work shows that the behaviour of the coupled phase oscillator can be accurately described by three different theories, which each work best in a different parameter regime. In the regime of weak coupling, low noise, and intrinsic frequency close to the driving frequency, the phase-averaging method is very accurate. In the regime that the driving is strong compared to the diffusion constant, the linear-noise approximation is most accurate. These are the two most relevant regimes for understanding the design of circadian clocks. There is also another regime, however, namely that of weak coupling and high noise, and in this regime linear-response theory is very accurate. That linear-response theory can describe any regime at all is perhaps surprising, since it has been argued that this theory should be applied to phase oscillators only with the greatest care [22]. The argument is that small but resonant forcing can have effects on ϕ that build up over time, meaning that the effect of perturbations that are nominally of order ϵ, and thus small, will eventually become large with time. However, noise can pre-empt this ac-

cumulation of resonant perturbations by effectively randomizing the phase and erasing the memory of earlier perturbations before they are able to accumulate over time. As a result, the full distribution of the phase can be written as a small perturbation around the uniform distribution, and this does make it possible to apply linear-response theory. While this regime is probably less relevant for understanding biological clocks, this approach may be useful in other contexts.

Finally, we have focused on the optimal design of the clock as a function of the intrinsic noise in the system. As Pfeuty *et al.* have shown, fluctuations in the input signal are an important consideration for understanding the design of circadian clocks [97]. It will be interesting to see whether maximizing the mutual information will reveal new design principles for clocks driven by fluctuating signals.

Acknowledgements: We thank Jeroen van Zon for a critical reading of the manuscript. This work is supported by the research programme of the Foundation for Fundamental Research on Matter (FOM), which is part of the Netherlands Organisation for Scientific Research (NWO), and by NSF grant DMR-1056456 (DKL).

APPENDIX:

3.6. ARNOLD TONGUE OF THE DETERMINISTIC MODEL

For completeness, we give here the inequalities for all scenarios. **Scenario 1:** As discussed in the main text: $\phi_3 - 2\pi < \phi_s < \phi_1$; $t_2 < T/2 < t_3$. If $\epsilon_- \leq \omega_0$, then

$$T \leq \frac{2\pi - \epsilon_- \Delta\phi_{12}/\omega_0}{\omega_0 - \epsilon_-/2} \tag{3.86}$$

$$T > \frac{2\pi + \epsilon_+ \Delta\phi_{12}/\omega_0}{\epsilon_+/2 + \omega_0} \tag{3.87}$$

$$T < \frac{2\pi + \epsilon_+ \Delta\phi_{12}/\omega_0 + \Delta\phi_{23}(\epsilon_+ + \epsilon_-)/(\omega_0 - \epsilon_-)}{\epsilon_+/2 + \omega_0} \tag{3.88}$$

$$T > \frac{(\Delta\phi_{13} - 2\pi)(\epsilon_+ + \epsilon_-)/(\omega_0 + \epsilon_+) + 2\pi - \epsilon_- \Delta\phi_{12}/\omega_0}{\omega_0 - \epsilon_-/2} \tag{3.89}$$

If $\epsilon_- > \omega_0$ then

$$T \leq \frac{2(2\pi - \Delta\phi_{12})}{\omega_0} \tag{3.90}$$

$$T > \frac{2\pi - \Delta\phi_{12} + (\Delta\phi_{12}/\omega_0)(\epsilon_+ + \omega_0)}{\epsilon_+/2 + \omega_0} \tag{3.91}$$

$$T > \frac{2\Delta\phi_{23}}{\omega_0} \tag{3.92}$$

Scenario 2: $\phi_1 < \phi_s < \phi_2$; $0 < t_2 < T/2 < t_3 < t_1 < T$. For $\epsilon_- < \omega_0$, the evolution of $\phi(t)$ is given by

$$\phi_s + \omega_0 t_2 + (-\epsilon_- + \omega_0)(T/2 - t_2) + \omega_0 T/2 = \phi_s + 2\pi. \tag{3.93}$$

This yields:

$$t_2 = \frac{2\pi - T(\omega_0 - \epsilon_-/2)}{\epsilon_-} < T/2 \;\&\; > 0 \tag{3.94}$$

$$t_3 = \frac{\Delta\phi_{23}}{\omega_0 - \epsilon_-} + t_2 > T/2 \tag{3.95}$$

$$t_1 = t_2 - \Delta\phi_{12}/\omega_0 + T < T. \tag{3.96}$$

$$\phi_s = \phi_2 - \omega_0 t_2 > \phi_1. \tag{3.97}$$

This yields the following inequalities:

$$T > \frac{2\pi}{\omega_0} \tag{3.98}$$

$$T < \frac{2\pi}{\omega_0 - \epsilon_-/2} \tag{3.99}$$

$$T < \frac{2\pi + \Delta\phi_{13}\epsilon_-}{\omega_0 - \epsilon_-/2} \tag{3.100}$$

$$T > \frac{2\pi - \epsilon_-\Delta\phi_{12}/\omega_0}{\omega_0 - \epsilon_-/2} \tag{3.101}$$

If $\epsilon_- > \omega_0$, the equation to solve is

$$\phi_s + \omega_0 t_2 + \omega_0 T/2 = \phi_s + 2\pi. \tag{3.102}$$

The solution is

$$t_2 = \frac{2\pi}{\omega_0} - T/2 < T/2 \tag{3.103}$$

$$t_3 = \infty > T/2. \tag{3.104}$$

$$t_1 = t_2 - \Delta\phi_{12}/\omega_0 + T < T. \tag{3.105}$$

$$\phi_s = \phi_2 - \omega_0 t_2 > \phi_1 \;\&\; < \phi_2. \tag{3.106}$$

This yields the following inequalities

$$T > 2\pi/\omega_0 \tag{3.107}$$

$$T > \frac{2(2\pi - \Delta\phi_{12})}{\omega_0} \tag{3.108}$$

$$T < 4\pi/\omega_0 \tag{3.109}$$

This scenario is stable, because $\phi(t)$ between $t = 0$ and $t = t_2$ is steeper than $\phi(t)$ between t_2 and $T/2$.

Scenario 3: $\phi_2 < \phi_s < \phi_3$; $0 < t_2 < T/2$. If $\epsilon_- < \omega_0$ then

$$\phi_s + (-\epsilon_- + \omega_0)T/2 + \omega_0 T/2 = \phi_s + 2\pi. \tag{3.110}$$

This equation does not depend on t_i. There is only one period that fits the solution:

$$T = \frac{2\pi}{\omega_0 - \epsilon_-/2}. \tag{3.111}$$

This period is on the boundary of the Arnold tongue of scenario 2. This solution seems degenerate, being neither stable nor unstable.

If $\epsilon_- > \omega_0$, the equation that solves $\phi(t)$ is

$$\phi_s + (-\epsilon_- + \omega_0)\, t_2 + \omega_0 T/2 = \phi_s + 2\pi. \tag{3.112}$$

The solution is

$$t_2 = \frac{2\pi - \omega_0 T/2}{-\epsilon_- + \omega_0} \tag{3.113}$$

$$\phi_s = \phi_2 + \omega_0 T/2 - 2\pi. \tag{3.114}$$

The requirement that $t_2 > 0$, yields the inequality

$$T > \frac{4\pi}{\omega_0}, \tag{3.115}$$

because the denominator of Eq. 3.113 is negative. The requirement that $t_2 < T/2$ yields

$$\frac{2\pi - T(\omega_0 - \epsilon_-/2)}{\omega_0 - \epsilon_-} < 0. \tag{3.116}$$

Since the denominator is negative for $\epsilon_- > \omega_0$, this means that $(2\pi - T(\omega_0 - \epsilon_-/2)) > 0$. When $\epsilon_- > 2\omega_0$, this is true for any T. When $\epsilon_- < 2\omega_0$ (but still larger than ω_0 because otherwise there is no solution at all, see above), then

$$T < \frac{2\pi}{\omega_0 - \epsilon_-/2}. \tag{3.117}$$

The constraints $\phi_2 < \phi_s < \phi_3$ yield

$$T > \frac{4\pi}{\omega_0} \tag{3.118}$$

$$T < \frac{2(\Delta\phi_{23} + 2\pi)}{\omega_0}. \tag{3.119}$$

This solution is rather strange. When the light comes up, the clock is being driven backwards. The solution seems stable, though. In fact, it seems extremely stable: after one period, the system is back on its limit cycle.

Scenario 4: $\phi_3 - 2\pi < \phi_s < \phi_1$; $0 < t_1 < T/2 < t_2$. The equation that determines the steady state is

$$\phi_s + (\omega_0 + \epsilon_+)\, t_1 + \omega_0 (T/2 - t_1) + \omega_0 T/2 = \phi_s + 2\pi. \tag{3.120}$$

The solution is

$$t_1 = \frac{2\pi - \omega_0 T}{\epsilon_+} < T/2 \;\&\; > 0 \tag{3.121}$$

$$t_2 = t_1 + \frac{\Delta\phi_{12}}{\omega_0} > T/2 \tag{3.122}$$

$$\phi_s = \phi_1 - (\epsilon_+ + \omega_0)\, t_1 = \phi_1 - (\epsilon_+ + \omega_0)(2\pi - \omega_0 T)/\epsilon_+ \tag{3.123}$$

The conditions for T are

$$T \leq \frac{2\pi}{\omega_0} \tag{3.124}$$

$$T > \frac{2\pi}{\omega_0 + \epsilon_+/2} \tag{3.125}$$

$$T < \frac{2\pi + \Delta\phi_{12}\epsilon_+/\omega_0}{\epsilon_+/2 + \omega_0} \tag{3.126}$$

$$T > \frac{\epsilon_+\Delta\phi_{13} + 2\pi\omega_0}{\omega_0(\omega_0 + \epsilon_+)}. \tag{3.127}$$

Scenario 5: $\phi_3 - 2\pi < \phi_s < \phi_1$; $t_1 > T/2$. The governing equation is

$$\phi_s + (\epsilon_+ + \omega_0)T/2 + \omega_0 T/2 = \phi_s + 2\pi. \tag{3.128}$$

This means that

$$T = \frac{2\pi}{\omega_0 + \epsilon_+/2}. \tag{3.129}$$

Clearly, for each ϵ_+ there is only one period, not a range of periods. Since $\phi(T/2) = \phi_s + (\epsilon_+ + \omega)T/2$, which must be smaller than ϕ_1, and $\phi_s > \phi_3 - 2\pi$, we find that there exists only a solution if $\Delta\phi_{13} < 2\pi\omega_0/(\epsilon_+ + 2\omega_0)$. Hence, for given ϕ_1 and ϕ_3, this puts an upper bound on ϵ_+. If a solution exists, the starting phase ϕ_s, must lie in the range $\phi_3 - 2\pi < \phi_s < \phi_1 - \pi(\epsilon_+ + \omega_0)/(\epsilon_+/2 + \omega_0)$. Moreover, the solution is neutral; it does not relax back to a unique ϕ_s. In fact, this is a very general observation: if the solution is neutral, it means that there can only be locking for one value of the period. Being able to locking over a range of periods of the driving signal, means that the clock should be able to adjust its period by changing the phase; but a neutral solution means that changing the phase does not lead to a change in its period.

Scenario 6: $\phi_3 - 2\pi < \phi_s < \phi_1$; $0 < t_1 < t_2 < t_3 < T/2$. This scenario can only arise when $\epsilon_- < \omega_0$, because otherwise the system never makes it to ϕ_3 before the sun sets. The equation to be solved is then:

$$\begin{aligned}\phi_s + (\epsilon_+ + \omega_0)t_1 + \Delta\phi_{13} + (\omega_0 + \epsilon_+)(T/2 - t_3) + \omega_0 T/2 \\ = \phi_s + 2\pi.\end{aligned} \tag{3.130}$$

This equation can be solved by noting that $\Delta\phi_{12} = \omega_0(t_2 - t_1)$ and $\Delta\phi_{23} = (-\epsilon_- + \omega_0)(t_3 - t_2)$. It follows that there is only one period that satisfies the above equation:

$$T = \frac{2\pi - \Delta\phi_{23} + \epsilon_+\Delta\phi_{12}/\omega_0 + (\epsilon_+ + \omega_0)\Delta\phi_{23}/(-\epsilon_- + \omega_0)}{\omega_0 + \epsilon_+/2} \tag{3.131}$$

Clearly, for a given ϵ_- and ϵ_+ there is only one period, not a range of periods to which the system can entrain. This means that the solution is neutral, which can indeed be understood by noting that the initial slope at $t = 0$, $\omega_0 + \epsilon_+$, is the same as that $t = T/2$. The condition for the solution to exist is that $\phi(T/2) = 2\pi + \phi_s - \omega_0 T/2 > \phi_3$. This yields for ϕ_s:

$$\phi_3 - 2\pi + \omega_0 T/2 < \phi_s < \phi_1. \tag{3.132}$$

There is thus only a solution when

$$T < \frac{2(2\pi - \Delta\phi_{13})}{\omega_0}. \tag{3.133}$$

One could use this condition to determine the range of $\epsilon_{+/-}$ over which there is a solution, given ϕ_1, ϕ_2, ϕ_3. But since this scenario only yields one line in the phase diagram, we do not pursue this further.

Scenario 7: $\phi_1 < \phi_s < \phi_2; 0 < T/2 < t_2 < t_3 < t_1$. The governing equation is

$$\phi_s + \omega_0 T/2 + \omega_0 T/2 = \phi_s + 2\pi. \tag{3.134}$$

This indeed yields only one solution

$$T = \frac{2\pi}{\omega_0}. \tag{3.135}$$

Indeed, there only exists a solution when the driving frequency equals the intrinsic frequency, which is to be expected, since with this solution the system does not see the driving. The solution exists only if $\Delta\phi_{12} > \pi$. This solution is neutral, in that all solutions $\phi_1 < \phi_s < \phi_2$ are valid, for all values of $\epsilon_{-/+}$. One may wonder what that implies for the dynamics. If one would perform a simulation for $\epsilon_{-/+} > 0$ and $\omega = \omega_0$, and if one would then start with $\phi_1 < \phi_s < \phi_2$, then due to the noise the simulation would initially perform a random walk where initially, at the beginning of each day, the phase of the clock would fluctuate between ϕ_1 and ϕ_2. However, once the oscillator due to noise would cross the boundary ϕ_1, then the system will be driven to a solution that is described under scenario 1.

Scenario 8: $\phi_1 < \phi_s < \phi_2; 0 < t_2 < t_3 < T_2 < t_1$. There can only be a solution, if it exists, when $\epsilon_- < \omega_0$. For $\epsilon_- > \omega_0$ the system never makes it to ϕ_3 before $T/2$. The governing equation is

$$\phi_s + \omega_0 t_2 + \Delta\phi_{23} + (\epsilon_+ + \omega_0)(T/2 - t_3) + \omega_0 T/2 = \phi_s + 2\pi. \tag{3.136}$$

To solve this, we note that

$$t_3 = t_2 + \Delta\phi_{23}/(-\epsilon_- + \omega_0). \tag{3.137}$$

This yields:

$$t_2 = \frac{T(\omega_0 + \epsilon_+/2) - 2\pi - \Delta\phi_{23}(\epsilon_+ + \epsilon_-)/(\omega_0 - \epsilon_-)}{\epsilon_+}. \tag{3.138}$$

We further have

$$\phi_s = \phi_2 - \omega_0 t_2. \tag{3.139}$$

The condition $t_2 > 0$ yields

$$T > \frac{2\pi + \Delta\phi_{23}(\epsilon_+ + \epsilon_-)/(\omega_0 - \epsilon_-)}{\omega_0 + \epsilon_+/2} \tag{3.140}$$

The condition $t_3 < T/2$ yields

$$T < \frac{2\pi + \Delta\phi_{23}\epsilon_-/(\omega_0 - \epsilon_-)}{\omega_0}. \tag{3.141}$$

The condition $\phi_1 < \phi_s = \phi_2 - \omega_0 t_2$ yields

$$T < \frac{2\pi + \epsilon_+\Delta\phi_{12}/\omega_0 + \Delta\phi_{23}(\epsilon_+ + \epsilon_-)/(\omega_0 - \epsilon_-)}{\omega_0 + \epsilon_+/2}. \tag{3.142}$$

The Arnold tongue of this scenario is embedded in those of scenarios 1 and 2. The solution corresponding to this scenario is indeed unstable: the system either converges to the solution of scenario 1 or 2. This can be easily proven by noting that the time it takes to cross $\Delta\phi_{23}$ is constant, as is the time to cross the night. The change in the phase a period later is then the change in the phase at $\phi(T/2)$. This is given by $\delta\phi(T/2) = \partial\phi(T/2)/\partial t_3 \delta t_1 = \partial\phi(T/2)/\partial t_3 \delta\phi_s/\omega_0 = (\epsilon_+ + \omega_0)/\omega_0 \delta\phi_s$, where we have noted that $\delta t_1 = -\delta\phi_s/\omega_0$ and $\partial\phi(T/2)/\partial t_3 = -(\epsilon_+ + \omega_0)$. Because $(\epsilon_+ + \omega_0)/\omega_0 > 1$, the change in the phase after a full period is larger than the initial change in the phase: $\delta\phi(T) = \delta\phi(T/2) > \delta\phi_s$. The solution is unstable.

Scenario 9: $\phi_1 < \phi_s < \phi_2$; $t_2 < t_3 < t_1 < T_2$. There can only be a solution if $\epsilon_- < \omega_0$. The equation to be solved is

$$\phi_s + \omega_0 t_2 + 2\pi - \Delta\phi_{12} + \omega_0(T - t_1) = \phi_s + 2\pi, \tag{3.143}$$

which gives

$$T = \Delta\phi_{12}/\omega_0 + t_1 - t_2. \tag{3.144}$$

We further have

$$t_1 - t_2 = \frac{2\pi - \Delta\phi_{13}}{\omega_0 + \epsilon_+} + \frac{\Delta\phi_{23}}{\omega_0 - \epsilon_-}. \tag{3.145}$$

Hence,

$$T = \frac{\Delta\phi_{12}}{\omega_0} + \frac{2\pi - \Delta\phi_{13}}{\omega_0 + \epsilon_+} + \frac{\Delta\phi_{23}}{\omega_0 - \epsilon_-}, \tag{3.146}$$

which we could have written down right away upon somewhat more careful thinking. We can obtain a bound on the parameters that allow a solution by noting that $0 < t_1 - t_2 < T/2$. Combining with Eq. 3.144 yields $\Delta\phi_{12}/\omega_0 < T < 2\Delta\phi_{12}/\omega_0$. Combing this with Eq. 3.146 yields

$$\frac{\Delta\phi_{12}}{\omega_0} < \frac{2\pi - \Delta\phi_{13}}{\omega_0 + \epsilon_+} + \frac{\Delta\phi_{23}}{\omega_0 - \epsilon_-}. \tag{3.147}$$

A visual inspection illustrates this content very clearly. The parameter ϵ_- should be small, that is not close to unity. A large ϵ_+ also helps.

Scenario 10: $\phi_2 < \phi_s < \phi_3$; $0 < T_2 < t_3, t_1, t_2$. Both for $\epsilon_- < \omega_0$ and $\epsilon_- > \omega_0$, the scenario corresponds to that of scenario 3, but with $\epsilon_- < \omega_0$) in that scenario. There is only a solution for

$$T = 2\pi/(\omega_0 - \epsilon_-/2). \tag{3.148}$$

Scenario 11: $\phi_2 < \phi_s \phi_3$; $0 < t_3 < T/2 < t_1, t_2$. Only if $\epsilon_- < \omega_0$ may a solution exist: if $\epsilon_- > \omega_0$, we are back to scenario 3 or 10. The governing equation is

$$\phi_s + (-\epsilon_- + \omega_0)\, t_3 + (\epsilon_+ + \omega_0)(T/2 - t_3) + \omega_0 T/2 = \phi_s + 2\pi. \tag{3.149}$$

The solution is

$$t_3 = \frac{T(\omega_0 + \epsilon_+/2) - 2\pi}{\epsilon_+ + \epsilon_-} \tag{3.150}$$

$$\phi_s = \phi_3 - (\omega_0 - \epsilon_-)\, t_3. \tag{3.151}$$

The condition $t_3 > 0$ yields

$$T > \frac{2\pi}{\omega_0 + \epsilon_+/2}. \tag{3.152}$$

The condition $t_3 < T/2$ yields the inequality

$$T < \frac{2\pi}{\omega_0 - \epsilon_-/2}. \tag{3.153}$$

The condition $\phi_s > \phi_2$ yields

$$T < \frac{\Delta\phi_{23}(\epsilon_+ + \epsilon_-)/(\omega_0 - \epsilon_-) + 2\pi}{\omega_0 + \epsilon_+/2}. \tag{3.154}$$

The condition $t_1 > T/2$ yields the inequality

$$T > \frac{2\pi - (2\pi - \Delta\phi_{13})(\epsilon_+ + \epsilon_-)/(\epsilon_+ + \omega_0)}{\omega_0 - \epsilon_-/2}. \tag{3.155}$$

The solution space overlaps with those of scenarios 1 - 3. Interestingly, we find again that this solution is unstable: $\delta\phi(T) = \delta\phi(T/2) = \partial\phi(T/2)/\partial t_3 \delta t_3 = -(\omega_0 + \epsilon_+)\delta t_3 = -(\omega_0 + \epsilon_+)\partial t_3/\partial\phi_s \delta\phi_s = (\omega_0 + \epsilon_+)/(\omega_0 - \epsilon_-)\delta\phi_s > \delta\phi_s$. We thus can see that when $\phi(t)$ is convex for $0 < t < T/2$, the solution tends to be unstable.

Scenario 12: $\phi_2 < \phi_s < \phi_3$; $t_3, t_1 < T/2 < t_2$. Only if $\epsilon_- < \omega_0$ may a solution exist. The governing equation is

$$\phi_s + (-\epsilon_- + \omega_0)\, t_3 + (2\pi - \Delta\phi_{13}) + \omega_0(T/2 - t_1) + \omega_0 T/2 = \phi_s + 2\pi. \tag{3.156}$$

Exploiting that $t_1 = t_3 + (2\pi - \Delta\phi_{13})/(\epsilon_+ + \omega_0)$, the solution is

$$t_3 = \frac{\omega_0 T - \Delta\phi_{13} - \omega_0(2\pi - \Delta\phi_{13})/(\epsilon_+ + \omega_0)}{\epsilon_-} \tag{3.157}$$

$$\phi_s = \phi_3 - (\omega_0 - \epsilon_-)\, t_3. \tag{3.158}$$

The condition $t_3 > 0$ yields the inequality

$$T > \frac{\Delta\phi_{13}}{\omega_0} + \frac{2\pi - \Delta\phi_{13}}{\epsilon_+ + \omega_0}. \tag{3.159}$$

The condition $t_1 < T/2$ gives

$$T < \frac{\Delta\phi_{13} + (\omega_0 - \epsilon_-)(2\pi - \Delta\phi_{13})/(\epsilon_+ + \omega_0)}{\omega_0 - \epsilon_-/2}. \tag{3.160}$$

The condition $t_2 = t_1 + \Delta\phi_{12}/\omega_0 > T/2$ yields

$$T > \frac{\Delta\phi_{13} + (\omega_0 - \epsilon_-)(2\pi - \Delta\phi_{13})/(\epsilon_+ + \omega_0) - \epsilon_-\Delta\phi_{12}/\omega_0}{\omega_0 - \epsilon_-/2}. \tag{3.161}$$

The condition $\phi_s > \phi_2$ yields the inequality

$$T < \frac{\Delta\phi_{13} + \omega_0(2\pi - \Delta\phi_{13})/(\epsilon_+ + \omega_0) + \epsilon_-\Delta\phi_{23}/(\omega_0 - \epsilon_-)}{\omega_0}. \tag{3.162}$$

This curve is convex, that is the part of $\phi(t)$ that really matters is convex: the initial slope near $t = 0$, $\omega_0 - \epsilon_-$, is smaller than the slope near $t = T/2$, which is ω. This gives an unstable solution.

Scenario 13: $\phi_2 < \phi_s < \phi_3$; $t_3, t_1, t_2 < T/2$. Again, a solution may only exist if $\epsilon_- < \omega_0$. The central equation is

$$\begin{aligned}\phi_s + (-\epsilon_- + \omega_0)t_3 + (2\pi - \Delta\phi_{23}) + (-\epsilon_- + \omega_0)(T/2 - t_2)\\ +\omega_0 T/2 = \phi_s + 2\pi.\end{aligned} \tag{3.163}$$

The solution is

$$T = \frac{\Delta\phi_{23}}{\omega_0} + \frac{(\omega_0 - \epsilon_-)(t_2 - t_3)}{\omega_0}. \tag{3.164}$$

The time difference is

$$t_2 - t_3 = \frac{\Delta\phi_{12}}{\omega_0} + \frac{2\pi - \Delta\phi_{13}}{\omega_0 + \epsilon_+}, \tag{3.165}$$

which gives for the period

$$T = \frac{\Delta\phi_{23}}{\omega_0} + \frac{\omega_0 - \epsilon_-}{\omega_0}\left(\frac{\Delta\phi_{12}}{\omega_0} + \frac{2\pi - \Delta\phi_{13}}{\omega_0 + \epsilon_+}\right). \tag{3.166}$$

3.7. HEAT MAPS MUTUAL INFORMATION AS A FUNCTION OF COUPLING STRENGTH AND INTRINSIC FREQUENCY

Fig. 3.3A shows the mutual information as a function of the coupling strength $\epsilon = \epsilon_+ = \epsilon_-$ and intrinsic frequency ω_0, for one value of the diffusion constant, $D = 0.1/T$. Fig. 3.9 shows the same plot, but then also for $D = 1/T$ and $D = 10^{-4}/T$. For $D = 10^{-4}/T$, the mutual information shows very rich behavior, corresponding to intrincate locking behavior.

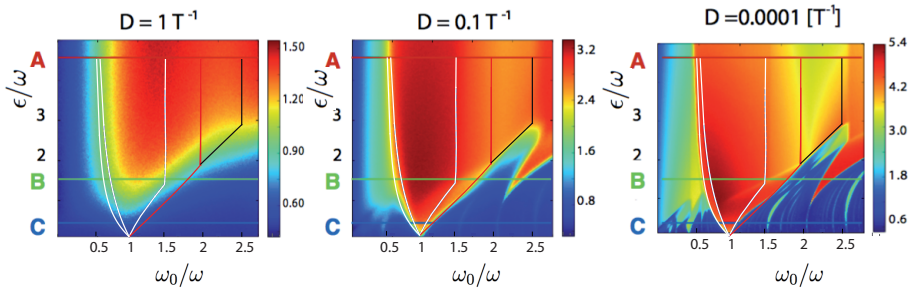

Figure 3.9: The mutual information as a function of the coupling strength ϵ and the intrinsic frequency ω_0, for three different values of the diffusion constant D. In all panels, $\Delta\phi_{12} = \Delta\phi_{23} = \pi/2$. Superimposed in black is the deterministic Arnold Tongue for scenarios 1 and 4. (A) $D = 1/T$. (B) $D = 0.1/T$ (the same panel as Fig. 3.3A). (C) $D = 10^{-4}/T$. Note the rich behaviour of the mutual information, corresponding to higher-order locking scenarios.

3.8. LINEAR-RESPONSE THEORY

As shown in the main text, the evolution of $p_1(\phi,t)$ is given by

$$\partial_t p_1(\phi,t) - D\partial_\phi^2 p_1(\phi,t) - \omega_0 \partial_\phi p_1(\phi,t) = L(t)\, p_0(\phi,t)\partial_\phi Z(\phi). \tag{3.167}$$

The solution to this non-homogeneous heat equation is:

$$p_1(\phi,t) = \int_0^{2\pi} d\xi G(\phi-\omega_0 t,\xi,t) f(\xi) + \int_0^{2\pi}\int_0^t d\tau d\xi G(\phi-\omega_0 t,\xi,t-\tau) A(\xi,\tau), \tag{3.168}$$

where $f(\phi)$ is the initial condition, $G(\phi-\omega_0 t,\phi_0,t,t_0)$ is the Green's function of the unperturbed diffusion operator, and
$A(\phi,t) \equiv L(t)\, p_0(\phi,t)\partial_\phi Z(\phi) = L(t)/(2\pi)\left(-\delta(\phi-\phi_1) - \delta(\phi-\phi_2) + 2\delta(\phi-\phi_3)\right)$.

The Green's function is given by

$$G(\phi-\omega_0 t,\phi_0,t) = \sum_{j=0}^{\infty} e^{-j^2 D t}[A_j(\phi_0)\cos(j(\phi-\omega_0 t)) + B_j(\phi_0)\sin(j(\phi-\omega_0 t))], \tag{3.169}$$

with

$$A_j(\phi_0) = \frac{1}{\pi}\int d\phi\delta(\phi-\omega_0 t-\phi_0)\cos(j(\phi-\omega_0 t)) = \frac{1}{\pi}\cos j\phi_0 \tag{3.170}$$

$$B_j(\phi_0) = \frac{1}{\pi}\int d\phi\delta(\phi-\omega_0 t-\phi_0)\sin(j\phi') = \frac{1}{\pi}\sin j\phi_0 \tag{3.171}$$

$$A_0 = \frac{1}{2\pi} \tag{3.172}$$

$$B_0 = 0 \tag{3.173}$$

This yields:

$$G(\phi,\phi_0,t) = \frac{1}{2\pi} + \frac{1}{\pi}\sum_{j=1}^{\infty} e^{-i^2 Dt} \times \left[\cos(j\phi_0)\cos(j(\phi-\omega_0 t)) + \sin(j\phi_0)\sin(j(\phi-\omega_0 t))\right] \tag{3.174}$$

Substituting this expression into Eq. 3.167 and Eq. 3.168 gives

$$p_1(\phi,t) = \int_0^{2\pi} d\xi G(\phi,\xi,t) f(\xi) + \int_0^{2\pi}\int_0^t d\tau d\xi G(\phi,\xi,t-\tau) \times \frac{L(\tau)}{2\pi}\left[-\delta(\xi-\phi_1) - \delta(\xi-\phi_2) + 2\delta(\xi-\phi_3)\right] \tag{3.175}$$

$$= G_0(\phi,t) + \frac{1}{2\pi}\int_0^t d\tau L(\tau)\Delta G(\phi,t-\tau), \tag{3.176}$$

where

$$G_0(\phi,t) = \int_0^{2\pi} d\xi G(\phi,\xi,t) f(\xi)$$
$$\Delta G(\phi,t-\tau) = -G(\phi,\phi_1,t-\tau) - G(\phi,\phi_2,t-\tau) + 2G(\phi,\phi_3,t-\tau). \tag{3.177}$$

We can integrate the second term of Eq. 3.176 by parts. Calling the primitive of ΔG,

$$C(\phi,\tau;t) = \int d\tau \Delta G(\phi,t-\tau), \tag{3.178}$$

we find

$$p_1(\phi,t) = G_0(\phi,t) + [L(\tau)C(\phi,\tau;t)]_{\tau=0}^{\tau=t} - \int_0^t d\tau \frac{dL(\tau)}{d\tau} C(\phi,\tau;t). \tag{3.179}$$

Since $L(\tau)$ is a sequence of step functions,

$$\frac{dL(\tau)}{d\tau} = \sum_{n=0}^{\infty} \delta(\tau - nT) - \delta(\tau - (nT + T/2)), \tag{3.180}$$

which yields

$$p_1(\phi,t) = G_0(\phi,t) + [L(\tau)C(\phi,\tau;t)]_0^t - \sum_{n=0}^{nT<t} [C(\phi,nT;t) - C(\phi,nT+T/2;t)] \tag{3.181}$$

Eq. 3.167 was derived assuming that the system is in steady state, and $p(\phi,t) = p(\phi,t+T)$. This means that we only have to consider times $0 < t < T$, in which case only the first two terms in the last sum on the right-hand side remain. More specifically, in steady state,

the initial condition $f(\phi)$ equals the steady-state distribution, and $f(\phi) = p(\phi, t = 0) = p(\phi, t = T)$, meaning that the above expression reduces to

$$\begin{aligned} f(\phi) &= G_0(\phi, T) + Q(\phi) \\ &= \int_0^{2\pi} f(\xi) G(\phi, \xi, t = T) + Q(\phi), \end{aligned} \tag{3.182}$$

where $Q(\phi)$ is defined as

$$\begin{aligned} Q(\phi) \equiv &-2C(\phi, \tau = 0; T) + C(\phi, \tau = T; T) + \\ &C(\phi, \tau = T/2; T). \end{aligned} \tag{3.183}$$

Eq. 3.182 an integral equation, more specifically an Fredholm equation of the second type. The integration kernel $G(\phi, \xi, T)$ has the form

$$\begin{aligned} G(\phi, \xi, T) = \frac{1}{2\pi} + \frac{1}{\pi} \sum_{j=1}^{\infty} e^{-j^2 DT} &[\cos(j(\phi - \omega_0 T)) \cos(j\xi) \\ &+ \sin(j(\phi - \omega_0 T)) \sin(j\xi)]. \end{aligned} \tag{3.184}$$

We define $G^*(\phi, \xi) = G(\phi, \xi) - 1/(2\pi)$, and rewrite Eq. 3.182 as:

$$f(\phi) = \int_0^{2\pi} d\xi f(\xi) G^*(\phi, \xi, t = T) + \frac{1}{2\pi} \int_0^{2\pi} d\xi f(\xi) + Q(\phi) \tag{3.185}$$

$$= \int_0^{2\pi} d\xi f(\xi) G^*(\phi, \xi, t = T) + \frac{1}{2\pi} + Q(\phi) \tag{3.186}$$

$$= \int_0^{2\pi} d\xi f(\xi) G^*(\phi, \xi, t = T) + Q^*(\phi), \tag{3.187}$$

where in going from the first to the second line we have exploited that $f(\phi)$ is normalized, and in the last line we have defined $Q^*(\phi) \equiv Q(\phi) - 1/(2\pi)$. The kernel $G^*(\phi, \xi, T)$ is separable, and we can rewrite Eq. 3.182 as

$$\begin{aligned} f(\phi) = \sum_{j=1}^{\infty} e^{-j^2 DT} \int_0^{2\pi} d\xi f(\xi) &[\cos(j(\phi - \omega_0 T)) \cos(j\xi) \\ &+ \sin(j(\phi - \omega_0 T)) \sin(j\xi)] + Q_j^*(\phi) \end{aligned} \tag{3.188}$$

with $Q^*(\phi) = \sum_j Q_j^*(\phi)$.

To solve this integral equation, we define

$$c1_j \equiv \int_0^{2\pi} d\xi e^{-j^2 DT} f(\xi) \cos(j\xi) \tag{3.189}$$

$$c2_j \equiv \int_0^{2\pi} d\xi e^{-j^2 DT} f(\xi) \sin(j\xi), \tag{3.190}$$

so that

$$\begin{aligned} f(\phi) = \sum_j \Big[&\cos(j(\phi - \omega_0 T)) c1_j + \sin(j(\phi - \omega_0 T)) c2_j \\ &+ Q_j^*(\phi) \Big]. \end{aligned} \tag{3.191}$$

We now multiply both sides, once with $e^{-j^2DT}\cos(j\phi)$ and once with $e^{-j^2DT}\sin(j\phi)$, and integrate from 0 to 2π. On the left-hand side, this gives c_{1j} and c_{2j}, respectively. We then arrive at the following set of linear equations:

$$c_{1j} = \sum_k A_{jk}c_{1k} + B_{jk}c_{2k} + Q^*_{1k}, \tag{3.192}$$

$$c_{2j} = \sum_k C_{jk}c_{1k} + D_{jk}c_{2k} + Q^*_{2k}, \tag{3.193}$$

$$\tag{3.194}$$

where

$$A_{jk} = \int_0^{2\pi} d\phi e^{-j^2DT}\cos(j\phi)\cos(k(\phi-\omega_0 T)) \tag{3.195}$$

$$B_{jk} = \int_0^{2\pi} d\phi e^{-j^2DT}\cos(j\phi)\sin(k(\phi-\omega_0 T)) \tag{3.196}$$

$$C_{jk} = \int_0^{2\pi} d\phi e^{-j^2DT}\sin(j\phi)\cos(k(\phi-\omega_0 T)) \tag{3.197}$$

$$D_{jk} = \int_0^{2\pi} d\phi e^{-j^2DT}\sin(j\phi)\sin(k(\phi-\omega_0 T)) \tag{3.198}$$

$$Q^*_{1k} = \int_0^{2\pi} d\phi e^{-j^2DT}\cos(j\phi)Q^*_k(\phi) \tag{3.199}$$

$$Q^*_{2k} = \int_0^{2\pi} d\phi e^{-j^2DT}\sin(j\phi)Q^*_k(\phi) \tag{3.200}$$

We can define the vectors $\mathbf{c}_1$ and $\mathbf{c}_2$ with elements c_{1j} and c_{2j}, respectively, as well as the matrices **A**, **B**, **C**, **D**, with elements $A_{jk}, B_{jk}, C_{jk}, D_{jk}$, respectively, and the vectors $\mathbf{q}_1$ and $\mathbf{q}_2$ with elements Q^*_{1j} and Q^*_{2j}, respectively. This allows us to define the vectors $\mathbf{c}^T \equiv (\mathbf{c}_1^T : \mathbf{c}_2^T)$ and $\mathbf{q}^T \equiv (\mathbf{q}_1^T : \mathbf{q}_2^T)$, where T denotes the transpose, and the matrix

$$\mathbf{M} = \begin{pmatrix} \mathbf{A} & \mathbf{B} \\ \mathbf{C} & \mathbf{D} \end{pmatrix}. \tag{3.201}$$

We can then rewrite Eqs. 4.88 and 3.193 as

$$\mathbf{c} = \mathbf{M}\mathbf{c} + \mathbf{q}, \tag{3.202}$$

which has as its solution

$$\mathbf{c} = (\mathbf{I} - \mathbf{M})^{-1}\mathbf{q}, \tag{3.203}$$

with **I** the identity matrix. With the coefficients c_{1j} and c_{2j} thus found, $f(\phi)$ can be obtained from Eq. 3.191, yielding, finally, the steady-state solution $p_{ss}(\phi) = 1/(2\pi) + f(\phi)$.

3.9. MUTUAL INFORMATION AS A FUNCTION OF ϵ_+ AND ϵ_-

Fig. 3.10 addresses how the mutual information depends on ϵ_+ and ϵ_-. To this end, the parameters are varied as $\epsilon_+ = (1-\alpha)\epsilon$ and $\epsilon_- = \alpha\epsilon$; varying α thus keeps the total absolute

coupling strength ϵ constant. The figure shows that the mutual information is rather insensitive to the relative values of ϵ_+ and ϵ_-.

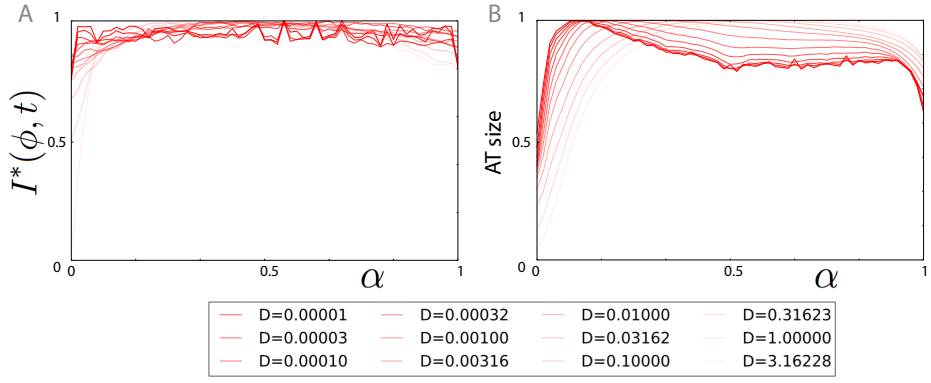

Figure 3.10: Information transmission is not much affected by the relative magnitudes of ϵ_+ and ϵ_- in the coupling function $Z(\phi)$ (see Fig. 3.1). We vary ϵ_+ and ϵ_- via a parameter α, defined as $\epsilon_+ = (1-\alpha)\epsilon$ and $\epsilon_- = \alpha\epsilon$; varying α thus keeps the total absolute coupling strength constant. We vary α and the diffusion constant D, and optimize over ϵ and ω_0, keeping $\Delta\phi_{12} = \Delta\phi_{23} = \pi/2$ constant in all simulations. (A) The maximal mutual information $I^*(\phi, t)$, obtained by optimizing $I(\phi, t)$ over ϵ and ω_0, as a function of α, for different values of D. It is seen that for most values of D, $I^*(\phi; t)$ is quite independent of α. (B) The size of the Arnold Tongue of the stochastic system as a function of α, for different values of D. The size is defined as $\int_{\omega_0^{\min}}^{\omega_0^{\max}} d\omega_0 \int_{\epsilon^{\min}}^{\epsilon^{\max}} d\epsilon I(\phi; t)/I^*(\phi; t)$, with $\omega_0^{\min}/\omega = 0.4$, $\omega_0^{\max} = 2.7$, $\epsilon_{\min}/\omega = 0$, $\epsilon_{\max}/\omega = 5$. It is seen that, except for the low and high values of α, the size of the Arnold Tongue of the stochastic system is fairly independent of α.

4

ROBUSTNESS OF CLOCKS TO INPUT NOISE

ABSTRACT

To estimate the time, many organisms, ranging from cyanobacteria to animals, employ a circadian clock which is based on a limit-cycle oscillator that can tick autonomously with a nearly 24h period. Yet, a limit-cycle oscillator is not essential for knowing the time, as exemplified by bacteria that possess an "hourglass": a system that when forced by an oscillatory light input exhibits robust oscillations from which the organism can infer the time, but that in the absence of driving relaxes to a stable fixed point. Here, using models of the Kai system of cyanobacteria, we compare a limit-cycle oscillator with two hourglass models, one that without driving relaxes exponentially and one that does so in an oscillatory fashion. In the limit of low input-noise, all three systems are equally informative on time, yet in the regime of high input-noise the limit-cycle oscillator is far superior. The same behavior is found in the Stuart-Landau model, indicating that our result is universal.

4.1. INTRODUCTION

Many organisms, ranging from animals, plants, insects, to even bacteria, need to know the time to synchronize their cellular and behavioral activity with the day-night rhythm. To this end, many employ a circadian clock. Circadian clocks are biochemical systems that can oscillate autonomously with a nearly 24h period, even though they are normally entrained by environmental signals to keep them in phase with the day-night cycle. While it is clear that circadian clocks which are locked to their environment make it possible to estimate the time of the day, it is far less obvious that clocks are essential for knowing the time [1, 2]. The oscillatory light input could also be used to drive a system which in the absence of any driving would relax to a stable fixed point rather than exhibit a limit cycle. The driving would then generate oscillations from which the organ-

ism could infer the time. It thus remains an open question what the benefits of circadian clocks are in estimating the time of the day.

This question is highlighted by the timekeeping mechanisms of prokaryotes. While circadian clocks are ubiquitous in eukaryotes, the only known prokaryotes to possess circadian clocks are cyanobacteria, which exhibit photosynthesis. The most studied and best characterized circadian clock is that of the cyanobacterium *Synechococcus elongatus*, which consists of three proteins, KaiA, KaiB, and KaiC [3]. The central clock component is KaiC, which forms a hexamer that is phosphorylated and dephosphorylated in a cyclical fashion under the influence of KaiA and KaiB. In a landmark study, Kondo and coworkers managed to reconstitute this protein phosphorylation cycle in the test tube, demonstrating that this Kai system forms a bonafide circadian clock that can tick autonomously in the absence of any oscillatory driving with a period of nearly 24 hours [4]. However, *S. elongatus* is not the only cyanobacterial species. Another species is *Prochlorococcus*, which possesses *kaiB* and *kaiC*, but lacks (functional) KaiA. Interestingly, this species exhibits daily rhythms in gene expression under light-dark (LD) cycles but no sustained circadian rhythms in constant conditions [5, 6]. Recently, Johnson and coworkers made similar observations for the purple bacterium *Rhodopseudomonas palustris*, which is unrelated to cyanobacteria but harbors homologs of KaiB and KaiC. Its growth rate depends on the KaiC homolog in LD conditions but not constant conditions [2], strongly suggesting that the bacterium uses the (homologous) Kai system to keep time. Moreover, this species too does not exhibit sustained rhythms in constant conditions, but does show daily rhythms in e.g. nitrogen fixation in cyclic conditions. *Proclorococcus* and *R. palustris* thus appear to keep time via an "hourglass" mechanism that relies on oscillatory driving [2, 5, 6]. These observations raise the question why some bacterial species like *S. elongatus* have evolved a bonafide clock that can run freely, while other species like *Proclorococcus* and *R. palustris* have evolved an hourglass timekeeping system. The question under what conditions do circadian clocks evolve was addressed by Troein *et al.* using computer simulations [7]. They used an evolutionary algorithm to evolve in *silico* biochemical networks that exhibit oscillations. They found that only in the presence of seasonal variations *and* stochastic fluctuations in the input signal, systems evolved that can also oscillate autonomously. However, they did not systematically study how the performance of the different network designs depended on these variations in the input signal. Moreover, as Johnson *et al.* pointed out [2], organisms near the equator have evolved self-sustained oscillations, showing that seasonal variations cannot be essential for the evolution of bonafide clocks.

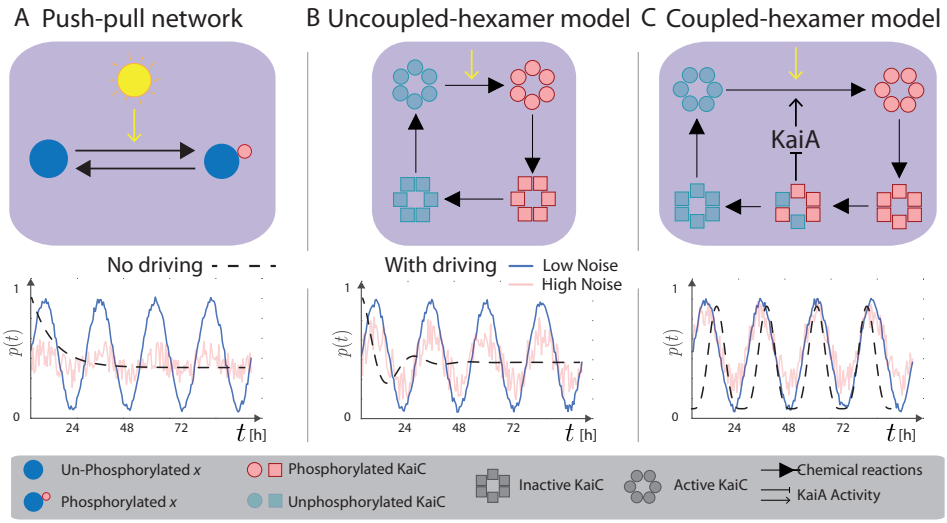

Figure 4.1: Overview of different timekeeping systems. (A) A push-pull network (PPN). Each protein can switch between a phosphorylated state and an unphosphorylated one, and the input signal enhances the rate of phosphorylation. In the absence of any driving, the PPN relaxes exponentially to a steady state (middle panel). Yet, in the presence of an oscillatory input, the system exhibits oscillations which can be used as an internal clock from which the time can be inferred. (lower panel) (B) The uncoupled-hexamer model (UHM), inspired by the Kai system of *Prochlorococcus*. It consists of KaiC hexamers which can switch between an active state in which the phosphorylation level tends to rise and an inactive one in which it tends to fall. The rate of phosphorylation is, presumably via changes in the ATP/ADP ratio, enhanced by the light input [8, 9]. The system is akin to a linear harmonic oscillator: it exhibits an intrinsic frequency ω_0, resulting from the protein phosphorylation cycle of the hexamers. However, the hexamers are not coupled via KaiA as in the coupled-hexamer model shown in panel C, such that it cannot sustain autonomous oscillations; in the absence of any driving, it relaxes in an oscillatory fashion to a stable fixed point (middle panel). (C) The coupled-hexamer model (CHM), inspired by tke Kai system of *S. elongatus*. Like the UHM, it consists of KaiC hexamers, which each tend to be phosphorylated in a cyclic fashion. However, in contrast to the UHM, the hexamers are coupled and synchronized via KaiA, such that the system can exhibit limit-cycle oscillations in the absence of any driving (middle panel). In all models, time is estimated from the fraction $p(t)$ of phosphorylated proteins.

4.2. THE MODEL

Here, we hypothesize that the optimal design of the readout system that maximizes the reliability by which cells can estimate the time depends on the noise in the input signal. To test this idea, we study three different network designs from which the cell can infer time (Fig. 4.1): 1) a simple push-pull network (PPN), in which a readout protein switches between a phosphorylated and an unphosphorylated state (Fig. 4.1A). Because the phosphorylation rate increases with the light intensity, the phosphorylation level oscillates in the presence of oscillatory driving, enabling the cell to estimate the time. This network lacks an intrinsic oscillation frequency, and in the absence of any driving it relaxes to a

stable fixed point in an exponential fashion; 2) an uncoupled hexamer model (UHM), which is inspired by the Kai system of *Plochorococcus* (Fig. 4.1B). This model consists of KaiC hexamers which each have an inherent propensity to proceed through a phosphorylation cycle. However, the phosphorylation cycles of the respective hexamers are not coupled among each other, and without a common forcing the cycles will therefore desynchronize, leading to the loss of macroscopic oscillations. In contrast to the proteins of the PPN, each hexamer is a tiny oscillator with an intrinsic frequency ω_0, which means that an ensemble of hexamers that has been synchronized initially, will, in the absence of driving, relax to its fixed point in an oscillatory manner. 3) coupled hexamer model (CHM), which is inspired by the Kai system of *S. elongatus* (Fig. 4.1C). As in the previous UHM, each hexamer has an intrinsic capacity to proceed through a phosphorylation cycle, but, in contrast to that system, the cycles of the respective hexamers are coupled and synchronized via KaiA, as described further below. Consequently, this system exhibits a limit cycle, yielding macroscopic oscillations with intrinsic frequency ω_0 even in the absence of any driving.

Here we are interested in the question how the accuracy of estimating time is limited by the noise in the input signal, and how this limit depends on the architecture of the readout network. We are therefore interested in the regime that the intrinsic noise can be ignored [10], which means that we model the different systens using mean-field (deterministic) chemical rate equations.

The chemical rate equation of the PPN model is given by $\dot{x}_p = k_\mathrm{f} s(t)(x_\mathrm{T} - x_p(t)) - k_\mathrm{b} x_p(t)$, where $x_p(t)$ is the concentration of phosphorylated protein, x_T is the total concentration, $k_\mathrm{f} s(t)$ is the phosphorylation rate k_f times the input signal $s(t)$, and k_b is the dephosphorylation rate. The uncoupled (UHM) and coupled (CHM) hexamer model are based on a minimal model of the Kai system of *S. elongatus*, which in the past decade has been modeled extensively due to a wealth of data [11–18]. In both models, KaiC switches between an active conformation in which the phosphorylation level tends to rise and an inactive one in which it tends to fall [11, 16]. Experiments indicate that the principal Zeitgeber is the ATP/ADP ratio [8, 9], which means that the clock predominantly couples to the input $s(t)$ during the phosphorylation phase of the oscillations [8, 18]. Inspired by this observation, in both the UHM and the CHM, $s(t)$ modulates the phosphorylation rate of active KaiC. Since, in *S. elongatus*, KaiB does not directly affect the (de)phosphorylation rate but mainly plays a role in stabilizing inactive KaiC and mediating KaiA binding [11, 12, 16, 17], KaiB is not modeled explicitly. The principal difference between the UHM and CHM is KaiA: (functional) KaiA is absent in *Prochlorococcus* and hence in the UHM [5, 6]. In contrast, in *S. elongatus* and hence the CHM, KaiA phosphorylates active KaiC, yet inactive KaiC can via KaiB strongly bind KaiA too. This gives rise to the synchronisation mechanism of differential affinity [11, 12], in which inactive hexamers that are still in the dephosphorylation phase of the cycle take away KaiA from those hexamers that have already finished their cycle, thereby halting their next round of phosphorylation. In all three models, the input is modeled as a sinusoidal signal with mean $\bar{s}$ and driving frequency $\omega = 2\pi/T$ plus additive noise $\eta_s(t)$: $s(t) = \sin(\omega t) + \bar{s} + \eta_s(t)$. The noise is uncorrelated with the mean signal, and has strength σ_s^2 and correlation time τ_c, $\langle \eta_s(t)\eta_s(t')\rangle = \sigma_s^2 e^{-|t-t'|/\tau_c}$. A detailed description of the different models is given in [20].

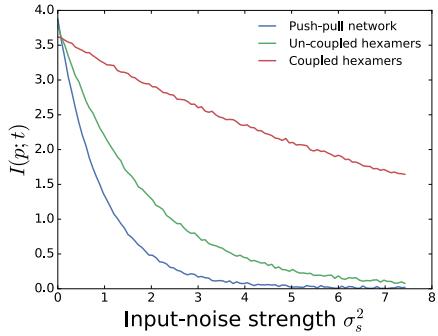

Figure 4.2: The mutual information $I(p;t)$ as a function of the input-noise strength σ_s^2, for the push-pull network (PPN), the uncoupled-hexamer model (UHM) and the coupled-hexamer model (CHM), see Fig. 4.1. In the limit of low input noise, all systems are equally informative on time, yet in the high-noise regime the CHM is most accurate. The parameters have been optimized to maximize $I(p;t)$; since these are (nearly) independent of σ_s^2, they are fixed (see Table S1 [20]).

4.3. RESULTS

As a performance measure for the accuracy of estimating time, we use the mutual information $I(p;t)$ between the time t and the phosphorylation level $p(t)$ [10, 19]:

$$I(p;t) = \int_0^T dt \int_0^1 dp P(p,t) \log_2 \frac{P(p,t)}{P(p)P(t)}. \tag{4.1}$$

Here $P(p,t)$ is the joint probability distribution while $P(p)$ and $P(t) = 1/T$ are the marginal distributions for observing p and t. The mutual information quantifies the number of distinct time points that can be inferred uniquely from the phosphorylation level $p(t)$. The distributions are obtained from running long simulations of the chemical rate equations of the different models [20].

For each system, we first optimized the parameters to maximize the mutual information [20]. For the PPN, there exists an optimal response time $\tau_r \sim 1/k_b$ that maximizes $I(p;t)$, which can be understood as a trade-off between maximizing the amplitude of $p(t)$, which increases with decreasing τ_r, and minimizing the noise in $p(t)$, which decreases with increasing τ_r because of time averaging [20, 21]. Similarly, for the UHM, there exists an optimal intrinsic frequency ω_0 of the individual hexamers. Because the UHM is linear, its behavior is similar to the simplest system with an intrinsic frequency, the (damped) harmonic oscillator. Analyzing this system shows that while the amplitude A of the output $x(t)$ is maximized at resonance, $\omega_0 \to \omega$, the standard deviation σ_x of x is maximized when $\omega_0 \to 0$, such that the signal-to-noise ratio A/σ_x peaks for $\omega_0 > \omega$ [20]. Interestingly, also the CHM exhibits a maximum in A/σ_x for intrinsic frequencies that are slightly off-resonance [20].

Fig. 4.2 shows the mutual information $I(p;t)$ as a function of the input-noise strength σ_s^2 for the three systems. In the limit that σ_s^2 is small, $I(p;t)$ is essentially the same for all systems. In this regime, they are equally informative on time. However, the figure also

shows that as σ_s^2 rises, $I(p;t)$ of the UHM and especially the PPN decrease very rapidly, while that of the CHM falls much more slowly. In fact, for $\sigma_s^2 \approx 3$, $I(p;t)$ of the CHM is still far above 2 bits, while $I(p;t)$ of the PPN and that of the UHM have already dropped below 1 bit, meaning that using these systems, the cell would no longer be able to distinguish between day and night. Indeed, this figure shows that in the regime of high input noise, a bonafide clock that can tick autonomously is a much better time-keeper than a system which relies on oscillatory driving for showing oscillations. This is the principal result of our paper. It is observed for other values of τ_c and other types of input signals, such as a truncated sinusoid corresponding to no driving at night (see Fig. S4 of [20]).

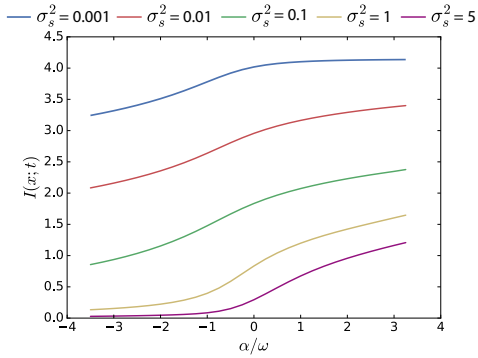

Figure 4.3: The mutual information $I(p;t)$ as a function of α of the Stuart-Landau model (see Eq. 4.2), for different strengths of the input noise σ_s^2. When $\alpha < 0$, the system corresponds to a damped oscillator like the uncoupled-hexamer model (UHM). When $\alpha > 0$, the system can sustain autonomous oscillations, like the coupled-hexamer model (CHM). Clearly, the mutual information rises as the system is changed from a damped oscillator into a bonafide clock that exhibits limit-cycle oscillations. Moreover, the increase is most pronounced when the input noise is large, as also observed for the UHM and the CHM (see Fig. 4.2). Parameters: $\nu = 0$; $\beta = \omega$; $\epsilon = 0.5\omega$.

The robustness of our observation that bonafide clocks are more reliable timekeepers especially when the input noise is large, suggests that it is a universal phenomenon, independent of the details of the system. We therefore analyzed a generic minimal model, the Stuart-Landau model. It allows us to study how the capacity to infer time changes as a system is altered from a damped (nearly) linear oscillator, which has a characteristic frequency but cannot sustain oscillations in the absence of driving, to a (weakly) non-linear oscillator that can sustain autonomous oscillations [20]. Near the Hopf bifurcation where a limit cycle appears the effect of the non-linearity is weak, so that the solution $x(t)$ is close to that of a linear harmonic oscillator; this means that when the system is driven by a sinusoidal signal $s(t)$ with frequency $\omega(t)$, the solution has the form $x(t) = 1/2(A(t)e^{i\omega t} + c.c.)$, where $A(t)$ is a complex amplitude that can be time-dependent [22]. The dynamics of $A(t)$ is then given by

$$\dot{A} = -i\nu A + \alpha A - \beta|A|^2 A - \epsilon E, \tag{4.2}$$

where $\nu \equiv (\omega^2 - \omega_0^2)/(2\omega)$ with ω_0 the intrinsic frequency, α and β are parameters that govern the linear and non-linear growth and decay of oscillations, E is the first harmonic

of $s(t)$ and ϵ describes the coupling strength [22]. Eq. 4.2 gives a universal description of a driven weakly non-linear oscillator near the Hopf bifurcation [22].

The non-driven system exhibits a Hopf bifurcation at $\alpha = 0$. This means that by varying α we can change the system from a *damped oscillator* (defined by $\alpha < 0$) which in the absence of driving exhibits oscillations that decay, to an *limit-cycle oscillator* ($\alpha > 0$) that shows free-running oscillations. The driven damped oscillator system ($\alpha < 0$) always has one stable fixed point with $|A| > 0$ corresponding to sinusoidal oscillations that are synchronized with the driving. The driven limit-cycle oscillator system ($\alpha > 0$), however, can exhibit different dynamics, ranging from perfect synchronization, where $x(t)$ has a constant amplitude A and constant phase shift with respect to $s(t)$, to quasi-periodic oscillations of $x(t)$, arising from limit-cycle dynamics of $A(t)$ [22]. Here we limit ourselves to perfect synchronisation.

To compute $I(x,t)$, we use an approach that is inspired by the linear-noise approximation for computing noise in biochemical networks, and which we have employed before in this context [10, 19]. It assumes that $P(x|t)$ is a Gaussian distribution with variance $\sigma_x^2(t)$ centered at the deterministic solution $x(t) = 1/2(Ae^{i\omega t} + c.c.)$, where A is obtained by solving Eq. 4.2 in steady state. To find σ_x^2, we first compute σ_A^2 from Eq. 4.2 by adding Gaussian white-noise of strength σ_s^2 to E and expanding A to linear order around its fixed point; $\sigma_x^2(t)$ is then obtained from σ_A^2 via a coordinate transformation [20].

Fig. 4.3 shows the mutual information $I(x;t)$ as a function α, for different values of σ_s^2. The figure shows that $I(x;t)$ rises as the system is changed from a damped oscillator $\alpha < 0$ to a self-sustained oscillator ($\alpha > 0$). Moreover, the increase is most pronounced when the input noise σ_s^2 is large. The Stuart-Landau model thus reproduces the behavior of the computational models in Fig. 4.2. It shows that the principal result of our study is universal: when the input noise is small, a system that shows sustained oscillations only in response to driving can keep time as reliably as a limit-cycle oscillator, which can generate oscillations autonomously; yet for high input noise, a limit-cycle oscillator is superior.

The PPN and UHM are readout systems that in the absence of driving relax to a stable fixed point. The signal generates oscillations by driving the fixed point around in state space, and noise in the input then moves the fixed point around in a stochastic fashion. While the driven system exhibits a cycle in state space, the trajectory is determined by the strength of the input, creating a trade-off between gain (amplitude) and noise that cannot be lifted [20]. The CHM is a limit-cycle oscillator, which is markedly different. In the absence of driving, it already moves around a cycle in state space with a well-defined amplitude and pace: the limit cycle. This cycle is an intrinsic and robust property of the system. While coupling the system to the input is necessary for maintaining a stable phase relationship with the environment, weak forcing does not significantly change the trajectory of the limit cycle, making these oscillators more robust to input noise [20]. Lastly, we note that in our minimal models the formal distinction between internal and input noise vanishes—the same additive noise term could be used to model either source. This leaves open the possibility that limit-cycle oscillators are also more robust to internal noise. We leave this question for future work.

SUPPLEMENT FOR "ROBUSTNESS OF CLOCKS TO INPUT NOISE"

This supporting information provides background information on the computational models and analytical models that we have studied. The computational models are described in the next section, while the analytical models are discussed in section 4.5.

4.4. COMPUTATIONAL MODELS

In this section, we describe the three computational models that we have considered in this study: the push-pull network; the uncoupled-hexamer model; and the coupled-hexamer model. We also describe how we have modeled the input signal and how the systems are coupled to the input. Finally, we investigate the robustness of the principal results shown in Fig. 2 of the main text. In the next section, we first describe how we have modeled the input signal. In the subsequent sections, we then describe the computational models, how they are coupled to the input, and how we have set their parameters. Table 4.1 lists the values of all the parameters of all the models. In section 4.4.5 we show that the principal findings of Fig. 2 are robust to the type of input signal and the noise correlation time.

4.4.1. INPUT SIGNAL

The input signal is modeled as a sinusoidal oscillation with additive noise:

$$s(t) = \sin(\omega t) + \bar{s} + \eta_s(t), \tag{4.3}$$

where $\bar{s}$ is the mean input signal and $\eta_s(t)$ describes the input noise. The noise in the input is assumed to be uncorrelated with the mean input signal $s(t)$. Moreover, we assume that the input noise has strength σ_s^2 and is colored, relaxing exponentially with correlation time τ_c: $\langle \eta_s(t)\eta_s(t')\rangle = \sigma_s^2 e^{-|t-t'|/\tau_c}$.

The input signal $s(t)$ is coupled to the system by modulating the phosphorylation rate k_α of the core clock protein, as we describe in detail for the respective computational models in the next sections. Here, $k_\alpha = k_\mathrm{f}, k_\mathrm{ps}, k_i$, depending on the computational model. As we will see, the net phosphorylation rate is given by

$$k_\alpha s(t) = k_\alpha s(t) \tag{4.4}$$

$$= k_\alpha \bar{s} + k_\alpha \left(\sin(\omega t) + \eta_s\right). \tag{4.5}$$

This expression shows that in the presence of oscillatory driving, the mean phosphorylation rate averaged over a period is set by $k_\alpha \bar{s}$, while the amplitude of the oscillation in the phosphorylation rate, which sets the strength of the forcing, is given by k_α. We also note that k_α amplifies not only the "true" signal $\sin(\omega t)$, but also the noise η_s, the consequences of which will be discussed below. Lastly, the absence of any oscillatory driving is modeled by taking $s(t) = \bar{s}$, such that the net phosphorylation rate is then $k_\alpha \bar{s}$. The phosphorylation rate in the presence of stochastic driving is thus characterized by the following parameters: the mean phosphorylation rate $k_\alpha \bar{s}$, the amplitude of the phosphorylation-rate oscillations k_α, and the noise $\eta_s(t)$, characterized by the noise strength σ_s^2 and correlation time τ_c. We will vary σ_s^2 and τ_c systematically, while $\bar{s}$ and

k_α, together with the other system parameters, will be optimized to maximize the mutual information, as described below.

In the simulations, realisations of $\eta_s(t)$ are generated via the Ornstein-Uhlenbeck process

$$\dot{\eta}_s = -\eta_s/\tau_c + \xi(t), \tag{4.6}$$

where $\xi(t)$ is Gaussian white noise $\langle \xi(t)\xi(t')\rangle = \langle \xi^2\rangle \delta(t-t')$. This generates colored noise of $\eta_s(t)$, $\langle \eta_s(t)\eta_s(t')\rangle = \sigma_s^2 e^{-|t-t'|/\tau_c}$, where $\sigma_s^2 = \langle \xi^2\rangle \tau_c/2$.

The results of Fig. 2 of the main text correspond to $\tau_c = 0.5$/h. However, we have tested the robustness of the results by varying the noise correlation time τ_c. In addition, to test the robustness of our observations to changes in the shape of the input signal, we have also varied that. These tests are described in section 4.4.5 and the results are shown in Fig. 4.7. Clearly, the principal result of Fig. 2 of the main text is robust to changes in both the noise correlation time τ_c and the shape of the mean-input signal.

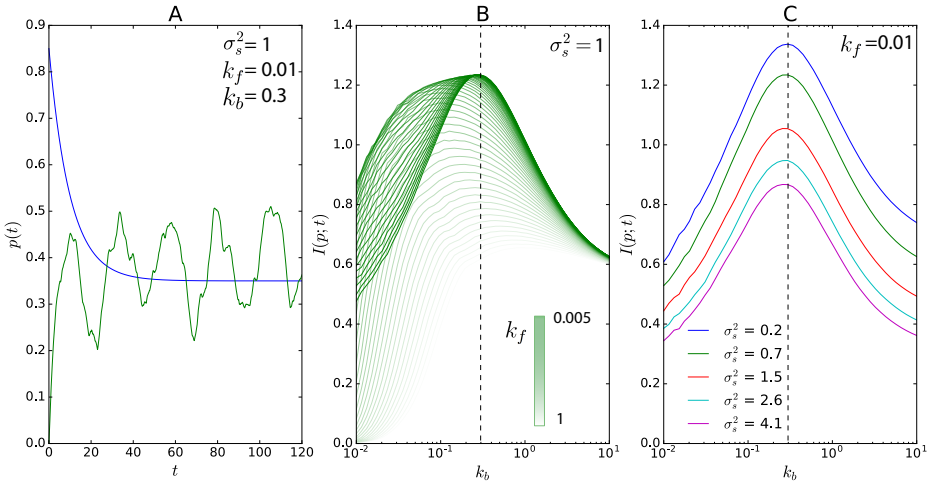

Figure 4.4: The push-pull network. (A) Time trace of $p(t)$ in the presence of driving (green line) and absence of driving (blue line). Please note that in the absence of driving, the system relaxes in an exponentially fashion to a stable fixed point. (B) The mutual information $I(p;t)$ as a function of k_b for different values of k_f (see Eq. 4.7), for $\sigma_s^2 = 1$. It is seen that for each phosphorylation rate k_f there is an optimal dephosphorylation rate k_b that maximizes the mutual information $I(p;t)$. Moreover, $I(p;t)$ increases as k_f decreases, but then saturates and hence becomes independent of k_f as the system enters the regime in which it responds linearly to the input s. The dashed line shows the optimal value of $k_\mathrm{b}^{\mathrm{opt}} \approx 0.3$/h, as predicted by Eq. 4.43. (C) The mutual information $I(p;t)$ as a function of the dephosphorylation rate k_b, for different values of the input-noise strength σ_s^2, keeping the phosphorylation rate fixed at $k_\mathrm{f} = 0.01$/h. The optimal dephosphorylation rate $k_\mathrm{b}^{\mathrm{opt}} \approx 0.3$/h (dashed line) is independent of σ_s^2, as predicted by Eq. 4.43. The input-noise correlation time $\tau_c = 0.5$h.

Parameter	Description	Value
Push-pull network, Eq. 4.7		
k_f	Phosphorylation rate	0.01/h
k_b	Dephosphorylation rate (Eq. 4.43)	0.3/h
Uncoupled-hexamer model, Eqs. 4.8-4.13		
k_f	Phosphorylation rate	0.26/h
k_b	Dephosphorylation rate	0.52/h
k_s	Conformational switching rate	100/h
Coupled-hexamer model, Eqs. 4.16-4.22		
k_ps	Autophosphorylation rate	0.0125/h
k_b	Dephosphorylation rate	0.1875/h
k_s	Conformational switching rate	100/h
K_0	KaiA dissociation constant C_0	0.0001
K_1	KaiA dissociation constant C_1	0.0003
K_2	KaiA dissociation constant C_2	0.001
K_3	KaiA aissociation constant C_3	0.003
K_4	KaiA dissociation constant C_4	0.01
K_5	KaiA dissociation constant C_5	0.03
k_0	KaiA-stimulated phosphorylation rate C_0	0.5/h
k_1	KaiA-stimulated phosphorylation rate C_1	0.5/h
k_2	KaiA-stimulated phosphorylation rate C_2	0.5/h
k_3	KaiA-stimulated phosphorylation rate C_3	0.5/h
k_4	KaiA-stimulated phosphorylation rate C_4	0.5/h
k_5	KaiA-stimulated phosphorylation rate C_5	0.5/h
$\tilde{b}_{2-4}$	Number KaiA dimers sequestered by $\tilde{\mathrm{C}}_{1-4}$	2
$\tilde{b}_{0,5,6}$	Number KaiA dimers sequestered by $\tilde{\mathrm{C}}_{0,5,6}$	0
$\tilde{K}_{1-4}$	KaiA dissociation constant $\tilde{\mathrm{C}}_{1-4}$	0.000001
$\tilde{K}_{0,5,6}$	KaiA dissociation constant $\tilde{\mathrm{C}}_{0,5,6}$	∞
c_T	Total concentration of KaiC	1
A_T	Total concentration of KaiA	1

Table 4.1: Parameter values of all the three computational models studied in the main text. The parameter values listed are those that maximize the mutual information $I(p;t)$ between the phosphorylation level p and time t; these values are nearly independent of the input-noise strength σ_s^2, and thus kept constant as σ_s^2 is varied in the simulations corresponding to Fig. 2 of the main text. For these optimal parameters values, the intrinsic period of the uncoupled-hexamer model is $T_0^{\mathrm{opt}} \approx 23.1$h while that of the coupled-hexamer model is $T_0^{\mathrm{opt}} \approx 25.1$h. All three models are coupled to the input by multiplying the phosphorylation rates with $s(t) = \sin(\omega) + \bar{s} + \eta_s(t)$, where $\bar{s} = 2$ and $\eta_s(t)$ describes colored noise with strength σ_s^2 and correlation time τ_c, $\langle \eta_s(t)\eta_s(t')\rangle = \sigma_s^2 e^{-|t-t'|/\tau_c}$. For Fig. 2 of the main text, $\tau_c = 0.5$h. Dissociation constants and protein concentrations are in units of the total KaiC concentration. Note that in the absence of oscillatory driving $s(t) = \bar{s} = 2$, meaning that in simulations of the non-driven systems the phosphorylation rates k_f, k_i, k_ps, still have to be multiplied by $\bar{s} = 2$.

4.4.2. PUSH-PULL NETWORK

The push-pull network is described by the following reaction

$$\dot{x}_p = k_\mathrm{f} s(t)(x_\mathrm{T} - x_p(t)) - k_\mathrm{b} x_p(t), \tag{4.7}$$

where $x_\mathrm{T} = x + x_p$ is the total protein concentration, x_p is the concentration of phosphorylated protein, $k_\mathrm{f} s(t)$ is the phosphorylation rate k_f times the input signal $s(t)$ (see Eq. 4.3) and k_b is the dephosphorylation rate. Fig. 4.4A shows a time trace of both a driven and a non-driven push-pull network.

Setting the parameters

The steady-state mean phosphorylation level is set by $\bar{p} = \bar{x}_p / x_T = k_\mathrm{f}\bar{s}/(k_\mathrm{f}\bar{s} + k_\mathrm{b})$. We anticipated, based on the analytical calculations described in section 4.5.1, that a key timescale is k_b and that the system should operate in the regime in which it responds linearly to changes in the mean input $\bar{s}$. This means that for a given k_b, k_f and $\bar{s}$ cannot be too large. We have chosen $\bar{s} = 2$, and then varied k_f and k_b to optimize the mutual information. We then verified a posteriori that the value of $\bar{s} = 2$ indeed puts the system in the optimal linear regime.

Optimal dephosphorylation rate Specifically, the parameters k_f and k_b are set as follows: for a given input noise strength $\sigma_s^2 = 1.0$, we first fix the phosphorylation rate k_f and compute the mutual information $I(p;t)$ between the phosphorylated fraction $p(t) = x_p(t)/x_T$ and time t as a function of the dephosphorylation rate k_b; we then repeat this procedure by varying k_f. The result is shown in Fig. 4.4B. Clearly, there exists an optimal value of k_b that maximizes $I(p;t)$. Moreover, the optimal value $k_\mathrm{b}^\mathrm{opt}$ becomes indepdendent of k_f when k_f becomes so small that the system enters the regime in which it responds linearly to changes in the mean input $\bar{s}$. We then fixed the phosphorylation rate to $k_\mathrm{f} = 0.01/\mathrm{h}$, and compute $I(p;t)$ as a function of k_b for different levels of the input-noise strength, see Fig. 4.4C. It is seen that the optimal dephosphorylation rate $k_\mathrm{b}^\mathrm{opt}$ is essentially independent of the input noise strength σ_s^2. In the simulations corresponding to Fig. 2 of the main text, we therefore kept k_b constant at $k_\mathrm{b}^\mathrm{opt} = 0.3/\mathrm{h}$ and k_f constant at $k_\mathrm{f} = 0.01/\mathrm{h}$ when we varied σ_s^2.

The observation that $k_\mathrm{b}^\mathrm{opt}$ is independent of k_f and σ_s^2 can be understood by noting that to maximize information transmission, the system should operate in the linear-response regime in which the mean output $\bar{x}$ responds linearly to changes in the mean input $\bar{s}$. This regime tends to enhance information because it ensures that in the presence of a sinusoidal input, the output $x_p(t)$ will not be distorted and be sinusoidal too. In this linear-response regime, the system can be analyzed analytically, see Eq. 4.43 in section 4.5.1 below. This equation, which accurately predicts the optimum seen in Fig. 4.4B and Fig. 4.4C, reveals that the optimal dephosphorylation rate depends on the frequency of the driving signal, ω, and the correlation time of the noise, τ_c, but not on the noise strength σ_s^2 and the coupling ρ to the input signal, given by $\rho = k_\mathrm{f} x_T$. Increasing the gain ρ amplifies not only the true signal, but also the noise in that signal (see also Eq. 4.5), such that the signal-to-noise ratio is unaltered. Indeed, increasing the gain only helps in the presence of internal noise, which here, however, is zero. Conversely, if intrinsic noise were present, simply decreasing k_f to bring the system in the optimal linear-response regime would lower the signal-to-noise ratio; however, the signal-to-noise ratio can always be enhanced by increasing x_T: this will not only increase the gain $\rho = k_\mathrm{f} x_\mathrm{T}$ and

thereby raise the output signal above the intrinsic noise, but also reduce the intrinsic noise itself.

We note that for (much) larger input-noise strength than that considered here, it might be beneficial to strongly increase the input signal and drive the system into the non-linear regime. This makes it possible to exploit the fact that the output $p(t)$ is naturally bounded between zero and unity; the input noise can thus be tamed by continually pushing $p(t)$ against either zero and unity. This generates, however, strongly non-sinusoidal, square-wave like oscillations, which are not experimentally observed [12]. We thus leave the regime of strong driving for future work.

4.4.3. UNCOUPLED-HEXAMER MODEL: KAI SYSTEM OF *Prochlorococcus*

Background The uncoupled-hexamer model (UHM) presented in the main text is a minimal model of the Kai system of the cyanobacterium *Proclorococcus* and, possibly, the purple bacterium *Rhodopseudomonas palustris*. The well characterized clock of the cyanobacterium *S. elongatus* consists of three proteins, KaiA, KaiB and KaiC, which are all essential for sustaining free-running oscillations [3]. And, indeed, many cyanobacteria possess at least one copy of each *kai* gene. One exception is *Proclororoccus*, which contains *kaiB* and *kaiC*, but misses a (functional) *kaiA* gene. Interestingly, in daily (12h:12h) light-dark (LD) cycles, the expression of many genes, including *kaiB* and *kaiC*, is rhythmic, but in constant conditions these rhythms damp very rapidly [5, 6]. Similar behavior is observed for the purple bacterium *R. palustris*, which possesses homologs of the *kaiB* and *kaiC* genes [2]: under LD conditions, the KaiC homolog appears to be phosphorylated in a circadian fashion, but under constant conditions, the oscillations decay very rapidly; physiological activities, such as the nitrogen fixation rates, follow a similar pattern [2]. Of particular interest is the observation that under LD conditions but not under LL conditions, the growth rate is significantly reduced in the strain in which the *kaiC* homolog was knocked out [2]. This strongly suggests that the (homologous) Kai system plays a role as a timekeeping mechanism, which relies, however, on oscillatory driving.

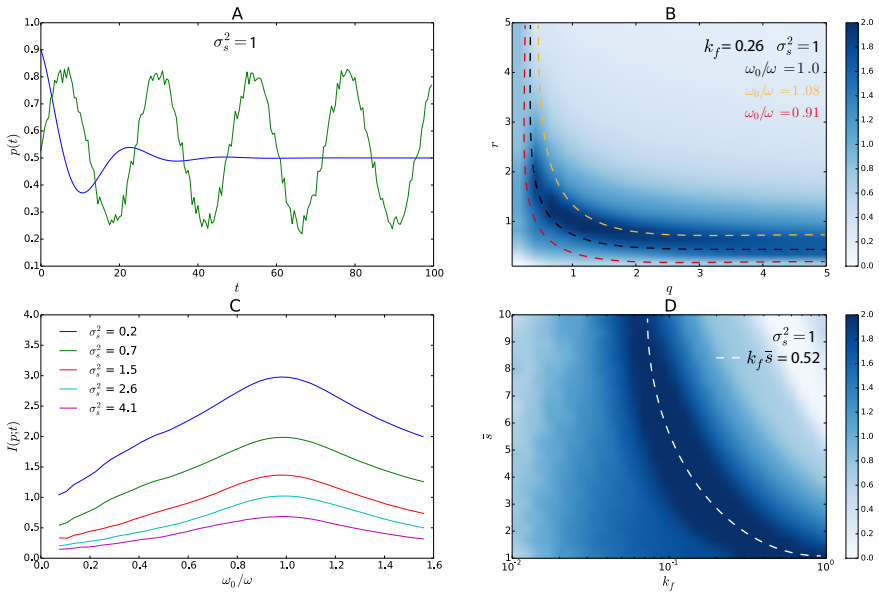

Figure 4.5: The uncoupled-hexamer model. (A) Time trace of $p(t)$ in the presence of driving (green line) and absence of driving (blue line). Please note that in the absence of driving, the system relaxes in an oscillatory fashion to a stable fixed point. (B) Heatmap of the mutual information $I(p;t)$ as a function of the scaling factor q that scales both the dephosphorylation rate k_b and the the mean phosphorylation rate $k_f\bar{s}$ (see Eq. 4.5) and the ratio $r = k_b/(k_f\bar{s})$ of these quantities. The mean phosphorylation rate $k_f\bar{s}$ is changed by varying $\bar{s}$ while keeping $k_f = 0.26/\text{h}$ constant; this ensures that the strength of the forcing, i.e. the amplitude of the phosphorylation-rate oscillations set by k_f, remains constant (see Eq. 4.5). Superimposed are contour lines of constant $\omega_0 = \omega_0(q,r)$ (see Eq. 4.15). It is seen that in the regime where $I(p;t)$ is high, $I(p,t)$ is almost constant along these contour lines, showing that $I(p;t)$ predominantly depends on $\bar{s}$ and k_b via ω_0. (C) The mutual information $I(p;t)$ as a function of ω_0, which was varied by scaling $\bar{s}$ and k_b keeping $r = k_b/(k_f\bar{s}) = 1$ and $k_f = 0.26/\text{h}$, for different values of the input-noise strength σ_s^2. It is seen that there exists an optimal intrinsic frequency ω_0^{opt} that maximizes $I(p;t)$. Moreover, ω_0^{opt} is nearly independent of σ_s^2, corresponding to an intrinsic period $T_0 = 2\pi/\omega_0^{\text{opt}} \approx 23.1\text{h}$. (D) The mutual information $I(p;t)$ as a function of k_f and $\bar{s}$, keeping $k_b = 0.52/\text{h}$ constant. Superimposed is the line along which $k_f\bar{s} = 0.52/\text{h}$ and hence the intrinsic period T_0 are constant (see Eq. 4.15). Along this line also $I(p;t)$ is nearly constant, meaning that the strength of the forcing, set by k_f, is not very critical. This mirrors the behavior seen for the push-pull network (see Fig. 4.4). It is due to the fact that increasing the forcing raises not only the amplitude but also the noise, keeping the signal-to-noise ratio and hence the mutual information essentially unchanged. The noise correlation time $\tau_c = 0.5\text{h}$.

Model Our model is inspired by the models that in recent years have been developed for *S. elongatus* [11, 12, 15–17]. These models share a number of characteristics that are essential for generating oscillations and entrainment (see also next section). The central clock component is KaiC, a hexamer, that can switch between an active state in which

the phosphorylation level tends to rise and an inactive one in which it tends to fall. The model lacks KaiA because *Prochlororoccus* and *R. palustris* miss a functional *kaiA* gene [2, 5, 6]. In *S. elongatus*, KaiB does not directly affect the rates of phosphorylation and dephosphorylation, but mainly serves to stabilize the inactive state and mediate KaiA binding by inactive KaiC [16, 17]. KaiB is therefore not modelled explicitly [16, 17]. The main entrainment signal for *S. elongatus* is the ratio of ATP to ADP levels, which depends on the light intensity, and predominantly couples to KaiC in its active conformation [8, 9, 17, 18]. These observations give rise to the following chemical rate equations:

$$\dot{c}_0 = k_s \tilde{c}_0 - k_f s(t) c_0 \tag{4.8}$$

$$\dot{c}_i = k_f s(t)(c_{i-1} - c_i) \qquad i \in (1,\dots,5) \tag{4.9}$$

$$\dot{c}_6 = k_f s(t) c_5 - k_s c_6 \tag{4.10}$$

$$\dot{\tilde{c}}_6 = k_s c_6 - k_f \tilde{c}_6 \tag{4.11}$$

$$\dot{\tilde{c}}_i = k_b(\tilde{c}_{i+1} - \tilde{c}_i) \qquad i \in (1,\dots,5) \tag{4.12}$$

$$\dot{\tilde{c}}_0 = k_b \tilde{c}_1 - k_s \tilde{c}_0 \tag{4.13}$$

Here, c_i, with $i = 0,\dots,6$, is the concentration of active i-fold phosphorylated KaiC in its active conformation, while $\tilde{c}_i$ is the concentration of inactive i-fold phosphorylated KaiC. The quantity k_s is the conformational switching rate, k_b is the dephosphorylation rate of inactive KaiC, and $k_f s(t)$ is the phosphorylation rate of active KaiC, k_f, times the input signal $s(t)$.

The output is the phosphorylation fraction of KaiC proteins (monomers), given by [11, 15, 17]

$$p(t) = \frac{1}{6} \frac{\sum_{i=0}^{6} i(c_i + \tilde{c}_i)}{\sum_{i=0}^{6} (c_i + \tilde{c}_i)}. \tag{4.14}$$

Fig. 4.5A shows a time trace of the phosphorylation level $p(t)$ of both a driven and a non-driven uncoupled-hexamer model.

Intrinsic frequency Because the cycles of the different hexamers are not coupled via KaiA as in the coupled-hexamer model and in *S. elnogatus*, the system cannot sustain free-running oscillations. In this respect, the system is similar to the push-pull network in the sense that a perturbation of the non-driven system will relax to a stable fixed point. However, this model differs from the push-pull network in that it has a characteristic frequency $\omega_0 = 2\pi/T_0$ with intrinsic period T_0, arising from the phosphorylation cycle of the KaiC hexamers. Consequently, while a perturbed (non-driven) push-pull network will relax exponentially to its stable fixed point, the uncoupled-hexamer model will, when not driven, relax in an oscillatory fashion to its stable fixed point with an intrinsic frequency ω_0 (see Fig. 4.5A). To predict the latter, we note that the dynamics of Eqs. 4.8-4.13 can be written in the form $\dot{\mathbf{x}} = \mathbf{A}\mathbf{x}$, and when all rate constants are equal, $k_f \bar{s} = k_b = k_s$, the eigenvalues and eigenvectors of $\mathbf{A}$ can be computed analytically. The eigenvectors are complex exponentials. For a cycle with N sites with hopping rate k, the frequency associated with the lowest-lying eigenvalue is $k\sin(2\pi/N)$, which to leading order is $2\pi k/N$, corresponding to a period $T_0 = N/k$. Please note that this is also the period of a single multimer with N (cyclic) sites with N equal rates of hopping from one site

to the next. We therefore expect that, to a good approximation, the intrinsic frequency $\omega_0 = 2\pi/T_0$ of an ensemble of hexamers corresponds to the intrinsic period of a single hexamer:

$$T_0 \simeq \frac{2}{k_s} + \frac{6}{k_f \bar{s}} + \frac{6}{k_b} \simeq \frac{6}{k_f \bar{s}} + \frac{6}{k_b}, \tag{4.15}$$

where we recall that in the non-driven system the phosphorylation rate is $k_f \bar{s}$. We verfied that this approximation is very accurate by fitting the relaxation of $p(t)$ of the UHM to a function of the form $e^{-\gamma t}\sin(\omega_0 t)$, with $\omega_0 = 2\pi/T_0$. The intrinsic period T_0 obtained in this way is to an excellent approximation given by Eq. 4.15.

Setting the parameters

The parameters were set as follows: the conformational switching rate k_s was set to be larger than the (de)phosphorylation rates $k_s \gg \{k_f, k_b\}$, as in the original models [11, 15, 17]. This leaves for a given input noise η_s, three parameters to be optimized: the phosphorylation rate k_f, the dephosphorylation rate k_b, and the mean input signal $\bar{s}$. The product $k_f \bar{s}$ determines the mean phosphorylation rate, while k_f separately determines the strength of the forcing, i.e. the amplitude of the oscillations in the phosphoryation rate (see Eq. 4.5). The quantities $k_f \bar{s}$ and k_b together determine the intrinsic frequency $\omega_0 = 2\pi/T_0$ (see Eq. 4.15) and the symmetry of the phosphorylation cycle, set by the ratio $r \equiv k_b/(k_f \bar{s})$.

Optimal intrinsic frequency We therefore first computed for different input-noise strengths σ_s^2, the mutual information $I(p;t)$ as a function of the ratio $r = k_b/(k_f \bar{s})$ and a scaling factor q that scales both $\bar{s}$ and k_b, keeping the strength of the forcing constant at $k_f = 0.26/\text{h}$. Fig. 4.5B shows the heatmap of $I(p;t) = I(r,q)$ for $\sigma_s^2 = 1$, but qualitatively similar results were obtained for other values of σ_s^2 (as discussed below). Since the intrinsic frequency ω_0 depends on both r and q (see Eq. 4.15), we have superimposed contourlines of constant ω_0. Interestingly, the figure shows that in the relevant regime of high mutual information, $I(p;t)$ follows the contourlines of constant ω_0. This shows that $I(p;t)$ depends on r and q predominantly through $\omega_0(r,q)$, $I(p;t) \approx I(\omega_0(r,q))$. It demonstrates that the mutual information is primarly determined by the intrinsic period T_0—the time to complete a single cycle—and not by the evenness of the pace around the cycle set by r.

To reveal the dependence of $I(\omega_0)$ on σ_s^2, we show in panel C for different values of σ_s^2, $I(p;t)$ as a function of ω_0, which was varied by scaling $\bar{s}$ and k_b via the scaling factor q, keeping the ratio of $k_f \bar{s}$ and k_b constant at $r = 1$. Clearly, there is an optimal frequency $\omega_0^{\text{opt}} \approx 1.04\omega$ corresponding to an optimal $k = k_f \bar{s} = k_b = 0.52/\text{h}$, that maximizes the mutual information which is essentially independent of σ_s^2. In Fig. 2 of the main text, when we vary σ_s^2, we thus kept $k = k_f \bar{s} = k_b = 0.52/\text{h}$ constant, with $k_f = 0.26/\text{h}$ and $\bar{s} = 2$.

Interestingly, the optimal intrinsic frequency ω_0^{opt} is not equal to the driving frequency ω: $\omega_0^{\text{opt}} > \omega$, yielding an intrinsic period $T_0^{\text{opt}} \approx 23.1\text{h}$ that is smaller than 24 hrs. This can be understood by analyzing the simplest model that mimics the uncoupled-hexamer model: the (damped) harmonic oscillator, which, like the uncoupled-hexamer model, is a linear system with a characteristic frequency. As described in 4.5.2, we expect generically for such a system that the optimal intrinsic frequency is larger than the driving frequency: $\omega_0^{\text{opt}} > \omega$. This is because while the amplitude A of the output (the "signal") is maximal at resonance, $\omega_0 = \omega$ (see Eq. 4.54), input-noise averaging is maximized

(i.e. output noise σ_x minimized) for large ω_0 (see Eq. 4.59), such that the signal-to-noise ratio A/σ_x is maximal for $\omega_0^{\text{opt}} > \omega$.

Mutual information is less sensitive to coupling strength Lastly, while $k_f\bar{s}$ and k_b are vital by setting the intrinsic period T_0 (Eq. 4.15) that maximizes the mutual information (panels B and C of Fig. 4.5), we now address the importance of the coupling strength, which is set by k_f separately (see Eq. 4.5). To this end, we computed the mutual information $I(p;t)$ as a function of k_f and $\bar{s}$, keeping the dephosphorylation rate constant at $k_b = 0.52/\text{h}$. Fig. 4.5D shows the result. It is seen that there is, as in panel B, a band along which the mutual information is highest. This band coincides with the superimposed dashed white line along which $k_f\bar{s} = 0.52/\text{h}$ and hence T_0 are constant (see Eq. 4.15). This shows that the mutual information $I(p;t)$ is predominantly determined by the intrinsic period T_0: as the parameters are changed in a direction perpendiular to this line (and T_0 changes most strongly), then $I(p;t)$ falls dramatically. In contrast, along the dashed white line of constant T_0, $I(p;t)$ is nearly constant. It shows that the precise strength of the forcing, set by k_f, is not critical for the mutual information. This behavior mirrors that observed for the push-pull network. While increasing k_f increases the amplitude of the oscillations in $p(t)$, it also increases the noise, such that the signal-to-noise ratio and hence the mutual information are essentially unchanged. The same behavior is observed for the minimal model of this system, the harmonic oscillator, described in 4.5.2.

To sum up, in the simulations corresponding to Fig. 2 of the main text, we kept $k_b = k_f\bar{s} = 0.52/\text{h}$, with $\bar{s} = 2$ and $k_f = 0.26/\text{h}$.

4.4.4. COUPLED-HEXAMER MODEL: KAI SYSTEM OF *S. elongatus*

Backgroud In contrast to the cyanobacterium *Prochlorococcus* and the purple bacterium *R. palustris*, the cyanobacterium *S. elongatus* harbors all three Kai proteins, KaiA, KaiB, and KaiC, and can (therefore) exhibit self-sustained, limit-cycle oscillations [3]. The circadian system combines a transcription-translation cycle (TTC) [23–25] with a protein phosphorylation cycle (PPC) of KaiC [26], and in 2005 the latter was reconstituted in the test tube [4]. The dominant pacemaker appears to be the protein phosphorylation cycle [15, 27], although at higher growth rates the transcription-translation cycle is important for maintaining robust oscillations [15, 27]. Changes in light intensity induce a phase shift of the in-vivo clock and cause a change in the ratio of ATP to ADP levels [8]. Moreover, when these changes in ATP/ADP levels were experimentally simulated in the test tube, they induced a phase shift of the protein phosphorylation cycle which is similar to that of the wild-type clock [8]. These experiments indicate that the phosphorylation cycle is not only the dominant pacemaker, but also the cycle that couples the circadian system to the light input. We therefore focused on the protein phosphorylation cycle.

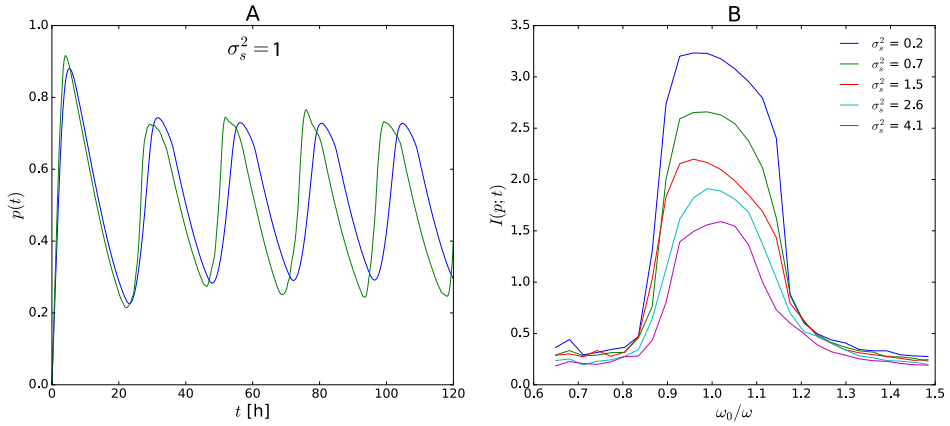

Figure 4.6: The coupled-hexamer model. (A) Time trace of $p(t)$ in the presence of driving (green line) and absence of driving (blue line). In the absence of driving, the system exhibits stable, limit-cycle oscillations. (B) The mutual information $I(p;t)$ as a function of the intrinsic frequency, which was varied by scaling all phosphorylation rates $\{k_{ps}, k_i, k_b\}$ by a factor q. It is seen that there exists an optimal (de)phosphorylation rate that maximizes $I(p;t)$, which weakly depends on σ_s^2. It corresponds to an intrinsic period $T_0 = 25.1$h of the free-running clock. The noise correlation time $\tau_c = 0.5$h.

Due to the wealth of experimental data, the in-vitro protein phosphorylation cycle of *S. elongatus* has been modeled extensively in the past decade [11–17]. In [17] we presented a very detailed thermodynamically consistent statistical-mechanical model, which is based on earlier models [11, 15, 16] and can explain most of the experimental observations. The coupled-hexamer model (CHM) presented here is a minimal version of these models. It contains the necessary ingredients for describing the autonomous protein-phosphorylation oscillations and the coupling to the light input, i.e. the ATP/ADP ratio.

The model is similar to the uncoupled-hexamer model described in the previous section, with KaiC switching between an active state in which the phosphorylation level tends to rise and an inactive in which it tends to fall. The key difference between the two systems is that the CHM also harbors KaiA, which synchronizes the oscillations of the individual hexamers via the mechanism of differential affinity [11, 12], allowing for self-sustained oscillations. Specifically, KaiA is needed to stimulate phosphorylation of active KaiC, yet inactive KaiC can bind kaiA too. Consequently, inactive hexamers that are in the dephosphoryation phase of the phosphorylation cycle—the laggards—can take away KaiA from those KaiC hexamers that have already finished their phosphorylation cycle—the front runners. These front runners are ready for a next round of phosphorylation, but need to bind KaiA for this. By strongly binding and sequestering KaiA, the laggards can thus take away KaiA from the front runners, thereby forcing them to slow down. This narrows the distribution of phosphoforms, and effectively synchronizes the phosphorylation cycles of the individual hexamers [11]. The mechanism appears to be active not only during the inactive phase, but also during the active phase: KaiA has a

higher binding affinity for less phosphorylated KaiC [11, 16]. Since KaiB serves to mainly stabilize the inactive state and mediate the sequestration of KaiA by inactive KaiC, KaiB is, as in the UHM and following [16, 17], only modelled implicitly.

Model Since computing the mutual information accurately requires very long simulations, we sought to develop a minimal version of the PPC model presented in [11, 15, 28], which can describe a wealth of data including the concentration dependence of the self-sustained oscillations and the coupling to ATP/ADP [11, 18, 28]. This model is described by the following chemical rate equations:

$$\dot{c}_0 = k_s \tilde{c}_0 - s(t) c_0 \left[k_0 \frac{A}{A+K_0} + k_{ps} \frac{K_0}{A+K_0} \right] \tag{4.16}$$

$$\dot{c}_i = s(t) c_{i-1} \left[k_{i-1} \frac{A}{A+K_{i-1}} + k_{ps} \frac{K_{i-1}}{A+K_{i-1}} \right] - s(t) c_i \left[k_i \frac{A}{A+K_i} + k_{ps} \frac{K_i}{A+K_i} \right] \quad i \in (1,\dots,5) \tag{4.17}$$

$$\dot{c}_6 = s(t) c_5 \left[k_5 \frac{A}{A+K_5} + k_{ps} \frac{K_5}{A+K_5} \right] - k_s c_6 \tag{4.18}$$

$$\dot{\tilde{c}}_6 = k_s c_6 - k_b \tilde{c}_6 \tag{4.19}$$

$$\dot{\tilde{c}}_i = k_b (\tilde{c}_{i+1} - \tilde{c}_i) \qquad i \in (1,\dots,5) \tag{4.20}$$

$$\dot{\tilde{c}}_0 = k_b \tilde{c}_1 - k_s \tilde{c}_0 \tag{4.21}$$

$$A = A_T - \sum_{j=0}^{5} c_j \frac{A}{A+K_j} - \sum_{j=0}^{6} b_j \tilde{c}_j \frac{A^{b_j}}{A^{b_j} + \tilde{K}_j^{b_j}} \tag{4.22}$$

Here, c_i and $\tilde{c}_i$ are the concentrations of active and inactive i-fold phosphorylated KaiC, A is the concentration of free KaiA. The rates k_i are the rates of KaiA-stimulated phosphorylation of active KaiC and k_{ps} is the spontaneous phosphorylation rate of active KaiC when KaiA is not bound. Please note that both rates are multiplied by the input signal $s(t)$, since both rates depend on the ATP/ADP ratio [17]. The dephosphorylation rate k_b is independent of the ATP/ADP ratio [16, 17] and hence k_b is not multiplied with $s(t)$. As in the UHM, k_s is the conformational switching rate. The last equation, Eq. 4.22, gives the concentration A of free KaiA under the quasi-equilibrium assumption of rapid KaiA (un)binding by active KaiC with affinity K_i (second term right-hand side) and rapid binding of KaiA by inactive KaiC, where each i-fold phosphorylated inactive KaiC hexamer can bind b_i KaiA dimers (last term right-hand side Eq. 4.22). The mechanism of differential affinity is implemented via two ingredients: 1) the dissociation constant of KaiA binding to active KaiC, K_i, depends on the phosphorylation level i, with less phosphorylated KaiC having a higher binding affinity: $K_i < K_{i+1}$ [11, 16, 17]; 2) inactive KaiC can strongly bind and sequester KaiA [11, 16, 17]; this is modeled by the last term in Eq. 4.22.

Autonomous oscillations Fig. 4.6A shows a time trace of $p(t)$ (Eq. 4.14) for both a driven and a non-driven coupled-hexamer model. Clearly, in contrast to the push-pull network and the uncoupled-hexamer model, this system exhibits free running simulations. Note also that the autonomous oscillations are slightly asymmetric as observed experimentally, and as shown also by the detailed models on which this minimal model

is based [11, 15]. Lastly, while the driving signal is sinusoidal, the output signal of the driven system remains non-sinusoidal. This is because this system is non-linear; this behavior is indeed in marked contrast to the behavior seen for the linear UHM (see Fig. 4.5) and that of the PPN (Fig. 4.4) which operates in the linear regime. The slight asymmetry in the oscillations also explains why in the regime of very low noise, this system has a slightly lower mutual information than that of push-pull network or the uncoupled-hexamer model, as seen in Fig. 1 of the main text.

Setting the parameters
We first set the parameters to get autonomous oscillations, keeping $s(t) = \bar{s} = 2$. These parameters were inspired by the parameters of the model upon which the current model is built [11]. Specifically, the KaiA binding affinity of active KaiC, given by K_i, was chosen such that it obeys differential affinity, $K_0 < K_1 < K_2 < K_3 < K_4 < K_5$, as in the PPC model of [11, 15, 28]. In addition, in our model, $b_i = 2$ for $i = 1,2,3,4$ and $b_i = 0$ for $i = 0,5,6$, meaning that $i = 1-4$ fold phosphorylated inactive KaiC hexamers can each bind two KaiA dimers with strong affinity $\tilde{K}_i = \tilde{K}$. The conformational switching rate k_s was set to be higher than all the (de)phosphorylation rates, $k_s >> \{k_i, k_{ps}, k_b\}$ and the values of k_i, k_{ps}, k_b were, again apart from a scaling factor to set the optimal intrinsic frequency, identical to those of the PPC model of [11, 16, 28]. These parameter values allowed for robust free-running oscillations (see Fig. 4.6A) in near quantitative agreement with the oscillations of the more detailed PPC model of [11, 16, 28].

Optimal intrinsic frequency We then studied the driven system. We varied the intrinsic frequency ω_0 of the autonomous oscillations by varying all (de) phosphorylation rates $\{k_i, k_{ps}, k_b\}$ by a constant factor and computed the mutual information $I(p;t)$ as a function of this factor and hence ω_0. The result is shown in Fig. 4.6B. Clearly, as for the uncoupled-hexamer model, there exists an optimal intrinsic frequency ω_0^{opt} that maximizes the mutual information $I(p;t)$. The optimal intrinic frequency depends on the input-noise strength: for low input noise, $\omega_0^{opt} < \omega$, but then ω_0^{opt} increases with σ_s^2 to become similar to ω in the high noise regime. We also see, however, that the dependence of ω_0^{opt} on σ_s^2 is weak (Fig. 4.6B), and we therefore kept the parameters in the simulations corresponding to Fig. 2 of the main text, constant. Lastly, we note that we have verified that, as observed for the uncoupled-hexamer model, the key parameter for optimizing $I(p;t)$ is $k_f\bar{s}$, because that sets the intrinsic frequency, and not k_f and $\bar{s}$ separately. Table 4.1 gives an overview of all the parameters; this parameter set thus corresonds to a free-running rhythm of $\omega_0^{opt} = 0.96\omega$, corresponding to an intrinsic period $T_0 = 25.1$h.

4.4.5. ROBUSTNESS OF OBSERVATIONS

We have tested the robustness of our principal result, shown in Fig. 2 of the main text, by varying a number of key parameters. We first varied the correlation time τ_c of the noise, see Fig. 4.7A. Clearly, the main result is robust to variations in the value of τ_c: in the limit of small input-noise σ_s^2 all three time-keeping systems are equally accurate, while for large input noise the bonafide clock is far superior. We have also varied the nature of the input signal. Specifically, instead of a sinusoidal signal we have also studied a truncated sinusoidal signal $s(t)$, which drops to zero for 12 hours during the night but is

a half-sinusoid for 12 hours during the day:

$$s(t) = h(t)\left\{\sin(\omega t) + \eta_s(t)\right\}, \tag{4.23}$$

where $h(t) = 0$ for $0 < t < 12$ and $h(t) = 1$ for $12 < t < 24$. The result is shown in Fig. 4.7B. It is seen that the principal result of Fig. 2 of the main text is also insensitive to the precise choice of the input signal.

The robustness of our principal observations indicate they are universal and should be observable in minimal generic models. These are described in the next sections.

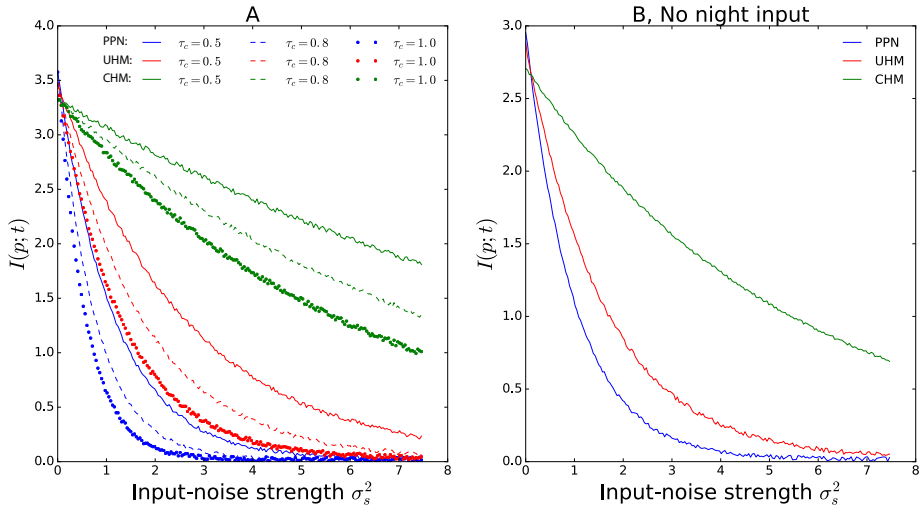

Figure 4.7: Robustness of the pricipal resut of our paper, Fig. 2 of the main text. (A) Robustness to correlation time of the input noise. It is seen that increasing the correlation time τ_c of the input noise lowers the mutual information $I(p;t)$. This is because a higher correlation time impedes noise averaging [29–31]. Yet, for all values of τ_c the result of Fig. 2 of the main text is recapitulated: when the input-noise strength σ_s^2 is low, all readout systems are equally accurate; yet, in the high noise regime, the coupled-hexamer model is superior. (B) Robustness to the shape of the input signal. Here, the input is a truncated sinusoidal signal so that during the night $s(t) = 0$, while during the day $s(t)$ is a half sinusoid (see Eq. 4.23). As expected, shutting off the driving during the night lowers the mutual information (compare with panel A). More strikingly, in the regime of low input noise, all readout systems are again equally informative on time. Clearly, the push-pull network and uncoupled-hexamer model do not need to be driven constantly; it is sufficient that the light drives the phosphorylation of the readout proteins during the day, so that they can dephosphorylate spontaneously during the night. In the regime of high input-noise, the coupled-hexamer system is again optimal. In panel B, the noise correlation time $\tau_c = 0.5$h. Other parameters are in Table 4.1.

4.4.6. COMPUTING THE MUTUAL INFORMATION

The mutual information is computed using the following relation

$$I(p;t) = H(p) - \langle H(p|t)\rangle_t. \tag{4.24}$$

where

$$H(p) = -\int_0^1 dp P(p) \log P(p) \tag{4.25}$$

is the entropy of the distribution $P(p)$ of the phosphorylation fraction $p(t)$ and

$$\langle H(p|t)\rangle_t = -\frac{1}{T}\int_0^T dt \int_0^1 dp P(p|t) \log P(p|t) \tag{4.26}$$

is the average of the conditional entropy of $P(p|t)$, with $P(p|t)$ the conditional distribution of p given t. In numerically computing the mutual information, we have verified that the results are independent of the bin size of the distribution of p, following the approach of [32]. We also note that when the input noise is exactly zero, the mutual information diverges because the system is deterministic. The highest mutual information reported corresponds to the smallest input-noise level modeled, which is non-zero, leading to a finite mutual information.

4.5. ANALYTICAL MODELS

4.5.1. PUSH-PULL NETWORK

The equation for the push-pull network is

$$\dot{x}_p = k_f s(t)(x_T - x_p(t)) - k_b x_p \tag{4.27}$$

$$\simeq k_f s(t) x_T - k_b x_p, \tag{4.28}$$

where in the last equation we have assumed that $x_T \gg x_p$, which is the case when $k_f s(t) \ll k_b$. In this regime, the push-pull network operates in the linear regime, leading to sinusoidal oscillations, which tend to enhance information transmission [19]. In what follows, we write, to facilitate comparison with other studies on noise transmission [19, 33] $\rho \equiv k_f x_T$, $\mu = k_b$ and, for notational convenience, $x_p = x$. We thus study

$$\dot{x} = \rho s(t) - \mu x(t). \tag{4.29}$$

The equation can be solved analytically to yield

$$x(t) = \int_{-\infty}^{t} dt' \chi(t-t') s(t), \tag{4.30}$$

with $\chi(t-t') = \rho e^{-\mu(t-t')}$. With the input signal given by

$$s(t) = \sin(\omega t) + \bar{s} + \eta_s(t), \tag{4.31}$$

the output is

$$x(t) = A\sin(\omega t - \phi) + \bar{x} + \eta_x(t) \tag{4.32}$$

where the amplitude is

$$A = \frac{\rho}{\sqrt{\mu^2 + \omega^2}}, \tag{4.33}$$

the phase difference of the output with the input is

$$\phi = \arctan(\omega/\mu), \tag{4.34}$$

the mean is

$$\bar{x} = \rho\bar{s}/\mu \tag{4.35}$$

and the noise is

$$\eta_x = \rho\int_{-\infty}^{t} dt' e^{-\mu(t-t')}\eta_s(t'). \tag{4.36}$$

The variance of the output, assuming the system is in steady state, is then

$$\sigma_x^2 = \langle(x(0) - \bar{x}(0))^2\rangle \tag{4.37}$$

$$= \rho^2\int_{-\infty}^{0}\int_{-\infty}^{0} dt dt' e^{\mu(t+t')}\langle\eta_s(t)\eta_s(t')\rangle. \tag{4.38}$$

Assuming that the input noise has variance σ_s^2 and decays exponentially with correlation time $\tau_c = \lambda^{-1}$, meaning that $\langle\eta_s(t)\eta_s(t')\rangle = \sigma_s^2 e^{-\lambda|t-t'|}$, the variance of the output is

$$\sigma_x^2 = \rho^2\sigma_s^2\left[\int_{-\infty}^{0}\int_{-\infty}^{t} dt dt' e^{\mu(t+t')}e^{-\lambda(t-t')} + \right. \tag{4.39}$$

$$\left.\int_{-\infty}^{0}\int_{t}^{0} dt dt' e^{\mu(t+t')}e^{+\lambda(t-t')}\right] \tag{4.40}$$

$$= g^2\frac{\mu}{\mu+\lambda}\sigma_s^2, \tag{4.41}$$

with the gain given by $g \equiv \rho/\mu$.

The signal-to-noise ratio A/σ_x is then

$$\frac{A}{\sigma_x} = \sqrt{\frac{\mu(\mu+\lambda)}{\mu^2+\omega^2}}\frac{1}{\sigma_s}, \tag{4.42}$$

which has a maximum at the optimal relaxation rate [19]

$$\mu^{\text{opt}} = \frac{\omega^2}{\lambda}\left(1 + \sqrt{1 + (\lambda/\omega)^2}\right). \tag{4.43}$$

This optimum arises from a trade-off between the amplitude, which increases as μ increases, and input-noise averaging, which improves as μ decreases. Another point to note is that the optimal signal-to-noise ratio does not depend on $\rho = k_f x_T$, and hence not on k_f and x_T: while increasing ρ increases the amplitude of the signal, it also amplifies the noise in the input signal. Increasing the gain ρ (via x_T and/or k_f) only helps in the presence of intrinsic noise, because increasing the amplitude of the signal helps to raise the signal above the intrinsic noise [19]. However, in the deterministic models considered in this study, the intrinsic noise is zero.

4.5.2. THE HARMONIC OSCILLATOR AND THE UNCOUPLED-HEXAMER MODEL

The uncoupled-hexamer model (UHM) is linear. Moreover, because each hexamer has a phosphorylation cycle with a characteristic oscillatino frequency ω_0, this system is akin to the harmonic oscillator. Indeed, when not driven, both the UHM and the harmonic oscillator relax in an oscillatory fashion to a stable fixed point. To develop intuition on the behavior of the UHM, we therefore here analyze the behavior of a harmonic oscillator driven by a noisy sinusoidal signal.

The equation of motion of the driven harmonic oscillator is

$$\ddot{x} + \omega_0^2 x + \gamma \dot{x} = \rho s(t), \tag{4.44}$$

where ω_0 is the characteristic frequency, γ is the friction and ρ describes the strength of the coupling to the input signal $s(t)$. We assume that $s(t) = \sin(\omega t) + \eta_s(t)$. We note that while the undriven harmonic oscillator is isomorphic to the undriven UHM, their coupling to the input is different: in the UHM, the hexamers are, motivated by the Kai system [8, 9], only coupled to the input during their active phosphorylation phase, while the harmonic oscillator is coupled continuously; moreover, in the harmonic oscillator the noise is additive, while in the UHM the signal multiplies the phosphorylation rate, leading to multiplicative noise. Yet, the behavior of the two models is qualitatively similar, as discussed below.

Solving Eq. 4.44 in Fourier space yields $\tilde{x}(\omega) = \tilde{\chi}(\omega)\tilde{s}(\omega)$, with

$$\tilde{\chi}(\omega) = \frac{\rho}{\omega_0^2 - \omega^2 - i\omega\gamma}. \tag{4.45}$$

Hence, the time evolution of $x(t)$ is

$$x(t) = \frac{1}{2\pi}\int_{-\infty}^{\infty} d\omega e^{-i\omega t}\tilde{\chi}(\omega)s(\omega) \tag{4.46}$$

$$= \frac{\rho}{2\pi}\int_{-\infty}^{\infty} d\omega \int_{-\infty}^{\infty} dt' \frac{e^{i\omega(t'-t)}s(t')}{\omega_0^2 - \omega^2 - i\omega\gamma}. \tag{4.47}$$

We do the integral over ω first. The integrand has poles at

$$\omega = \frac{-i\gamma}{2} \pm \sqrt{\omega_0^2 - \frac{\gamma^2}{4}} \equiv \frac{-i\gamma}{2} \pm \omega_1. \tag{4.48}$$

This yields

$$x(t) = \frac{\rho}{2\pi}\int_{-\infty}^{\infty} s(t')\theta(t-t')(2\pi i)\times \tag{4.49}$$

$$\left[\frac{e^{i(-i\frac{\gamma}{2}+\omega_1)(t'-t)}}{2\omega_1} - \frac{e^{i(-i\frac{\gamma}{2}-\omega_1)(t'-t)}}{2\omega_1}\right] \tag{4.50}$$

$$= \frac{\rho}{\omega_1}\int_{-\infty}^{t} dt' e^{-\frac{\gamma}{2}(t-t')}\sin(\omega_1(t-t'))s(t'). \tag{4.51}$$

With $s(t) = \sin(\omega t)$, this yields

$$x(t) = \frac{-\gamma\omega\cos[\omega t] + (-\omega^2 + \omega_0^2)\sin[\omega t]}{\gamma^2\omega^2 + (\omega^2 - \omega_0^2)^2} \tag{4.52}$$

This can also be rewritten as

$$x(t) = A\sin(\omega t + \phi), \tag{4.53}$$

with the amplitude given by

$$A = \frac{\rho}{\sqrt{\gamma^2\omega^2 + (\omega^2 - \omega_0^2)^2}} \tag{4.54}$$

and the phase given by

$$\phi = \arctan\left[\frac{-4\gamma\omega}{\gamma^2 + 4(\omega_1^2 - \omega^2)}\right]. \tag{4.55}$$

Eq. 4.54 shows that the amplitude increases as the friction decreases and that the amplitude is maximal when the intrinsic frequency equals the driving frequency; in fact, when $\gamma \to 0$ and $\omega_0 = \omega$, the amplitude diverges.

With an input noise with variance σ_s^2 and decay rate λ, the noise in the output, $\sigma_x^2 = \langle \delta x^2(0) \rangle$, is given by

$$\sigma_x^2 = \frac{\rho^2}{\omega_1^2}\int_{-\infty}^{0} dt \int_{-\infty}^{0} dt' e^{\frac{\gamma}{2}(t+t')}\sin(\omega_1 t)\sin(\omega_1 t')\langle \eta_s(t)\eta_s(t')\rangle \tag{4.56}$$

$$= \frac{\rho^2\sigma_s^2}{\omega_1^2}\left[\int_{-\infty}^{0} dt \int_{-\infty}^{t} dt' e^{\frac{\gamma}{2}(t+t')}\sin(\omega_1 t)\sin(\omega_1 t)e^{-\lambda(t-t')}\right.$$

$$\left. + \int_{-\infty}^{0} dt \int_{t}^{0} dt' e^{\frac{\gamma}{2}(t+t')}\sin(\omega_1 t)\sin(\omega_1 t')e^{-\lambda(t'-t)}\right] \tag{4.57}$$

$$= \rho^2\sigma_s^2 \frac{16(\gamma+\lambda)}{\gamma[(\gamma+2\lambda)^2 + 4\omega_1^2](\gamma^2 + 4\omega_1^2)} \tag{4.58}$$

$$= \rho^2\sigma_s^2 \frac{(\gamma+\lambda)}{\gamma\omega_0^2[\lambda(\gamma+\lambda) + \omega_0^2]} \tag{4.59}$$

This expression shows that the noise diverges for all frequencies when the friction $\gamma \to 0$. It also shows that the noise diverges for $\omega_0 \to 0$ for all values of γ, or, conversely, that it goes to zero for $\omega_0 \to \infty$. This can be understood by imagining a particle with mass $m = 1$ in a harmonic potential well with spring constant k, giving a resonance frequency $\omega_0^2 = k/m = k$, which is buffeted by stochastic forces: its variance decreases as the spring constant k and intrinsic frequency ω_0 increase.

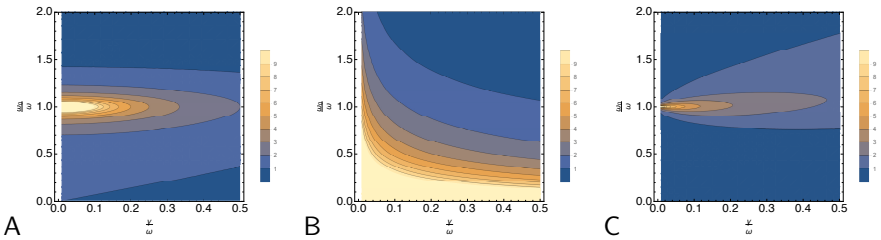

Figure 4.8: The amplitude (A), standard deviation σ_x (B), and signal-to-noise ratio A/σ_x (C) as a function of the the intrinsic frequency ω_0 and friction γ for the harmonic oscillator. It is seen that the amplitude peaks when $\gamma = 0$ and the intrinsic frequency equals the driving frequency, $\omega_0 = \omega$ (A). The noise peaks at $\gamma = 0$ and at $\omega_0 = 0$ (B). Because the amplitude peaks at $\omega_0 = \omega$, while the noise peaks at $\omega_0 = 0$, there is an optimal intrinsic frequency $\omega_0^{\text{opt}} > \omega$ that maximizes the signal-to-noise ratio (C). See also Fig. 4.9.

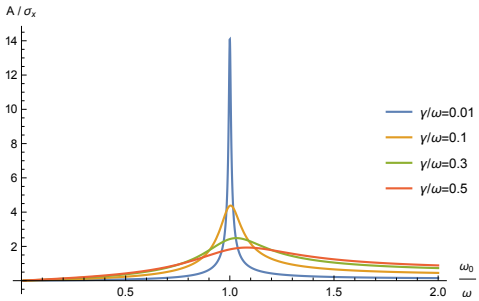

Figure 4.9: The signal-to-noise A/σ_x of the harmonic oscillation as a function of ω_0 for different values of γ. Because the amplitude A exhibits a strong maximum at $\omega_0 = \omega$, the SNR peaks around $\omega_0 = \omega$. However, the maximum is not precisely at $\omega_0 = \omega$, because the noise σ_x peaks at $\omega_0 = 0$ and not at $\omega_0 = \omega$. Depending on the friction, there thus exists an optimal intrinsic frequency $\omega_0^{\text{opt}} > \omega$. Note also that when $\omega \neq \omega_0$, it is actually beneficial to have friction, $\gamma \neq 0$.

Figs. 4.8 and 4.9 show the amplitude A, noise σ_x^2, and signal-to-noise ratio A/σ_x for the harmonic oscillator. Clearly, the amplitude is maximal at resonance, diverging when $\gamma \to 0$ (Fig. 4.8A). The noise is maximal at $\omega_0 \to 0$, and also diverges for all frequencies when $\gamma \to 0$ (Fig. 4.8B). However, the amplitude rises more rapidly as $\gamma \to 0$ than the noise does, leading to a global optimum of the signal-to-noise ratio for $\omega_0 = \omega$ and $\gamma \to 0$ (Fig. 4.8C). However, biochemical networks have, in general, a finite friction, and then the optimal intrinsic frequency is off resonance, as most clearly seen in Fig. 4.9. In fact, since the noise is minimized for $\omega_0 \to \infty$ while the amplitude is maximized at resonance, $\omega_0 = \omega$, the optimal frequency ω_0^{opt} that maximizes the signal-to-noise ratio is in general $\omega_0^{\text{opt}} > \omega$, as indeed also observed for the uncoupled hexamer model (see Fig. 4.5B).

Because noise is commonly modeled as Gaussian white noise, as in our Stuart-Landau model below, rather than colored noise as assumed here, we also give, for completeness, the expression for σ_x^2 when the input noise is Gaussian and white, $\langle \eta_s(t)\eta_s(t')\rangle =$

$\sigma^2_{s,\text{white}}\delta(t-t')$. It is

$$\sigma_x^2 = \frac{\rho^2\sigma^2_{s,\text{white}}}{2\gamma\omega_0^2}. \tag{4.60}$$

This is consistent with Eq. 4.59, by noting that the integrated noise strength of the colored noise is $2\int_0^\infty dt\sigma_s^2 e^{-\lambda t} = 2\sigma_s^2/\lambda$, while the integrated noise strength of the white noise case is $\sigma^2_{s,\text{white}}$. Indeed, with this identification, Eq. 4.59 in the limit of large λ reduces to the above expression for the white noise case.

4.5.3. COMPARISON BETWEEN PUSH-PULL NETWORK AND HARMONIC OSCILLATOR IN THE HIGH FRICTION LIMIT

Intuitively, one would expect that in the high-friction limit the harmonic oscillator performs similarly to the push-pull network. The signal-to-noise ratio SNR = A/σ_x indeed becomes the same in this limit. However, the amplitude and the noise separately scale differently, because the friction in the harmonic oscillator also reduces the strength of the signal and the noise: in the high-friction limit, the equation of motion of the harmonic oscillator becomes $\dot{x}_{\text{HO}} = \rho s(t)/\gamma - \omega_0^2/\gamma x(t) + \rho\eta_s(t)/\gamma$, showing that the friction renormalizes both the signal and the noise. However, such a renormalization of both the signal and the noise should not affect the signal-to-noise ratio. Moreover, we now see that in this high-friction limit the harmonic oscillator relaxes with a rate ω_0^2/γ, which is to be compared with μ of the push-pull network, for which $\dot{x}_{\text{PP}} = \rho s(t) - \mu x(t) + \rho\eta_s(t)$. From this we can anticipate that while the amplitude and the noise will be different, the signal-to-noise ratio will be the same. Concretely, in the high-friction limit the amplitude, the noise and the signal-to-noise ratio of the harmonic oscillator become

$$A^{\text{HO}} = \frac{\rho}{\gamma\omega} \tag{4.61}$$

$$\sigma_x^{\text{HO}} = \frac{\rho\sigma_s}{\omega_0\sqrt{\gamma\lambda}} \tag{4.62}$$

$$\text{SNR}^{\text{HO}} = \sqrt{\frac{\omega_0^2}{\gamma}}\frac{\sqrt{\lambda}}{\omega} = \frac{\sqrt{\mu\lambda}}{\omega}, \tag{4.63}$$

where in the last line we have made the identification $\mu = \omega_0^2/\gamma$. For the push-pull network, the corresponding quantities, in the limit that $\mu \to 0$, are

$$A^{\text{PP}} = \frac{\rho}{\mu} \tag{4.64}$$

$$\sigma_x^{\text{PP}} = \frac{\rho\sigma_s}{\mu\lambda} \tag{4.65}$$

$$\text{SNR}^{\text{PP}} = \frac{\sqrt{\mu\lambda}}{\omega}. \tag{4.66}$$

Clearly, the signal-to-noise ratio of the two models are the same in the limit of high friction.

Fig. 4.10 compares the behaviour of the harmonic oscillator against that of the push-pull system. Clearly, for small γ, the signal-to-noise ratio SNR of the harmonic oscillator is larger than that of the push-pull network, showing that building an oscillatory tendency with a resonance frequency into a readout system can enhance the signal-to-noise ratio. However, in the large-friction limit, the SNR is the same of both models, as expected.

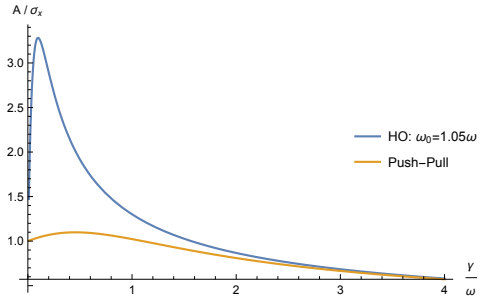

Figure 4.10: The signal-to-noise A/σ_x as a function of γ for the harmonic oscillator and the push-pull network. For the harmonic oscillator, the friction is varied, while ω_0 is kept constant; for the push-pull network μ is varied according to $\mu = \omega_0^2/\gamma$. It is seen that for low and intermediate friction the harmonic oscillator outperforms the push-pull network, but that in the high-friction limit they perform similarly.

4.5.4. WEAKLY NON-LINEAR OSCILLATOR AND THE COUPLED-HEXAMER MODEL

The coupled-hexamer model (CHM) is a non-linear oscillator that can sustain autonomous limit-cycle oscillations in the absence of any driving. Here, we describe the Stuart-Landau model, which provides a universal description of a weakly non-linear system near the Hopf bifurcation where a limit cycle appears. We use it to analyze the time-keeping properties of a system as it is altered from essentially a damped linear oscillator to a weakly non-linear oscillator, see Fig. 3 of the main text. Our treatment follows largely that of Pikovsky *et al.* [22].

THE AMPLITUDE EQUATION

We consider the weakly non-linear oscillator [22]:

$$\ddot{x} + \omega_0^2 x = f(x, \dot{x}) + \rho s(t), \tag{4.67}$$

with $s(t) = \sin(\omega t) + \bar{s} + \eta_s$ being the driving signal as before. The quantity $f(x, \dot{x})$ describes the non-linearity of the autonomous oscillator and the parameter ρ controls the strength of the forcing. The description presented below is valid in the regime where the non-linearity $f(x, \dot{x})$ is small and the strength of the driving, quantified by ρ, is small. We begin by developing the formalism in the deterministic limit $\eta_s = 0$, in which $s(t)$ is periodic with period $T = 2\pi/\omega$, before returning to the effects of noisy driving. In contrast to previous sections, our discussion here is limited to input noise that is not only Gaussian but white, $\langle \eta_s(t) \rangle = 0$ and $\langle \eta_s(t)\eta_s(t') \rangle = \sigma_s^2 \delta(t - t')$.

Eq. 4.67 is close to that of a linear oscillator. We therefore expect that its solution has a nearly sinusoidal form. Moreover, we expect at least over some parameter range the frequency of the system is entrained by that of the driving signal. We therefore write the solution as

$$x(t) = \mathrm{Re}\left[A(t)e^{i\omega t}\right] = \frac{1}{2}\left(A(t)e^{i\omega t} + \text{c.c.}\right), \tag{4.68}$$

where c.c. denotes complex conjugate. The above equation has the form of an harmonic oscillation with frequency ω, but with a time-dependent complex amplitude $A(t)$. We emphasize that the observed frequency may deviate from ω, when the amplitude $A(t)$ rotates in the complex plane.

The above equation determines only the real part of the complex number $A(t)e^{i\omega t}$. To fully specify $A(t)$, we also need to set the imaginary part of $A(t)e^{i\omega t}$, which we choose to do via

$$y(t) = -\omega \mathrm{Im}\left[A(t)e^{i\omega t}\right] = \frac{1}{2}\left(i\omega A(t)e^{i\omega t} + \text{c.c.}\right) \tag{4.69}$$

$$= \dot{x}. \tag{4.70}$$

The relation $y(t) = \dot{x}$ thus specifies the imaginary part of the amplitude $A(t)$. Hence, the complex amplitude can be written as

$$A(t)e^{i\omega t} = x(t) - i\,y(t)/\omega. \tag{4.71}$$

Writing $A(t) = R(t)e^{i\phi(t)}$, it can be verified that

$$x(t) = R(t)\cos(\phi(t) + \omega t) \tag{4.72}$$

$$y(t) = -\omega R(t)\sin(\phi(t) + \omega t) \tag{4.73}$$

$$R^2(t) = x^2(t) + y^2(t)/\omega^2, \tag{4.74}$$

and that the specification $\dot{x}(t) = y(t)$ implies that

$$\frac{\dot{R}(t)}{R(t)} = \dot{\phi}(t)\tan(\phi(t) + \omega t). \tag{4.75}$$

Eq. 4.73 shows that the time derivative of $y(t)$ is

$$\begin{aligned}\dot{y} &= -\omega^2 x \\ &\quad - \omega\left[\dot{R}(t)\sin(\phi(t) + \omega t) + R(t)\dot{\phi}(t)\cos(\phi(t) + \omega t)\right]\end{aligned} \tag{4.76}$$

On the other hand, we know that

$$\begin{aligned}i\omega\dot{A}e^{i\omega t} &= -\omega\left[\dot{R}(t)\sin(\phi(t) + \omega t) + R(t)\dot{\phi}(t)\cos(\phi(t) + \omega t)\right] \\ &\quad + i\omega\left[\dot{R}(t)\cos(\phi(t) + \omega t) - R(t)\dot{\phi}(t)\sin(\phi(t) + \omega t)\right] \qquad (4.77) \\ &= \dot{y} + \omega^2 x. \qquad (4.78)\end{aligned}$$

where in Eq. 4.77 we have exploited that the imaginary part is zero because of Eq. 4.75. Combing the above equation with Eq. 4.67, noting that $\dot{y} = \ddot{x}$, yields the following equation for the time evolution of the amplitude:

$$\dot{A} = \frac{e^{-i\omega t}}{i\omega}\left[(\omega^2 - \omega_0^2)x + f(x,y) + \rho s(t)\right]. \tag{4.79}$$

AVERAGING

The above transformation is exact. To make progress, we will use the method of averaging [34]. Specifically, we will time average Eq. 4.79 over one period T [22, 34]. Averaging the driving $e^{-i\omega t}s(t)/(i\omega)$ yields the complex constant $E/(2\omega)$. The second term of Eq. 4.79 can be expanded in polynomials of $x(t) = (1/2)\mathrm{Re}A(t)e^{i\omega t}$ and $y(t) = (1/2)\mathrm{Im}A(t)e^{i\omega t}$, yielding powers of the type $(A(t)e^{i\omega t})^n(A^*(t)e^{-i\omega t})^m$. After multiplying with $e^{-i\omega t}$ and averaging over one period T, only the terms with $m = n-1$ do not vanish. Consequently, the terms that remain after averaging have the form $g(|A|^2)A$, with an arbitrary function g. For small amplitudes only the linear term proportional to A and the first non-linear term, $\propto |A|^2A$ term are important. Finally, averaging the first term of Eq. 4.79 yields a term linear in A.

Summing it up, the time evolution of the amplitude of the system with deterministic driving ($\eta_s = 0$) is given by [22]

$$\dot{A} = -i\frac{\omega^2-\omega_0^2}{2\omega}A + \alpha A - (\beta + i\kappa)|A|^2A - \frac{\rho}{2\omega}E \tag{4.80}$$

The parameters have a clear interpretation. The parameters α and β describe, respectively, the linear and non-linear growth or decay of oscillations. To have stable oscillations, both in the presence and absence of driving, large amplitude oscillations dominated by the non-linear term need to decay, which means that β must be positive, $\beta > 0$; this parameter is fixed in all our calculations. The parameter that allows us to alter the system from one that shows damped oscillations in the absence of driving to one that can generate autonomous oscillations which do not rely on forcing, is α. For the system to sustain free-running oscillations, small amplitude oscillations, dominated by the linear term, must grow, meaning that α must be positive, $\alpha > 0$. The case with $\alpha > 0$ thus describes a system that can perform stable limit cycle oscillations, making it a bonafide clock. The case $\alpha < 0$ describes a system that in the absence of any driving, $E = 0$, relaxes in an oscillatory fashion to a stable fixed point with $A = 0$. In the presence of weak driving, the amplitude A at the fixed point will be non-zero but small, making the effect of the non-linearity weak. The case $\alpha < 0$ thus describes a system that is effectively a damped harmonic oscillator, which only displays sustained oscillations when forced by an oscillatory signal. This system mimics the uncoupled-hexamer model.

The parameter κ describes the non-linear dependence of the oscillation frequency on the amplitude. For the isochronous scenario in which the phase moves with a constant velocity, $\kappa = 0$, which is what we will assume henceforth.

Defining the parameter $\nu \equiv (\omega^2-\omega_0^2)/(2\omega)$ and the parameter $\epsilon \equiv \rho/(2\omega)$, we can then rewrite the above equation as

$$\dot{A} = -i\nu A + \alpha A - \beta|A|^2A - \epsilon E, \tag{4.81}$$

where A is the complex time-dependent amplitude, E is a complex constant, and ν, α, and β are real constants. Eq. 4.81 is Eq. 2 of the main text. It provides a universal description of a driven weakly non-linear system near the Hopf bifurcation where the limit cycle appears [22].

To model the input noise we will add the noise term to Eq. 4.81:

$$\dot{A} = -i\nu A + \alpha A - \beta|A|^2A - \epsilon E + \rho\bar{\eta}_s(t), \tag{4.82}$$

where $\bar{\eta}_s(t)$ is the noise $\eta_s(t)$ averaged over one period of the driving:

$$\bar{\eta}_s(t) \equiv \frac{1}{T}\int_{t-T/2}^{t+T/2} dt' \frac{e^{-i\omega t'}}{i\omega}\eta_s(t'). \tag{4.83}$$

Since $\eta_s(t)$ is real but its pre-factor $e^{-i\omega t}/i\omega$ is complex, $\bar{s}(t)$ is, in general, complex. Below we will describe the characteristics of the noise $\bar{\eta}_s$.

LINEAR-NOISE APPROXIMATION

Scenarios By varying α we will interpolate between two scenarios: the damped oscillator, modelling the UHM, with $\alpha < 0$, and the weakly non-linear oscillator that can sustain free-running oscillations, modelling the CHM, with $\alpha > 0$. For the system with $\alpha < 0$, the amplitude of $x(t)$ when not driven is $A = 0$: the system comes to a standstill. When the system is driven, the amplitude will be nonzero, but constant since the system is essentially linear as described above. For the system with $\alpha > 0$, $A(t)$ can exhibit distinct types of dynamics, depending on the strength of driving and the frequency mismatch characterized by ν [22]. However, here we do not consider the regimes that $A(t)$ rotates in the complex plane; we will limit ourselves to the scenario that $A(t) = A$ is constant, meaning that ν cannot be too large [22].

Overview Before we discuss the linear-noise approximation in detail, we first give an overview. The central observation is that both for the driven damped oscillator with $\alpha < 0$ and the driven limit-cycle oscillator with $\alpha > 0$, the complex amplitude A is constant, corresponding to a stable fixed point of the amplitude equation, Eq. 4.81. In the spirit of the linear-noise approximation used to calculate noise in biochemical networks, we then expand around the fixed point to linear order, and evaluate the noise at the fixed point. This approach thus assumes that the distribution of the variables of interest is Gaussian, centred at the fixed point. More concretely, we first expand $A(t)$ to linear order around its stable fixed point, which is obtained by setting $\dot{A}$ in Eq. 4.81 to zero. This makes it possible to compute the variance of A. Importantly, this variance is that of a Gaussian distribution in the frame that co-rotates with the driving, as can be seen from Eqs. 4.72 and 4.73. To obtain the variance of x and y in the original frame, we then transform this distribution back to original frame of x and y. If we can make this transformation linear, then it is guaranteed that the distribution of x and y will also be Gaussian. As we will see, the transformation can be made linear by writing A as $A = u + iv$, where u and v are the real and imaginary parts of A, respectively.

Expanding A around its fixed point We write $A(t) = u(t) + iv(t)$. Eq. 4.82 then yields for the real and imaginary part of $a(t)$:

$$\dot{u} = \nu v + \alpha u - \beta(u^2 + v^2)u - \epsilon e_u + \rho\bar{\eta}_u \tag{4.84}$$

$$\dot{v} = -\nu u + \alpha v - \beta(u^2 + v^2)v - \epsilon e_v + \rho\bar{\eta}_v \tag{4.85}$$

Here, $\bar{\eta}_u$ and $\bar{\eta}_v$ are the real and imaginary parts of the averaged noise $\bar{\eta}_s$, given by Eq. 4.83; they are discussed below. The quantities e_u and e_v are the real and imaginary parts of the driving E. Their respective values depend on the phase of the driving, which is arbitrary and can be chosen freely. For example, when the driving is $s(t) = \sin(\omega t)$, then $e_u = 1$ and $e_v = 0$, while if the signal is $s(t) = \cos(\omega t)$, then $e_u = 0$ and $e_v = 1$.

We now expand $u(t)$ and $v(t)$ around their steady-state values, u^* and v^*, respectively. Inserting this in the above equations and expanding up to linear order yields

$$\dot{\delta u} = c_1 \delta u + c_2 \delta v + \rho \bar{\eta}_u \tag{4.86}$$

$$\dot{\delta v} = c_3 \delta u + c_4 \delta v + \rho \bar{\eta}_v, \tag{4.87}$$

with

$$c_1 = \alpha - \beta(3u^{*2} + v^{*2}) \tag{4.88}$$

$$c_2 = \nu - \beta 2u^* v^* \tag{4.89}$$

$$c_3 = -\nu - \beta 2u^* v^* \tag{4.90}$$

$$c_4 = \alpha - \beta(u^{*2} + 3v^{*2}). \tag{4.91}$$

The fixed points u^* and v^* are obtained by solving the cubic equations Eqs. 4.84 and 4.85 in steady state.

Noise characteristics We next have to specify the noise characteristics of $\bar{\eta}_u(t)$ and $\bar{\eta}_v(t)$. Eq. 4.83 reveals that the noise terms are given by

$$\bar{\eta}_u(t) = -\frac{1}{\omega T} \int_{t-T/2}^{t+T/2} dt' \sin(\omega t') \eta_s(t') \tag{4.92}$$

$$\bar{\eta}_v(t) = -\frac{1}{\omega T} \int_{t-T/2}^{t+T/2} dt' \cos(\omega t') \eta_s(t'). \tag{4.93}$$

The method of averaging [35] reveals that to leading order the statistics of these quantities can be approximated by

$$\langle \bar{\eta}_u(t) \bar{\eta}_u(t') \rangle = \langle \bar{\eta}_v(t) \bar{\eta}_v(t') \rangle = \frac{\sigma_s^2}{2\omega^2} \delta(t - t') \tag{4.94}$$

$$\langle \bar{\eta}_u(t) \bar{\eta}_v(t') \rangle = 0. \tag{4.95}$$

Variance-co-variance From here, there are (at least) three ways to obtain the variance and co-variance matrix of u and v. Since the system is linear, it can be directly solved in the time domain. Another route is via the power spectra [30, 36]. Here, we obtain it from [37]

$$\mathbf{A}\mathbf{C}_{uv} + \mathbf{C}_{uv}\mathbf{A}^{\mathrm{T}} = -\mathbf{D}_{uv}. \tag{4.96}$$

The matrix $\mathbf{C}_{uv}$ is the variance-covariane matrix with elements $\sigma_{uu}^2, \sigma_{uv}^2, \sigma_{vu}^2, \sigma_{vv}^2$ and $\mathbf{A}$ is the Jacobian of Eqs. 4.86 and 4.87 with elements $A_{11} = c_1, A_{12} = c_2, A_{21} = c_3, A_{22} = c_4$. The matrix $\mathbf{D}_{uv}$ is the noise matrix of $\langle \bar{\eta}_{u/v}^2 \rangle$, where we absorb the coupling strength $\rho = 2\omega\epsilon$ (cf. Eq. 4.81) in the noise strength:

$$\mathbf{D}_{uv} = \begin{pmatrix} 2\epsilon^2\sigma_s^2 & 0 \\ 0 & 2\epsilon^2\sigma_s^2 \end{pmatrix}. \tag{4.97}$$

Transforming back The variance-covariance matrix $\mathbf{C}_{uv}$, with elements $\sigma_{uu}^2, \sigma_{uv}^2, \sigma_{vu}^2, \sigma_{vv}^2$, characterizes a Gaussian distribution in the complex plane

$$P(u, v) = \frac{1}{2\pi\sqrt{|\mathbf{C}_{uv}|}} e^{-\frac{1}{2}\mathbf{a}^{\mathrm{T}}\mathbf{C}_{uv}^{-1}\mathbf{a}}, \tag{4.98}$$

where $|\mathbf{C}_{uv}|$ is the determinant of the variance-covariance matrix $\mathbf{C}_{uv}$ and $\mathbf{C}_{uv}^{-1}$ is the inverse of $\mathbf{C}_{uv}$, and $\mathbf{a}$ is a vector with elements $\delta u, \delta v$ (the deviations of the real and imaginary parts of $A = a$ from their respective fixed points u^* and v^*) with $\mathbf{a}^{\mathrm{T}}$ its transpose. This distribution $P(u, v)$ defines a distribution in the co-rotating frame of the oscillator in the complex plane. To obtain $P(x, y)$ in the original non-co-rotating frame, we need to rotate this distribution. Eq. 4.71 shows that the corresponding rotation is described by

$$x(t) = u\cos(\omega t) - v\sin(\omega t) \tag{4.99}$$

$$y(t) = -\omega u\sin(\omega t) - \omega v\cos(\omega t), \tag{4.100}$$

which defines the rotation matrix

$$\mathbf{Q} = \begin{pmatrix} \cos(\omega t) & -\sin(\omega t) \\ -\omega\sin(\omega t) & -\omega\cos(\omega t) \end{pmatrix} \tag{4.101}$$

such that $\mathbf{z} = \mathbf{Qa}$, with $\mathbf{z}$ the vector with elements $\delta x(t) = x(t) - x^*(t), \delta y(t) = y(t) - y^*(t)$, where x^*, y^* are the rotating "fixed" points of $x(t)$ and $y(t)$, i.e. their time-dependent mean values, given by Eqs. 4.99 and 4.100 with $u = u^*$ and $v = v^*$. Hence, the distribution of interest is given by

$$P(x, y|t) = \frac{1}{2\pi\sqrt{|\mathbf{C}_{xy}|}} e^{-\frac{1}{2}\mathbf{z}^{\mathrm{T}}\mathbf{C}_{xy}^{-1}\mathbf{z}}, \tag{4.102}$$

where

$$\mathbf{C}_{xy}^{-1} = [\mathbf{Q}^{-1}]^{\mathrm{T}}\mathbf{C}_{uv}^{-1}\mathbf{Q}^{-1} \tag{4.103}$$

and its inverse $\mathbf{C}_{xy}$ is the variance-covariance matrix for x, y, with elements $\sigma_{xx}^2(t), \sigma_{xy}^2(t), \sigma_{yx}^2(t), \sigma_{yy}^2(t)$, which depend on time because $\mathbf{Q}$ depends on time.

Mutual information $I(p; t)$ Lastly, the oscillations in the phosphorylation $p(t)$ of the hexamer models correspond to the oscillations in $x(t)$ in the Stuart-Landau model. We therefore need to compute the mutual information $I(x; t)$, not $I(x, y; t)$. Specifically, we calculate the mutual information from

$$I(x, t) = H(x) - \langle H(x|t)\rangle_t, \tag{4.104}$$

where the entropy $H(x) = -\int dx P(x)\log P(x)$ with $P(x) = 1/T\int_0^T dt P(x|t)$ and the conditional entropy $H(x|t) = -1/T\int_0^T dt\int dx P(x|t)\log P(x|t)$, with $P(x|t) = 1/\sqrt{2\pi\sigma_{xx}^2(t)}e^{-(x(t)-x^*(t))^2/(2\sigma_{xx}^2(t))}$. We emphasize that both the variance $\sigma_{xx}^2(t)$ and the average $x^*(t)$ depend on time.

Summing up Approach and Parameters Fig. 3 main text To sum up the procedure, to compute the noise in $A = a$ we first need to obtain the steady state values of its real and imaginary part, $\bar{u}$ and $\bar{v}$ (see Eqs. 4.88-4.91). These are obtained from setting the time derivatives of $u(t)$ and $v(t)$ in Eqs. 4.84 and 4.85 to zero; this involves solving a cubic equation, which we do numerically. We then compute the variance-covariance matrix $\mathbf{C}_{uv}$ via Eq. 4.96, where the elements of the Jacobian $\mathbf{A}$ are given by Eqs. 4.88-4.91 and the

noise matrix $\mathbf{D}_{uv}$ is given by Eq. 4.97. After having obtained $\mathbf{C}_{uv}$, we find the variance-covariance matrix for x and y, $\mathbf{C}_{xy}$, from Eq. 4.103. For Fig. 3 of the main text, $\nu = 0$, $\beta = \omega$, $\epsilon = 0.5\omega$.

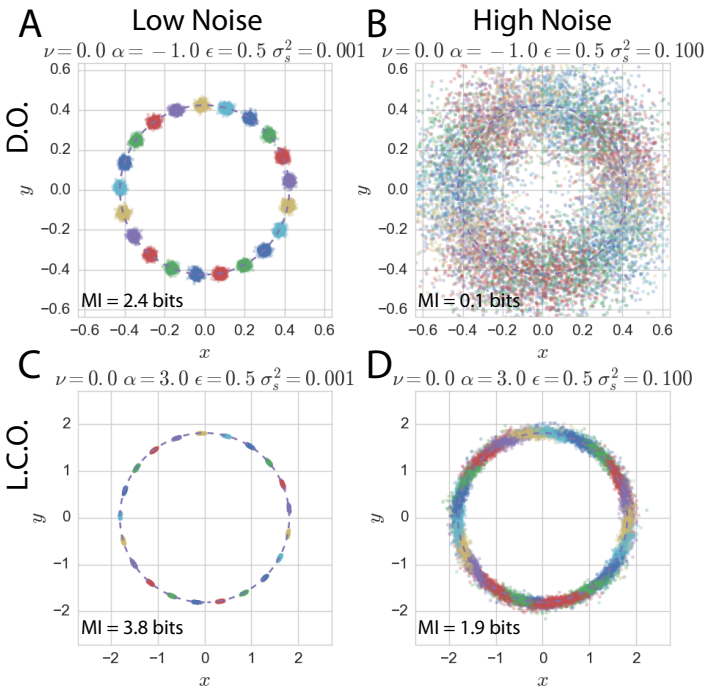

Figure 4.11: The dynamics of the Stuart-Landau model when $\alpha = -\omega$, corresponding to a damped oscillator (D.O., top row), and when $\alpha = 3\omega$, corresponding to a limit-cycle oscillator (L.C.O.,bottom row), both for low input noise, $\sigma_s^2 = 0.001$ (left column) and high input noise, $\sigma_s^2 = 0.1$ (right column). Dashed line denotes the mean trajectory of (x, y), and the points are samples of (x, y) from the distribution $P(x, y|t_i)$ for evenly spaced time points t_i; $P(x, y|t)$ is given by Eq. 4.102 and points belonging to the same time have the same color. It is seen that when the input noise is low, the distributions corresponding to the different times are still well separated, both for the limit-cycle oscillator and the damped oscillator. Yet, for high noise, only for the L.C.O. are the distributions still reasonably separated, leading to a mutual information that is still close to 2 bits. In contrast, for the D.O., the distributions are mixed, leading to a low mutual information close to zero.

COMPARING LIMIT CYCLE OSCILLATOR WITH DAMPED OSCILLATOR

Fig. 3 of the main text shows that the mutual information $I(x;t)$ increases with α, especially when the input noise is large. To elucidate this further, we show in Fig. 4.11 for two different values of α and for two levels of the input noise, the dynamics of the system in the plane of x and y. The panels not only show the mean trajectory, indicated by the dashed line, but also samples (x, y) from $P(x, y|t_i)$ for evenly spaced time points t_i;

$P(x, y|t)$ is given by Eq. 4.102 and samples from the same time point t_i have the same color. It is seen that when the input noise is low (left two panels), the respective distributions ("blobs") are well separated, both for $\alpha = -\omega$, when the system is a damped oscillator (D.O.) (top row), and for $\alpha = 3\omega$ (bottom row), when the system is a limit-cycle oscillator (L.C.O.). However, when the input noise is large (right column), the blobs of the damped oscillator become mixed, while the distributions $P(x, y|t)$ of the limit-cycle oscillator are still fairly well separated.

To interpret this further, we note that the mutual information $I(x;t) = H(t) - H(t|x)$. Here, $H(t)$ is the entropy of the input signal, which is constant, i.e. does not depend on the design of the system. The dependence of $I(x;t)$ on the design of the system is thus governed by the conditional entropy, given by $H(t|x) = \langle\langle -\log P(t|x)\rangle_{P(t|x)}\rangle_{P(x)}$. The quantity $\langle -\log P(t|x)\rangle_{P(t|x)}$ quantifies the uncertainty in estimating the time t from a given output x; the average $\langle\ldots\rangle_{P(x)}$ indicates that this uncertainty should be averaged over all output values x weighted by $P(x)$. The conditional entropy $H(t|x)$ is low and $I(x;t)$ is high when, averaged over x, the distribution $P(t|x)$ of times t for a given x is narrow. We can now interpret Fig. 4.11: The smaller the number of blobs that intersect the line x, the higher the mutual information. Or, concomitantly, the more the distributions are separated, the higher the mutual information—information transmission is indeed a packing problem. Clearly, when the input noise is low, the time can be inferred reliably from the output even with a damped oscillator (top left panel). For high input noise, however, the mutual information of the damped oscillator falls dramatically because the blobs now overlap strongly. In contrast, the distributions of the limit-cycle oscillator are still reasonably separated and $I(x;t)$ is still almost close to 2 bits.

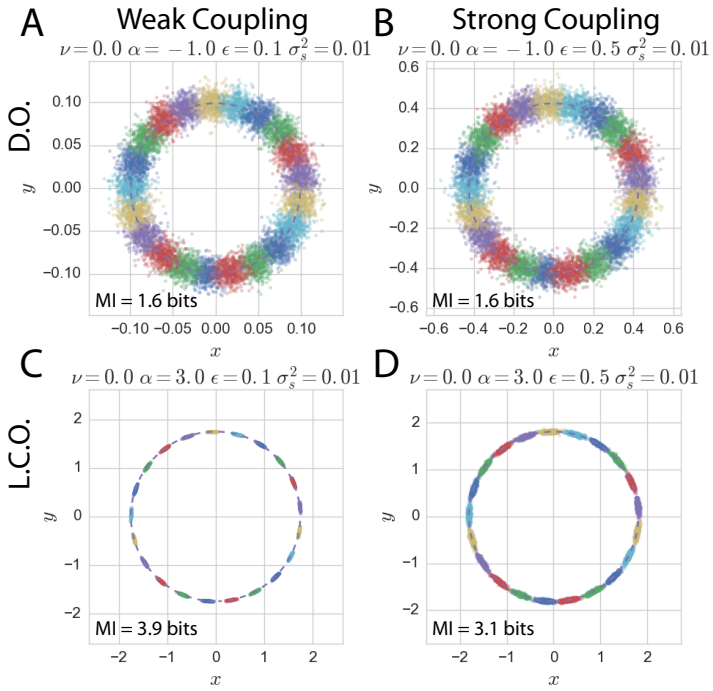

Figure 4.12: The dynamics of the Stuart-Landau model when $\alpha = -\omega$, corresponding to a damped oscillator (D.O., top row), and when $\alpha = 3\omega$, corresponding to a limit-cycle oscillator (L.C.O., bottom row), both for weak coupling, $\epsilon = 0.1\omega$ (left column) and strong coupling, $\epsilon = 0.5\omega$ (right column). Dashed line denotes the mean trajectory of (x, y), and the points are samples of (x, y) from the distribution $P(x, y|t_i)$ for evenly spaced times t_i; $P(x, y|t)$ is given by Eq. 4.102 and points belonging to the same time have the same color. It is seen that for the D.O. the amplitude and the noise are small when the coupling is small (top left panel; note the scale on the x- and y-axis). Increasing the coupling, however, not only raises the amplitude, but also amplifies the noise, leaving the mutual information unchanged: a damped oscillator cannot lift the trade-off between gain and noise. In contrast, the limit-cycle oscillator already exhibits large amplitude oscillations even for weak coupling. Especially the fluctuations in the radial direction, the amplitude fluctuations, are strongly reduced in the L.C.O., due to the non-linearity of the system.

Fig. 4.11 also nicely illustrates that the mutual information would be increased if the system could estimate the time not from x only, but instead from x *and* y: this removes the degeneracy in estimating t for a given x associated with sinusoidal oscillations [19]. One mechanism to remove the degeneracy is to have a readout system that not only reads out the amplitude of the clock signal, but also its derivative, for example via incoherent feedback loops [21]. Another possibility is that the clock signal is read out by 2 (or more) proteins that are out of phase with each other, as shown in [19]. Indeed, while we have computed the instantaneous mutual information between time and the output at a given time, the trajectory of the clock signal provides more information about time, which could in principle be extracted by appropriate readout systens [19].

Lastly, we show in Fig. 4.12 the dynamics for two different values of α and for two different values of the coupling strength ϵ. The top left panel shows that when ϵ is small, the amplitude of the damped oscillator is very weak—note the scale on the x- and y-axis. To increase the amplitude of the output, the coupling strength must be increased. However, this amplifies the input noise as well, such that the mutual information remains unchanged (top right panel): the damped oscillator faces a fundamental trade-off between gain and input noise that cannot be lifted. In contrast, the limit-cycle oscillator (bottom row) already exhibits strong amplitude oscillations even when the coupling strength ϵ is small: the amplitude of the cycle—a bonafide limit-cycle—is determined by the properties of the system, and is only very weakly affected by the strength of the forcing. Moreover, Figs. 4.11 and 4.12 show that while the fluctuations in the phase are not significantly smaller for the limit-cycle oscillator than for the damped oscillator, the relative fluctuations in the amplitude (compared to the mean) are much smaller for the limit-cycle oscillator, due to the non-linearity of the confining potential.

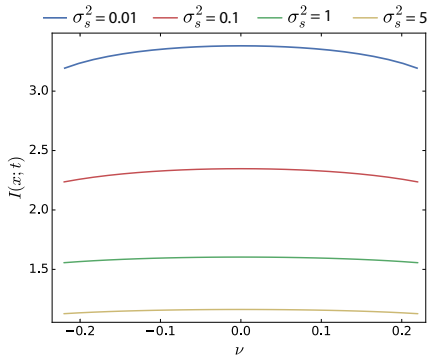

Figure 4.13: The mutual information $I(x;t)$ in the Stuart-Landau model as a function of $\nu = (\omega^2 - \omega_0^2)/(2\omega)$, for different input-noise strengths σ_s^2. It is seen that the mutual information is maximized at $\nu = 0$ (corresponding to $\omega_0 = \omega$) for all input noise levels. $\beta = 1.0\omega$; $\epsilon = 0.5\omega$; $\alpha = 3\omega$.

OPTIMAL INTRINSIC FREQUENCY

Fig. 4.6B shows that the optimal intrinsic frequency ω_0^{opt} that maximizes the mutual information $I(p;t)$ for the coupled-hexamer model (CHM) depends, albeit very weakly, on the input-noise strength σ_s^2. Here we wondered whether the Stuart-Landau model could reproduce this feature. Fig. 4.13 shows the result. The figure shows the mutual information $I(x;t)$ as a function of $\nu = (\omega^2 - \omega_0^2)/(2\omega)$ for different values of σ_s^2. It is seen that the dependence of $I(x;t)$ on ν is rather weak, yielding a broad maximum that peaks at $\nu = 0$ (corresponding to $\omega_0 = \omega$) for all noise strengths. This suggests that the optimal $\omega_0^{\text{opt}} < \omega$ observed for low input noise in the CHM arises from a stronger non-linearity in that system than captured by the Stuart-Landau model, which describes weakly non-linear oscillators.

5

THEORY OF CIRCADIAN METABOLISM

ABSTRACT

Many organisms repartition their proteome in a circadian fashion in response to the daily nutrient changes in their environment. A striking example is provided by cyanobacteria, which perform photosynthesis during the day to fix carbon. These organisms not only face the challenge of rewiring their proteome every 12 hours, but also the necessity of storing the fixed carbon in the form of glycogen to fuel processes during the night. In this manuscript, we extend the framework developed by Hwa and coworkers (Scott *et al.*, Science **330**, 1099 (2010)) for quantifying the relatinship between growth and proteome composition to circadian metabolism. We then apply this framework to investigate the circadian metabolism of the cyanobacterium *Cyanothece*, which not only fixes carbon during the day, but also nitrogen during the night, storing it in the polymer cyanophycin. Our analysis reveals that the need to store carbon and nitrogen tends to generate an extreme growth strategy, in which the cells predominantly grow during the day, as observed experimentally. This strategy maximizes the growth rate over 24 hours, and can be quantitatively understood by the bacterial growth laws. Our analysis also shows that the slow relaxation of the proteome, arising from the slow growth rate, puts a severe constraint on implementing this optimal strategy. Yet, the capacity to estimate the time of the day, enabled by the circadian clock, makes it possible to anticipate the daily changes in the environment and mount a response ahead of time. This significantly enhances the growth rate by counteracting the detrimental effects of the slow proteome relaxation.

5.1. INTRODUCTION

Bacterial cells alter gene expression in response to nutrient changes in their environment [40, 41, 44, 45, 105]. In recent years, experiments have demonstrated that the relation between the proteome composition and the growth rate can be quantitatively described

by growth laws, which are based on the idea that cells need to balance the supply of amino-acids via catabolic and anabolic reactions with the demand for amino-acids in the synthesis of proteins by ribosomes [40, 41, 44, 45, 105]. While in the original studies this relationship was tested for conditions that do not vary on the timescale of the cellular response [40, 41, 105], more recently it has been demonstrated that these growth laws can also describe the transient relaxation dynamics of the proteome in response to a nutrient shift [44, 45]. Here, we extend this framework to predict how bacterial cells repartition their proteome in response to periodic, circadian environmental changes.

Many organisms, ranging from cyanobacteria, to plants, insects, and mammals, possess a circadian clock, which means that they can anticipate daily changes in their environment, and adjust their proteome ahead of time. Moreover, many organisms face the challenge that they can fix carbon and/or nitrogen only during one part of the day, which means that they then need to store these resources to fuel processes the other part of the day. In this manuscript, we study by mathematical modeling the optimal strategy for allocating cellular resources that maximizes the growth rate of cyanobacterial cells living in a periodic environment. We show that storing carbon and nitrogen puts a fundamental constraint on the growth rate, and tends to generate extreme growth behavior, where cells predominantly grow in one part of the day. Moreover, we show that in cyanobacteria with cell-doubling times that are typically longer than 10h [27, 106, 107], the slow relaxation of the proteome severely limits the growth rate, but that anticipation makes it possible to alleviate the detrimental effects of the slow relaxation.

Cyanobacteria are among the most studied and best characterized organisms that exhibit circadian metabolism. Their metabolism is shaped by the constraint that not all the principal elements can be fixed during the day and the night. For cyanobacteria, the primary source of carbon is CO_2, which they fix during the day via photosynthesis. Yet, cyanobacteria also need carbon during the night, not only for protein synthesis, but also for the generation of fuel molecules such as ATP, required for maintenance processes such as DNA repair. To this end, they use not all the fixed carbon to fuel growth during the day: they also store a fraction in the form of glycogen, which then becomes the principal source of carbon during the night.

Like all living cells, cyanobacteria not only need carbon, but also nitrogen. Some cyanobacteria, such as *Synechococcus* and *Synechocystis*, rely on nitrogen that has been fixed by other organisms in the form of, e.g., nitrate. Other cyanobacteria, such as *Cyanothece* [108] and *Anabaena* [109, 110], have, however, the ability to fix the nitrogen that is available in the form of the most abundant gas in the atmosphere, N_2. Yet, this process requires an enzyme, nitrogenase, which cannot tolerate O_2. Since O_2 is produced during photosynthesis, cyanobacterial cells cannot simultaneously fix carbon and nitrogen during the day. *Anabaena* has solved this problem at the population level, where some cells fix carbon while others fix nitrogen [110]. *Cyanothece* has solved the problem at the single-cell level by temporally separating these processes [108]. In this manuscript, we will use *Cyanothece* as a model organism to study the design principles of circadian metabolism.

During the day *Cyanothece* stores carbon in the form of glycogen, while during the night it fixes nitrogen and stores it in the form of cyanophycin [111]. Like glycogen, cyanophycin is a large polymer that accumulates in the cytoplasm in the form of in-

soluble granules. The polymer is a large polypeptide and consists of two amino-acids: aspartic acid, which forms the back bone, and arginine, which constitutes the side group. Arginine is the amino acid with the largest number of nitrogen atoms in its side chain, namely 3; indeed, its side chain has the largest ratio of nitrogen (N) to carbon (C) atoms: 3:4. Cyanophycin is thus exceedingly rich in nitrogen, having an N:C ratio of about 1:2, which is about an order of magnitude larger than that in typical proteins. While cyanophycin may serve as a carbon-storage compound, its principal role is therefore believed to serve as a nitrogen reservoir.

Under LD conditions, Cyanothece fix nitrogen in the dark, as measured by the nitrogenase activity, and store glycogen during the day [111]. Also in continuous light [111] or continuous dark conditions [112], the nitrogenase activity and cyanophycin storage peak during the subjective night while glycogen storage peaks during the subjective day, indicating the presence of a circadian clock that coordinates these activities. Interestingly, under LD conditions, *Cyanothece* exclusively grows during the day [113], but in continuous dark, when grown on glycerol [112], it still predominantly grows during the subjective day, although Fig. 8 of Ref. [112] leaves open the possibility it may also grow during the subjective night.

These physiological rhythms of *Cyanothece* are mirrored by circadian rhythms in gene expression [114–119]. About 30% of the 5000 genes examined exhibit oscillating expression profiles [114]. Moreover, these genes are primarily involved in core metabolic processes, such as photosynthesis, respiration, energy metabolism, and amino-acid biosynthesis [114]; in contrast, most genes involved in transport, DNA replication and repair, were not differentially expressed [114]. Importantly, genes associated with nitrogen fixation are primarily expressed in the dark, while those underlying photosynthesis are up-regulated during the light and down-regulated during the dark period [114]. Proteomic analysis using partial metabolic heavy isotope labelling identified 721 proteins with changing levels of isotope incorporation [117], of which 425 proteins matched the previously identified cycling transcripts [114]. In particular, the nitrogen fixation proteins were most abundant during the dark [117] while many proteins involved in photosynthesis are present in higher abundance during the light. Interestingly, proteins involved in storing glycogen, such as the glycogen synthase, peak during the light, while enzymes involved in glycogen metabolism, such as glycogen phosphorylase, GlgP1, have higher levels during the dark [114]. Conversely, the cyanophycin processing enzyme cyanophycinase, CphB, which breaks down cyanophycin into arginine and aspartic acid, shows higher synthesis in the light [117], although, perhaps surprisingly, cyanophycin synthetase, dCphA, appears not to be strongly coupled with the light-dark cycle.

These transcriptomic and proteomic analyses [114–117, 119], together with large-scale computational modeling of the metabolic network [120], provide detailed information about the proteome repartitioning dynamics during the 24 h period. Yet, many questions remain open: First and foremost, why do cyanobacterial cells typically exclusively grow during the day? Cyanobacterial cells have the components to grow at night, which suggests that the strategy to not grow during the dark arises from a cellular trade-off that maximizes the growth rate over 24h [120]. Can this trade-off be quantified, and do cellular growth laws predict that it is optimal to not grow at all during the night? Secondly, in the absence of active protein degradation, the timescale for the relaxation of

the proteome is given by the growth rate [44, 45, 121], while at the same time the growth rate of these cyanobacterial cells is affected by how fast the proteome can adjust to the changing light and nutrient levels (glycogen and cyanophycin). This observation is particularly pertinent, because the growth rate of these cyanobacterial cells tend to be low, with cell-division times that are typically longer than 10 hours [27, 106, 107]. How much is the growth rate limited by the slow relaxation of the proteome? Thirdly, cyanobacterial cells have a circadian clock, which allows them to predict and anticipate the changes in light and nutrient levels. In general, anticipation becomes potentially beneficial especially when the cellular response is slow [21]. Does anticipation allow cyanobacterial cells to significantly raise their growth rate?

To address these questions, we employ the framework developed by Hwa and coworkers for quantifying the relationship between growth and proteome composition [40, 41, 44, 45, 105] and extend it to describe circadian metabolism. This framework is inspired by two key observations: On the one hand the response to a changing environment tends to be extremely complex at the molecular level, involving a myriad of signaling and metabolic pathways. On the other hand, it tends to be global, meaning that in response to a nutrient limitation certain subsets of enzymes are upregulated while others are downregulated. The system is therefore not described in terms of the detailed signaling and metabolic networks, but rather via coarse-grained protein sectors. Each sector contains a subset of enzymes, which share a common purpose, according to the supply-and-demand picture of protein synthesis [105]. Each sector is described by a single coarse-grained enzyme, which can be thought of as representing the average activity of the enzymes in that sector. It is this coarse-grained description that allows for a quantitative mathematical analysis. The framework has been used to describe the effect of protein overexpression [40], cAMP-mediated catabolite repression [41], growth bistability in response to anti-biotics [42], and methionine biosynthesis [43]. And importantly for our analysis, it has recently been extended to describe the transient relaxation dynamics of the proteome in response to a nutrient shift [44, 45]. While these studies have focused on the bacterium *Escherichia coli*, we here employ this framework to study circadian metabolism of cyanobacteria.

The model that we present aims to describe the circadian metabolism of cyanobacteria like *Cyanothece*, which fix carbon during the day and nitrogen during the night, although it can straightforwardly be amended to describe the metabolism of cyanobacteria such as *Synechococcus* and *Synechocystis* that only fix carbon. Arguably the most minimal model to capture the interplay between carbon and nitrogen fixation is one that consists of a ribosome sector, a carbon sector and a nitrogen sector. However, to capture the fact that storing glycogen and cyanophycin does not directly contribute to growth, but only indirectly, by providing carbon and nitrogen the next part of the day, our model also contains two other protein sectors: a glycogen and a cyanophycin synthesis sector. Our model therefore naturally includes two important consequences of building a carbon and nitrogen reservoir: 1) it requires the synthesis of enzymes that do not directly contribute to growth, and hence lower the instantaneous growth rate [40]; 2) storing carbon and nitrogen atoms drains carbon and nitrogen flux away from protein synthesis. Our model further incorporates the dynamics of the carbon and nitrogen reservoirs (glycogen and cyanophycin), the slow relaxation of the proteome in response

to the changing nutrient levels, and the capacity to anticipate the changing nutrient levels by mounting a response ahead of time.

We first use this model to study the optimal strategy that maximizes the growth rate over 24 hours. Our analysis reveals that the need to store carbon and nitrogen tends to generate an extreme strategy, in which cells predominantly grow during the day, as observed experimentally [112, 113]. However, our analysis also reveals that the slow relaxation of the proteome, arising from the slow growth rate, puts a severe constraint on implementing this optimal strategy. In essence, to store enough cyanophycin during the night to fuel growth during the day, the cyanophycin-storing enzymes need to be expressed at levels that cannot be reached if the cells would only start expressing these enzymes at night. Indeed, to implement the optimal strategy, the cells need to express these enzymes already before the beginning of the night, when they still grow significantly. Interestingly, recent transcriptomics and proteomics data provide evidence for this prediction [119].

5.2. THEORY

The central ingredients of the framework of Hwa and co-workers [40, 41, 44, 45, 105] are the coarse-grained protein sectors and the balance of fluxes between them. We describe these elements in turn.

Protein sectors The sectors are defined experimentally by how the enzyme expression levels vary with the growth rate in response to different types of nutrient limitation [105]. The C-sector is defined as the subset of enzymes whose expression levels increase as the growth rate decreases upon a Carbon limitation, yet decrease as the growth rate decreases upon a nitrogen limitation or translation inhibition [105]. A mass-spec analysis of *E. coli* revealed that this sector contains enzymes involved in ion-transport, the TCA- cycle and locomotion [105]. The A-sector is defined as the group of proteins that are up-regulated in response an A-limitation—a nitrogen limitation— yet down-regulated in response to carbon or translation limitation. In *E. coli*, this sector consists of enzymes that are involved in the incorporation of nitrogen into amino-acids [105]. The R-sector contains the ribosomes, which increase in abundance as the growth rate decreases upon the addition of a translation inhibitor. The study of Hui and co-workers on *E. coli* also identified an S-sector, consisting of enzymes whose expression levels increase in response to both carbon and nitrogen limitation, and a U-sector, consisting of proteins that are un-induced under any of the applied limitations [105].

In our model, we are interested in the interplay between carbon and nitrogen assimilation, and the simplest model that can capture this interplay is one that considers an R-sector, a C-sector and an A-sector. The mass fractions of the proteins in these sectors are denoted by ϕ_R, ϕ_C and ϕ_A, respectively. Our model does not explicitly contain an S- and a U-sector, although we emphasize that as experimental data becomes available the model can straightforwardly be extended to include these sectors [105]. Following Hui *et al.*, we also stress that these sectors are ultimately defined experimentally [105]. In our case, the C-sector is defined as consisting of those enzymes that are up-regulated in response to a carbon limitation, yet down-regulated in response to an A- or R-limitation. The carbon limitation can be in the form of reduced CO_2 and light levels during the day,

but also reduced glycogen levels during the night. Our model thus lumps all proteins that are involved in providing carbon skeletons for amino-acid synthesis into one sector, the C-sector. We anticipate that this sector contains enzymes of not only the photosynthesis machinery, but also the TCA cycle, as well as enzymes involved in degrading glycogen, such as glycogen phosphorylase GlgP. Experiments need to establish whether it would be necessary to split this C-sector up into separate sectors for, e.g., photosynthesis, glycogen breakdown and downstream carbon processing (e.g. TCA cycle).

Similarly, we define the A-sector as the set of enzymes that are up-regulated in response to nitrogen limitation, yet down-regulated in response to a C- or R-limitation. We envision that nitrogen limitation can be imposed by reducing N_2 levels, by employing a titratable nitrogen uptake system [105], or by lowering levels of cyanophycin. While, again, experiments need to identify which enzymes belong to this sector, we expect that it contains not only the nitrogenase enzymes that reduce N_2 into ammonia and the enzymes that subsequently incorporate the nitrogen into amino-acids, but also the proteins that are involved in the breakdown of cyanophycin, such as cyanophycinase CphB.

Following Scott *et al.*, the model also includes an unresponse fraction ϕ_{Q}, although this parameter will be absorbed in the maximal ribosomal fraction $\phi_{\mathrm{R,max}}$, as described below [40, 41, 105].

Storing fractions While this model is indeed highly coarse-grained, we do consider two other sectors, which contain enzymes that store glycogen during the day and nitrogen during the night. Their fractions are denoted by ϕ_{SC} and ϕ_{SA}, respectively. Enzymes belonging to ϕ_{SC} are glycogenin and glycogen synthase, which are indeed up-regulated during the day [116, 117]. Cyanophycin is synthesized from arginine and aspartate by a single enzyme, cyanophycin synthetase, CphA, which thus forms the ϕ_{SA} sector [116]. A key point is that expressing the glycogen-storing enzymes slows down growth during the day yet enables growth during the night, while expressing cyanophycin synthetase slows down growth during the night, yet enables growth during the day. Even though the growth laws are linear, this creates a feedback between growth at night and during the day that yields a non-linear response, as we discuss in more detail below.

Steady-state flux balance The experiments by Hwa and coworkers on *E. coli* have revealed that the steady-state growth rate varies linearly with the size of the protein sectors [40, 41, 105]. These linear relationships can be understood by combining the following ideas: a) in steady-state the fluxes J_α through the different sectors $\alpha = \mathrm{R,C,A}$ are balanced, so that there is no build-up of intermediates like amino-acids; b) the growth rate λ is proportional to the flux through the sectors; c) the flux through a sector scales linearly with the size of the sector. Combining these ideas makes it possible to quantitatively describe the experiments of [41, 105], explaining how each sector is upregulated in response to one type of limitation, while downregulated in response to another type of limitation [41, 105]. Moreover, the model can quantitatively describe how the growth rate decreases as an unnecessary protein, which does not directly contribute to growth, is expressed via an artificial inducer [40]. The latter is important, because the proteins that store glycogen and cyanophycin, respectively, can be thought of as proteins that do not directly contribute to growth; they only contribute by providing the carbon- and nitrogen sources for the next part of the day. Our model incorporates these three ingredients a)-c), but adds a fourth, d): a certain fraction of the flux through the carbon and

nitrogen sector is reserved for storing glycogen during the day and cyanophycin during the night, respectively.

While our full model is time dependent, we will first consider a simpler model in which we can directly use the growth laws derived by Hwa and coworkers [40, 41, 105]. Specifically, during the day the principal source of carbon is CO_2, while that of nitrogen is cyanophycin, which decreases with time. During the night, the principal source of nitrogen is N_2, while that of carbon is glycogen, which falls with time. As a result, the growth rate λ will, in general, be time-dependent, $\lambda = \lambda(t)$. Moreover, because the glycogen and cyanophycin concentrations vary with time, the proteome fractions, which are adjusted in accordance with the nutrient availability, will change not only upon the shift from day to night, but also continue to change throughout the day and night. As was pointed out in [121] and also in [44, 45], in the absence of active protein degradation, the proteome relaxes with a timescale that is set by the growth rate $\lambda(t)$. This means that when the growth rate is low, the proteome will relax slowly, and may not be in quasi-equilibrium with respect to the instantaneous levels of glycogen during the night and cyanophycin during the day. Below we will take this slow relaxation of the proteome into account. However, to introduce the main elements of the model, it will be instructive to first assume that the growth rate is so high, that the proteome is always in quasi-equilbrium with respect to the instantaneous nutrient levels, set by the CO_2/light and cyanophycin levels during the day, and the glycogen and N_2 levels during the night. The growth thus depends on time, but not explicitly, and only implicitly via the levels of glycogen and cyanophycin: $\lambda(t) = \lambda([\mathrm{C}](t), [\mathrm{N}](t))$, where $[\mathrm{C}](t)$ and $[\mathrm{N}](t)$ are the time-dependent carbon and nitrogen sources. We call this model the quasi-equilibrium model.

The first two ingredients a) and b) imply that in the quasi-equilibrium model

$$\lambda^{\beta}(t) = c_{\mathrm{R}} J_{\mathrm{R}}(t) = c_{\mathrm{C}} J_{\mathrm{C}}^{\beta}(t) = c_{\mathrm{A}} J_{\mathrm{A}}^{\beta}(t), \tag{5.1}$$

where c_α are the stochiometric requirements for cell growth [105]. Here, we have added the superscript $\beta = \mathrm{L}, \mathrm{D}$, with L standing for light and D for dark, to remind ourselves that the fluxes through the carbon and nitrogen sector and thereby the growth rate, depend on the source of carbon and nitrogen used, which differs between day and night.

The third observation c) means that for the ribosomal sector

$$\lambda^{\mathrm{L/D}}(t) = c_{\mathrm{R}} J_{\mathrm{R}}(t) = \nu_{\mathrm{R}}(\phi_{\mathrm{R}}(t) - \phi_{\mathrm{R},0}). \tag{5.2}$$

Here, $\nu_{\mathrm{R}} = c_{\mathrm{R}} k_{\mathrm{R}}$, where k_{R} describes the translation efficiency, which can be varied experimentally using a translation inhibitor such as cloramphenicol [40, 41, 105]. The quantity $\phi_{\mathrm{R},0}$ is the fraction of ribosomes that is not active in steady-state, yet can become active during the transition from one environment to the next [44, 45]. In the quasi-equilibrium model considered here, it is a constant, independent of time.

The ingredients c) and d) imply that the flux through the carbon sector that flows into the other sectors is given by

$$\lambda^{\beta}(t) = c_{\mathrm{C}} J_{\mathrm{C}}^{\beta}(t) = \nu_{\mathrm{C}}^{\beta}(t)(\phi_{\mathrm{C}}(t) - \phi_{\mathrm{C},0}) - L(t)\nu_{\mathrm{SC}}\phi_{\mathrm{SC}}(t). \tag{5.3}$$

Here, $L(t)$ is an indicator function that is 1 during the day and 0 during the night. Indeed, during the day both terms are present. The first term on the right-hand side describes the

carbon flux that would flow into the other sectors if no carbon were stored into glycogen during the day. The second term indeed describes the flux that is not used for growth during the day, but rather lost in storing glycogen. During the night, no glycogen is stored and the second term is absent. In the first term, ν_C^β is a measure for the efficiency of the carbon sector. It depends on the quality and the amount of nutrient [41, 105], but can also be varied experimentally—in *E. coli* by titrating a key enzyme such as the lactose permease [41, 105]. In our model, ν_C^β depends on the part of the day, as indicated by $\beta = \mathrm{L}, \mathrm{D}$: during the day, the principal carbon source is CO_2, which means that the value of ν_C^L will depend on the concentration of CO_2 and light levels. Since we will model the light intensity as a step function, during the day the light level and hence $\nu_C^\mathrm{L}(t)$ is constant, and equal to $\nu_C^\mathrm{L}(t) = \tilde{\nu}_C^\mathrm{L}$. In contrast, during the night, the principal source of carbon is glycogen, which decreases during the night. This affects the carbon-processing efficiency. We will model this as

$$\nu_C^\mathrm{D}(t) = \tilde{\nu}_C^\mathrm{D} \frac{[\mathrm{C}](t)}{[\mathrm{C}](t) + K_\mathrm{C}}, \tag{5.4}$$

5

where $[\mathrm{C}](t)$ is the time-dependent concentration of glycogen and K_C is the glycogen concentration at which the enzyme efficiency is reduced by a factor of 2. The quantity $\tilde{\nu}_C^\mathrm{D}$ is the maximal efficiency of the carbon-sector with glycogen as the carbon source; it does not depend on time. The quantity $\phi_{\mathrm{C},0}$ is the fraction of carbon-processing enzymes that is not used for growth. For *E. coli* it is very close to zero, and from here on we assume it to be zero. The quantity ν_SC describes the efficiency of the glycogen-storing enzymes, and is taken to be constant.

For the nitrogen-sector, we similarly obtain

$$\begin{aligned} \lambda^\beta(t) &= c_\mathrm{A} J_\mathrm{A}^\beta(t) \\ &= \nu_\mathrm{A}^\beta(t)(\phi_\mathrm{A}(t) - \phi_{\mathrm{A},0}) - (1 - L(t))\nu_\mathrm{SA}\phi_\mathrm{SA}(t), \end{aligned} \tag{5.5}$$

where in the calculations performed here we assume that $\phi_{\mathrm{A},0}$ is zero, even though the experiments indicate that for *E. coli* the unused fraction in the A-sector is about 10% [105]. The nitrogen-processing efficiency during the day depends on the concentration of stored cyanophycin, [N], via

$$\nu_\mathrm{A}^\mathrm{L}(t) = \tilde{\nu}_\mathrm{A}^\mathrm{L} \frac{[\mathrm{N}](t)}{[\mathrm{N}](t) + K_\mathrm{A}}. \tag{5.6}$$

The nitrogen-uptake efficiency during the night depends on the amount of N_2, which we assume to be constant throughout the night. The efficiency is thus given by $\nu_\mathrm{A}^\mathrm{D} = \tilde{\nu}_\mathrm{A}^\mathrm{D}$.

Combining all four ingredients a) - d), i.e. Eqs. 5.1-5.6, yields

$$\lambda^\beta(t) = \nu_\mathrm{R}(\phi_\mathrm{R}(t) - \phi_{\mathrm{R},0}) \tag{5.7}$$

$$= \nu_\mathrm{C}^\beta(t)\phi_\mathrm{C}(t) - L(t)\nu_\mathrm{SC}\phi_\mathrm{SC}(t) \tag{5.8}$$

$$= \nu_\mathrm{A}^\beta(t)\phi_\mathrm{A} - (1 - L(t))\nu_\mathrm{SA}\phi_\mathrm{SA}(t). \tag{5.9}$$

Proteome balance The protein sectors obey at all times t the constraint

$$\phi_R(t) + \phi_C(t) + \phi_A(t) + \phi_{SC}(t) + \phi_{SA}(t) + \phi_Q = 1. \tag{5.10}$$

The growth rate λ will be maximal, $\lambda \to \lambda_{max}$, when the storing, carbon- and nitrogen-processing fractions approach zero, and the ribosomal fraction becomes maximal

$$\lim_{\lambda \to \lambda_{max}} \phi_R \equiv \phi_{R,max} = 1 - \phi_Q, \tag{5.11}$$

allowing us to rewrite the constraint as:

$$\phi_R(t) + \phi_C(t) + \phi_A(t) + \phi_{SC}(t) + \phi_{SA}(t) = \phi_{R,max}. \tag{5.12}$$

We note that this definition of $\phi_{R,max}$ differs slightly from ϕ_{max} defined in Ref. [41, 105].

Growth rate in quasi-equilibrium model In our model, the input parameters are ν_α^β and $\phi_{R,0}$, while the storing fractions $\phi_{SC}(t)$ and $\phi_{SA}(t)$ are control parameters over which we will optimize to maximize the growth rate over a 24h period. In the quasi-equilibrium model, the optimal ϕ_{SC} during the night is zero and the optimal ϕ_{SA} during the day is zero. In this model, we thus have one optimization parameter ϕ_{SC} for the day, and another for the night, ϕ_{SA}. In this quasi-equilibrium model, the other protein sectors relax instantaneously, to values that, for the day, are determined by the efficiencies ν_R, ν_C^L, the instantaneous efficiency $\nu_A^D(t)$ and the optimization parameter $\phi_{SC}(t)$, and, for the night to values given by ν_R, ν_A^D, the instantaneous value of $\nu_A^L(t)$ and the optimization parameter $\phi_{SA}(t)$. The 4 equations, Eqs. 5.7-5.9 together with the constraint Eq. 5.12, thus contain 4 unknowns $\phi_R, \phi_C, \phi_A, \lambda$, which can be solved to obtain the instantaneous growth rate for the day and night, respectively, for the quasi-equilibrium model:

$$\lambda^L(t) = \frac{\nu_R \nu_C^L \nu_A^L(t)}{\nu_R \nu_C^L + \nu_R \nu_A^L(t) + \nu_A^L(t)\nu_C} \times (\phi_{R,max} - \phi_{R,0} - (1 + \nu_{SC}/\nu_C^L)\phi_{SC}(t)) \tag{5.13}$$

$$\lambda^D(t) = \frac{\nu_R \nu_C^D(t) \nu_A^D}{\nu_R \nu_C^D(t) + \nu_R \nu_A^D + \nu_A^D \nu_C^D(t)} \times (\phi_{R,max} - \phi_{R,0} - (1 + \nu_{SA}/\nu_A^D)\phi_{SA}(t)) \tag{5.14}$$

Clearly, during the day the growth rate, for given CO_2 and cyanophycin levels, is maximal when no glycogen is stored and $\phi_{SC} = 0$. This defines a maximum growth rate during the day

$$\lambda_{max}^L([N](t)) = \frac{\nu_R \nu_C^L \nu_A^L(t)}{\nu_R \nu_C^L + \nu_R \nu_A^L(t) + \nu_A^L(t)\nu_C^L} \Delta\phi_{R,max}, \tag{5.15}$$

where $\Delta\phi_{R,max} = \phi_{R,max} - \phi_{R,0}$. The maximal growth rate depends on the instantaneous amount of cyanophycin, $[N](t)$, because $\nu_A^L(t)$ depends on $[N](t)$ (see Eq. 5.6). From Eq. 5.13 we find the storing fraction ϕ_{SC}^0 that reduces the growth rate to zero during the day:

$$\phi_{SC}^0 = \frac{\Delta\phi_{R,max}}{1 + \nu_{SC}/\nu_C^L}. \tag{5.16}$$

This allows us to rewrite Eq. 5.13 as

$$\lambda^{\mathrm{L}}(\phi_{\mathrm{SC}}) = \lambda^{\mathrm{L}}_{\mathrm{max}}([\mathrm{N}](t))\left(1-\phi_{\mathrm{SC}}/\phi^{0}_{\mathrm{SC}}\right). \tag{5.17}$$

Equivalently, we find for the growth rate during the night

$$\lambda^{\mathrm{D}}(\phi_{\mathrm{SA}}) = \lambda^{\mathrm{D}}_{\mathrm{max}}([\mathrm{C}](t))\left(1-\phi_{\mathrm{SA}}/\phi^{0}_{\mathrm{SA}}\right), \tag{5.18}$$

with

$$\lambda^{\mathrm{D}}_{\mathrm{max}} = \frac{\nu_{\mathrm{R}}\nu^{\mathrm{D}}_{\mathrm{C}}(t)\nu^{\mathrm{D}}_{\mathrm{A}}}{\nu_{\mathrm{R}}\nu^{\mathrm{D}}_{\mathrm{C}}(t)+\nu_{\mathrm{R}}\nu^{\mathrm{D}}_{\mathrm{A}}+\nu^{\mathrm{D}}_{\mathrm{A}}\nu^{\mathrm{D}}_{\mathrm{C}}(t)}\Delta\phi_{\mathrm{R,max}} \tag{5.19}$$

and

$$\phi^{0}_{\mathrm{SA}} = \frac{\Delta\phi_{\mathrm{R,max}}}{1+\nu_{\mathrm{SA}}/\nu^{\mathrm{D}}_{\mathrm{A}}}. \tag{5.20}$$

5

A few points are worthy of note. Firstly, Eqs. 5.17 and 5.18 show that the growth rate decreases linearly with ϕ_{SC} and ϕ_{SA}, respectively. In fact, Scott *et al.* derived a similar relation for the growth rate when an unnecessary protein is expressed [40]. This highlights the idea that storing glycogen and cyanophycin reduces the growth rate, because synthesizing these storage molecules requires proteins that do not directly contribute to growth—thus taking up resources that could have been devoted to making more ribosomes. Indeed, building carbon and nitrogen reservoirs only pays off the next part of the day, which can be seen by noting that the maximum growth rate during the day, $\lambda^{\mathrm{L}}_{\mathrm{max}}$, increases with the amount of cyanophycin that has been stored the night before (via $\nu^{\mathrm{L}}_{\mathrm{A}}$, see Eq. 5.6), while the maximum growth rate during the night, $\lambda^{\mathrm{D}}_{\mathrm{max}}$ increases with the amount of glycogen that has been stored the day before (via $\nu^{\mathrm{D}}_{\mathrm{C}}$, see Eq. 5.4). Clearly, the cell needs to strike a balance between maximizing the instantaneous growth rate and storing enough resources to fuel growth the next part of the day.

However, there is also another effect: building the reservoirs reduces the growth rate not only because it requires proteins that do not directly contribute to growth, but also because it drains carbon and nitrogen flux. This manifests itself in the intercepts ϕ^{0}_{SC} and ϕ^{0}_{SA} at which the growth rate is zero (see Eq. 5.16). This effect puts a hard fundamental bound on the maximum rate at which glycogen and cyanophycin can be stored. For glycogen the maximum storing rate is given by

$$v^{\mathrm{max}}_{\mathrm{store,G}} = c_{\mathrm{G}}\nu_{\mathrm{SC}}\phi^{0}_{\mathrm{SC}} \tag{5.21}$$

$$= c_{\mathrm{G}}\frac{\nu_{\mathrm{SC}}\nu^{\mathrm{L}}_{\mathrm{C}}}{\nu_{\mathrm{SC}}+\nu^{\mathrm{L}}_{\mathrm{C}}}\Delta\phi_{\mathrm{R,max}}. \tag{5.22}$$

Here, c_{G} is a stoichiometric coefficient that reflects the number of carbon atoms that are stored in a glycogen molecule. This expression shows that the maximal storing rate $v^{\mathrm{max}}_{\mathrm{store,G}}$ increases with $\Delta\phi_{\mathrm{R,max}}$. This is because $\Delta\phi_{\mathrm{R,max}}$ limits the fraction of the proteome that can be allocated to storing glycogen, ϕ^{0}_{SC}. The expression also reveals that $v^{\mathrm{max}}_{\mathrm{store,G}}$ depends on ν_{SC} and $\nu^{\mathrm{L}}_{\mathrm{C}}$. The maximum storing rate $v^{\mathrm{max}}_{\mathrm{store,G}}$ initially increases

with ν_{SC}, simply because that increases the rate at which the glycogen storing enzymes operate. However, the increased flux of carbon into glycogen also means that less carbon is available for making the glycogen-storing enzymes themselves. As a result, as ν_{SC} increases, the maximal fraction ϕ^0_{SC} of glycogen-storing enzymes decreases (see Eq. 5.16). In the limit that ν_{SC} becomes very large, i.e. much larger than ν_C, then ϕ^0_{SC} becomes zero, and the rate at which glycogen is stored becomes independent of ν_{SC}. In this regime, all the carbon flows into glycogen and the storing rate instead becomes limited by ν^L_C, $\upsilon^{max}_{storage,G} = c_G \nu^L_C \Delta\phi_{R,max}$. In this limit, $\phi_R = \phi_A = 0$ and $\phi_C = \Delta\phi_{R,max}$, such that there is no carbon flow devoted to growth, $\nu^L_C \phi_C - \nu_{SC}\phi_{SC} = 0$ (Eq. 5.3), but only to storing glycogen. As we will see below, this will put a strong constraint on the maximal growth rate of the cyanobacteria.

Reservoir dynamics The growth rate depends on the efficiencies $\nu^D_C(t)$ and $\nu^L_A(t)$, which depend on the amount of glycogen and cyanophycin, respectively (see Eqs. 5.4 and 5.6). The dynamics of their concentration is given by

$$\frac{d[N](t)}{dt} = (1 - L(t))c_{CP}\nu_{SA}\phi_{SA}(t) - L(t)c_{CP}\lambda(t) - \lambda(t)[N](t) \tag{5.23}$$

$$\frac{d[C](t)}{[dt]} = L(t)c_G\nu_{SC}\phi_{SC}(t) - (1 - L(t))c_G\lambda(t) - \lambda(t)[C](t) \tag{5.24}$$

The last term in both equations is a dilution term, where we have exploited that cells grow exponentially with rate $\lambda(t)$. The first term describes the accumulation of the stores due to the storing enzymes, with c_{CP}, c_G being stoichiometric coefficients that reflect how many nitrogen and carbon atoms are stored in a cyanophycin and glycogen molecule, respectively. The second term describes the consumption of cyanophycin and glycogen that fuels growth. Focusing on glycogen, this term can be understood by noting that the depletion of glycogen during the night is given by the rate at which the carbon sector consumes glycogen:

$$\frac{d[C](t)}{dt} = (1 - L(t))c_G\tilde{\nu}^D_C \frac{[C](t)}{[C](t) + K_C}\phi_C(t) \tag{5.25}$$

$$= (1 - L(t))c_G\lambda(t) \tag{5.26}$$

where in the second line we have exploited that in quasi-equilibrium the growth rate $\lambda(t)$ is given by the flux through the carbon sector (see Eqs. 5.3 and 5.4). Importantly, this expression reveals that the depletion of the store depends on the growth rate not only because that sets the dilution rate (reflected by the third term in Eqs. 5.23 and 5.24), but also because the growth rate sets the rate at which the store is consumed (second term).

Slow proteome dynamics The proteome will in general not be in quasi-equilibrium with respect to the instantaneous nutrient levels. To take into account the relaxation of the proteome we first define the mass fractions ϕ_α of the different sectors

$$\phi_\alpha = \frac{M_\alpha}{M} \tag{5.27}$$

where M_α is the protein mass of sector $\alpha = R, C, A, SC, SA, Q$ and M is the total mass. The

total rate at which proteins are synthesized is given by

$$\frac{dM(t)}{dt} = \sigma(t) M_{\mathrm{R}}(t), \tag{5.28}$$

where M_{R} is the mass of the ribosomal sector, consisting of the mass of the ribosomes and the ribosome-affiliated proteins [45]. The quantity $\sigma(t)$ is the instantaneous translational efficiency. It corresponds to the average translational efficiency, and does not distinguish between active and inactive ribosomes [45]. When we divide the above equation by $M(t)$, we obtain the instantaneous growth rate [45, 121]

$$\lambda(t) = \frac{1}{M(t)} \frac{dM(t)}{dt} = \sigma(t)\phi_R(t). \tag{5.29}$$

To obtain the evolution of the different protein sectors, we denote the fraction of the number of ribosomes that are allocated to making protein sector α as χ_α. The evolution of the proteome mass M_α is then

$$\frac{dM_\alpha(t)}{dt} = \chi_\alpha(t)\sigma(t)M_{\mathrm{R}} \tag{5.30}$$

and that of the proteome fraction [45, 121]

$$\frac{d\phi_\alpha(t)}{dt} = \frac{1}{M(t)}\frac{dM_\alpha(t)}{dt} - \frac{M_\alpha(t)}{M^2(t)}\frac{dM(t)}{dt} \tag{5.31}$$

$$= \frac{1}{M(t)}\chi_\alpha(t)\sigma(t)M_{\mathrm{R}} - \phi_\alpha(t)\lambda(t) \tag{5.32}$$

$$= \chi_\alpha(t)\sigma(t)\phi_{\mathrm{R}}(t) - \phi_\alpha(t)\lambda(t) \tag{5.33}$$

$$= \lambda(t)(\chi_\alpha(t) - \phi_\alpha(t)), \tag{5.34}$$

where in going to the last line we have exploited Eq. 5.29. This equation shows that when $\chi_\alpha(t)$ adjusts rapidly to a new nutrient environment, as recent experiments indicate [44, 45], the relaxation of the proteome is dominated by the growth rate $\lambda(t)$. Importantly, the equation also shows that when $\chi_\alpha(t) = \phi_\alpha(t)$, the proteome has equilibrated: the fractions no longer change with time.

Recent experiments indicate that after a nutrient upshift the translational efficiency $\sigma(t)$ and the fraction $\chi_\alpha(t)$ of ribosomes devoted to making proteins of sector α rapidly approach their new steady-state values as set by the new environment [44, 45]. We therefore make the simplification [121], also used in [45], that after a day-night (and night-day) transition $\sigma(t)$ immediately takes the final value σ^* set by the new environment and that $\chi_\alpha(t)$ immediately takes the value of the final fraction ϕ_α^* in the new environment. However, in our system, the amounts of glycogen and cyanophycin change with time, and the proteome fractions continually adjust to this. The "final" fractions ϕ_α^* are thus target fractions that themselves change with time, and similarly for the translation efficiency σ:

$$\chi_\alpha(t) = \phi_\alpha^*([\mathrm{C}](t), [\mathrm{N}](t)) \tag{5.35}$$

$$\sigma(t) = \sigma^*([\mathrm{C}](t), [\mathrm{N}](t)). \tag{5.36}$$

These quantities are set such that if $\phi_\alpha(t)$ were equal to $\chi_\alpha(t) = \phi^*_\alpha([\mathrm{C}](t),[\mathrm{N}](t))$ and $\sigma(t)$ were equal to $\sigma^*([\mathrm{C}](t),[\mathrm{N}](t))$, the fluxes through the different sectors would be balanced and the growth rate would be equal to $\lambda^*(t)$:

$$\lambda^*(t) = \sigma^*(t)\phi^*_\mathrm{R}(t) = \nu_R(\phi^*_\mathrm{R}(t) - \phi_{\mathrm{R},0}) \tag{5.37}$$

$$= \nu^\beta_\mathrm{C}([\mathrm{C}](t))\phi^*_\mathrm{C}(t) - L(t)\nu_{\mathrm{SC}}\phi^*_{\mathrm{SC}}(t) \tag{5.38}$$

$$= \nu^\beta_\mathrm{A}([\mathrm{N}](t))\phi^*_\mathrm{A}(t) - (1-L(t))\nu_{\mathrm{SA}}\phi^*_{\mathrm{SA}}(t) \tag{5.39}$$

Importantly, we do not only need to consider the target fractions for the R-, C-, A-, and Q-sector, but also for the storing fractions: $\chi_{\mathrm{SC}}(t) = \phi^*_{\mathrm{SC}}(t)$ and $\chi_{\mathrm{SA}}(t) = \phi^*_{\mathrm{SA}}(t)$. Eqs. 5.37-5.39 are thus solved subject to the following constraint

$$\phi^*_\mathrm{R}(t) + \phi^*_\mathrm{C}(t) + \phi^*_\mathrm{A}(t) + \phi^*_{\mathrm{SC}}(t) + \phi^*_{\mathrm{SA}}(t) = \phi_{\mathrm{R,max}}, \tag{5.40}$$

where $\phi_{\mathrm{SC}}(t)$ and $\phi_{\mathrm{SA}}(t)$ are optimization parameters described in more detail below. This equation states that the total ribosome protein synthesis fraction $\sum_\alpha \chi_\alpha(t) = 1$ at all times, which guarantees that $\sum_\alpha \phi_\alpha(t) = 1$ at all times.

Anticipation The cell needs to repartition its proteome every 12h as the cells move from day to night, and vice versa. Moreover, the cell needs to continually adjust its proteome to the changing levels of cyanophycin and glycogen. However, the relaxation of the proteome is, in the absence of protein degradation, set by the growth rate (see Eq. 5.34), which for cyanobacteria, with cell division times in the range of 10 - 70h, is low compared to the 24 hr period of the day-night cycle. This slow relaxation of the proteome will tend to make the growth rate suboptimal. Interestingly, cyanobacteria, ranging from *Synechococcus*, *Synechocystis*, to *Cyanothece* have a circadian clock, which allows them to anticipate the changes between day and night and to adjust their proteome ahead of time.

To include this into the model, we introduce the notion of the anticipation time T_a. That is, the cells will compute the target protein fraction $\phi^*_\alpha(t)$ at time t (see Eqs. 5.37-5.39) based on the values of $\nu^\beta_\alpha(t+T_\mathrm{a})$ at the later time $t+T_\mathrm{a}$. The ribosome fraction $\chi_\alpha(t) = \phi^*_\alpha(t)$ devoted to making proteins of sector α at time t is thus determined by the protein efficiencies $\nu^\beta_\alpha(t+T_\mathrm{a})$ at a later time $t+T_\mathrm{a}$. This allows cells to already adjust their proteome before the end of the day (night) is over, and steer it towards the target protein fractions set by the efficiencies $\nu^\beta_\alpha(t+T)$ in the following night (day).

There is one subtlety, which we address in a rather ad-hoc fashion. The efficiencies $\nu^\mathrm{L}_\mathrm{A}(t) = \tilde{\nu}^\mathrm{L}_\mathrm{A}[\mathrm{N}](t)/([\mathrm{N}](t)+K_\mathrm{A})$ and $\nu^\mathrm{D}_\mathrm{C}(t) = \tilde{\nu}^\mathrm{D}_\mathrm{C}[\mathrm{C}](t)/(cC(t)+K_\mathrm{C})$ depend on the concentrations of cyanophycin and glycogen at time t, respectively. Experiments on plant cells in combination with modeling [122] suggest that cells might be able to extrapolate the current concentrations $[\mathrm{C}](t)$ and $[\mathrm{N}](t)$ to estimate the concentrations at time $t+T$, $[\mathrm{C}](t+T)$ and $[\mathrm{N}](t+T)$, respectively. While this could be included into our model, we make the simplication that the cells base the future efficiency based on the current concentration of the store.

The target fractions $\phi^*_\alpha(t)$ are thus obtained by solving Eqs. 5.37-5.39 but with the

protein efficiencies given by

$$\nu_{\mathrm{C}}^{\beta}(t) \to L(t+T_{\mathrm{a}})\tilde{\nu}_{\mathrm{C}}^{\mathrm{L}} + (1-L(t+T_{\mathrm{a}}))\tilde{\nu}_{\mathrm{C}}^{\mathrm{D}}\frac{[\mathrm{C}](t)}{[\mathrm{C}](t)+K_{\mathrm{C}}} \tag{5.41}$$

$$\nu_{\mathrm{A}}^{\beta}(t) \to L(t+T_{\mathrm{a}})\tilde{\nu}_{\mathrm{A}}^{\mathrm{D}}\frac{[\mathrm{N}](t)}{[\mathrm{N}](t)+K_{\mathrm{A}}} + (1-L(t+T_{\mathrm{a}}))\tilde{\nu}_{\mathrm{A}}^{\mathrm{L}}, \tag{5.42}$$

where, as before, $L(t)$ is an indicator function that is 1 during the day and 0 during the night.

In addition, in this anticipation model, we also take into account that the protein storing fractions ϕ_{SC} and ϕ_{SA} can be made ahead of time: the synthesis of the glycogen-storing enzymes can already start before the beginning of the day, while the production of the cyanophycin-storing enzyme can already start before the beginning of the night. As we will see, especially the latter can significantly enhance the growth rate. Importantly, while the storing enzymes are synthesized ahead of time, we assume that they become active only when they need to be, i.e. the cyanophycin-storing enzymes are active only during the night, while those storing glycogen are only active during the day.

Overview full model The model that takes into account the slow proteome relaxation dynamics but *not* anticipation, is given by Eq. 5.29 which gives the instantaneous growth rate $\lambda(t)$, Eq. 5.34 that describes the evolution of $\phi_\alpha(t)$, and Eqs. 5.35-5.40, which are solved to yield $\chi_\alpha(t) = \phi_\alpha^*(t)$ in Eq. 5.34 and $\sigma(t) = \sigma^*(t)$ in Eq. 5.29, together with the dynamics for the concentrations of cyanophycin and glycogen, Eqs. 5.23 and 5.24. Moreover, in this so-called slow-proteome model, we set ϕ_{SC} to be zero during the night and ϕ_{SA} to be zero during the day, and optimize over the magnitude of their values during the day and night, respectively.

The full model, called the anticipation model, is based on the idea that the cell possesses a clock that not only makes it possible to anticipate the changes in protein efficiencies $\nu_\alpha^\beta(t)$ between day and night, but also to express the protein storing fractions in an anticipatory fashion. The full model is thus exactly the same as the slow-proteome model, except for the following two ingredients: 1) the efficiencies $\nu_{\mathrm{C}}^{\beta}(t)$ and $\nu_{\mathrm{A}}^{\beta}(t)$ in Eqs. 5.37-5.38 are replaced by those of Eqs. 5.41 and 5.42; 2) the protein-storing fractions $\phi_{\mathrm{SC}}(t)$ and $\phi_{\mathrm{SA}}(t)$ are optimized not only with respect to their magnitude, but also with respect to the timing of their expression.

5.3. PARAMETER SETTINGS

In our model, the key parameters that can be varied experimentally are $\nu_{\mathrm{C}}^{\mathrm{L}}$, which is determined by the CO_2 and light levels during the day, $\nu_{\mathrm{A}}^{\mathrm{D}}$, which is set by the N_2 level, and ν_{R}, which can be varied experimentally via a translational inhibitor such as chloramphenicol. The parameters $\nu_{\mathrm{C}}^{\mathrm{D}}$ and $\nu_{\mathrm{A}}^{\mathrm{L}}$ are set by the nutrient quality of glycogen and cyanophycin, respectively, while ν_{SC} and ν_{SA} are determined by the efficiencies of the glycogen and cyanophycin storing enzymes, respectively. We will keep these parameters constant in all the results that we present below. The parameters are set such that for the baseline parameter values the average cell-division time is roughly 24h. The values of $\phi_{\mathrm{R,max}}$ and $\phi_{\mathrm{R},0}$ are inspired by those measured for *E. coli* [105]. The parameters ϕ_{SC} and ϕ_{SA} are optimization parameters, as described above. We optimize these parameters

by numerically propagating our model for given values of ϕ_{SC} and ϕ_{SA} and numerically computing the average growth rate $\langle\lambda\rangle_T = 1/T \int_0^T \lambda(t)$ over one period of duration T, which under normal conditions is $T = 24$h.

5.4. RESULTS

5.4.1. QUASI-EQUILIBRIUM MODEL

It is instructive to first consider the scenario in which the relaxation of the proteome is instantaneous, such that at any moment in time the protein fractions are optimally balanced based on the values of the protein efficiencies ν_C^β and ν_A^β and the instantaneous levels of glycogen, $[C](t)$, and cyanophycin, $[N](t)$, respectively. Fig. 5.1A shows a heat map of the average growth rate over 24h, $\langle\lambda\rangle_{24}$ as a function of the fractions of proteins that store glycogen and cyanophycin, ϕ_{SC} and ϕ_{SA}, respectively. The parameters have been set such that the system is symmetric, $\nu_{SC} = \nu_{SA}$, $\nu_C^L = \nu_A^D$, $K_C = K_A$, $c_G = c_{CP}$, except that the maximum growth rate during the day is slightly larger than that during the night because $\tilde{\nu}_A^L = 6$/h is slightly larger than $\tilde{\nu}_C^D = 2$/h. The prominent feature of the figure is that even though the system is slightly asymmetric, meaning that the system could grow during the dark, the storing fractions that maximize the growth rate are such that the optimal cyanophycin-storing protein fraction ϕ_{SA}^{opt} is markedly non-zero, while the optimal glycogen-storing protein fraction, ϕ_{SC}^{opt}, is essentially zero.

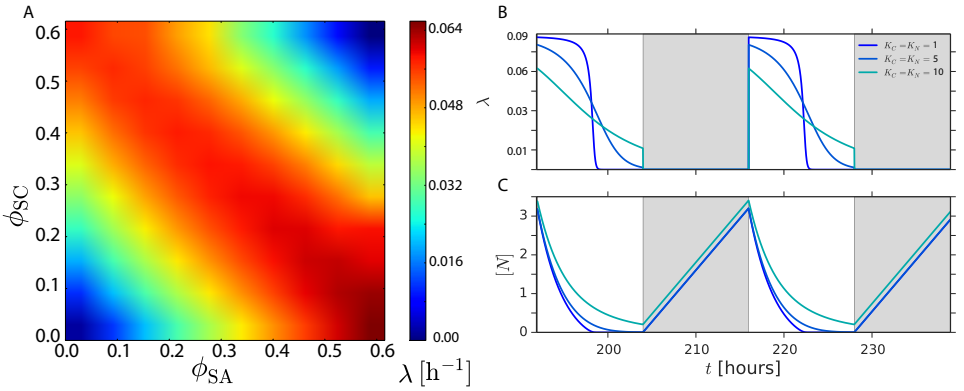

Figure 5.1: Optimal growth strategy in the quasi-equilibrium model. In this model, the proteome fractions relax instantaneously and as such are always in quasi-equilibrium with the instantaneous levels of glycogen, [C](t), and cyanophycin, [N](t). In this model, the instantaneous growth rate is given by Eqs. 5.13 and 5.14 (or equivalently Eqs. 5.17 and 5.18), while the reservoir dynamics is given by Eqs. 5.23 and 5.24. The model is nearly symmetric between day and night, $\tilde{\nu}_C^L = \tilde{\nu}_A^D$, $\nu_{SC} = \nu_{SA}$, $c_G = c_{CP}$, $K_C = K_A$, except that $\nu_A^L = 3/\text{h}$ is slightly larger than $\nu_C^D = 1/\text{h}$. (A) Heat map of the average growth rate over 24h, $\langle\lambda\rangle_{24}$, as a function of ϕ_{SC} and ϕ_{SA}. The heatmap is obtained by numerically propagating Eqs. 5.23 and 5.24, with $\lambda(t)$ given by Eqs. 5.13 and 5.14, for different values of ϕ_{SC} and ϕ_{SA}; the average growth rate is obtained by numerically evaluating $\langle\lambda\rangle_{24} = 1/24\int_0^{24}\lambda(t)$. It is seen that there exists a combination of storing fractions that maximizes the growth rate, ϕ_{SC}^{opt} and ϕ_{SA}^{opt}; moreover, ϕ_{SC}^{opt} is close to zero, while ϕ_{SA}^{opt} is close to the maximal fraction ϕ_{SA}^0 at which the growth rate becomes zero, see Eq. 5.20. (B) Time traces of $\lambda(t)$ at ϕ_{SC}^{opt} and ϕ_{SA}^{opt}, not only for $K_C = 5c_G = K_A = 5c_{CP}$, as in panel A, but also for two other values. Clearly, the cells only grow during the day. The growth rate during the night is zero, because the storing fraction ϕ_{SA}^{opt} is close to the maximal fraction ϕ_{SA}^0 at which the growth rate is zero. This shows that the the optimal strategy in the quasi-equilibrium model is to store as much cyanophycin as possible during the night, because that maximizes the growth rate during the day. The explanation of this behavior is given in Fig. 5.2. (C) Time traces of the cyanophycin levels for different values of $K_C = K_A$. Parameter values: $\nu_C^L = 2/\text{h} = \nu_A^D = 2/\text{h}$; $\tilde{\nu}_C^D = 2/\text{h}$; $\tilde{\nu}_A^L = 6/\text{h}$; $\nu_R = 0.2/\text{h}$; $\nu_{SC} = \nu_{SA} = 0.6/\text{h}$; $K_C = 5c_G = K_A = 5c_A$.

To elucidate Fig. 5.1A, we show in panel B the growth rate $\lambda(t)$ of the system with the optimal storing fractions ϕ_{SC}^{opt} and ϕ_{SA}^{opt}, for three different values of $K_C = K_A$. Strikingly, the growth rate is zero during the night. The cells only grow during the day, even though with these parameters the cells would have the capacity to grow during the night, had they not to store so much cyanophycin. Indeed, the optimal storing fraction ϕ_{SA}^{opt} that maximizes the growth rate is close to the fraction ϕ_{SA}^0 at which the growth rate becomes zero, see Eq. 5.20.

The mechanism that underlies the optimal strategy is illustrated in Fig. 5.2. Panel A shows the average growth rate during the day $\langle\lambda\rangle_L$ as a function of ϕ_{SC} for different values of ϕ_{SA}, while panel B of this figure shows the average growth rate during the night, $\langle\lambda\rangle_D$, as a function of ϕ_{SA} for different values of ϕ_{SC}. First of all, note that the maximum

growth rate during the day is only slightly larger than that during the night—the asymmetry between day and night is indeed (chosen to be) weak. Yet, the optimal strategy, which maximizes the average growth rate over 24h, is to not grow at all during the night. To understand this, note that storing more cyanophycin during the night will enhance the growth rate during the day (panel A), yet lower it during the night (panel B). Similarly, storing more glycogen during the day will raise the growth rate during the night (right B), yet lower it during the day (panel A). The crux is that the cost of storing less glycogen during the day—a lower growth rate at night—decreases when more cyanophycin is stored, while at the same time the benefit of storing more cyanophycin—growing faster during the day—is largest when the amount of stored glycogen is minimal. This tends to favor a strategy where the maximum amount of cyanophycin is stored during the night, while a minimal amount of glycogen is stored during the day. Naturally, the argument also works in the converse direction, yielding a strategy where the maximal amount of glycogen is stored during the day and the minimal amount of cyanophycin is stored during the night. Yet, because the maximal growth rate during the day is larger than the maximal growth rate during the night, the former strategy is favoured.

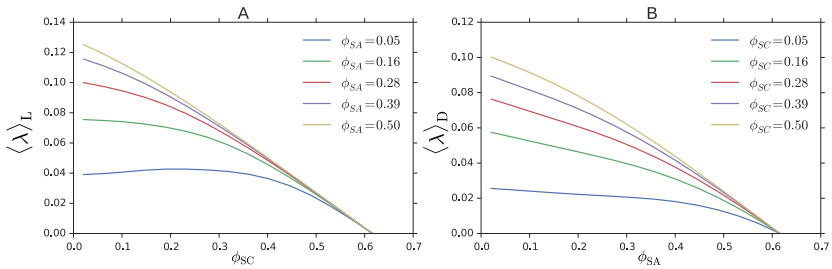

Figure 5.2: Mechanism underlying the optimal strategy that maximizes the growth rate in the quasi-equilibrium model, given by Eqs. 5.13 and 5.14 and Eqs. 5.23 and 5.24. (A) The average growth rate during the day, $\langle\lambda\rangle_L$ as a function of ϕ_{SC} for different values of ϕ_{SA}. (B) The average growth rate during the night, $\langle\lambda\rangle_D$ as a function of ϕ_{SA} for different values of ϕ_{SC}. These figures have been obtained by numerically propagating Eqs. 5.13 and 5.14 and Eqs. 5.23 and 5.24 for different combinations of ϕ_{SC} and ϕ_{SA}. The key point is that the cost of storing less glycogen—a lower growth rate at night—decreases when more cyanophycin is stored (and vanishes in fact when ϕ_{SA} approaches its maximum ϕ^0_{SA} where the growth rate becomes zero), while the benefit of storing more cyanophycin—a higher growth rate during the day—increases as less glycogen is stored during the day (because ϕ_{SC} is smaller). This yields an optimal strategy that maximizes the growth rate in which the cells exclusively grow during the day. Parameter values as in Fig. 5.1: $\nu^{\mathrm{L}}_{\mathrm{C}} = 2/\mathrm{h} = \nu^{\mathrm{D}}_{\mathrm{A}} = 2/\mathrm{h}$; $\tilde{\nu}^{\mathrm{D}}_{\mathrm{C}} = 2/\mathrm{h}$; $\tilde{\nu}^{\mathrm{L}}_{\mathrm{A}} = 6/\mathrm{h}$; $\nu_{\mathrm{R}} = 0.2/\mathrm{h}$; $\nu_{\mathrm{SC}} = \nu_{\mathrm{SA}} = 0.6/\mathrm{h}$; $K_{\mathrm{C}} = 5c_G = K_{\mathrm{A}} = 5c_A$. Growth rates are in units of 1/h.

An important question is how generic this tipping-point strategy in which cells predominantly grow in one phase of the day, is. What is essential is that the maximum growth rate during the day, $\lambda^{\mathrm{L}}_{\mathrm{max}}$ (Eq. 5.15), is larger than that during the night, $\lambda^{\mathrm{D}}_{\mathrm{max}}$ (Eq. 5.19). Yet, the precise values of the efficiencies $\nu^{\mathrm{L/D}}_{\mathrm{C}}$, $\nu^{\mathrm{L/D}}_{\mathrm{A}}$ tend to be less important, depending on the values of ν_{SC} and ν_{SA}. If the model is fully symmetric, $\nu_{\mathrm{SC}} = \nu_{\mathrm{SA}}$,

$\tilde{\nu}_C^D = \tilde{\nu}_A^L$, $c_{CP} = c_G$, except that $\nu_C^L > \nu_A^D$, then a tipping-point strategy is still favored, provided that ν_{SC} and ν_{SA} are not too large with respect to ν_C^L and ν_A^D, respectively. The reason is that while increasing ν_C^L with respect to ν_A^D increases the maximum growth rate during the day, which tends to favor growing exlucisely during the day, it also enhances the capacity to store glycogen (as compared to that of storing cyanophycin), which tends to favor growing at night. This effect is particularly pronounced when ν_{SC} and ν_{SA} are large compared to ν_C^L and ν_A^D, respectively, because then the storing rates become limited by ν_C^L and ν_A^D, rather than being determined by ν_{SC} and ν_{SA}, respectively (see discussion below Eq. 5.22).

The panels of Fig. 5.2 also reveal that the growth rate is initially fairly constant, before it markedly drops to zero when the storing fraction becomes equal to the maximal storing fraction, given by Eq. 5.16 for ϕ_{SC} (panel A) and Eq. 5.20 for ϕ_{SA} (panel B). The curves deviate from the linear relationship between λ and the expression of an unused protein, as found in Scott *et al.* [40]. In fact, also Eqs. 5.13 and 5.14 would predict a linear relationship between $\langle\lambda\rangle_{L/D}$ and ϕ_{SC}/ϕ_{SA} if $\nu_A^L(t)$ and $\nu_C^D(t)$ were constant in time. However, $\nu_A^L(t)$ and $\nu_C^D(t)$ are not constant in time, because the cyanophycin and glycogen concentrations decrease with time, as can be seen for the cyanophycin concentration in panel C of Fig. 5.1 (where ϕ_{SC} and hence [C] are very small). As a result of this reservoir depletion, also the growth rate varies in time. Moreover, the reservor depletion also underlies the observation that the rise in the growth rate upon decreasing ϕ_{SC}/ϕ_{SA} becomes less pronounced for low ϕ_{SC}/ϕ_{SA} (Fig. 5.2): in this regime, the growth rate during the day (night) is limited by the amount of cyanophycin (glycogen) during the night (day); decreasing ϕ_{SC} (ϕ_{SA}) only means that the reservoir is depleted more rapidly, yielding no significant net increase in $\langle\lambda\rangle_L$ and $\langle\lambda\rangle_D$; indeed, only by storing more can the growth rate be enhanced further.

The central prediction of this quasi-equilibrium model is thus that the cells do not tend to grow at night, as observed experimentally for *Cyanothece* [113], because that allows it to grow so much faster during the day that the average growth rate over 24h increases. However, this quasi-equilibrium model is based on the assumption that the proteome relaxes instantly, while the relaxation rate, in the absence of protein degradation, is set by the growth rate, which, with typical cell-division times of 10-70h [27, 106, 107], is fairly low for cyanobacteria. In fact, to grow faster, the cell needs to store more, while the maximum storing capacity is limited by ϕ_{SC}^0 and ϕ_{SA}^0, which depend not only on $\Delta\phi_{R,max}$, but also on ν_C^L and ν_A^D, respectively, as discussed below Eqs. 5.22 and 5.22. How severe this constraint can be, is seen in panel B of Fig. 5.1: for the lowest value of $K_C = K_A$ shown, the cell grows faster during the beginning of the day. However, because the cyanophycin stored is then depleted more rapidly (see panel C below), the growth rate drops sharply well before the end of the day. Here, more cyanophycin can not be stored, simply because ϕ_{SA} has already reached its maximum, ϕ_{SA}^0. The limited capacity to store thus puts a severe constraint on the growth rate, which limits the proteome relaxation rate. Can the cell under these conditions implement the optimal strategy to maximize the growth rate, as shown in Fig. 5.1 and Fig. 5.2? To address this question, we will turn in the next section to the influence of the slow proteome dynamics.

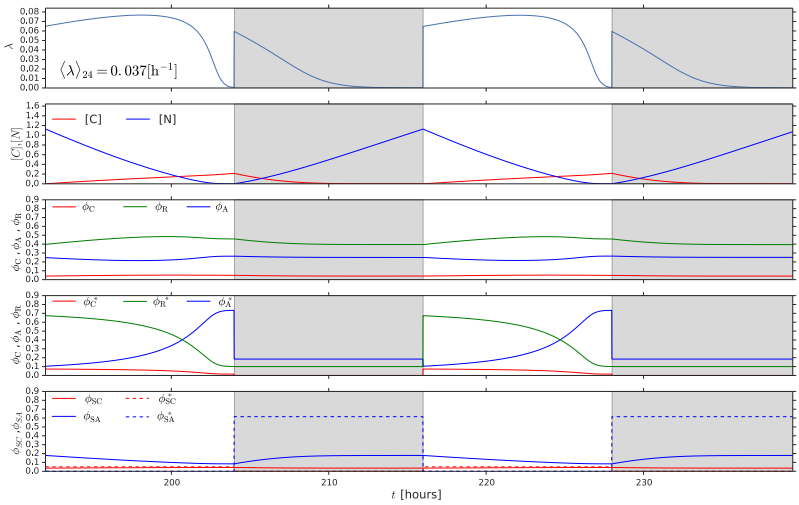

Figure 5.3: Dynamics of the slow-proteome model, given by Eq. 5.29 for $\lambda(t)$, Eq. 5.34 for $\phi_\alpha(t)$, and Eqs. 5.35-5.40, which are solved to yield $\chi_\alpha(t) = \phi^*_\alpha(t)$ in Eq. 5.34 and $\sigma(t) = \sigma^*(t)$ in Eq. 5.29, together with Eqs. 5.23 and 5.24 for the reservoir dynamics. Time traces of the growth rate $\lambda(t)$ (1/h, top row), glycogen levels [C](t) and cyanophycin levels [N](t) (second row), protein fractions $\phi_R(t), \phi_C(t), \phi_A(t)$ (third row), their target fractions $\phi^*_R(t), \phi^*_C(t), \phi^*_A(t)$ (fourth row), and the instantaneous storing fractions $\phi_{SC}(t)$ and $\phi_{SA}(t)$ (solid lines, bottom row)), and their target fractions $\phi^*_{SC}(t)$ and $\phi^*_{SA}(t)$ (dashed lines, bottom row). Note that because of the slow proteome relaxation resulting from the slow growth rate $\lambda(t)$ (see Eq. 5.29), the cell also needs to grow significantly during the night in order to maintain ϕ_{SA}, necessary to make cyanophycin for growth during the day. This is in marked contrast to the dynamics in the quasi-equilibrium model, in which the proteome relaxes instantaneously to changing nutrient levels and the cell does not grow at night (see Fig. 5.1). Please also note that the average growth rate is significantly lower in this slow-proteome model, $\langle\lambda\rangle_{24} = 0.039$/h, than in the quasi-equilibrium model, $\langle\lambda\rangle_{24} = 0.064$/h. Parameter values the same as in Fig. 5.1: $\nu^L_C = 2/\mathrm{h} = \nu^D_A = 2/\mathrm{h}$; $\tilde{\nu}^D_C = 2/\mathrm{h}$; $\tilde{\nu}^L_A = 6/\mathrm{h}$; $\nu_R = 0.2/\mathrm{h}$; $\nu_{SC} = \nu_{SA} = 0.6/\mathrm{h}$; $K_C = 5c_G = K_A = 5c_A$.

5.4.2. SLOW-PROTEOME MODEL

Fig. 5.3 shows time traces of the growth rate, the protein fractions and the glycogen and cyanophycin levels for our slow-proteome model. The parameters ν^β_α are identical to those of the quasi-equilibrium model corresponding to Fig. 5.1, yet ϕ_{SC} and ϕ_{SA} have been optimized to maximize the growth rate $\langle\lambda\rangle_{24}$ over 24h.

The first point to note is that the average growth rate in the slow-proteome model, $\langle\lambda\rangle_{24} = 0.037$, is lower than in the quasi-equilibrium model, which is $\langle\lambda\rangle_{24} = 0.064$. Clearly, the slow relaxation of the proteome drastically lowers the growth rate. The second point is that while the cells predominantly grow during the day (top row), the growth rate during the night is markedly non-zero near the beginning of the night, in marked contrast to the behavior in the quasi-equilibrium model (Fig. 5.1B),

To characterize the growth dynamics further, we show in the second row of Fig. 5.3 the concentration of cyanophycin and glycogen, respectively. It is seen that the cyanophycin levels rise during the night, when nitrogen is stored into cyanophycin, yet fall during the day, when the cyanophycin provides the nitrogen source for protein production. Near the end of the day, the cyanophycin levels approach zero, causing the growth rate to drop to zero. The glycogen levels rise during the day, which makes it possible to grow during the night. During the night, however, the glycogen levels rapidly fall, causing the growth at night to come to a halt.

While the behavior of the reservoir dynamics explains the time-dependent growth rate $\lambda(t)$ to a large degree, a few puzzling features remain to be resolved. The first is that the growth rate at the beginning of the day first rises, even though the levels of cyanohycin already fall. The second is that the growth rate drops rather abruptly near the end of the day, even though the concentration of cyanophycin, [N], is well below the enzyme activation threshold K_A. But perhaps the most important question that needs to be addressed is why the cells decide to store glycogen and grow at night, given that the optimal strategy in the quasi-equilibrium model is not to grow at all during the night (see Fig. 5.1).

To elucidate these questions, we turn to the time traces of the protein fractions, shown in the third to fifth row of Fig. 5.3. The third row shows ϕ_R, ϕ_C, ϕ_A, while the fourth row shows the target fractions $\phi_R^*, \phi_C^*, \phi_A^*$ that the cell aims to reach. The fifth row shows the storing fractions ϕ_{SC} and ϕ_{SA}, together with their target fractions, ϕ_{SC}^* and ϕ_{SA}^*, respectively.

To explain the initial rise of the growth rate, we start by noting that at the end of the night, ϕ_A is large because the cell needs to store cyanophycin during the night, which drains nitrogen flux. The next day, the cell does not need to store nitrogen, while at the beginning of the day the cyanophycin level—the nitrogen source during the day—is still high; taken together this means that the target fraction ϕ_A^* will be relatively low (fourth row). Indeed, at the beginning of the day, the target fraction ϕ_A^* is smaller than the current fraction ϕ_A, causing ϕ_A to fall initially. This allows ϕ_R to rise, and since the growth rate is proportional to ϕ_R (see Eq. 5.29), this tends to raise the growth rate. The growth thus rises initially, because the proteome slowly adapts to maximize the growth rate.

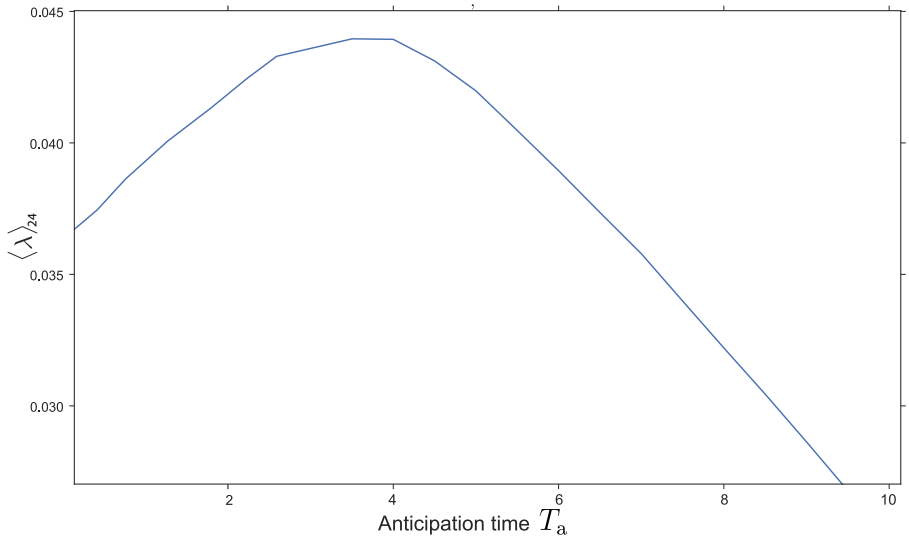

Figure 5.4: The average growth over 24 hours, $\langle\lambda\rangle_{24}$ (1/h), as a function of the anticipation time T_a (h) in the full model, including anticipation. The anticipation model is identical to the slow-proteome model in that it is given by Eq. 5.29 for $\lambda(t)$, Eq. 5.34 for $\phi_\alpha(t)$, and Eqs. 5.35-5.40, which are solved to yield $\chi_\alpha(t) = \phi_\alpha^*(t)$ in Eq. 5.34 and $\sigma(t) = \sigma^*(t)$ in Eq. 5.29, except that the storing fractions ϕ_{SC} and ϕ_{SA} start to be expressed an anticipation time T_a before the beginning of the day and night, respectively; the reservoir dynamics is, as for the other models, given by Eqs. 5.23 and 5.24. It is seen that there is an optimal anticipation time $T_a^{opt} \approx 4.5$h that maximizes the average growth rate over 24 hours. This maximal growth rate is about 15% higher than in the slow-proteome model (see Fig. 5.3). The principal reason is that the cyanophycin-storing fraction can already be made before the beginning of the night, as elucidated in Fig. 5.5. Parameter values the same as in Fig. 5.1: $\nu_C^L = 2/h = \nu_A^D = 2/h$; $\tilde{\nu}_C^D = 2/h$; $\tilde{\nu}_A^L = 6/h$; $\nu_R = 0.2/h$; $\nu_{SC} = \nu_{SA} = 0.6/h$; $K_C = 5c_G = K_A = 5c_A$.

As time progresses, the cyanophycin level falls, which causes the target fraction ϕ_A^* to rise (fourth row). At some point, the current fraction ϕ_A becomes equal to the target fraction ϕ_A^*. From this moment on, ϕ_A will rise in order to maintain the flux of nitrogen in the face of the falling cyanophycin levels. This rise in ϕ_A is accompanied by a drop in ϕ_C and ϕ_R, causing the growth rate to go down.

Finally, why does the cell grow at night? In this model, the cyanophycin storing proteins are not made during the day, which means that then the storing fraction ϕ_{SA} will fall, because of dilution due to growth. Inevitably, at the beginning of the night, the fraction ϕ_{SA} will always be smaller than that at the end of the night before. Consequently, ϕ_{SA} must rise to move towards the target fraction ϕ_{SA}^*, which in this case is close to the maximium at which the growth rate is zero, ϕ_{SA}^0 (dashed blue line in last row). However, in the absence of protein degradation, the proteome can only relax because of growth, and, indeed, this is the reason why the cell needs to grow during the night: without growth, ϕ_{SA} would eventually become zero, and no cyanophycin could be stored. During the night, new storing proteins have to be made, in order to compensate for the drop in ϕ_{SA}

resulting from dilution during the day.

Lastly, in order to grow during the night, the cell needs to store glycogen during the day, which explains why ϕ_{SC} is non-zero during the day. The cell thus adopts a mixed strategy in which it grows during the day and during the night, because this is the optimal strategy in the presence of slow proteome relaxation. In the next section, we will study whether anticipation makes it possible to counteract the detrimental effects of slow proteome relaxation, by initiating a response ahead of time.

5.5. ANTICIPATION

To study the importance of anticipation, we first consider the scenario where the cell can express the storing fractions ϕ_{SC} and ϕ_{SA} before the beginning of the day and the night, respectively; here, we thus do not consider the possibility that cells can anticipate the changes in the protein efficiencies ν_α^β (see Eqs. 5.41 and 5.42). More specifically, we consider 4 optimization parameters: the magnitudes of ϕ_{SC} and ϕ_{SA} and the timings of their expression; to limit the optimisation space, we take the duration of the expression window to be constant, namely 12h. Performing the optimisation, we observed that the growth-rate dependence on the expression timing of ϕ_{SC} was rather weak, because, as we will see below, the optimal ϕ_{SC} is very small. We therefore considered one anticipation time T_a, which determines the times $k24 - T_a$ and $12 + k24 - T_a$, with $k = 0, 1, 2, \ldots$, from which ϕ_{SC} and ϕ_{SA} respectively are expressed for 12 hours at constant values, respectively. This limits the optimisation space to 3 parameters: the magnitudes of ϕ_{SA} and ϕ_{SC}, respectively, and the anticipation time T_a.

To analyze the importance of anticipation, we optimized the growth rate over ϕ_{SA} and ϕ_{SC} for each value of T_a, for the same set of parameters as in Figs. 5.1-5.3. Fig. 5.4 shows the result. It is seen that expressing the storing enzymes about 4.5 hours before the beginning of the next part of the day can speed up growth by about 15%.

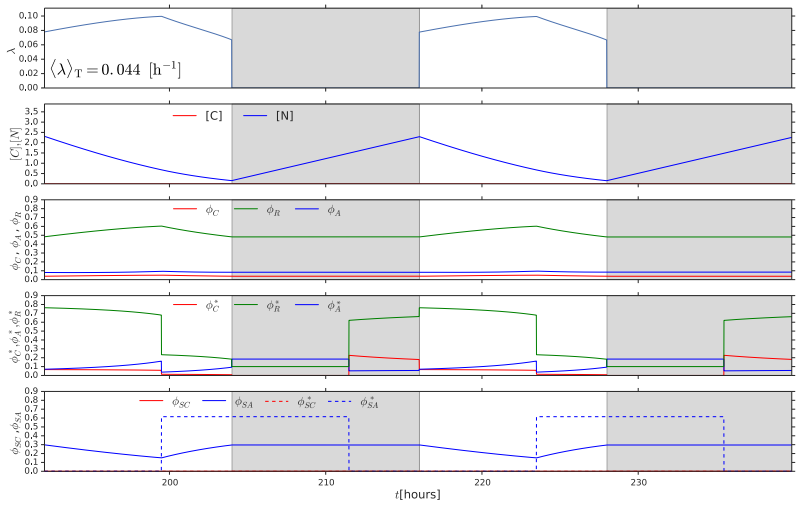

Figure 5.5: Dynamics of the full model, including anticipation. The model is identical to the slow-proteome model in that it is given by Eq. 5.29 for $\lambda(t)$, Eq. 5.34 for $\phi_\alpha(t)$, and Eqs. 5.35-5.40, which are solved to yield $\chi_\alpha(t) = \phi^*_\alpha(t)$ in Eq. 5.34 and $\sigma(t) = \sigma^*(t)$ in Eq. 5.29, except that the storing fractions $\phi_{\rm SC}$ and $\phi_{\rm SA}$ start to be expressed at the optimal anticipation time $T_{\rm a}^{\rm opt} = 4.5$h before the beginning of the day and night, respectively (see Fig. 5.4); the reservoir dynamics is, as for the other models, given by Eqs. 5.23 and 5.24. Time traces of the growth rate $\lambda(t)$ (1/h, top row), glycogen levels [C](t) and cyanophycin levels [N](t) (second row), protein fractions $\phi_{\rm R}(t), \phi_{\rm C}(t), \phi_{\rm A}(t)$ (third row), their target fractions $\phi^*_{\rm R}(t), \phi^*_{\rm C}(t), \phi^*_{\rm A}(t)$ (fourth row), and the instantaneous storing fractions $\phi_{\rm SC}(t)$ and $\phi_{\rm SA}(t)$ (solid lines, bottom row)), and their target fractions $\phi^*_{\rm SC}(t)$ and $\phi^*_{\rm SA}(t)$ (dashed lines, bottom row). The average growth rate over 24 hours in this model, $\langle\lambda\rangle_{24} = 0.044$/h, is about 15% higher than in the slow proteome model. Note also that the growth rate during the day first rises because the proteome is still adapting to the nutrient levels (top row); however, $T_{\rm a} = 4.5$h before the beginning of the night, the growth rate goes down, because the cell prepares for the night by expressing the cyanohycin storing fraction $\phi_{\rm SA}$ (bottom panel). Before the end of the day, $\phi_{\rm SA}$ has reached a level that is sufficient to store enough cyanophycin during the night for fueling growth the next day. Concomitantly, the growth rate is now zero during the night, in contrast to the scenario in the slow-proteome model where $\phi_{\rm SA}$ has to be made during the night, and the cells therefore have to grow during the night Fig. 5.3. Parameter values the same as in Fig. 5.1: $\nu^{\rm L}_{\rm C} = 2$/h $= \nu^{\rm D}_{\rm A} = 2$/h; $\tilde{\nu}^{\rm D}_{\rm C} = 2$/h; $\tilde{\nu}^{\rm L}_{\rm A} = 6$/h; $\nu_{\rm R} = 0.2$/h; $\nu_{\rm SC} = \nu_{\rm SA} = 0.6$/h; $K_{\rm C} = 5{\rm c}_G = K_{\rm A} = 5{\rm c}_A$.

To elucidate this behavior, we show in Fig. 5.5 the time traces for the optimal anticipation time $T_{\rm a}^{\rm opt} = 4.5$h that maximizes the growth rate (Fig. 5.4). The top row shows that, as in the slow-proteome model, the growth rate first rises at the beginning of the day, because the proteome still adapts to the changing nutrient levels. However, at about $T_{\rm a}^{\rm opt} = 4.5$h before the end of the day, the growth rate goes down markedly. This is because the cell starts to express the proteins $\phi_{\rm SA}$ that store cyanophycin during the night (bottom row). Clearly, there is a cost to anticipation: it lowers the instantaneous growth rate. The cell should therefore not express the cyanophycin-storing proteins too early

in the day. Yet, expressing cyanophycin-storing enzymes already during the day also has a marked benefit: it makes it possible to reach a sufficiently high level of ϕ_{SA} before the beginning of the night such that enough cyanophycin can be stored during the night. The cell therefore does not need to grow during the night to raise ϕ_{SA}, as in the slow-proteome model; indeed, even though ϕ_{SA} does not rise during the night, the level is much higher than the average level in the slow-proteome model, so that more cyanophycin is stored during the night, as a result of which the cells grow much faster during the day (compare with Fig. 5.3). Anticipation thus makes it possible to implement the optimal growth strategy as revealed by the quasi-equilibrium model (see Fig. 5.1), which is to grow exclusively during the day, as observed experimentally.

We also considered anticipation of ν_C^β and ν_A^β, as described around Eqs. 5.41 and 5.42. However, because the growth rate is zero at night, the benefit of optimising ν_C^β, ν_A^β is marginal, for two reasons. Firstly, because the cell cannot grow at night, it cannot adjust the proteome before the beginning of the day. Secondly, adjusting the proteome fractions during the day based on the anticipated efficiencies ν_C^D and ν_A^D during the night would lower the instantaneous growth rate, because the instantaneous protein fractions ϕ_α would become suboptimal, i.e. not given by the current efficiencies ν_C^L and ν_A^L.

5.6. DISCUSSION

The power of the framework of Hwa and co-workers is that it provides a coarse-grained description of the proteome with only a limited number of sectors, characterized by enzyme efficiencies that can be measured experimentally [40, 41, 44, 45, 105]. We therefore sought to develop a minimal model, consisting of a small number of sectors that can be characterized experimentally, also given the fact that as yet there is no experimental data that warrants a more detailed model. Nonetheless, even though the model consists of only 3 main sectors and 2 storing sectors, the dynamical behaviour of our model is already very rich. Specifically, our analysis shows that the requirement to store carbon and nitrogen means that the cells tend to adopt an extreme strategy in which they exclusively grow during the day. The fundamental reason is contained in the growth laws uncovered in refs. [40, 41, 44, 45, 105]: storing more glycogen during the day will increase the growth rate during the night, yet this benefit decreases as more cyanophycin-storing enzymes are expressed during the night (and vanishes in fact when this fraction approaches its maximum at which the growth rate becomes zero, see Fig. 5.2); at the same time, the benefit of storing more cyanophycin during the night—growing faster during the day—increases as less glycogen is stored during the day. The interplay between these two effects creates a positive feedback loop in which the cells store as much cyanophycin as possible during the night and as little glycogen as needed during the day to maximize the growth rate during the day.

While we focus here on the cyanobacterium *Cyanothece*, the application of our framework to cyanobacteria such as *Synechococcus* and *Synechocystis* predicts that also these bacteria tend to grow predominantly during the day (data not shown). If the marginal cost of storing glycogen—the reduction in the growth rate during the day—is higher than the marginal benefit—the increase in the growth rate during the night—then the optimal strategy is to not store any glycogen at all for growth during the night, and hence exclu-

sively grow during the day.

Our analysis also reveals that the slow relaxation of the proteome creates a severe challenge in implementing the optimal strategy. In the absence of protein degradation, the cells need to grow in order to adjust their proteome. Yet, cyanobacterial cells grow slowly, which means that the relaxation time will be long compared to the 24h period of the day-night rhythm. As a result, to reach the required cyanophycin-storing fraction, cells would need to grow significantly during the night, in the absence of anticipation. Indeed, the principal benefit of anticipation, according to our model, is that it makes it possible to express the storing fractions ahead of time. Interestingly, this prediction appears to be supported by recent mass-spectrometry proteomics data and RNA-sequencing transcriptomics data: the expression of cyanophycin is highest in the late *light* and progressively diminishes during the night into the early light [119].

While the dynamics of our minimal model is already complex, it seems natural to increase the number of sectors as more data becomes available. In particular, it might be of interest to distinguish between proteins of a given sector that are generic, i.e. expressed at significant levels both during the day and during the night, and proteins that are specific to one part of the day, such as the photosynthesis components. The challenge will be to define major sub-sectors and devise experiments which make it possible to measure the associated enzyme efficiencies.

Another natural extension of our model is to include protein degradation. First of all, active protein degradation makes it possible to increase the proteome relaxation rate. While active protein degradation by itself tends to slow down the growth rate, reaching the optimal proteome partitioning faster might offset this cost. Secondly, some proteins tend to be unstable, meaning that degradation by spontaneous decay is inevitable. In our full model, the amount of glycogen stored is vanishingly small, because our model only considers glycogen as a source of carbon for protein synthesis and the cells do not grow during the night. At the same time, it is well known that cyanobacteria store glycogen. Some of the stored glycogen will be essential for providing the energy to run maintenance processes, such as DNA repair, or to drive the cyanophycin-storing reactions—storing cyanophycin is ATP consuming [123]. However, it is also possible that glycogen is needed to synthesize those proteins that have decayed significantly during the night, such as the components of the protein synthesis machinery. It would then be interesting to see whether including this into the model would yield the prediction that it is beneficial to start expressing these proteins before the end of the night, as observed experimentally [119].

In our model, cyanophycin serves exclusively as a source of nitrogen, which is a reasonable starting point given that cyanophycin is very rich in nitrogen. However, cyanophycin also contains carbon and it has indeed been speculated that it also provides a carbon store [117]. Our model could be extended to include this. While the benefit of providing a carbon source during the day might be small in the presence of high CO_2 and light levels, the cost of draining carbon flux at night might be more significant—this effect could be included by adding a term to the equation for the carbon flux (Eq. 5.3), representing the carbon flux into cyanophycin during the night. Including this effect in the model will also raise the required levels of glycogen.

In future work, we will use this model to predict the growth rate of mutants with

altered clock periods and wild-type cells growing in light-dark cycles with periods deviating from 24h [39]. When wild-type cells of *Synechococcus elongatus* are competed against an arrhythmic strain, then the latter are rapidly out-competed by the wild-type when the cells are exposed to 12h:12h light:dark cycles [39]. Under competition in constant light conditions, however, arrhythmic strains grew slightly better than the wild type [39]. This indicates that the clock may confer a fitness benefit, but only if the organism lives in a circadian environment. Apparently, an oscillatory pattern of gene expression is a disadvantage in continuous light. In another set of experiments, mutants with different clock periods lengths were competed with wild-type strains and with each other, with the result that the strain whose clock period most closely matched that of the light-dark cycle won the competition [38, 39]. It will be of interest to see whether the framework presented here can describe these types of experiments.

BIBLIOGRAPHY

[1] T. Roenneberg and M. Merrow, Journal of Biological Rhythms **17**, 495 (2002).

[2] P. Ma *et al.*, PLoS genetics **12**, e1005922 (2016).

[3] M. Ishiura *et al.*, Science **281**, 1519 (1998).

[4] M. Nakajima *et al.*, Science (New York, N.Y.) **308**, 414 (2005).

[5] J. Holtzendorff *et al.*, Journal of Biological Rhythms **23**, 187 (2008).

[6] E. R. Zinser *et al.*, PLoS ONE **4**, e5135 (2009).

[7] C. Troein, J. C. W. Locke, M. S. Turner, and A. J. Millar, Current Biology **19**, 1961 (2009).

[8] M. J. Rust, S. S. Golden, and E. K. O'Shea, Science (New York, N.Y.) **331**, 220 (2011).

[9] G. K. Pattanayak, G. Lambert, K. Bernat, and M. J. Rust, Cell Reports **13**, 2362 (2015).

[10] M. Monti, D. K. Lubensky, and P. R. ten Wolde, arXiv.org:1706.02226 (2017).

[11] J. S. van Zon, D. K. Lubensky, P. R. H. Altena, and P. R. ten Wolde, Proc Natl Acad Sci USA **104**, 7420 (2007).

[12] M. J. Rust *et al.*, Science **318**, 809 (2007).

[13] S. Clodong *et al.*, Molecular Systems Biology **3**, 90 (2007).

[14] T. Mori *et al.*, PLoS Biology **5**, e93 (2007).

[15] D. Zwicker, D. K. Lubensky, and P. R. ten Wolde, Proceedings of the National Academy of Sciences of the United States of America **107**, 22540 (2010).

[16] J. Lin, J. Chew, U. Chockanathan, and M. J. Rust, Proceedings of the National Academy of Sciences of the United States of America **111**, E3937 (2014).

[17] J. Paijmans, D. K. Lubensky, and P. R. ten Wolde, PLoS Computational Biology **13**, e1005415 (2017).

[18] J. Paijmans, D. K. Lubensky, and P. R. ten Wolde, Biophys. J. **113**, 157 (2017).

[19] M. Monti and P. R. ten Wolde, Physical Biology **13**, 1 (2016).

[20] Supporting Information.

[21] N. B. Becker, A. Mugler, and P. R. ten Wolde, Physical Review Letters **115**, 258103 (2015).

[22] A. Pikovsky, M. Rosenblum, and J. Kurths, *Synchronisation: A universal concept in nonlinear sciences* (Cambridge University Press, Cambridge, 2003).

[23] Y. Xu, T. Mori, and C. H. Johnson, The EMBO journal **19**, 3349 (2000).

[24] Y. Nakahira *et al.*, Proceedings of the National Academy of Sciences of the United States of America **101**, 881 (2004).

[25] T. Nishiwaki *et al.*, Proceedings of the National Academy of Sciences **101**, 13927 (2004).

[26] J. Tomita, M. Nakajima, T. Kondo, and H. Iwasaki, Science **307**, 251 (2005).

[27] S. W. Teng *et al.*, Science **340**, 737 (2013).

[28] J. Paijmans, M. Bosman, P. R. ten Wolde, and D. K. Lubensky, Proceedings of the National Academy of Sciences of the United States of America **113**, 4063 (2016).

[29] J. Paulsson, Nature **427**, 415 (2004).

[30] S. Tănase-Nicola, P. B. Warren, and P. R. ten Wolde, Physical Review Letters **97**, 068102 (2006).

[31] C. C. Govern and P. R. ten Wolde, Physical Review Letters **113**, 258102 (2014).

[32] R. Cheong *et al.*, Science **334**, 354 (2011).

[33] F. Tostevin and P. R. ten Wolde, Physical Review E **81**, 061917 (2010).

[34] J. Guckenheimer and P. J. Holmes, *Nonlinear Oscillations, Dynamical Systems, and Bifurcations of Vector Fields* (Springer, New York, ADDRESS, 1983).

[35] V. S. Anishchenko *et al.*, Nonlinear dynamics of chaotic and stochastic systems: tutorial and modern developments (2007).

[36] P. B. Warren, S. Tănase-Nicola, and P. R. ten Wolde, The Journal of Chemical Physics **125**, 144904 (2006).

[37] C. W. Gardiner, *Handbook of Stochastic Methods* (Springer-Verlag, Berlin, 1985).

[38] Ouyang Y, Andersson CR, Kondo T, Golden SS, Johnson CH (1998) Resonating circadian clocks enhance fitness in cyanobacteria. *Proceedings of the National Academy of Sciences of the United States of America* 95:8660–8664.

[39] Woelfle MA, Ouyang Y, Phanvijhitsiri K, Johnson CH (2004) The Adaptive Value of Circadian ClocksAn Experimental Assessment in Cyanobacteria. *Current Biology* 14:1481–1486.

[40] Scott M, Gunderson CW, Mateescu EM, Zhang Z, Hwa T (2010) Interdependence of Cell Growth and Gene Expression: Origins and Consequences. *Science* 330:1099–1102.

[41] You C, et al. (2013) Coordination of bacterial proteome with metabolism by cyclic AMP signalling. *Nature* pp 1–6.

[42] Deris JB, et al. (2013) The Innate Growth Bistability and Fitness Landscapes of Antibiotic-Resistant Bacteria. *Science* 342:1237435–1237435.

[43] Li GW, Burkhardt D, Gross C, Weissman JS (2014) Quantifying Absolute Protein Synthesis Rates Reveals Principles Underlying Allocation of Cellular Resources. *Cell* 157:624–635.

[44] Erickson DW, et al. (2017) A global resource allocation strategy governsgrowth transition kinetics of Escherichia coli. *Nature* 551:119–123.

[45] Mori M, Schink S, Erickson DW, Gerland U, Hwa T (2017) Quantifying the benefit of a proteome reserve in fluctuating environments. *Nature Communications* pp 1–7.

[46] Ziv E, Nemenman I, WIggins CH (2007) Optimal signal processing in small stochastic biochemical networks. *PloS one* 2:e1077.

[47] Tostevin F, ten Wolde PR (2009) Mutual Information between Input and Output Trajectories of Biochemical Networks. *Physical Review Letters* 102:218101.

[48] Mehta P, Goyal S, Long T, Bassler BL, Wingreen NS (2009) Information processing and signal integration in bacterial quorum sensing. *Molecular systems biology* 5:325.

[49] Tkačik G, Walczak AM, Bialek W (2009) Optimizing information flow in small genetic networks. *Physical Review E* 80:031920.

[50] Tostevin F, ten Wolde PR (2010) Mutual information in time-varying biochemical systems. *Phys Rev E Stat Nonlin Soft Matter Phys* 81:061917.

[51] de Ronde W, Tostevin F, ten Wolde PR (2010) Effect of feedback on the fidelity of information transmission of time-varying signals. *Physical Review E* 82.

[52] Tkacik G, Prentice JS, Balasubramanian V, Schneidman E (2010) Optimal population coding by noisy spiking neurons. *Proceedings of the National Academy of Sciences of the United States of America* 107:14419–24.

[53] Walczak AM, Tkačik G, Bialek W (2010) Optimizing information flow in small genetic networks. II. Feed-forward interactions. *Physical Review E* 81:041905.

[54] de Ronde W, Tostevin F, ten Wolde P (2011) Multiplexing Biochemical Signals. *Physical Review Letters* 107:1–4.

[55] de Ronde W, Tostevin F, ten Wolde P (2012) Feed-forward loops and diamond motifs lead to tunable transmission of information in the frequency domain. *Physical Review E* 86:021913.

[56] Dubuis JO, Tkacik G, Wieschaus EF, Gregor T, Bialek W (2013) Positional information, in bits. *Proceedings of the National Academy of Sciences of the United States of America* 110:16301–8.

[57] Bowsher CG, Voliotis M, Swain PS (2013) The fidelity of dynamic signaling by noisy biomolecular networks. *PLoS Computational Biology* 9:e1002965.

[58] Selimkhanov J, et al. (2014) Systems biology. Accurate information transmission through dynamic biochemical signaling networks. *Science* 346:1370–1373.

[59] de Ronde W, Wolde PRt (2014) Multiplexing oscillatory biochemical signals. *Physical Biology* 11:026004.

[60] Sokolowski TR, Tkačik G (2015) Optimizing information flow in small genetic networks. IV. Spatial coupling. *Physical Review E* 91:062710.

[61] Becker NB, Mugler A, ten Wolde PR (2015) Optimal Prediction by Cellular Signaling Networks. *Physical Review Letters* Accepted.

[62] Monti M, ten Wolde PR (2016) The accuracy of telling time via oscillatory signals. *Physical Biology* 13:1–14.

[63] Shannon CE (1948) The mathematical theory of communication. 1963. *M.D. computing : computers in medical practice* 14:306–17.

[64] Johnson CH, Egli M, Stewart PL (2008) Structural insights into a circadian oscillator. *Science* 322:697–701.

[65] Liu C, Weaver DR, Strogatz SH, Reppert SM (1997) Cellular construction of a circadian clock: period determination in the suprachiasmatic nuclei. *Cell* 91:855–860.

[66] Yamaguchi S (2003) Synchronization of Cellular Clocks in the Suprachiasmatic Nucleus. *Science* 302:1408–1412.

[67] Mihalcescu I, Hsing WH, Leibler S (2004) Resilient circadian oscillator revealed in individual cyanobacteria. *Nature* 430:81–85.

[68] Mugler A, Walczak A, Wiggins C (2010) Information-Optimal Transcriptional Response to Oscillatory Driving. *Physical Review Letters* 105:058101.

[69] Kageyama H, Kondo T, Iwasaki H (2003) Circadian formation of clock protein complexes by KaiA, KaiB, KaiC, and SasA in cyanobacteria. *J Biol Chem* 278:2388–95.

[70] Nishiwaki T, et al. (2007) A sequential program of dual phosphorylation of KaiC as a basis for circadian rhythm in cyanobacteria. *EMBO J* 26:4029–4037.

[71] Kitayama Y, Nishiwaki T, Terauchi K, Kondo T (2008) Dual KaiC-based oscillations constitute the circadian system of cyanobacteria. *Genes Dev* 22:1513–1521.

[72] Takai N, et al. (2006) A KaiC-associating SasA-RpaA two-component regulatory system as a major circadian timing mediator in cyanobacteria. *Proc Natl Acad Sci USA* 103:12109–14.

[73] Taniguchi Y, et al. (2007) labA: a novel gene required for negative feedback regulation of the cyanobacterial circadian clock protein KaiC. *Gens Dev* 21:60–70.

[74] Taniguchi Y, Takai N, Katayama M, Kondo T, Oyama T (2010) Three major output pathways from the KaiABC-based oscillator cooperate to generate robust circadian kaiBC expression in cyanobacteria. *Proc Natl Acad Sci USA* 107:3263–8.

[75] Gutu A, O'Shea EK (2013) Two antagonistic clock-regulated histidine kinases time the activation of circadian gene expression. *Mol Cell* 50:288–294.

[76] Markson JS, Piechura JR, Puszynska AM, O'Shea EK (2013) Circadian control of global gene expression by the cyanobacterial master regulator RpaA. *Cell* 155:1396–408.

[77] Paulsson J (2004) Summing up the noise in gene networks. *Nature* 427:415.

[78] Berg HC, Purcell EM (1977) Physics of chemoreception. *Biophysical Journal* 20:193.

[79] Ueda M, Shibata T (2007) Stochastic signal processing and transduction in chemotactic response of eukaryotic cells. *Biophysical Journal* 93:11–20.

[80] Bialek W, Setayeshgar S (2005) Physical limits to biochemical signaling. *Proceedings of the National Academy of Sciences USA* 102:10040.

[81] Wang K, Rappel WJ, Kerr R, Levine H (2007) Quantifying noise levels in intercellular signals. *Physical Review E* 75:061905.

[82] Rappel WJ, Levine H (2008) Receptor noise and directional sensing in eukaryotic chemotaxis. *Physical Review Letters* 100:228101.

[83] Endres RG, Wingreen NS (2009) Maximum likelihood and the single receptor. *Physical Review Letters* 103:158101.

[84] Hu B, Chen W, Rappel WJ, Levine H (2010) Physical limits on cellular sensing of spatial gradients. *Physical Review Letters* 105:048104.

[85] Mora T, Wingreen NS (2010) Limits of sensing temporal concentration changes by single cells. *Physical Review Letters* 104:248101.

[86] Govern CC, ten Wolde PR (2012) Fundamental limits on sensing chemical concentrations with linear biochemical networks. *Physical Review Letters* 109:218103.

[87] Mehta P, Schwab DJ (2012) Energetic costs of cellular computation. *Proceedings of the National Academy of Sciences USA* 109:17978–17982.

[88] Skoge M, Meir Y, Wingreen NS (2011) Dynamics of Cooperativity in Chemical Sensing among Cell-Surface Receptors. *Physical Review Letters* 107:178101.

[89] Skoge M, Naqvi S, Meir Y, Wingreen NS (2013) Chemical sensing by nonequilibrium cooperative receptors. *Physical Review Letters* 110:248102.

[90] Kaizu K, et al. (2014) The berg-purcell limit revisited. *Biophysical journal* 106:976–985.

[91] Govern CC, ten Wolde PR (2014) Optimal resource allocation in cellular sensing systems. *Proceedings of the National Academy of Sciences of the United States of America* 111:17486–17491.

[92] Lang AH, Fisher CK, Mora T, Mehta P (2014) Thermodynamics of Statistical Inference by Cells. *Physical Review Letters* 113:148103.

[93] Tkačik G, Walczak AM (2011) Information transmission in genetic regulatory networks: a review. *Journal of physics. Condensed matter : an Institute of Physics journal* 23:153102.

[94] Taniguchi Y, et al. (2010) Quantifying E. coli Proteome and Transcriptome with Single-Molecule Sensitivity in Single Cells. *Science* 329:533–538.

[95] Tănase-Nicola S, Warren PB, ten Wolde PR (2006) Signal detection, modularity, and the correlation between extrinsic and intrinsic noise in biochemical networks. *Physical Review Letters* 97:068102.

[96] Mitra PP, Stark JB (2001) Nonlinear limits to the information capacity of optical fibre communications. *Nature*.

[97] Pfeuty B, Thommen Q, Lefranc M (2011) Robust entrainment of circadian oscillators requires specific phase response curves. *Biophysical journal* 100:2557–65.

[98] Hasegawa Y, Arita M (2013) Circadian clocks optimally adapt to sunlight for reliable synchronization. *Journal of the Royal Society, Interface / the Royal Society* 11:20131018–20131018.

[99] Hasegawa Y, Arita M (2014) Optimal Implementations for Reliable Circadian Clocks. *Physical Review Letters* 113:108101.

[100] Gillespie DT (2000) The chemical Langevin equation. *The Journal of Chemical Physics* 113:297–306.

[101] Liu X, et al. (2007) A G Protein-Coupled Receptor Is a Plasma Membrane Receptor for the Plant Hormone Abscisic Acid. *Science* 315:1712–1716.

[102] Phong C, Markson JS, Wilhoite CM, Rust MJ (2013) Robust and tunable circadian rhythms from differentially sensitive catalytic domains. *Proceedings of the National Academy of Sciences of the United States of America* 110:1124–9.

[103] Paijmans J, Lubensky DK, Rein ten Wolde P (2017) Robustness of synthetic oscillators in growing and dividing cells. *Physical Review E* 95:052403.

[104] Paijmans J, Lubensky DK, Wolde PR (2016) Period robustness and entrainability under changing nucleotide concentrations in the post-translational Kai circadian clock. *arXiv.org*.

[105] Hui S, et al. (2015) Quantitative proteomic analysis reveals a simple strategy of global resource allocation in bacteria. *Molecular Systems Biology* 11:e784–e784.

[106] Sinetova MA, Červený J, Zavřel T, Nedbal L (2012) Journal of Biotechnology. *Journal of Biotechnology* 162:148–155.

[107] Bernstein HC, et al. (2014) Effect of mono- and dichromatic light quality on growth rates and photosynthetic performance of Synechococcus sp. PCC 7002. *Frontiers in Microbiology* 5:488.

[108] Reddy KJ, Haskell JB, Sherman DM, Sherman LA (1993) Unicellular, aerobic nitrogen-fixing cyanobacteria of the genus Cyanothece. *Journal of Bacteriology* 175:1284–1292.

[109] Haselkorn R (1978) HETEROCYSTS. *Ann. Rev. Plant Physiol* 29:319–344.

[110] Flores E, Herrero A (2010) Compartmentalized function through cell differentiation in filamentous cyanobacteria. *Nature Reviews Microbiology* 8:39–50.

[111] Schneegurt MA, Sherman DM, Nayar S, Sherman LA (1994) Oscillating behavior of carbohydrate granule formation and dinitrogen fixation in the cyanobacterium Cyanothece sp. strain ATCC 51142. *Journal of Bacteriology* 176:1586–1597.

[112] Schneegurt MA, Tucker DL, Ondr JK, Sherman DM, Sherman LA (2000) Metabolic rhythms of a diazotrophic cyanobacterium, Cyanothece sp. strain ATCC 51142, heterotrophically grown in continuous dark. *Journal of Phycology* pp 107–117.

[113] Červený J, Nedbal L (2009) Metabolic Rhythms of the Cyanobacterium Cyanothece sp. ATCC 51142 Correlate with Modeled Dynamics of Circadian Clock. *Journal of Biological Rhythms* 24:295–303.

[114] Stöckel J, et al. (2008) Global transcriptomic analysis of Cyanothece 51142 reveals robust diurnal oscillation of central metabolic processes. *Proceedings of the National Academy of Sciences of the United States of America* 105:6156–6161.

[115] Toepel J, Welsh E, Summerfield TC, Pakrasi HB, Sherman LA (2008) Differential Transcriptional Analysis of the Cyanobacterium Cyanothece sp. Strain ATCC 51142 during Light-Dark and Continuous-Light Growth. *Journal of Bacteriology* 190:3904–3913.

[116] Stöckel J, et al. (2011) Diurnal Rhythms Result in Significant Changes in the Cellular Protein Complement in the Cyanobacterium Cyanothece 51142. *PLoS ONE* 6:e16680.

[117] Aryal UK, et al. (2011) Dynamic proteomic profiling of a unicellular cyanobacterium Cyanothece ATCC51142 acrosslight-dark diurnal cycles. *BMC Systems Biology* 5:194.

[118] Aryal UK, et al. (2011) Dynamic Proteome Analysis of Cyanothecesp. ATCC 51142 under Constant Light. *Journal of Proteome Research* 11:609–619.

[119] Welkie D, et al. (2014) Transcriptomic and proteomic dynamics in the metabolism of a diazotrophic cyanobacterium, Cyanothece sp. PCC 7822 during a diurnal light–dark cycle. *BMC Genomics* 15:1185.

[120] Reimers AM, Knoop H, Bockmayr A, Steuer R (2017) Cellular trade-offs and optimal resource allocation during cyanobacterial diurnal growth. *Proceedings of the National Academy of Sciences of the United States of America*.

[121] Van den Ende M (2017) Master's thesis (Universiteit van Amsterdam).

[122] Scialdone A, et al. (2013) Arabidopsis plants perform arithmetic division to prevent starvation at night. *eLife* 2:e00669–e00669.

[123] Aboulmagd E, Oppermann-Sanio FB, Steinbuchel A (2001) Purification of Synechocystis sp. Strain PCC6308 Cyanophycin Synthetase and Its Characterization with Respect to Substrate and Primer Specificity. *Applied and Environmental Microbiology* 67:2176–2182.

SUMMARY

Almost all organisms on our planet exhibit phases of rest and activity. It is not well understood why these two phases have evolved. However, it is clear that these phases are synchronized with the day-night cycle in the environment. To do so, the organism must know the time. Many organisms, ranging from cyanobacteria, fungi, to plants and animals, employ a circadian clock to estimate the time of the day. A hallmark of these clocks is that they can oscillate autonomously with a period of nearly 24 hours. Yet, to keep the clock in synchrony with the environment, the clocks are also coupled to environmental signals, such as light or temperature.

These clocks orchestrate the cellular and behavioral activity of the organism with the day-night cycle. It is possible to observe in our daily life the signs of their existence. For instance, an Albizia tree (the silk worm tree) opens its leaves during the day to do photosynthesis, yet during the night it closes them to protect the leaves from insects. When an Albizia tree is grown under constant light conditions, the open-close rhythmic behavior of the leaves continues to exist. It shows that this tree has an internal clock that allows it to estimate the time, and regulate its activity even in the absence of any environmental cue.

How do cells infer the time? What is the precision by which a clock can estimate the time? What are the properties of these clocks that allow them to be robustly entrained by environmental signals in the presence of biochemical noise? What is the benefit of a bona fide clock that can tick autonomously, as compared to an hour glass clock that relies on a daily resetting? What are the principles of circadian metabolism? These are the questions that I addressed in this thesis. Using numerical simulations and analytical approaches I studied the dynamics of circadian clocks and their ability to transmit information. Moreover, I introduced, for the first time in the clock field, the mutual information as a measure to quantify the precision by which clocks can estimate the time.

In the first project, I addressed the question how accurately the cell can estimate the time from an ensemble of oscillatory proteins driven by a circadian clock. Using an analytical approach, I studied how the precision depends on the number of readout proteins, and on the magnitude and cross-correlations in and between the noise in the different readout proteins. Interestingly, I found that in the regime of low noise (compared to the amplitude), cross-correlations in the noise between the readout proteins can increase the precision.

How circadian clocks are coupled to their environment is one of the wide-open questions in chronobiology. This coupling is characterized by a so-called Phase Response Curve (PRC), which describes the change in the phase of the clock as a function of the phase of the clock at which the stimulus is applied. Different organisms exhibit different PRCs, although many share a number of characteristics: they often have a positive lobe (corresponding to a positive phase shift), followed by a dead-zone in which the clock does not respond to the stimulus at all, which in turn is followed by a negative lobe.

How the performance of the clock depends on the shape of the phase-response curve, the coupling strength, the intrinsic period of the clock, and the internal noise, is not understood. I addressed this question by modeling the clock as a noisy phase oscillator coupled to an external signal. My results reveal that there is an optimal coupling strength that maximizes the mutual information: indeed, the surprising result is that coupling the clock too strongly, causes the mutual information to go down; this is because coupling the system too strongly leads to a non-linearity in the mapping between the actual time and the phase of the clock, which hampers information transmission. However, the optimal coupling strength does increase with the strength of the internal noise. In addition, I found that the optimal intrinsic clock period can differ from 24 hours. Furthermore, I studied extensively the optimal shape of the PRC as a function the internal-noise strength. Interestingly, I found that the width of the dead-zone depends on the magnitude of the internal noise. This leads to clear predictions that can be tested experimentally. Lastly, I developed different theories, and show that they successfully describe the system in different regimes.

In chapter 4, I addressed the most fundamental question of this thesis: What is the benefit of a bona fide clock that can tick autonomously with a period of 24 hours? Many organisms employ such a circadian clock. However, there are cyanobacteria and purple bacteria that possess an hour glass, which cannot oscillate autonomously, but relies on periodic driving for exhibiting oscillations. A canonical (bona fide) clock is a limit-cycle oscillator – a system with a limit-cycle attractor – while an hour glass is a damped oscillator – a system with a fixed-point attractor. I first studied three different computational models, which are inspired by the cyanobacteria and purple bacteria; two are damped oscillators, while one is a limit-cycle oscillator. The principal result is that for low input noise, the performance of the damped oscillator and the limit-cycle oscillator is very similar, but that for high input noise, the limit-cycle oscillator is far superior. Clearly, the limit-cycle is much more robust to input noise. I continue the analysis by asking whether this observation depends on the intricate details of the system, or whether it is a general phenomenon. Using a well-known model called the Stuart-Landau oscillator, we tackled the problem analytically, looking for universal behavior. The Stuart-Landau model describes a weakly non-linear oscillator close to the Hopf bifurcation where the autonomous oscillations emerge. By changing a single parameter, the system can be moved from a regime in which it exhibits damped oscillations in the absence of driving, to a regime in which it can sustain autonomous oscillations. I found that this model can reproduce the principal result of the computational models. This shows that limit-cycle oscillators are generically more robust to input noise than damped oscillators. The intuitive explanation is that damped oscillators cannot lift the trade-off between signal and noise, whereas limit-cycle oscillators can: lowering the coupling of a damped oscillator to the input reduces the propagation of input noise, but it also lowers the amplitude of the oscillations (the signal), such that the signal-to-noise ratio remains unchanged; in contrast, lowering the coupling of the limit-cycle oscillator also reduces input-noise propagation, yet the amplitude remains essentially constant, because this is an inherent, robust property of the limit-cycle.

In the last chapter of the thesis, I have studied the design principles of circadian metabolism. I investigate the metabolism of cyanobacterial cells that exhibit photo-

synthesis, which means that they have a constraint set by the environment: during the day they can perform photosynthesis, but during the night they need to switch their metabolic activity to obtain energy from other sources. Here, I tried to understand what the optimal strategy for circadian metabolism is, and whether this can explain why many cyanobacteria grow exclusively during the day. To this end, I have adopted a phenomenological model that can successfully describe the relationship between growth and the organization of the proteome in the bacterium Escherichia coli. I extended this model to study a particular cyanobacterium, called Cyanothece. During the day, this bacterium fixes carbon via photosynthesis, using one fraction for growth and storing another in the form of glycogen. During the night, it fixes nitrogen, storing it in the form of a polymer called cyanophycin. The model predicts that the need to store glycogen during the day and nitrogen during the night, tends to generate an extreme growth strategy, in which the cells grow exclusively during the day, as observed experimentally. This behavior can be understood from the growth laws that have been identified for E. coli. Yet, the analysis also shows that the slow growth during the night poses a major challenge for implementing this strategy. Interestingly, by exploiting the knowledge on time, as provided by the circadian clock, the cell can anticipate the changes between and night, thereby enabling it to implement the optimal growth strategy. My study is arguably the first to give a quantitative demonstration of the benefit of a circadian clock.

Concluding, using tools from statistical physics, I have analyzed how reliably cells can infer the time using circadian clocks, the coupling of clocks to entrainment signals, the benefit of circadian clocks in estimating the time, and what the benefit of knowing the time is for steering metabolism.

SAMENVATTING

Vrijwel alle organismen op onze planeet leggen fasen van rust en activiteit aan de dag. Waarom deze twee toestanden zijn geëvolueerd is nog steeds niet volledig begrepen. Het is echter duidelijk dat organismen de activiteitsschommelingen met het dag-nacht ritme synchroniseren, en dat ze hiervoor de tijd bijhouden. Veel organismen, van cyanobacteriën en schimmels tot planten en dieren, hebben een biologische klok om het tijdstip te kunnen schatten. Eén van de belangrijkste eigenschap van deze klokken is dat ze zelfstandig kunnen oscilleren met een periode van ongeveer 24 uur. Maar om deze synchroon te laten lopen met het dag-nacht ritme, moet de klok aanwijzingen halen uit de omgeving, door bijvoorbeeld licht- of temperatuursignalen te meten.

Biologische klokken orkestreren de activiteit van een organisme met het dag-nacht ritme. In ons dagelijks leven kunnen we de gevolgen van biologische klokken zien. Zo opent de Albizia, of Perzische slaapboom, overdag zijn bladeren om het zonlicht op te vangen, om ze 's nachts weer te sluiten als bescherming tegen insectenvraat. Deze ritmes gaan zelfs door als de Albizia altijd in het licht staat. Dit laat zien dat de boom een interne klok heeft waarmee hij kan schatten hoe laat het is, en hij reguleert zijn activiteit ook zonder een signaal van buitenaf. Hoe kunnen cellen het tijdstip schatten? Hoe precies kunnen ze dat? Wat zijn de eigenschappen van deze klokken die ervoor zorgen dat ze robuust worden gesynchroniseerd met omgevingssignalen, terwijl er ruis zit in die signalen? Wat is het voordeel van een bonafide klok die zelf tikt, in plaats van een soort zandloper die elke dag opnieuw gezet moet worden? Wat zijn de principes die cellen volgen in hun metabole ritmes? Dit zijn de vragen waarop ik me richt in dit proefschrift. Ik heb de dynamica van biologische klokken en hun vermogen om informatie door te geven bestudeerd, gebruikmakend van computersimulaties en analytische methoden. Verder heb ik voor het eerst de wiskundige grootheid wederzijdse informatie toegepast om te kwantificeren met welke precisie klokken de tijd kunnen schatten. In mijn eerste project heb ik de vraag behandeld hoe nauwkeurig een cel de tijd kan schatten uit een collectie van oscillerende eiwitten die aangedreven worden door een biologische klok. Met analytische formules heb ik berekend hoe de precisie afhangt van het aantal uitlees-eiwitten, van de ruissterkte in chemische reacties, en van de kruiscorrelatie tussen de hoeveelheden van verschillende uitleeseiwitten. Uit dit onderzoek blijkt dat wanneer er weinig ruis is, kruiscorrelatie de nauwkeurigheid kan bevorderen. Hoe biologische klokken aan hun omgeving gekoppeld zijn is een van de meest prangende vragen van de chronobiologie. De koppeling wordt gekarakteriseerd via de zogenoemde Fase-Respons Curve (FRC). Deze beschrijft hoe de fase van een klok verandert na een toegediend signaal, als functie van de fase waarin de klok zich bevindt op het moment dat het signaal aankomt. Elk organisme heeft een andere FRC, maar toch delen ze vaak bepaalde karakteristieken: vaak is er een positieve lob, die correspondeert met een positieve faseverschuiving. Daarna komt er een dode zone waarin de klok niet op externe signalen reageert, uiteindelijk gevolgd door een negatief dal. Hoe de prestatie van de klok afhangt van de precieze vorm

van de FRC, de sterkte van de koppeling tussen de klok en de omgeving, de intrinsieke periode van de klok, en de interne ruis, is niet goed begrepen. Om hier meer inzicht in te krijgen heb ik de klok gemodelleerd als een fase-oscillator met ruis, gekoppeld aan een extern signaal. Mijn resultaten laten zien dat er een optimale koppelingssterkte bestaat waarbij de wederzijdse informatie wordt gemaximaliseerd. Verrassend genoeg daalt de informatie bij een te sterke koppeling; dit wordt veroorzaakt door een niet-lineariteit in de afbeelding van de werkelijke tijd naar de fase van de klok, waardoor informatietransmissie bemoeilijkt wordt. Toch neemt de optimale koppelingssterkte toe met de interne ruissterkte. Daarnaast heb ik gevonden dat de optimale intrinsieke periode van de klok niet altijd precies 24 uur is. Vervolgens heb ik uitgebreid gekeken naar de optimale vorm van de FRC als functie van de ruissterkte. Een interessant resultaat is dat de breedte van de dode zone afhangt van de ruissterkte. Dit is een duidelijke voorspelling die experimenteel getest kan worden. Tenslotte heb ik verschillende theorieën ontwikkeld die het systeem succesvol beschrijven in diverse domeinen. In hoofdstuk vier komt de meest fundamentele vraag van dit proefschrift aan de orde: wat is het nut van een bonafide klok die autonoom kan tikken met een periode van 24 uur? Veel organismen gebruiken een dergelijke biologische klok. Er zijn echter cyanobacteriën en paarse bacteriën die in plaats van een klok een soort zandloper hebben die niet zelf kan oscilleren, maar die elke dag opnieuw gezet moet worden. Een bonafide klok is een zogenaamde limietcyclus oscillator, een systeem met een limietcyclus attractor, terwijl een zandloper een gedempte oscillator is, een systeem met een puntattractor. Ik heb eerst drie verschillende computermodellen bestudeerd, die door cyano- en paarse bacteriën geïnspireerd zijn; twee modellen zijn gedempte oscillatoren, terwijl het laatste een limietcyclus oscillator is (een ongedempte oscillator die zelfstandig, zonder aandrijving, kan oscilleren). Het hoofdresultaat is dat de gedempte en limietcyclus oscillator ongeveer even goed werken bij weinig ruis in het signaal, maar dat de laatste oscillator veel beter is bij een hoge ruissterkte. Het is dus duidelijk dat de limietcyclus oscillator veel robuuster is tegen signaalruis. Ik vervolg de analyse met de vraag of deze observatie afhangt van de details van het systeem, of dat dit een generiek fenomeen is. Hiervoor gebruiken we het gevestigde Stuart-Landau model, dat analytisch kan worden bestudeerd en waarin we naar universeel gedrag hebben gezocht. Het Stuart-Landau model beschrijft een zwak-niet lineaire oscillator dichtbij de Hopf-bifurcatie, waar autonome trillingen tevoorschijn komen. Door een enkele parameter te veranderen kan het systeem met gedempte oscillaties omslaan naar een systeem met autonome oscillaties. Ik vond dat dit model de hoofdresultaten van de computermodellen kon reproduceren. Dit laat zien dat limietcyclus oscillatoren in het algemeen robuuster zijn tegen signaalruis dan gedempte oscillatoren Een intuïtieve verklaring is dat gedempte oscillatoren zich niet kunnen ontdoen van het volgende compromis tussen signaal en ruis, terwijl limietcyclus oscillatoren dat wel kunnen: door de koppeling tussen oscillator en signaal in een gedempte oscillator te verzwakken wordt de ruis minder doorgegeven, maar wordt de amplitude van de oscillatie evenredig aangetast. Bij limietcyclus oscillatoren gaat de doorgegeven ruis ook naar beneden bij een lagere koppelingssterkte, maar in tegenstelling tot het gedempte systeem blijft de amplitude hier praktisch gelijk. Dit is een inherente, robuuste eigenschap van de limietcyclus. In het laatste hoofdstuk van dit proefschrift behandel ik de ontwerpprincipes van het circadiaan metabolisme. Hierbij onder-

zoek ik specifiek het metabolisme van cyanobacteriën, welke fotosynthese gebruiken om energie te verkrijgen. Dit betekent dat de omgeving een beperking oplegt aan de cyanobacteriën: fotosynthese is alleen gedurende de dag mogelijk, zodat de bacteriën 's nachts andere energiebronnen nodig hebben. Hier heb ik geprobeerd te begrijpen wat de optimale strategie is om het metabolisme in te richten en of dit kan verklaren waarom veel cyanobacteriën alleen gedurende de dag groeien. Daartoe heb ik een fenomenologisch model genomen dat de relatie tussen de groei en het proteoom in de bacterie Escherichia coli succesvol beschrijft. Ik heb dit model uitgebreid zodat ik er de specifieke cyanobacterie Cyanothece mee kon onderzoeken. Gedurende de dag fixeert deze bacterie koolstof door fotosynthese, waarbij een deel wordt gebruikt voor de groei en een ander deel wordt opgeslagen in de vorm van glycogeen. 's Nachts fixeert de bacterie stikstof en slaat deze op in het polymeer cyanofycine. Het model voorspelt een extreme groeistrategie, waarbij cellen alleen overdag groeien, zoals ook experimenteel is vastgesteld. Dit komt voort uit de noodzaak om overdag glycogeen en 's nachts cyanofycine op te slaan, en is te begrijpen via de groeiwetten die voor E. coli gelden. De analyse laat echter ook zien dat de langzame nachtelijke groei een groot struikelblok vormt voor het implementeren van deze strategie. Hierbij komt de klok van pas, want door de kennis over te tijd te gebruiken kan de cel anticiperen op overgangen tussen dag en nacht, en zo de cel in staat stellen om de optimale groeistrategie toe te passen. Dit is waarschijnlijk het eerste onderzoek dat kwantitatief laat zien hoeveel voordeel een biologische klok oplevert. Concluderend heb ik in dit proefschrift methoden uit de statistische natuurkunde toegepast om te onderzoeken hoe cellen de tijd betrouwbaar kunnen schatten, hoe de klok gekoppeld moet zijn aan externe signalen, wat de voordelen van een zelfstandig opererende klok zijn, en hoe kennis over het tijdstip nuttig is om het metabolisme bij te sturen.

ACKNOWLEDGMENTS

Almost five years ago I crossed for the first time the amolf gate. Full of hope and curiosity for this shiny green institute I immediately felt welcome. The sensation that here there is an environment where I can freely develop rigorous ideas with creativity amused me strongly. This outstanding environment has helped me to try answering scientific questions with freedom and curiosity.

First I would like to thank Pieter Rein, to have taught me a lot of things, helped to define my ideas and transmitted to me a beautiful passion for science. I admire you for the extraordinary enthusiasm and strength that you put in understanding problems. I learnt how to try to tackle scientific questions in the most exhaustive way without letting anything to doubt. I feel honoured to have discussed problems and ideas until late in the night, improving knowledge together. I really thank you also to have shown me how not to be arrogant and presumptuous with ideas and conclusion, but always willing to question yourself and be open to learn. To have been able to sharpen my chaotic thoughts and give to them always the correct direction. I want to thank you also to have shared with me beautiful experiences also outside the working environment. I am really happy to had the occasion to spend my last four years in your group.

David, you have been a great source of inspiration and always have given to me a critical and deep point of view on our subjects. I have really learned from you not to be sloppy on ideas and conclusion from any point of view. I guess this is a great way to develop science.

To Klaas, to give to me always a practical and experimental point of view on our theories.

I want to thank also all the people in my group, Joris, Adithya, Harmen, Giulia, Maarten, Yao, Matthijs, to have shared with me useful discussions and helped me to get different point of view on my research. Particularly I would like to thank Maarten for have shared a project with me and to have had a great back and forward exchange of ideas. To Adithya, to have been close to me through all my phd. To have helped me to write manuscripts and to have been open to discuss whatever kind of scientific problems. Worthy of note, the endless ping-pong night where the velocity of your balls crossed the physical limit of the light velocity several times. Saala. Joris, to have shared with me a lot of knowledge on circadian clocks, and to have been always helpful and available to discuss and solve problems. Harmen to have solved riddles together, and to be always open to hear my ideas. To be interested in a wide range of scientific argument and to share with me the beauty of finding the same math to describe completely different scientific topics. Giulia, to often have tried to solve together problems regarding information theory and probabilities. Matthijs, to try to understand together the details of the computation of tricky probability functions. Moreover I would like to thank all the other group members passed in our group when I was here: Chris, Tomek, Rasa, Annouk, Renske, Sostke to had the patience to hear my group meeting presentations and give me good insights.

I want to thank Jacopo and Pepe, to have shared with me the life in these last years. To have been close to me in happiness and sad moment, to always have given me a smile and a hug when I needed. To have being available to hear my psychological and scientific troubles helping me with a real friend point of view. To have the strength to be light for the daily problems going always towards each other. Also Tarq and Titta to have given to me the opportunity to go together in the countryside, to have cooked together, to have the strength of smiling in tough moment and always being positive. To share the beauty of living putting a little bit of fantasy in the daily things. To have thrown dais together and adulated the laser sword. Pia bene.

I want to thank Shanti, to have been a great partner in this last period of my life. To have given me energy to do whatever passed through my mind without feeling any tire never. To help me to go beyond my limits and do not be ashamed to do errors. To always give me more than smile in tough moments and the courage to overcome my weaknesses. To have shared an enormous amount of amazing experiences and adventures together, that helped me to find a peaceful life where I could freely express my creativity. Di sopra.

I want to thank all my former office mates and paranymphs: Jenny, Agata, Simone Maga and Joleen. . Agata, to have been a great friend and office mate through all my phd. To have given to me great moments of happiness in normal working days, and to sharpen me back in foggy moments. To have reassured me in sad moments, to have given open fire to the craziness when it was needed. Thank you to have tolerated all my weirdness and have shared yours. Thank you Colonel.

To Simone, to have share the office together and always have been great with me. To share our sentimental problems, and always been open to hear me in anything. To have tolerated something that maybe was not tolerable like the engine of my boat inside the office close to your desk for a week.

Maga to have introduced me in amolf, to have shared with me all kind of scientific knowledge, to have fun to speak about science in every moment. Sharing a project together was amazing, still maybe the most fun part of my phd. I would like to thank you also to have given to me strength to believe in myself and in my ideas, to be proud of my little results and not to be depressed when things were not working.

Jenny to the power that you spread around. To the cloud of happiness that you are able to transmit to the environment. Your smiles and your laugh have been always a sunny island also in gray days. Thank you to have understood my limits and helping me to face them. For the trips together and to always have the strength to let me feel light. On fire.

A particular remarks I want to give to the Amolf Python team: Jacopo, Nicola, Mario, Luc, Joleen and Bela. To have developed together the knowledge of a new programming language and to have fun to organize courses for the other Amolf people. Particularly I want to thank Bela, you have strongly transmitted to me the sensation of having fun on learning something, that I feel it is one of the most deep thing that I have got in these past years.

Moreover, I want to thank all the other colleagues of amolf that shared with me these years. Like Marco to have shared with me a point of view on a lot of theoretical problems. Nico that has done his literature thesis with me, we had very nice and high quality

discussions about metabolism and general wonders of biology. Martijn to have been my dutch guide everywhere. Giorgio mbare, Yuval, Bart, Celine, Federica, Giulia, Melle, Felicio, Guizela, Keita, Giuzzio, Florian, Anders, Steven, Viktoria, Cristina, Parisa, Jasmijn to have had lunches and coffees together always helping me to have a minute out of the focus. Wibe and Clyde to have shared very funny moments. Marjo, Juliette and Ad to have donated me a welcome smile every morning. The Vu people, Felix, Douwe, Fabio and Luca to have shared a parallel existence and many fun moments, like swimming in the canals in winter nights. Andrea Tiseni, for the bike adventures, the running time, the marathons, the table tennis at Nikef, the forex, the crypto currency, the irrationality and the maghine.

Friends from everywhere that have been close to me from a long period and always supported me in everything, Vins, Adriano, Marco, Saverio, Emilio, Matteo, Nippa, Michele, Dario, Giacometto, Giuseppe, Chiara, Lucia e Fiammetta. Francesca to have given me a great help for the cover, Steven and his amazing energy, Bertus for the chess matches, Ben for the affection and Oreste to be the most holy god cat ever appeared.

My colleagues-friends from the university of Rome, Edoardo, Andrea, Roberto, Carlo, Paolo, Jonny, Alfredo, Francesca, Marco, Ilaria and many others with whom I have studied together and developed a beautiful love for physics. To have the patience to explain me things that maybe I would not have understood, to share stresses and excitement for exams and to have grown up together. Andrea de Martino to have introduced me to biological physics and have taught me an enormous amount of knowledge on this topic.

In fondo (non nel senso alla fine ma nel profondo) voglio ringraziare la mia famiglia, mia mamma Nicoletta mio papà Franco e mia sorella Anna. Mi avete aiutato a diventare curioso e trasmesso passioni, mi avete supportato attraverso tutta la mia vita standomi vicini sempre in momenti belli e difficili, facendomi sentire orgoglioso e coraggioso di quello che facevo e di avermi aiutato a crederci. Daje.

LIST OF PUBLICATIONS

Chapter 2
Monti M., ten Wolde PR, Lubensky DK (2016) *The accuracy of telling time via oscillatory signals* Phys. Biol. 13 (2016) 035005
doi:10.1088/1478-3975/13/3/035005

Chapter 3
Monti M, Lubensky DK, ten Wolde PR - *Optimal entrainment of circadian clocks in the presence of noise.*
Physical Review **97** (2018), 032405
doi.org/10.1103/PhysRevE.97.032405

Chapter 4
Monti M, Lubensky DK, ten Wolde PR - *Robustness of clocks to input noise.*
Submitted to Physical Review Letters

Chapter 5
Monti M, Lubensky DK, ten Wolde PR - *Theory of circadian metabolism*
Manuscript in preparation